Open problems in the physics of neutrino interactions with nucleons and nuclei

Tesis doctoral

David Eduardo Saúl Sala

Programa de Doctorat en Física
Institut de Física Corpuscular
Universitat de València

Director:
Luis Álvarez Ruso

Octubre 2020

Dr. Luis Álvarez Ruso, Científico Titular del Consejo Superior de Investigaciones Científicas,

CERTIFICA:

Que la presente memoria **"Open problems in the physics of neutrino interactions with nucleons and nuclei"** ha sido realizada bajo su dirección en el Departamento de Física Teórica de la Universidad de Valencia por **David Eduardo Saúl Sala** como Tesis para obtener el grado de Doctor.

Y para que así conste, en cumplimiento con la legislación vigente, presenta ante el Departamento de Física Teórica, la referida memoria, firmando el presente certificado.

Valencia, a 28 de octubre de 2020.

Firmado por ALVAREZ RUSO LUIS - 26748459B el día 28/10/2020 con un certificado emitido por AC FNMT Usuarios

Fdo: Luis Álvarez Ruso

A Lara

Agradecimientos

En primer lugar quiero agradecer a mi director de tesis, Luis, por su orientación y ayuda en todos los proyectos que hemos iniciado durante el doctorado. Le agradezco a Manolo que me introdujera en su grupo de investigación para hacer el TFG allá por 2013, lo que terminó desembocando en la realización de la presente tesis. También tengo presente a Eulogio y Juan, con los que he compartido muchas horas del café a lo largo de estos años.

I want to thank Rafi for all the time he spent with me and all his help when I needed it.

I am also grateful to Krzysztof for being so kind during my stay at Wroclaw. I am very happy to have had the opportunity to work at his group, where I learned so many things. Jan, Cezary and Tomasz, also made being away from home more bearable during those months, and I really appreciate it.

Thanks to Jorge Morfin, because he made it possible for me to do a research stay at Fermilab. It was great to be with the members of Minerva's group in the village. Also I had the opportunity to work with Steve Dytman, who found some time to teach me the basics of GENIE. Thank for the funny moments to Huma, Marvin, Ivan, Luis, Edgar, Miguel, Raquel, Barbara, Jose, Faiza, Carlos, David and Zubair.

Sin duda, las personas con las que más momentos he pasado en el IFIC han sido Pedro, "gurú del fortran y líder de la secta del pgfplots", Rafael y Vinicius. En ellos he encontrado un gran apoyo y amistad.

En estos años he podido conocer a mucha gente que de una manera u otra ha pasado por el grupo y con la que he compartido muy buenos momentos, gracias a Javi Fuentes, Francesca, Astrid, Asia, Gustavo, Neus, Fernando, Noemi, Uchino, Zhi-Feng, Melahat y Miguel.

Me siento también muy afortunado de contar con numerosos amigos, que significan mucho para mi. No puedo no mencionar aquí a Miguel, mi "asesor gastor", Juan, que me enseñó que se puede programar mucho mejor,

Laura y Carmen, con los que he compartido viajes, cenas y una infinidad de momentos para recordar A Fabri mi compañero de fatigas en el laboratorio años atrás, que sigue escuchando mis problemas a día de hoy No me olvido tampoco de las videollamadas multitudinarias durante la cuarentena, que me alegraron el cumpleaños, gracias a todos los miembros del "Macrogrupo" que, aun en la distancia, se preocuparon de seguir en contacto. Especialmente, gracias a Gustavo, Manolo y José Antonio, que han llegado a ser como una segunda familia, pudiendo contar con ellos para todo, y repitiendo incluso en las mudanzas...

Quiero agradecer también a mi familia, cuyo apoyo ha sido fundamental no solo durante el periodo del doctorado, sino durante toda mi vida. A mi madre, sin la que no habría podido llegar hasta aquí. A Tomás y Loli, por todo su cariño y apoyo (y los táperes de comida...) y a Jaime y Raquel, por las sobremesas los domingos de paella.

Finalmente, quiero agradecer a Lara por todo su amor y comprensión, por compartir conmigo los buenos momentos y por aguantarme, consolarme y animarme en los malos. No me imagino una vida sin ella a mi lado.

A todos ellos les agradezco toda la ayuda y los consejos que me han ofrecido durante esta etapa de mi vida y les deseo una vida larga y prospera.

Contents

Resumen

Ha pasado casi un siglo desde que Wolfgang Pauli postulara la existencia de neutrinos por primera vez, en su carta a la conferencia de Tubingen en 1930. Esta partícula, que fue propuesta como una medida desesperada para resolver el problema de la conservación de la energía en la desintegración β, se ha convertido en un campo de estudio muy importante, tanto de la física teórica como de la experimental. Siendo una partícula que solo interacciona débilmente, su detección presenta un gran desafío. De hecho, pasaron más de 20 años hasta que se detectó por primera vez en el experimento de Cowan y Reines en 1956.

Con la detección de los neutrinos solares apareció un nuevo problema, debido a que se detectaban menos neutrinos de los que se predecían. La solución a esta cuestión vino de la teoría de oscilaciones de Pontecorvo. En esta teoría los neutrinos serían partículas capaces de oscilar entre sus estados de sabor. Este fenómeno implicaría que los neutrinos tendrían masa, en contradicción con las conclusiones de Fermi y Perrin en 1933. La solución completa al problema de los neutrinos solares fue la combinación de esta teoría con el efecto Mikheyev-Smirnov-Wolfenstein, que describe cómo se ve afectado el patrón de oscilaciones debido a la interacción con la materia.

Hoy en día, los neutrinos tienen un papel fundamental en la descripción de los procesos débiles, englobados en la teoría del Modelo Estándar, que es capaz de dar una buena descripción de las partículas fundamentales y sus interacciones. Sin embargo, en esta teoría los neutrinos aparecen como partículas sin masa, en contradicción con la evidencia experimental de las oscilaciones de sabor. Durante las últimas décadas han aparecido numerosas teorías, que incluyen términos de masa para los neutrinos, como extensiones del Modelo Estándar, y los experimentos todavía no son capaces de excluir algunos de ellos. Para extraer los parámetros de oscilación de las medidas experimentales, los análisis dependen de modelos de interacción entre neutrinos y núcleos. Por lo tanto, la comprensión teórica de los efectos nucleares

es esencial para la interpretación de los datos. Solo con medidas precisas y modelos bien probados es posible minimizar las incertidumbres sistemáticas en los flujos de neutrinos, fondos y respuestas de los detectores.

A lo largo de esta tesis abordamos la interacción de neutrinos con nucleones y núcleos, en diferentes escenarios. En el rango entre 0.1-20 GeV, los procesos entre neutrinos y núcleos se pueden dividir en tres categorías principales [1]: cuasielásticos (QE), producción de resonancias y dispersión profundamente inelástica (DIS). Estos tres tipos de procesos se pueden dar tanto por corrientes cargadas (CCs), mediadas por un bosón W, como por corrientes neutras, donde el mediador es el bosón Z, Fig. 1.1.

Los procesos QE, Fig. 1.1a, es el mecanismo principal para neutrinos de energías de hasta 1 GeV. La denominación cuasiélastica se refiere al hecho de que el neutrino cambia su identidad por un leptón cargado. Si el leptón saliente sigue siendo un neutrino, la reacción es elástica, pero es conveniente agrupar los dos tipos de interacción juntos.

Los procesos de producción de resonancias, Fig. 1.1b, son parte importante en las interacciones de neutrinos con energías en el rango 0.5-3 GeV. En esta región, los grados de libertad efectivos que se escogen son bariones y mesones; un nucleón tiene una transición a un estado excitado (N^* o Δ). Aunque la desintegración a un pión es el proceso más importante, las resonancias también pueden desintegrarse emitiendo múltiples piones, kaones y fotones.

A energías mayores, la sección eficaz está dominada por el DIS, Fig. 1.1c, donde las funciones de estructura del nucleón se pueden escribir en términos de las funciones de distribución de partones (PDFs) para quarks, antiquarks y gluones. La habilidad única de las corrientes débiles de "probar" sabores aislados de quarks, mejora significativamente el estudio de las PDFs. Los estudios con alta estadística de la estructura de partones de los nucleones, usando neutrinos, complementan los estudios con sondas electromagnéticas.

Una situación análoga se da cuando la interacción tiene lugar en el núcleo atómico. En este caso, sin embargo, las dinámicas internas de los nucleones constituyentes complican en gran medida su descripción. La sección eficaz de la dispersión de neutrinos en núcleos es sensible a la misma estructura interna determinada por la cromodinámica cuántica, que también ha sido probada en procesos electromagnéticos, como la dispersión de leptones cargados en núcleos.

En el Capítulo 2 se discuten de forma general los principales conceptos sobre interacciones de neutrinos. El Capítulo 3 presenta en más detalle la dispersión QE de neutrinos en nucleones y núcleos, utilizada a lo largo de la

tesis.

Durante las últimas décadas se han llevado a cabo una serie de experimentos de neutrinos. Gracias a ellos se han realizado medidas de precisión de los ángulos de mezcla y la diferencia de masas al cuadrado de los tres sabores de neutrinos del Modelo Estándar. En la realización de este tipo de medidas se han utilizando diferentes fuentes de neutrinos, como son los solares, los atmosféricos o los procedentes de aceleradores. Ejemplos de experimentos que han sido importantes en esta tarea son K2K, T2K, MINOS o SNO.

Sin embargo, durante el desarrollo de algunos experimentos de oscilaciones de neutrinos aparecieron anomalías cuya explicación podría implicar nueva física. Una de estas discrepancias se observó en el detector LSND (*Liquid Scintillator Neutrino Detector*) construido en el Laboratorio Nacional de Los Álamos. En este experimento se producían antineutrinos muónicos de baja energía, de 0 a 53 MeV, a partir de la desintegración de piones en reposo, que se detectaban en el LNSD a 31 m del blanco [2]. Se observó un exceso de antineutrinos electrónicos de 3.8 σ, que se interpretó como una oscilación en la región de diferencias de masa al cuadrado en torno a 1 eV^2 en el marco de una conjetura de oscilaciones de neutrinos con un modelo simplificado con solo dos sabores.

Para estudiar en mayor detalle la señal detectada por LSND, se diseñó MiniBooNE (*Mini Booster Neutrino Experiment*) en Fermilab (*Fermi National Accelerator Laboratory*). En este nuevo experimento la energía del haz de neutrinos era un orden de magnitud mayor, lo que implica errores sistemáticos muy diferentes, aunque para reproducir unas condiciones similares se mantuvo aproximadamente la misma relación entre distancia al detector y energía del flujo de neutrinos. Al aumentar la distancia de forma proporcional, las dos posibilidades eran: que las medidas fueran consistentes con las de LSND, lo que confirmaría el modelo de dos sabores como buena aproximación para la explicación del efecto; o que no se detectara señal, lo que descartaría la hipótesis hecha en LSND. Una vez sustraído el fondo, tanto en modo neutrino como antineutrino se encontró un exceso de neutrinos electrónicos similar al de LSND, pero no totalmente compatible.

Actualmente la anomalía de MiniBooNE es difícil de explicar en el marco de las oscilaciones de neutrinos de tres sabores, bien establecido por otros experimentos. Han aparecido muchas teorías para intentar resolver este problema. Análisis recientes descartan la posibilidad de que este exceso se deba a una, dos o tres familias de neutrinos estériles Esto apunta a una nueva explicación, que no involucre oscilaciones. Otras maneras de explicar

la anomalía pasan por estudios más profundos de las señales de fondo, como por ejemplo en la Ref. [3] aunque de momento no se ha propuesto ninguna explicación convincente de este tipo.

En el Capítulo 4 analizamos una propuesta para explicar el exceso de eventos en el experimento MiniBooNE, desarrollada en la Ref. [4] y basada en un modelo propuesto en la Ref. [5]. En este modelo tenemos un neutrino pesado, con una masa en torno a los 50 GeV, que se produciría en la interacción entre el neutrino ligero incidente y el propio material del detector. Después, este neutrino pesado se desintegraría emitiendo un fotón y un neutrino ligero. Los detectores de tipo Cherenkov, como MiniBooNE, no son capaces de distinguir entre la señal producida por un fotón de la de un electrón. Por este motivo este modelo podría ser capaz de explicar la anomalía.

En nuestro análisis, hemos mejorado el cálculo de las interacciones de neutrinos con nucleones y núcleos del modelo de neutrinos pesados, tanto para los canales coherentes como para los incoherentes. Nuestros resultados incluyen la producción de neutrinos pesados en procesos electromagnéticos y también de interacción débil. Hemos considerado la propagación de esta partícula en el interior del detector, antes de su desintegración. Los resultados que hemos obtenido se encuentran en desacuerdo con los datos del exceso de MiniBooNE. Al añadir la eficiencia de detección del detector al cálculo, los resultados se acercan un poco más a los datos, pero aún así no tenemos un buen acuerdo entre ambos. La mayor discrepancia entre la teoría y los datos está en las distribuciones angulares de fotones. Con los parámetros originales del modelo, la contribución incoherente está muy suprimida, lo que resulta en distribuciones angulares con picos muy pronunciados para ángulos muy pequeños, lejos de las observaciones experimentales. A continuación, realizamos un ajuste de los parámetros a los datos, respetando de los rangos permitidos por otros experimentos. Con el nuevo set de valores, la influencia de los canales de producción incoherentes es mayor que la de los canales coherentes, resultando en distribuciones angulares más anchas. En lo referente a las distribuciones de energía de los fotones, los nuevos cálculos también se encuentran más cerca de los datos experimentales. Asimismo hemos realizado un segundo ajuste de los parámetros, considerando las cotas más restrictivas de la Ref. [6], con resultados que, aunque se alejan más que nuestro primer ajuste de los datos, siguen siendo mejores que los cálculos con los parámetros originales. A pesar de obtener un mejor acuerdo, los resultados todavía no son capaces de hacer una descripción completa del exceso en ninguno de los casos que hemos considerado. Las cotas de los parámetros

no permiten realizar un ajuste que resulte en una mejor descripción de los datos. Aún así, no podemos descartar este modelo como una fuente de señal en el detector.

El Short-Baseline Neutrino Program de Fermilab cuenta con una nueva generación de detectores para hacer un estudio más profundo de las oscilaciones de neutrinos. Estos detectores utilizan la tecnología de LArTPCs para detectar neutrinos provenientes del haz de neutrinos producido en FNAL. Este tipo de detectores son capaces de distinguir la señal de un fotón de la de un electrón y, por lo tanto, comprobar la validez del modelo de neutrinos pesados. Siguiendo el mismo procedimiento que para el caso de MiniBooNE, hemos hecho predicciones de las distribuciones de fotones para los tres detectores del programa. Estos cálculos preliminares deberán ser mejorados en un futuro, teniendo en cuenta los flujos reales de los detectores, así como su eficiencia de detección. También hemos mostrado como la comparación de las distribuciones de la señal de fotones del modelo de neutrinos pesados con otras puede ser utilizada para distinguir su causa.

En el Capítulo 5 hacemos un análisis del factor de forma axial del nucleón que, siendo una propiedad fundamental del nucleón es además una fuente de incertidumbre en las amplitudes de las interacciones entre neutrinos y núcleos y, por lo tanto, en su sección eficaz, que es el ingrediente clave en los modelos de interacción. La parametrización más utilizada en la literatura es la función dipolar, que depende de un solo parámetro, M_A, y que no tiene un fundamento teórico sólido. Asimismo, esta parametrización se ha utilizado comúnmente para describir los factores de forma electromagnéticos del nucleón, aunque se han observado desviaciones de este comportamiento. En la Ref. [7] se muestra un análisis completo sobre este tema. Así pues, parece natural esperar desviaciones similares en el factor de forma axial.

Las parametrizaciones empíricas se ajustan a partir de datos experimentales de dispersión de leptones en nucleones. Como las interacciones electromagnéticas no ven la parte axial de la corriente, en el caso del factor de forma axial esta información se debe extraer de interacciones débiles. La reacción $\nu_l n \to l^- p$ es un proceso bastante simple y particularmente sensible a este factor de forma. Sin embargo, las medidas modernas de la sección eficaz se realizan en núcleos atómicos (principalmente ^{12}C), donde la determinación del factor de forma axial es difícil, debido a la presencia de correcciones nucleares, que tienen incertidumbres, y a la dificultad de aislar el canal de cuasielástico de una manera independiente de modelo. Una discusión más detallada se puede encontrar, por ejemplo, en la Sec. III de la Ref. [8]. Una determinación más directa y, en principio, menos dependiente del modelo

de determinar el factor de forma axial recae en los datos experimentales sobre deuterio de cámaras de niebla. Bodek y sus colaboradores realizaron un análisis globales de los datos de ANL, Refs. [9–11], BNL, Refs. [12, 13], FNAL, Ref. [14], y el CERN, Ref. [15], con actualizaciones de los factores de forma vectoriales, basadas en datos modernos de dispersión de electrones. En la Ref. [16] se obtuvo el valor de referencia de $M_A = 1.016 \pm 0.026$ GeV, con un error del 2.5%.

Por otro lado, recientemente se ha realizado un nuevo análisis del factor de forma axial basado en la expansión-z. Esta función solo está acotada por la estructura analítica y el comportamiento asintótico dictado por la cromodinámica cuántica. Los resultados se muestran en la Ref. [17] y son consistentes con la parametrización dipolar, pero con una incertidumbre mucho mayor. En particular el radio axial que obtienen es $r_A^2 = 0.46 \pm 0.22$ fm^2, que es compatible con el extraído de la parametrización dipolar, $r_A^2 = 12/M_A^2$, pero con un error ~ 20 veces mayor. Este radio axial también puede ser extraido de la captura de muones en protones. Un análisis reciente, Ref. [18], que utiliza la expansión-z obtuvo el resultado, $r_A^2 = 0.43 \pm 0.24$ fm^2, compatible con los resultados de dispersión de neutrinos.

Una prometedora fuente de información sobre el factor de forma axial es la simulación de la cromodinámica cuántica en el retículo (*lattice QCD*). Aunque el valor experimental del acoplamiento axial, g_A, ha sido repetidamente infravalorado en sus predicciones, el uso de mejores algoritmos ha llevado recientemente a resultados consistentes. Un análisis global de la zona de bajos Q^2 y dependencia en las masas de los quarks ligeros, de los resultados de las Refs. [19–21], utilizando teoría quiral perturbativa de bariones, ha encontrado $g_A = 1.237 \pm 0.074$ y $r_A^2 = 0.263 \pm 0.038$, Ref. [22]. El valor central de r_A^2 es considerablemente menor que los correspondientes de las determinaciones empíricas, pero al considerar las grandes barras de incertidumbre de la expansión-z resultan compatibles.

La elección de una forma funcional para el factor de forma axial puede alterar los resultados del análisis. Además, la elección de la cantidad de parámetros de una paramaterización dada es una cuestión delicada. Muy pocos parámetros resultan en poca versatilidad del modelo. A medida que el número de parámetros aumenta, el valor de χ^2 de los ajustes se reduce, pero llegado a cierto punto el ajuste tiende a reproducir las fluctuaciones estadísticas de los datos experimentales [23]. Utilizando métodos de redes neuronales se pueden obtener resultados con una menor dependencia del modelo. Este enfoque se ha utilizado en la colaboración *neural network parton distribution function* (NNPDF) para obtener funciones de distribución

de partones en nucleones a partir de datos de DIS, en la Ref. [24].

En nuestro análisis demostramos que se puede extraer información del factor de forma axial de forma independiente del modelo, a partir de los datos de dispersión de neutrinos en deuterio. En contraste con los métodos paramétricos, donde se adopta una parametrización concreta de la función, en base a argumentos físicos, el análisis semi-paramétrico permite construir un modelo estadístico, en términos de densidades de probabilidad, que son utilizadas para la inferencia estadística. Al estar basada en motivaciones físicas, el resultado obtenido no es extrapolable más allá de la región donde el ajuste es válido. Por otro lado, los resultados pueden contener nueva física, fuera de las suposiciones de un modelo específico y tampoco se ven afectados por un posible modelo erróneo o deficiencias en el conjunto de datos experimentales.

Para realizar el análisis, hemos utilizado redes neuronales *feed forward*, que constituyen un conjunto de funciones con habilidades adaptativas ilimitadas [25]. Con esta elección se puede eliminar cualquier prejuicio en los resultados, introducidos por la elección de una forma funcional concreta de la función para realizar el ajuste. Dependiendo del número de parámetros adaptativos, se pueden obtener diferentes variantes del modelo estadístico. En este contexto, la estadística bayesiana ha probado ser una herramienta muy efectiva [26]. Sus métodos permiten hacer comparaciones entre diferentes modelos y controlar el número de parámetros en los ajustes. Nosotros utilizamos el marco de referencia para redes neuronales formulado por MacKay en la Ref. [27]. Éste se adaptó anteriormente para modelar los factores de forma eléctrico y magnético en la Ref. [28].

Nuestros resultados con el set completo de datos de ANL muestran un factor de forma axial con una pendiente positiva a $Q^2 = 0$, y un máximo local a bajo Q^2. La inclusión de las correcciones nucleares del deuterón reduce el pico del factor de forma. Al eliminar del ajuste los datos de la zona por debajo de $Q^2 = 0.10$ GeV^2, obtenemos un valor del radio axial consistente con las determinaciones previamente disponibles. Esto en principio sugiere que las correcciones del deuterón juegan un papel crucial a bajos Q^2, pero también podría ocurrir que los errores en los datos experimentales de esta región hubieran sido subestimados. Los análisis eliminando los datos correspondientes a bajos Q^2, si bien no muestran desviaciones significativas de las parametrizaciones previas, se caracterizan por tener unas incertidumbres menores que en el caso de la parametrización dipolar. En este punto se hacen necesarias nuevas medidas experimentales en hidrógeno y deuterio para mejorar nuestra comprensión de la estructura axial del nucleón. Técnicas

como las que hemos utilizado se presentan como una valiosa opción a tener en cuenta en futuros estudios.

Con las mejoras en los detectores de neutrinos se abren la posibilidad de explorar nuevos procesos con secciones eficaces más pequeñas. Este es el caso de la producción de kaones en la dispersión entre neutrinos y nucleones. La producción de kaones cargados ($\nu_\mu \mathrm{CH} \to \mu^- K^+ X$) se ha medido recientemente en el experimento MINERνA, lo que abre una nueva ventana al estudio en más detalle de los mecanismos de producción de extrañeza. Los procesos débiles con kaones en el estado final pueden ser iniciados, bien por mecanismos que conservan extrañeza ($\Delta S = 0$), o bien por los que la cambian ($\Delta S = 1$). A pesar de que los procesos con cambio de extrañeza ($1K$) están suprimidos por el ángulo de Cabibbo, comparados con los que la conservan (YK), estos últimos involucran la producción masiva de hiperones (Y), lo que impulsa la cota de la reacción a mayores energías del neutrino incidente. Por lo tanto, para neutrinos por debajo de 2 GeV, las reacciones $1K$ están favorecidas [29, 30]. En núcleos, las interacciones en los estados finales de los kaones producidos no son muy fuertes, debido a la ausencia de resonancias bariónicas. Sin embargo, los kaones también se pueden producir en colisiones secundarias, aumentando en gran medida la dificultad de la extracción de información sobre procesos elementales de producción $1K$, en experimentos con blancos nucleares.

En el Capítulo 6 estudiamos el modelo propuesto en la Ref. [30] para reacciones del tipo $\nu_l N \to l^- K N$. Este modelo está basado en diagramas de tipo árbol, por lo que la unitariedad de la matriz S no se respeta. Nosotros hemos modificado el modelo, restaurando parcialmente la unitariedad. Esto se ha hecho imponiendo el teorema de Watson a la parte dominante de las contribuciones vectorial y axial, en el sector de los números cuánticos apropiados de momento e isospín. Este método se basa en el modelo desarrollado en la Ref. [31], que incluye el cálculo de las fases de Olsson para la amplitud del término dominante, en nuestro caso el de contacto. Estas fases toman los valores requeridos para que se cumpla el teorema de Watson. En última instancia, los datos experimentales deben discriminar entre las dos soluciones matemáticas que se obtienen para las fases de Olsson, pero una de ellas es una firme candidata a ser una solución no física, debido a que produce grandes cambios en los observables, que son poco probables debido a que la interacción KN es relativamente débil. En su lugar, la solución alternativa produce correcciones pequeñas en la sección eficaz, que entrarían en las incertidumbres del modelo. Esto le daría validez al modelo de diagramas tipo árbol, construido a partir del orden dominante del Lagrangiano

quiral en la región cinemática que consideramos. También hemos estudiado el comportamiento de las funciones de estructura que caracterizan la dependencia en el ángulo azimutal de la sección eficaz, encontrando también una clara diferencia entre ambas soluciones. El impacto de la unitarización es visible en el hecho de que las funciones de estructura de los términos que violan paridad no se cancelan.

En el Capítulo 7 abordamos un interesante proceso coherente que resulta relevante actualmente: la emisión coherente de fotones mediada por corrientes neutras. Como los detectores de tipo Cherenkov tienen una señal fondo que proviene de los fotones producidos mediante este tipo de procesos, entre neutrinos y el propio material del detector, una buena estimación del número de eventos resulta importante. Existen modelos anteriores de interacción, basados en la conservación parcial de la corriente axial, que son capaces de realizar predicciones simples de la señal, pero los experimentos modernos, que tienen una mejor precisión, requieren mejores estimaciones. En las Refs. [32–34], la reacción coherente de producción de fotones por corrientes neutras se ha estudiado utilizando modelos microscópicos, que incluyen tanto contribuciones no resonantes, como la excitación de la resonancia $\Delta(1232)3/2^+$ y su posterior desintegración radiativa.En la Ref. [34] se incluyen también las resonancias bariónicas $N^*(1440)1/2^+$, $N^*(1520)3/2^-$ y $N^*(1535)1/2^-$.

En el Capítulo 7 presentamos una extensión del modelo de la Ref. [34], incluyendo resonancias bariónicas más pesadas, lo que amplía su validez a un mayor rango de energías, como las utilizadas en el experimento MINERνA. Además hemos realizado un tratamiento simplificado de las modificaciones de la $\Delta(1232)3/2+$ debidas al medio nuclear, que permite factorizar el factor de forma nuclear, comprobando la validez de los resultados obtenidos. De esta manera hemos acelerado significativamente los cálculos computacionales, haciendo posible la implementación del modelo en GENIE. Actualmente, en los generadores de eventos no hay ningún modelo para la emisión de fotones en procesos coherentes de corrientes neutras, por lo que la implementación de este modelo facilitará el trabajo experimental en el estudio de esta reacción en MINERνA, así como en los detectores del programa SBND.

Estimamos un rango de de validez de nuestros resultados para fotones con una energía de hasta 2.5 GeV aproximadamente. Hemos verificado que, para neutrinos incidentes con una energía por debajo de 1 GeV, el impacto en los resultados de la adición de resonancias más pesadas no es apreciable. El proceso mediado por la resonancia $\Delta(1232)3/2^+$ se presenta como la contribución dominante para neutrinos incidente de cualquier energía. Hemos

calculado las distribuciones de energía y angulares de los fotones emitidos en la dispersión coherente de neutrinos con núcleos, tanto para el caso de interacciones con neutrinos como con antineutrinos. La dependencia en la masa del blanco también ha sido explorada.

Los resultados que obtenemos predicen una señal fuerte para fotones emitidos en torno a 0.3 GeV, debida a la $\Delta(1232)3/2^+$, seguida por una cola donde también contribuyen de las resonancias $N(1520)3/2^-$, $\Delta(1700)3/2^-$ y $\Delta(1950)7/2^+$. Esta cola resulta en una señal de fotones en la que predominan ángulos pequeños. Para estimar la incertidumbre en el conocimiento actual sobre las propiedades de las resonancias bariónicas, incluyendo sus excitaciones electromagnéticas, hemos realizado los cálculos usando dos conjuntos de parámetros, con dos parametrizaciones diferentes de la dependencia en la masa invariante de la anchura de cada resonancia. Como era de esperar, la contribución de la $\Delta(1232)3/2^+$, de la que se conocen bien sus parámetros, es independiente de estos cambios, mientras que varios de los demás estados muestran una alta sensibilidad a las modificaciones en la masa, anchura, proporción del canal πN (del que el acoplamiento axial dominante se obtiene) y, particularmente, los acoplamientos de helicidad.

Por último en la Parte III se resumen los principales resultados y conclusiones obtenidos a lo largo de esta tesis.

Chapter 1

Introduction

Almost a century has passed since Wolfgang Pauli postulated for the first time the existence of neutrinos, in his letter to the Tübingen conference in 1930. This particle, which at that time was proposed as a desperate measure to restore energy conservation in nuclear β decay, has become the epicenter of a very active field of research in both theoretical and experimental physics. Being a particle which can only interact weakly, its detection becomes a very hard challenge. Indeed, its first confirmed signal took more than 20 years to appear, in the Cowan and Reines experiment at 1956.

With the solar neutrino detection, a new problem arose, as the number of detected neutrinos was smaller than the predicted one. The solution to this question was the Pontecorvo oscillation theory. In this theory, neutrinos would be particles able to oscillate between their flavor states. This phenomenon implies that neutrinos have masses, in contradiction to the suggestion by Fermi and Perrin in 1933. The full solution to the neutrino solar problem was the combination of this theory with the Mikheyev-Smirnov-Wolfenstein effect, which describes how the interaction with matter changes the oscillation pattern.

Nowadays neutrinos play a fundamental role in the description of weak processes, encompassed inside the Standard Model (SM) theory, which provides a comprehensive description of all the known fundamental particles and their interactions. However, in this theory neutrinos appear as massless particles, in contradiction with the experimental evidence of flavor oscillations. At present there are many alternative models to generate neutrino masses and to extend the SM, and the experiments are not yet able to exclude some of them. To extract the oscillation parameters from the measured particle yields, the experimental analyses have to rely on models for the neutrino-

nucleus interaction. Thus, the theoretical understanding of nuclear effects is essential for the interpretation of the data and represents both a challenge and an opportunity. Only with precise and well-tested models it is possible to minimize the systematic uncertainties in neutrino fluxes, backgrounds and detector responses.

Along this thesis we address the interaction of neutrinos with nucleons and nuclei, in different scenarios. In the range between $0.1 - 20$ GeV there are three main neutrino-nucleon scattering categories [1]: quasi-elastic (QE) processes, resonance production and Deep Inelastic Scattering (DIS). These three kinds of processes can proceed by both, charged-currents (CCs), mediated by a W boson, and neutral-currents (NCs), where the mediator is a Z boson, Fig. 1.1.

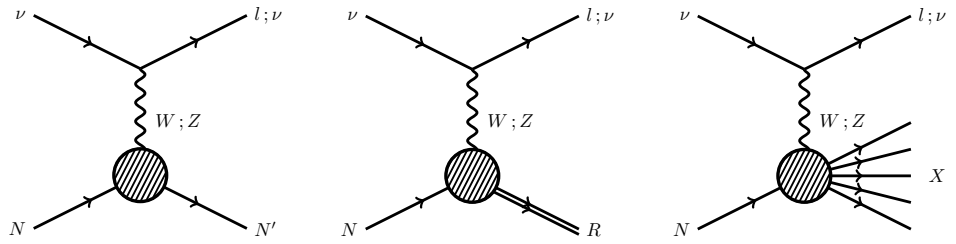

Figure 1.1: Diagrams of QE process (a), resonance excitation (b) and DIS between a neutrino and a nucleon.

QE, Fig. 1.1a, scattering is the main interaction mechanism for neutrinos with energies up to about 1 GeV. The term QE refers to the fact that the neutrino changes its identity to a charged lepton. If the outgoing lepton is still a neutrino, the reaction is denoted as elastic, but it is convenient to group them together.

Resonance excitation, Fig. 1.1b, is a large part of the response for neutrinos of energy in the range 0.5-3 GeV. In this region, the effective degrees of freedom are chosen to be baryons and mesons; a nucleon has a transition to an excited state (N^* or Δ). Although decay to single pion is most important, resonances also decay with emission of multiple pions, kaons, and photons.

At higher energies, the cross section is dominated by DIS, Fig. 1.1c, where the nucleon structure functions can be written in terms of Parton Distribution Functions (PDFs) for quarks, antiquarks and gluons. The weak current's unique ability to "taste" only particular quark flavors significantly

enhances the study of PDFs. High-statistics measurement of the nucleon's partonic structure, using neutrinos, will complement studies with electromagnetic probes.

An analogous situation occurs when the interaction takes place on a nucleus. In this case, however, the underlying dynamics of the constituent nucleons makes the description more demanding. The cross section for neutrino scattering from nuclei is sensitive to the same underlying structure determined by QCD, and as probed with pure electromagnetic processes, such as charged lepton scattering from nucleons and nuclei.

In Chapter 2 the main general concepts of neutrino interactions are discussed. Chapter 3 presents in more detail the QE scattering of neutrinos on nucleons and nuclei, which are used along the whole thesis.

The paradigm of three mixing flavors of neutrinos emerges from oscillation experiments with solar, atmospheric, reactor and accelerator neutrinos in which the square-mass differences and mixing angles have been determined with ever growing precision. However, some oscillations experiments reported anomalies which can imply new physics. One of them was reported by the MiniBooNE experiment at Fermilab. It has found an excess of electron-like events over the predicted background in both neutrino and antineutrino modes. Many theories have been proposed trying to explain this problem. Recent analyses discard the possibility that this excess is due to one, two or three families of sterile neutrinos [35]. This points out to a new explanation not involving oscillations. Other paths to explain the anomaly go through deeper studies about the background signal, for example in Ref. [3].

In Chapter 4 we critically analyze a proposal to explain the excess of events in the MiniBooNE experiment, developed in Ref. [4] and based in a model proposed in Ref. [5]. In this model we have a heavy neutrino, with a mass around 50 GeV, which would be produced in the interaction between the incoming light neutrino and the detector material. Then this heavy neutrino would decay emitting a light neutrino and a photon. The Cherenkov detectors, like MiniBooNE which are unable to distinguish a photon signal from an electron one. For this reason this model would be able to explain the anomaly.

In our work we describe in detail the different processes of heavy neutrino production, improving and expanding the models used before to calculate the interaction of the neutrino with nucleons and nuclei. We then analyze the propagation of the heavy neutrino inside the detector and its decay. Taking into account the detector parameters we make an estimation of the

signal that would be produced in MiniBooNE and we compare it with the excess.

The Short-Baseline Neutino Program (SBN) program at Fermilab incorporates a new generation of detectors to make a further study of neutrino oscillations. These experiments shall be able to confirm or discard the MiniBooNE signal. We have also predicted the signal from the heavy neutrino decays, for all the SBN detectors.

In Chapter 5 we analyze the nucleon axial form factor (FF), F_A, which is not only a fundamental nucleon property but also a source of uncertainty in the amplitudes of the interactions between neutrinos and nucleons and, therefore, in the cross sections, which are the key ingredient of the interaction models and simulations. The most common parametrization used in the literature is the dipole ansatz which depends only on a single parameter, M_A, and is not theoretically well founded. Bubble chamber experiments of neutrino scattering on deuterium collected a data set for the QE process, from which F_A can be extracted. For this purpose we have performed a semi-parametric analysis and obtained model-independent information about F_A from the ANL experimental data. For the analysis we have used feed-forward neural networks in a multilayer perceptron (MLP) configuration. The tool that allows us to choose between all the different results given by the neural networks is Bayesian statistics [26]. This framework has been applied to the extraction of electromagnetic FF from electron scattering data [28].

With the improvements in neutrino detection, new processes with smaller cross sections can be explored. This is the case of kaon production in neutrino-nucleon scattering. In Chapter 6 we study the model proposed in Ref. [30] for this kind of reactions. In this tree-level model, the unitarity of the S matrix is not respected. We have modified this model, by partially restoring unitarity. This has been done by imposing Watson's theorem to the dominant vector and axial-vector contributions in appropriate angular momentum and isospin quantum number sectors.

Chapter 7 presents a deep insight into another relevant and interesting coherent process: coherent photon emission mediated by NCs. As Cherenkov detectors have a background which comes from the signal of photons produced in this type of process between neutrinos and the detector material, a good estimate of the number of events is important. While previous interaction models based on partial conservation of the axial current (PCAC) [36] are obtain simplified predictions of the signal, more accurate experiments require better models. The microscopic model of Ref. [34] considers the neutrino interactions with a nucleon, taking into account the most relevant

processes at neutrino energies around 1 GeV. Then a coherent sum over all the nucleons in the nucleus is performed, including the nuclear effects form the medium. The main contributions to this reaction come from resonance excitation of the nucleons, with the $\Delta(1232)$ as the dominant interaction. In the original model three more resonances are considered, the $N(1440)$, $N(1520)$ and $N(1535)$.

While there are experiments with high energy fluxes as MINERνA, were the peak of the medium energy flux is at 6 GeV approximately, the range of validity of the microscopic model is insufficient. To extend this range, we added heavier resonances with invariant masses up to 2 GeV to the calculation, making the model useful for this type of fluxes. We have also performed and validated several approximations to speed up the computations, facilitating the implementation of the model in event generators. Indeed, its implementation in GENIE, where no description for this process is available, is currently under way.

Finally, in Chapter III we present an outlook of the thesis and our main conclusions.

Part I

Theoretical background

Chapter 2

Electroweak interactions in the Standard Model

In this chapter a brief description of the basic principles that rule the interaction between leptons and hadrons in the SM of Particle Physics is presented. The objective here is to clarify the conventions and notation used throughout the thesis, not giving a full description of the SM, that can be found in Quantum Field Theory (QFT) textbooks, *e.g.* Refs [37, 38].

2.1 Electroweak interaction Lagrangian

The electromagnetic (EM) and weak interactions are unified in the SM by the electroweak $\mathrm{SU}(2)_L \times \mathrm{U}(1)_Y$ theory of Glashow-Weinberg-Salam. Weak processes are divided in CC and NC interactions, where the mediators are the $W^{\pm}$ and Z massive bosons, respectively. The photons are responsible for EM interactions. In contrast to the latter, in the case of NC interactions, the coupling of left-handed chiral components of the fermionic fields to the Z boson differs to right-handed ones.[1]. In CC mediated reactions, only left-handed fermionic fields are involved.

The weak isospin (T) is the symmetry group $\mathrm{SU}(2)_L$ of the SM. Under this symmetry, fermionic fields with left-handed chirality are grouped in doublets, while right-handed fermionic fields are singlets [39]. For only one generation of leptons and quarks the weak isospin doublets are:

$$L_L = \begin{pmatrix} \nu_{eL} \\ e_L \end{pmatrix}, \qquad Q_L = \begin{pmatrix} u_L \\ d_L \end{pmatrix}. \tag{2.1}$$

[1]The chirality projection matrices for the Dirac fields are given in Appendix A.1

Singlets are the right handed fields e_R, u_R and d_R, since there are no right-handed components for neutrinos in the SM. The value of the third component of T is presented in Table 2.1. The generalization to three generations of fermions is straight forward adding analogous doublets and singlets for each family.

Table 2.1: Eigenvalues of the weak isospin T, and its third component T_3, for one generation of fermions.

	ν_L	e_L	e_R	u_L	d_L	u_R	d_R
T	1/2		0	1/2		0	0
T_3	1/2	-1/2	0	1/2	-1/2	0	0

The Lagrangian density, which describes electroweak interactions in the SM in terms of the electromagnetic, neutral and charged currents coupled to the corresponding gauge bosons, is given by

$$\mathcal{L}_{\text{int}} = -eJ^{\mu}_{\text{EM}}A_{\mu} - \frac{g}{2\cos\theta_W}J^{\mu}_{\text{NC}}Z_{\mu} - \frac{g}{2\sqrt{2}}\left(J^{\mu}_{\text{CC}}W^{\dagger}_{\mu} + \text{h.c.}\right) , \tag{2.2}$$

where A_μ is the photon while Z_μ and W_μ stand for the fields of the massive bosons. The coupling for the EM term is the electron charge, e. The weak angle θ_W defines the ratio of the vector boson masses and also relates the strength of the EM interaction with the weak coupling, g,

$$\cos\theta_W = \frac{M_W}{M_Z} , \qquad \sin\theta_W = \frac{e}{g} . \tag{2.3}$$

This coupling is also connected to the Fermi constant, G_F, by

$$\frac{G_F}{\sqrt{2}} = \frac{g^2}{8M_W^2} . \tag{2.4}$$

2.2 Leptonic currents

The lepton sector includes the interaction between the gauge bosons and electron, muon, tau leptons and the three flavors of neutrinos, Fig. 2.1. Although there is experimental evidence that neutrinos are massive particles, see *e.g.* Sec. 14 of Ref. [40], these masses are too small to be relevant in comparison with the energies at the scale of 1 GeV, that we consider throughout this thesis, therefore we only take into account left-handed massless neutrinos and the corresponding antineutrinos.

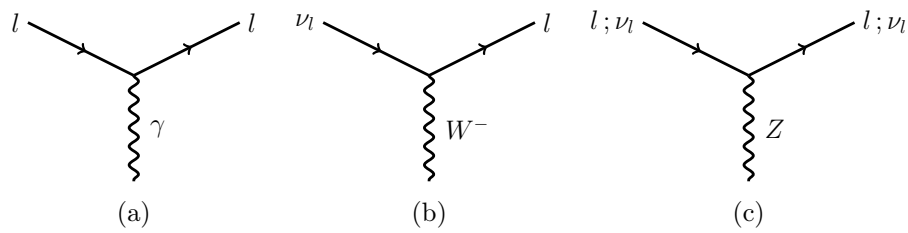

Figure 2.1: Diagram of the interaction vertex between a lepton and a vector boson for (a) electromagnetic, (b) charge current and (c) neutral current interactions.

The EM current is a Lorentz vector which couples to the photon field and reads,

$$j^{\mu}_{\mathrm{EM}} = \bar{l}\gamma^{\mu} l \,. \tag{2.5}$$

The relevant properties of the Dirac matrices γ^{μ} are discussed in Appendix A.1.

Even though the interaction between a lepton and a $W^{\pm}$ boson does not change the leptonic flavor, it turns a charged lepton into a neutrino or vice versa. The CC interaction has a V−A structure given by

$$j^{\mu}_{\mathrm{CC}} = \overline{\nu}_l \gamma^{\mu} \left(1 - \gamma_5\right) l \,. \tag{2.6}$$

The NC, as the EM interactions, does not change the identity of the lepton, but its structure is V−A like in the CC case,

$$\begin{gathered} j^{\mu}_{\mathrm{NC}} = \frac{1}{2}\overline{\nu}_l \gamma^{\mu} \left(1 - \gamma_5\right) \nu_l + \frac{1}{2}\bar{l}\gamma^{\mu} \left(g_V - g_A\gamma_5\right) l \,, \\ g_V = -1 + 4\sin^2\theta_W \,, \qquad g_A = -1 \,. \end{gathered} \tag{2.7}$$

In the above expressions for the currents, a sum over all the three leptonic flavors is implicitly understood.

2.3 Quark currents

Before considering nucleons or other hadrons, it is important to understand some properties of their constituents, the quarks. Although there are six flavors of quarks, we restrict our discussion to the light sector, which contains only u, d and s quarks. They form a triplet field in flavor space under the

symmetry of the unitary group SU(3). If we define q_f as a quark field of flavor f, for the triplet we have

$$q = \begin{pmatrix} q_u \\ q_d \\ q_s \end{pmatrix} . \tag{2.8}$$

We have dropped the color labels as electroweak interactions are color blind and the corresponding currents have a trace over color. This symmetry is exactly fulfilled if the quark masses are equal. For further details see for example Refs. [41, 42]. Under SU(3) there are eight conserved currents,

$$V_a^\mu = \overline{q}\gamma^\mu \frac{\lambda_a}{2} q \,, \qquad \partial_\mu V_a^\mu = 0 \,, \qquad a = 1 - 8 \,, \tag{2.9}$$

with λ_a the Gell-Mann matrices, that are summarised in Appendix A.4. If we consider the difference between quark masses , flavor currents are not conserved; instead, one has that

$$\partial_\mu V_a^\mu = \overline{q} \left[\mathbf{m}, \frac{\lambda_a}{2} \right] q \,, \qquad \mathbf{m} = \text{diag}\,(m_u, m_d, m_s) \,. \tag{2.10}$$

We will explore the conservation of currents later in this section.

Notice that if we restrict to only two flavors, with u and d quarks, the corresponding symmetry is the isospin SU(2) group. Under this symmetry, the u and d quarks form a doublet where the eigenvalue of the isopin operator is $I = 1/2$. The action of its third component on the quark isospin states is

$$I_3 \begin{pmatrix} q_u \\ q_d \end{pmatrix} = \frac{1}{2} \begin{pmatrix} q_u \\ -q_d \end{pmatrix} . \tag{2.11}$$

In this case, with only two quarks, Eq. (2.10) is reduced to

$$\partial_\mu V_a^\mu = \overline{q} \left[\mathbf{m}, \frac{\tau_a}{2} \right] q \,, \qquad a = 1 - 3 \,, \qquad q = \begin{pmatrix} q_u \\ q_d \end{pmatrix} . \tag{2.12}$$

where $\mathbf{m} = \text{diag}\,(m_u, m_d)$, and τ_{1-3} are the Pauli matrices described in Appendix A. Given the mass difference between quarks, isospin symmetry is more accurate than the SU(3) flavor one.

Since nucleons can be described as combinations of u and d quarks, isospin symmetry is inherited by the nucleon. Its consequences for nucleon electroweak currents are discussed in Sec. 3.2.

2.3.1 Electromagnetic quark currents

In the case of quarks, charges are different than for leptons, and, consequently, the coupling of the EM interaction in Eq. 2.2 shall be modified by a charge factor. The electric charge of the quarks, in units of e, are $Q_u = 2/3$ and $Q_d = Q_s = -1/3$. In matrix form in the SU(3) flavor space we have

$$Q = \begin{pmatrix} 2/3 & 0 & 0 \\ 0 & -1/3 & 0 \\ 0 & 0 & -1/3 \end{pmatrix} . \tag{2.13}$$

The charge operator can also be written in terms of the hypercharge and the third component of the isospin as

$$Q = \frac{Y}{2} + I_3 \, , \tag{2.14}$$

where the third component of isospin is a generalization of the SU(2) subgroup, given by

$$I_3 = \frac{\lambda_3}{2} = \begin{pmatrix} 1/2 & 0 & 0 \\ 0 & 1/2 & 0 \\ 0 & 0 & 0 \end{pmatrix} . \tag{2.15}$$

The hypercharge is defined as the sum of the baryon number and the strangeness, $Y = B + S$. The number of quarks, n_q, and antiquarks, $n_{\overline{q}}$, determine the baryon number, $B = \frac{1}{3}\left(n_q - n_{\overline{q}}\right)$. The strangeness depends on the number of s quarks and antiquarks, $S = -\left(n_s - n_{\overline{s}}\right)$. The hypercharge can also be expressed using the Gell-Mann matrix λ_8,

$$Y = \frac{\lambda_8}{\sqrt{3}} = \begin{pmatrix} 1/3 & 0 & 0 \\ 0 & 1/3 & 0 \\ 0 & 0 & -2/3 \end{pmatrix} . \tag{2.16}$$

As quarks are Dirac elementary particles, the structure of the electromagnetic current is given by,

$$j^{\mu}_{\mathrm{EM}} = Q\overline{q}\gamma^{\mu}q = \frac{2}{3}\overline{q}_u\gamma^{\mu}q_u - \frac{1}{3}\left(\overline{q}_d\gamma^{\mu}q_d + \overline{q}_s\gamma^{\mu}q_s\right) . \tag{2.17}$$

If we substitute Eqs. (2.14-2.16) in (2.17),

$$j^{\mu}_{\mathrm{EM}} = \frac{1}{2}\overline{q}\frac{\lambda_8}{\sqrt{3}}\gamma^{\mu}q + \overline{q}\frac{\lambda_3}{2}\gamma^{\mu}q = \frac{1}{2}V_Y + V_3 \, , \tag{2.18}$$

where we have defined the hypercharge current, V_Y, and the isospin current, V_3.

2.3.2 Weak quark currents

In NC interactions flavor is conserved. The expression for the current reads,

$$j^{\mu}_{\rm NC} = \sum_{f=u,d,s} \overline{q}_f \gamma^{\mu} \left[\left(T_3 - Q_f \sin^2\theta_W \right) (1-\gamma_5) - Q_f \sin^2\theta_W \, (1+\gamma_5) \right] q_f \,, \tag{2.19}$$

in terms of the third component of T and the electric charge. Explicitly for the three flavors of quarks, we have

$$\begin{aligned} j^{\mu}_{\rm NC} =& \overline{q}_u \gamma^{\mu} \left[\frac{1}{2} - \left(\frac{2}{3} \right) 2\sin^2\theta_W - \frac{1}{2}\gamma_5 \right] q_u \\ &+ \overline{q}_d \gamma^{\mu} \left[-\frac{1}{2} - \left(-\frac{1}{3} \right) 2\sin^2\theta_W + \frac{1}{2}\gamma_5 \right] q_d \\ &+ \overline{q}_s \gamma^{\mu} \left[-\frac{1}{2} - \left(-\frac{1}{3} \right) 2\sin^2\theta_W + \frac{1}{2}\gamma_5 \right] q_s \\ =& V^{\mu}_{\rm NC} - A^{\mu}_{\rm NC} \,. \end{aligned} \tag{2.20}$$

The expression for the NC shows the V−A structure. We can use Eqs. (2.14-2.16) in Eq. (2.20) to rewrite the vector part as

$$V^{\mu}_{\rm NC} = \left(1 - 2\sin^2\theta_W \right) V^{\mu}_3 - 2\sin^2\theta_W \frac{1}{2} V^{\mu}_Y - \frac{1}{2} V^{\mu}_S \,, \tag{2.21}$$

with

$$V^{\mu}_S = \overline{q}_s \gamma^{\mu} q_s \,. \tag{2.22}$$

For the axial part of the current we can write

$$A^{\mu}_{\rm NC} = A^{\mu}_3 - \frac{1}{2} A^{\mu}_S \,, \tag{2.23}$$

where we have defined

$$A^{\mu}_a = \overline{q} \gamma^{\mu} \gamma_5 \frac{\lambda_a}{2} q \,, \tag{2.24}$$

and

$$A^{\mu}_S = \overline{q}_s \gamma^{\mu} \gamma_5 q_s \,. \tag{2.25}$$

While the NC is diagonal in flavor, in the CC the initial and final quarks are different flavor states. Besides,the states with $T_3 = -1/2$ are not the weak eigenstates, instead, they are mixed. For three generations of fermions,

the unitary transformation that connects both sets of states is the Cabibbo-Kobayashi-Masakawa (CKM) matrix, U, given in Appendix A.3. The general expression for the CC reads,

$$j^{\mu}_{\mathrm{CC}} = (\overline{q}_u \overline{q}_c \overline{q}_t)\, \gamma^{\mu}\, (1-\gamma_5)\, U \begin{pmatrix} q_d \\ q_s \\ q_b \end{pmatrix} . \tag{2.26}$$

In our case, with only three flavors, the corresponding 2×2 section of the CKM matrix can be expressed in terms of the Cabibbo angle,

$$j^{\mu}_{\mathrm{CC}} = \overline{q}_u \gamma^{\mu}\, (1-\gamma_5) \begin{pmatrix} \cos\theta_C & \sin\theta_C \\ -\sin\theta_C & \cos\theta_C \end{pmatrix} \begin{pmatrix} q_d \\ q_s \end{pmatrix} . \tag{2.27}$$

With this mixing, Eq. (2.26) reduces to

$$j^{\mu}_{\mathrm{CC}} = \overline{q}_u \gamma^{\mu}\, (1-\gamma_5)\, (q_d \cos\theta_C + q_s \sin\theta_C) = V^{\mu}_{\mathrm{CC}} - A^{\mu}_{\mathrm{CC}} . \tag{2.28}$$

For the vector part of Eq. (2.28) we can write

$$V^{\mu}_{\mathrm{CC}} = \overline{q}_u \gamma^{\mu}\, (q_d \cos\theta_C + q_s \sin\theta_C) = V^{\mu}_1 + V^{\mu}_4 + \mathbb{i}\, (V^{\mu}_2 + V^{\mu}_5) , \tag{2.29}$$

where we have used that

$$\begin{aligned} \overline{q}_u \gamma^{\mu} q_d &= \overline{q} \gamma^{\mu} \frac{\lambda_1 + \mathbb{i}\lambda_2}{2} q = V^{\mu}_1 + \mathbb{i} V^{\mu}_2 , \\ \overline{q}_u \gamma^{\mu} q_s &= \overline{q} \gamma^{\mu} \frac{\lambda_4 + \mathbb{i}\lambda_5}{2} q = V^{\mu}_4 + \mathbb{i} V^{\mu}_5 . \end{aligned} \tag{2.30}$$

Similarly, for the axial part we have

$$A^{\mu}_{\mathrm{CC}} = \overline{q}_u \gamma^{\mu} \gamma_5\, (q_d \cos\theta_C + q_s \sin\theta_C) = A^{\mu}_1 + A^{\mu}_4 + \mathbb{i}\, (A^{\mu}_2 + A^{\mu}_5) , \tag{2.31}$$

since

$$\begin{aligned} \overline{q}_u \gamma^{\mu} \gamma_5 q_d &= \overline{q} \gamma^{\mu} \gamma_5 \frac{\lambda_1 + \mathbb{i}\lambda_2}{2} q = A^{\mu}_1 + \mathbb{i} A^{\mu}_2 , \\ \overline{q}_u \gamma^{\mu} \gamma_5 q_s &= \overline{q} \gamma^{\mu} \gamma_5 \frac{\lambda_4 + \mathbb{i}\lambda_5}{2} q = A^{\mu}_4 + \mathbb{i} A^{\mu}_5 . \end{aligned} \tag{2.32}$$

2.3.3 Chiral symmetry and current conservation

When electromagnetically and weakly interacting leptons collide with matter, strong processes are triggered. The fundamental theory of strong interactions, Quantum Chromodynamics (QCD), is a gauge theory for quarks and gluons with local SU(3) color symmetry. Its Lagrangian reads

$$\mathcal{L}_{\mathrm{QCD}} = \overline{q}\, (\mathbb{i}\gamma^{\mu} D_{\mu} - m_q)\, q - \frac{1}{4} G^{a}_{\mu\nu} G^{\mu\nu}_{a} , \qquad a = 1 - 8 . \tag{2.33}$$

with

$$D_\mu\, q = \left(\partial_\mu - \mathbb{i} g \frac{\lambda_a}{2} A^a_\mu\right) q\,. \tag{2.34}$$

The gluon tensor field is given by

$$G^{\mu\nu}_a = \partial^\mu A^\nu_a - \partial^\nu A^\mu_a + g f_{abc} A^\mu_b A^\nu_c\,. \tag{2.35}$$

In the massless quark limit, *i.e.* $m_u = m_d = m_s = 0$, in terms of left and right handed quark fields,[2], we have

$$\mathcal{L}_{\rm QCD} = -\frac{1}{4} G^a_{\mu\nu} G^{\mu\nu}_a + \mathbb{i}\overline{q}_L \gamma^\mu D_\mu q_L + \mathbb{i}\overline{q}_R \gamma^\mu D_\mu q_R\,. \tag{2.36}$$

In this scenario, the Lagrangian is symmetric under $\mathrm{SU}(3)_L \times \mathrm{SU}(3)_R$ transformations, which is known as chiral symmetry. The corresponding Noether conserved currents are

$$R^\mu_a = \overline{q}_R \gamma^\mu \frac{\lambda_a}{2} q_R\,, \tag{2.37}$$

$$L^\mu_a = \overline{q}_L \gamma^\mu \frac{\lambda_a}{2} q_L\,. \tag{2.38}$$

The combination of Eqs. (2.37,2.38) give as result the already introduced vector and axial currents, Eqs. (2.9, 2.24).

$$V^\mu_a = R^\mu_a + L^\mu_a = \overline{q}\gamma^\mu \frac{\lambda_a}{2} q\,, \tag{2.39}$$

$$A^\mu_a = R^\mu_a - L^\mu_a = \overline{q}\gamma^\mu\gamma_5 \frac{\lambda_a}{2} q\,. \tag{2.40}$$

As quarks are massive particles, chiral symmetry is explicitly broken. The divergence of the vector current is given in Eq. (2.10) and for the axial one we have

$$\partial_\mu A^\mu_a = \mathbb{i}\overline{q}\left\{\mathbf{m}, \frac{\lambda_a}{2}\right\}\gamma_5 q\,. \tag{2.41}$$

In contrast to the vector currents, in the case of axial currents the divergence does not vanish for quarks with the same mass. The axial current is only conserved when quark masses are neglected, which is known as PCAC. The equivalent of Eq. (2.41) for SU(2), where we only consider u and d quarks, is

$$\partial_\mu A^\mu_a = \mathbb{i}\overline{q}\left\{\mathbf{m}, \frac{\tau_a}{2}\right\}\gamma_5 q\,. \tag{2.42}$$

In the following section we explore some aspects of chiral symmetry and current conservation at the hadronic level.

[2] A brief description of the chiral projections of the fields is given in the Appendix A.1

2.4 Hadronic currents

Hadrons are strongly interacting states made of quarks and gluons. In the previous section the QCD Lagrangian was presented, Eq. (2.33) and its approximate chiral symmetry was introduced. This Lagrangian is also symmetric under $\mathrm{U}(1)_V$ transformations, which results in the baryon number conservation, and leads to a classification of hadrons into mesons ($B = 0$) and baryons ($B = 1$). Besides, all hadrons are singlets in color space, which means that the sum of color charges of their constituent quarks is always zero. To meet these conditions, mesons must be composed by a quark and an anti-quark and baryons must be states made up of three quarks.

2.4.1 Chiral Lagrangians for mesons

Besides its explicit breaking by quark masses, the chiral symmetry of QCD is also spontaneously broken. The hadron spectrum is not chirally symmetric even in the presence of only u and d quarks, for which the explicit breaking is small. For example, chiral partners such as the vector meson ρ and the axial a_1 have very different masses ($m_\rho = 770$ MeV $\neq m_{a_1} = 1230$ MeV) rather than being degenerate as chiral symmetry would dictate. Indeed $\mathrm{SU}(3)_L \times \mathrm{SU}(3)_R$ is spontaneously broken down to $\mathrm{SU}(3)_V$. Then, according to the Goldstone theorem,[3] this spontaneous symmetry breaking (SSB) implies the existence of eight pseudoscalar Nambu-Goldstone bosons. The effect of the $\mathrm{SU}(3)_L \times \mathrm{SU}(3)_R$ SSB is reflected by a gap in the hadron spectrum between the vector mesons (ρ, ω, ϕ) and the light pseudoscalar mesons (π, K, η), which are the Nambu-Goldstone bosons of the symmetry breaking and, as such, would be massless if it was not for the explicit breaking driven by the quark masses. The eight fields corresponding to these bosons can be collected in a 3×3 unitary matrix, that under chiral rotations transforms as

$$U(x) \to \hat{R} U(x) \hat{L}^\dagger \,, \tag{2.43}$$

with $\hat{R}$ and $\hat{L}$ the operators of the $\mathrm{SU}(3)_{R,L}$ rotations. The explicit representation of $U(x)$ in terms of the octet of pseudoscalar Nambu-Goldstone boson fields, $\pi_a(x)$, is

$$U(x) = e^{i \frac{\phi(x)}{f}} \,, \tag{2.44}$$

[3] See *e.g.* Refs. [37, 41] for a full description of this topic.

where

$$\phi(x) = \sum_{a=1}^{8} \lambda_a \pi_a = \begin{pmatrix} \pi^0 + \frac{1}{\sqrt{3}}\eta & \sqrt{2}\pi^+ & \sqrt{2}K^+ \\ \sqrt{2}\pi^- & -\pi^0 + \frac{1}{\sqrt{3}}\eta & \sqrt{2}K^0 \\ \sqrt{2}K^- & \sqrt{2}\bar{K}^0 & -\frac{2}{\sqrt{3}}\eta \end{pmatrix} . \tag{2.45}$$

The pattern of spontaneous chiral symmetry breaking is a crucial ingredient in the formulation of effective models of neutrino interactions with hadrons (and, in general, of interactions of hadrons among themselves and with external probes). The fact that Goldstone bosons interact weakly (for strong interactions) at low energies allows to use perturbative methods. Such a framework is known as chiral perturbation theory (ChPT). In this section we present a very brief description of some elements of this effective theory that will be used along this thesis. A detailed introduction for both meson and baryon sectors can be found *e.g.* in Ref.[41].

The basic idea of ChPT is to describe the dynamics by an effective Lagrangian, $\mathcal{L}_{\text{eff}}$, incorporating all relevant symmetries of the underlying fundamental theory. In this case, we replace the QCD Lagrangian by $\mathcal{L}_{\text{eff}}$ which involves the field $U(x)$ and its derivatives. At low energy, an expansion in powers of the meson momenta is equivalent to an expansion of $\mathcal{L}_{\text{eff}}$ in powers of the derivatives $\partial^\mu U$. Lorentz invariance restricts this series to terms with even numbers of derivatives, see Ref. [42]. The leading order Lagrangian that fulfills all these conditions is given by

$$\mathcal{L}_M^{(2)} = \frac{f^2}{4} \text{Tr}\left[D_\mu U \left(D^\mu U\right)^\dagger\right] . \tag{2.46}$$

where $D_\mu U$ is the covariant derivative. In the presence of external right and left-handed fields, r_μ and l_μ, it reads

$$D_\mu U \equiv \partial_\mu U - \mathbb{i} r_\mu U + \mathbb{i} U l_\mu . \tag{2.47}$$

These external fields allows us to incorporate the electromagnetic and semileptonic weak interactions [41, 43]. In terms of vector and axial external fields, v_μ and a_μ respectively, we can write

$$\begin{aligned} r_\mu &\equiv v_\mu + a_\mu , \\ l_\mu &\equiv v_\mu - a_\mu . \end{aligned} \tag{2.48}$$

The explicit expressions in the case of an electromagnetic interaction are given by

$$l_\mu^{\text{EM}} = r_\mu^{\text{EM}} = eQA_\mu , \tag{2.49}$$

where Q is the diagonal matrix defined in Eq. (2.13). In the case of weak CC interactions, the external fields are

$$r_\mu^{\rm CC} = 0, \qquad l_\mu^{\rm CC} = -\frac{g}{\sqrt{2}}\left(W_\mu^\dagger T_+ + W_\mu T_-\right) , \tag{2.50}$$

with

$$T_+ = \begin{pmatrix} 0 & V_{ud} & V_{us} \\ 0 & 0 & 0 \\ 0 & 0 & 0 \end{pmatrix}; \qquad T_- = \begin{pmatrix} 0 & 0 & 0 \\ V_{ud} & 0 & 0 \\ V_{us} & 0 & 0 \end{pmatrix} , \tag{2.51}$$

where V_{ud} and V_{us} are elements of the CKM matrix introduced in Eq. 2.26. Finally for NC interactions we have

$$\begin{aligned} l_\mu^{\rm NC} &= \left(-\frac{g}{2\cos\theta_W}\right)\left(2\cos^2\theta_W\right) Q Z_\mu \, , \\ r_\mu^{\rm NC} &= \left(-\frac{g}{2\cos\theta_W}\right)\left(-2\sin^2\theta_W\right) Q Z_\mu \, . \end{aligned} \tag{2.52}$$

Introducing the explicit symmetry breaking term, linear in the quark masses, we have

$$\mathcal{L}_M^{(2)} = \frac{f^2}{4}{\rm Tr}\left[D_\mu U \left(D^\mu U\right)^\dagger\right] + \frac{f^2}{4}{\rm Tr}\left(\chi U^\dagger + U\chi^\dagger\right) \tag{2.53}$$

with $\chi = 2B_0\mathbf{m}$, which is proportional to quark mass matrix $\mathbf{m}$, Eq. (2.10). The quantity B_0 is related to the scalar singlet quark condensate through $3f^2B_0 = -\langle 0|\,\bar{q}q\,|0\rangle$, and its value is a measure of the dynamical breaking of chiral symmetry, Ref. [41]. By expanding U and $U^\dagger$ and identifying the quadratic terms in ϕ one obtains the meson masses at leading order in terms of B_0 and the quark masses (Gell-Mann, Oakes, Renner relations):

$$m_\pi^2 = 2B_0\hat{m}\,; \qquad m_K^2 = B_0(\hat{m}+m_s)\,; \qquad m_\eta^2 = \frac{2}{3}B_0(\hat{m}+2m_s)\,, \tag{2.54}$$

in the isospin limit $m_u = m_d = \hat{m}$. Furthermore, in this limit $\chi = {\rm diag}(m_\pi^2, m_\pi^2, 2m_K^2 - m_\pi^2)$

Let us consider now infinitesimal left and right transformations given by

$$\hat{R} = e^{-{\rm i}\theta_R^a\frac{\lambda_a}{2}} \simeq 1 - {\rm i}\theta_R^a\frac{\lambda_a}{2} \, , \tag{2.55}$$

$$\hat{L} = e^{-{\rm i}\theta_L^a\frac{\lambda_a}{2}} \simeq 1 - {\rm i}\theta_L^a\frac{\lambda_a}{2} \, . \tag{2.56}$$

Here we promote the global symmetry to a local one, following the method of Ref.[44] to identify the Noether currents (see also Ref.[41]), where the variation of the Lagrangian reads

$$\delta\mathcal{L} = \theta^a \partial_\mu J^\mu_a + \partial_\mu \theta^a J^\mu_a \,. \tag{2.57}$$

Taking $\theta^a_R = 0$ and using that $U^\dagger U = 1$, the effective Lagrangian of Eq. (2.46) transforms as

$$\mathcal{L}^{(2)}_M \to \mathcal{L}^{(2)}_M + \delta\mathcal{L}_M \,, \tag{2.58}$$

with

$$\delta\mathcal{L}_M = \frac{f^2}{4}\mathbb{i}\partial_\mu\theta^a_L \mathrm{Tr}\left[\lambda_a \left(\partial^\mu U^\dagger\right) U\right] \,. \tag{2.59}$$

Therefore, comparing with Eq. (2.57) we can identify the current

$$L^{(M)\mu}_a = \mathbb{i}\frac{f^2}{4}\mathrm{Tr}\left[\lambda_a \partial^\mu U^\dagger U\right] \,, \tag{2.60}$$

and its divergence,

$$\partial_\mu L^{(M)\mu}_a = 0 \,, \tag{2.61}$$

proving that the current is conserved in the chiral limit.

Proceeding analogously for $\theta^a_L = 0$, we find that the conserved Noether current now is

$$R^{(M)\mu}_a = -\mathbb{i}\frac{f^2}{4}\mathrm{Tr}\left[\lambda_a U \partial^\mu U^\dagger\right] \,. \tag{2.62}$$

Using these results we can write the vector and axial currents,

$$\begin{aligned} V^{(M)\mu}_a &= R^{(M)\mu}_a + L^{(M)\mu}_a = -\mathbb{i}\frac{f^2}{4}\mathrm{Tr}\left[\lambda_a \left[U, \partial^\mu U^\dagger\right]\right] \,, \\ A^{(M)\mu}_a &= R^{(M)\mu}_a - L^{(M)\mu}_a = -\mathbb{i}\frac{f^2}{4}\mathrm{Tr}\left[\lambda_a \left\{U, \partial^\mu U^\dagger\right\}\right] \,. \end{aligned} \tag{2.63}$$

which, because of the symmetry of $\mathcal{L}^{(2)}_M$ under $\mathrm{SU}(3)_L \times \mathrm{SU}(3)_R$, are both conserved in the chiral limit.

Applying the same method to the symmetry breaking term of the effective Lagrangian, corresponding to the second term in Eq. (2.53), taking $\theta^a_R = 0$ we find

$$\delta\mathcal{L}^{(2)}_{\mathrm{SB}} = -\mathbb{i}\theta^a_L \frac{f^2}{4} B_0 \mathrm{Tr}\left[\lambda_a U^\dagger \mathbf{m} - \mathbf{m} U \lambda_a\right] \,, \tag{2.64}$$

and then

$$\partial_\mu L^{(\mathrm{SB})\mu}_a = -\mathbb{i}\frac{f^2}{4} B_0 \mathrm{Tr}\left[\lambda_a \left(U^\dagger \mathbf{m} - \mathbf{m} U\right)\right] \,. \tag{2.65}$$

Analogously, for $\theta_L^a = 0$ we obtain

$$\delta\mathcal{L}_{\rm SB}^{(2)} = -\mathbb{i}\theta_R^a \frac{f^2}{4} B_0 {\rm Tr}\left[\lambda_a U\mathbf{m} - \mathbf{m}U^\dagger\lambda_a\right] , \tag{2.66}$$

and

$$\partial_\mu R_a^{({\rm SB})\mu} = -\mathbb{i}\frac{f^2}{4} B_0 {\rm Tr}\left[\lambda_a\left(U\mathbf{m} - \mathbf{m}U^\dagger\right)\right] . \tag{2.67}$$

In this case, for the vector current we have that

$$\partial_\mu V_a^\mu = \partial_\mu V_a^{({\rm SB})\mu} = -\mathbb{i}\frac{f^2}{4} B_0 {\rm Tr}\left[[\mathbf{m},\lambda_a]\left(U + U^\dagger\right)\right] , \tag{2.68}$$

which is conserved only in the SU(3) flavor-symmetric limit, where $m_u = m_d = m_s$. In the same way, for the axial current of the symmetry breaking we find that

$$\partial_\mu A_a^\mu = \partial_\mu A_a^{({\rm SB})\mu} = -\mathbb{i}\frac{f^2}{4} B_0 {\rm Tr}\left[\{\mathbf{m},\lambda_a\}\left(U - U^\dagger\right)\right] , \tag{2.69}$$

showing that the axial current is not conserved in presence of non-zero quark masses. Equations (2.68) and (2.69) are the effective-theory realizations of the QCD identities (2.10) and (2.41) for mesons at leading order.

Expanding the meson field up to the linear term in ϕ

$$U \simeq 1 + \frac{\mathbb{i}}{f}\lambda_a\pi_a \tag{2.70}$$

we can write

$$\partial_\mu A_a^{({\rm SB})\mu} = \frac{f}{2} B_0 {\rm Tr}\left[\{\mathbf{m},\lambda_a\}\,\lambda_b\right]\pi_b . \tag{2.71}$$

Applying the properties of the Gell-Mann matrices, described in Appendix. A.4, in the trace of Eq. (2.71), we find

$${\rm Tr}\left[\{\mathbf{m},\lambda_a\}\,\lambda_b\right] = {\rm Tr}\left[\mathbf{m}\,\{\lambda_a,\lambda_b\}\right] = \frac{4}{3}\delta_{ab}\sqrt{\frac{2}{3}}\,3\,m_0 + 4d_{ab3}m_3 + 4d_{ab8}m_8 , \tag{2.72}$$

where we have written $\mathbf{m}$ as

$$\mathbf{m} = \sqrt{\frac{2}{3}}m_0\mathbb{I} + m_3\lambda_3 + m_8\lambda_8 , \tag{2.73}$$

with

$$\begin{aligned} m_0 &= \frac{m_u + m_d + m_s}{\sqrt{6}} , \\ m_3 &= \frac{m_u - m_d}{2} , \\ m_8 &= \frac{m_u + m_d - 2m_s}{2\sqrt{3}} . \end{aligned} \tag{2.74}$$

The totally antisymmetric SU(3) symbols $d_{abc} = 1/4\mathrm{Tr}\left[\{\lambda_a, \lambda_b\}\lambda_c\right]$.

In the isospin limit, $m_u = m_d = \hat{m}$, using Eqs. 2.54 one finds for the divergence of the axial current that

$$\begin{aligned}
\partial_\mu (A_1 \pm \mathbb{i} A_2)^\mu &= \sqrt{2} f m_\pi^2 \pi^\mp \,, \\
\partial_\mu A_3^\mu &= f m_\pi^2 \pi^0 \,, \\
\partial_\mu (A_4 \pm \mathbb{i} A_5)^\mu &= \sqrt{2} f m_K^2 K^\mp \,, \\
\partial_\mu (A_6 \pm \mathbb{i} A_7)^\mu &= \sqrt{2} f m_K^2 \bar{K}^0 \,, \\
\partial_\mu A_8^\mu &= f m_\eta^2 \eta \,,
\end{aligned} \tag{2.75}$$

where the only contribution comes from the symmetry breaking term. The axial current in the first row couples to the $W^\pm$ fields leading to the pion decay $\pi^\pm \to \mu^\pm \nu_\mu$ from where the parameter f can be experimentally fixed: $f = f_\pi = 92.4$ MeV.

2.4.2 Chiral Lagrangians for baryons

We incorporate now the ground state SU(3) baryon octet, represented by a Dirac spinor field given by the matrix

$$\Psi_B(x) = \sum_{a=1}^{8} \frac{1}{\sqrt{2}} \lambda_a \Psi_B^a = \begin{pmatrix} \frac{1}{\sqrt{2}}\Sigma^0 + \frac{1}{\sqrt{6}}\Lambda & \Sigma^+ & p \\ \Sigma^- & -\frac{1}{\sqrt{2}}\Sigma^0 + \frac{1}{\sqrt{6}}\Lambda & n \\ \Xi^- & \Xi^0 & -\frac{2}{\sqrt{6}}\Lambda \end{pmatrix} . \tag{2.76}$$

The lowest order Lagrangian for baryons in the presence of external currents is

$$\begin{aligned}
\mathcal{L}_{MB}^{(1)} =& \mathrm{Tr}\left[\overline{\Psi}_B \left(\mathbb{i}\not{D} - \mathbf{M}\right) \Psi_B\right] - \frac{D}{2}\mathrm{Tr}\left[\overline{\Psi}_B \gamma^\mu \gamma_5 \left\{u_\mu, \Psi_B\right\}\right] \\
&- \frac{F}{2}\mathrm{Tr}\left[\overline{\Psi}_B \gamma^\mu \gamma_5 \left[u_\mu, \Psi_B\right]\right] \,,
\end{aligned} \tag{2.77}$$

where $\mathbf{M}$ is the mass of the baryon octet, and the parameters $D = 0.804$ and $F = 0.463$ can be determined from the baryon semileptonic decays, Ref. [45]. In this case, the covariant derivative is given by

$$D_\mu \Psi_B = \partial_\mu \Psi_B + \left[\Gamma_\mu, \Psi_B\right] - \mathbb{i}\mathrm{Tr}\left[v_\mu^0\right] \Psi_B \,, \tag{2.78}$$

with

$$\Gamma_\mu = \frac{1}{2}\left[u^\dagger \left(\partial_\mu - \mathbb{i} r_\mu\right) u + u \left(\partial_\mu - \mathbb{i} l_\mu\right) u^\dagger\right] . \tag{2.79}$$

The meson fields appear thought $u^2 = U$ and

$$u_\mu = \mathbb{i} \left[u^\dagger \left(\partial_\mu - \mathbb{i} r_\mu \right) u - u \left(\partial_\mu - \mathbb{i} l_\mu \right) u^\dagger \right] . \tag{2.80}$$

The singlet external vector field is present only for NC interactions [4]:

$$v_\mu^0 = \left(-\frac{g}{2 \cos\theta_W} \right) \left(-\frac{1}{6} \right) Z_\mu . \tag{2.81}$$

From the next order meson baryon Lagrangian we include only the terms relevant to this thesis,[5] corresponding to weak magnetism

$$\mathcal{L}_{MB}^{(2)} = d_5 \mathrm{Tr} \left[\overline{\Psi}_B \left[f_{\mu\nu}^+, \sigma^{\mu\nu} \Psi_B \right] \right] + d_4 \mathrm{Tr} \left[\overline{\Psi}_B \left\{ f_{\mu\nu}^+, \sigma^{\mu\nu} \Psi_B \right\} \right] + \dots , \tag{2.82}$$

where, in this case, the tensor $f_{\mu\nu}^+$ can be reduced to

$$f_{\mu\nu}^+ = \partial_\mu l_\nu - \partial_\nu l_\mu - \mathbb{i} \left[l_\mu, l_\nu \right] . \tag{2.83}$$

The coupling constants $d_{4,5}$ are fully determined by the proton and neutron anomalous magnetic moments. The same approximation has also been used in calculations of single pion production induced by neutrinos, Ref. [47].

[4] We have omitted the coupling to the singlet axial current which has an anomaly.

[5] As it will be shown in Chapter 6, where we make reference to the results of Ref. [46].

Chapter 3

Lepton-hadron quasi-elastic scattering

In this chapter we explore the hadrons and scalar nuclei using elastic and QE processes. For elastic scattering, we consider the cases where all the interacting particles keep their identities,

$$\begin{aligned} l^{\pm} + A &\to l^{\pm} + A \,, \\ \nu\,(\overline{\nu}) + A &\to \nu\,(\overline{\nu}) + A \,. \end{aligned} \tag{3.1}$$

In these reactions A stands for any scalar nucleus. Analogous interactions can be written replacing the scalar nucleus by a nucleon, N. While any of these reactions can be mediated by NCs, only charged leptons have non-negligible EM interactions in the Standard Model.

In the case of QE scattering on nucleons one understands one of the following reactions:

$$\begin{aligned} \nu + n &\to l^{-} + p \,, \\ \overline{\nu} + p &\to l^{+} + n \,, \end{aligned} \tag{3.2}$$

mediated by CC. QE scattering can occur in nuclei leading to a modification of the target composition.

3.1 Lepton-hadron inclusive scattering

In the first place, we address the general case of a lepton interacting with an hadronic target, given as result a lepton in any allowed final state. For inclusive processes in which a sum over all allowed final hadronic states is performed, the differential cross section can be written in terms of structure

functions that encode information about the hadronic structure. Once we have the general expression for the cross section, we can particularise for the specific cases of interest.

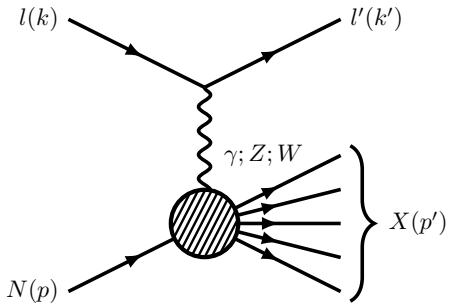

Figure 3.1: Diagram of the scattering between a lepton, with momentum k, and an hadron, with momentum p. The sum of all the hadronic final-state momenta is p' and the momentum of the outgoing lepton is k'.

In the process of Fig. 3.1,

$$l(k) + N(p) \to l'(k') + X(p') \,, \tag{3.3}$$

there is a sum over all the final states. We define the momenta of the incoming particles, $p^\mu \equiv (E, \vec{p})$ and $k^\mu \equiv (k^0, \vec{k})$, and the outgoing ones, $p'^\mu \equiv (E', \vec{p'}) = \sum_f p'^\mu_f$ and $k'^\mu \equiv (k'^0, \vec{k'})$. The momentum transfer is $k^\mu - k'^\mu = p'^\mu - p^\mu \equiv q^\mu = (\omega, \vec{q})$. In the Born approximation, the amplitude for a generic lepton-hadron interaction will be given in terms of the leptonic and hadronic currents, j^μ and J^μ,

$$\mathrm{i}\mathcal{M} = \lambda^2 D_{\mu\nu} \langle l'|j^\mu(0)|l\rangle \langle X|J^\nu(0)|N\rangle \,, \tag{3.4}$$

where $D_{\mu\nu}$ is the propagator of the virtual mediator.[1] λ stands for the coupling in the two vertices, which is taken off from the currents for convenience.[2] For the squared modulus of the amplitude we can write

$$\left|\overline{\mathcal{M}}\right|^2 = \lambda^4 D_{\mu\nu} \left(D_{\alpha\beta}\right)^\dagger L^{\mu\alpha} H^{\nu\beta} \,, \tag{3.5}$$

[1] Translational invariance has been used to factorize the dependence of the currents on the four-vector x. The resulting exponential leads to the Dirac delta of momentum conservation in the cross section. We will omit the argument of the currents in the rest of this thesis to simplify the notation.

[2] The specific expressions for the coupling and the propagator depend on the exchanged particle in the interaction.

where we define the leptonic tensor, $L_{\mu\nu}$, and the tensor $H^{\mu\nu}$ as

$$\begin{aligned} L_{\mu\nu} &= \overline{\sum} \langle l'|j_\mu|l\rangle^* \langle l'|j_\nu|l\rangle \ , \\ H^{\mu\nu} &= \overline{\sum} \langle X|J^\mu|N\rangle^* \langle X|J^\nu|N\rangle \ , \end{aligned} \tag{3.6}$$

with $\overline{\sum}$, the average over the initial polarizations and the sum over the final ones.

For this general process with a lepton as one of the final state particles, we can write the differential cross section (see Appendix C.2) as

$$\begin{aligned} d\sigma =& \frac{1}{4\left[(k\cdot p)^2 - m_l^2 M^2\right]} \frac{d^3k'}{(2\pi)^3 2k'_0} \left(\prod_f \frac{d^3p'_f}{(2\pi)^3 2E'_f}\right) \\ & \times (2\pi)^4 \delta^{(4)}\left(p' + k' - p - k\right) \left|\overline{\mathcal{M}}\right|^2 \ , \end{aligned} \tag{3.7}$$

with m_l and M the masses of the incoming lepton and hadron respectively.

In spherical coordinates we can write $d^3k' = |\vec{k'}|^2 d|\vec{k'}| d\Omega$, in terms of the momentum of the outgoing lepton and the solid angle between the directions of the momenta of the outgoing and incoming leptons, $d\Omega = d\cos\theta d\phi$. Using the relation $(k'_0)^2 = |\vec{k'}|^2 + m_{l'}^2$, where $m_{l'}$ is the mass of the outgoing lepton, we obtain

$$\begin{aligned} d\sigma =& \frac{1}{8M(2\pi)^3} \frac{|\vec{k'}|}{|\vec{k}|} dk'_0 d\Omega \left(\prod_f \frac{d^3p'_f}{(2\pi)^3 2E'_f}\right) \\ & \times (2\pi)^4 \delta^{(4)}\left(p' + k' - p - k\right) \left|\overline{\mathcal{M}}\right|^2 \ , \end{aligned} \tag{3.8}$$

in the laboratory frame, where $\vec{p} = 0$ and $E = M$. Using (3.5) in (3.8) we can write the differential cross section in terms of the leptonic and hadronic tensors

$$\frac{d\sigma}{dk'_0 d\Omega} = \frac{1}{4(2\pi)^2} \frac{|\vec{k'}|}{|\vec{k}|} \lambda^4 D_{\mu\nu} \left(D_{\alpha\beta}\right)^\dagger L^{\mu\alpha} W^{\nu\beta} \ . \tag{3.9}$$

The hadronic tensor is given by

$$W^{\mu\nu} \equiv \frac{1}{2M} \int \left(\prod_f \frac{d^3p'_f}{(2\pi)^3 2E'_f}\right) (2\pi)^3 \delta^{(4)}\left(p' + k' - p - k\right) H^{\mu\nu} \ . \tag{3.10}$$

Structure functions

We now consider the structure of the hadronic tensor for an inclusive process, where all the possible final states are summed. As the final hadronic

momentum is not an independent variable, $p' = p + q$, the most general tensor that can be built is

$$\begin{aligned} W^{\mu\nu} = &- W_1 g^{\mu\nu} + W_2 \frac{p^\mu p^\nu}{M^2} + W_3\, i\, \epsilon^{\mu\nu\alpha\beta} \frac{p_\alpha q_\beta}{2M^2} + W_4 \frac{q^\mu q^\nu}{M^2} \\ &+ W_5 \frac{p^\mu q^\nu + q^\mu p^\nu}{M^2} + W_6 \frac{p^\mu q^\nu - q^\mu p^\nu}{M^2} \,, \end{aligned} \tag{3.11}$$

where the structure functions, W_i, are function of all the independent scalars, which can be written in terms of q^2 and $(q \cdot p)$. There can not be any dependence on the individual p'_f as this is an inclusive process. In the laboratory frame $(q \cdot p = M\omega)$, therefore $W_i\left(\omega, q^2\right)$.

In the case of an EM interaction, current conservation, $q_\mu J^\mu_{\text{EM}} = 0$, implies that

$$q_\mu W^{\mu\nu}_{\text{EM}} = W^{\mu\nu}_{\text{EM}} q_\nu = 0 \,. \tag{3.12}$$

The resolution of the system of equations derived from Eq. (3.12) leads to the cancellation of W_6 and gives relations between the rest of structure functions. A detailed derivation can be found, for example, in Ref. [48]. With these conditions, Eq. 3.11 is reduced to

$$W^{\mu\nu}_{\text{EM}} = W_1 \left(\frac{q^\mu q^\nu}{q^2} - g^{\mu\nu} \right) + \frac{W_2}{M^2} \left(p^\mu - \frac{p \cdot q}{q^2} q^\mu \right) \left(p^\nu - \frac{p \cdot q}{q^2} q^\nu \right) \,. \tag{3.13}$$

3.1.1 Electron-hadron interaction

In this section, we provide an specific example of the lepton-hadron scattering. Indeed, we particularise now the inclusive process general expressions of the lepton-hadron EM interaction for the case where the lepton is an electron. This interaction is described by the diagram of Fig. 3.1 with a photon as the mediator of the reaction. In this case, the incoming and outgoing particles in the leptonic current are electrons, hence[3]

$$\left\langle e\left(k'\right) \right| j^\mu_{\text{EM}} \left| e\left(k\right) \right\rangle = \overline{u}(k') \gamma^\mu u(k) \,. \tag{3.14}$$

The leptonic tensor is then,

$$\begin{aligned} L_{\mu\nu} =& \frac{1}{2} \text{Tr} \left[\left(\not{k}' + m_e \right) \gamma_\mu \left(\not{k} + m_e \right) \gamma_\nu \right] \\ =& \, 2 \left[k'_\mu \, k_\nu + k'_\nu \, k_\mu - g_{\mu\nu} \left((k' \cdot k) - m_e^2 \right) \right] \,, \end{aligned} \tag{3.15}$$

with m_e the electron mass.

[3] The normalization of Dirac spinors is given in Appendix A.1.

Taking the hadronic tensor of Eq. (3.13), the contraction with the leptonic tensor reads

$$\begin{aligned} L_{\mu\nu}W^{\mu\nu} =& 2W_1\left[2\frac{(k\cdot q)^2}{q^2} - 2m_e^2 - 3(k\cdot q)\right] \\ &+ \frac{2W_2}{M_{\mathrm{N}}^2}\left[2(k\cdot p)^2 + M_{\mathrm{N}}^2(k\cdot q) - \frac{(p\cdot q)}{q^2}\left(4(k\cdot p)(k\cdot q)\right.\right. \\ &\left.\left. + \; 2(p\cdot q)(k\cdot q) - \frac{(p\cdot q)}{q^2}\left(2(k\cdot q)^2 + q^2(k\cdot q)\right)\right)\right] . \end{aligned} \tag{3.16}$$

In the case of elastic processes, where the masses of the initial and final hadrons are the same, this expression is reduced to

$$L_{\mu\nu}W^{\mu\nu} = 2W_1\left[-2m_e^2 - t\right] + \frac{W_2}{M_{\mathrm{N}}^2}\left[\left(s - m_e^2 - M_{\mathrm{N}}^2\right)^2 + t\left(s - m_e^2\right)\right], \tag{3.17}$$

in terms of the Mandelstam variables, $s = (k+p)^2$ and $t = q^2$.

In the limit where we neglect the electron mass, $m_e \simeq 0$, in the laboratory frame, for the Mandelstam we have

$$\begin{aligned} t &= -4k^0k'^0\sin^2\frac{\theta}{2}\,, \\ s &= M_{\mathrm{N}}^2 + 2k^0M_{\mathrm{N}}\,, \end{aligned} \tag{3.18}$$

where k^0 is the energy on the incoming electron and θ is the scattering angle of the outgoing electron with respect to the direction of the incoming one in laboratory frame. In this scenario, the contraction of the leptonic and hadronic tensors is:

$$L_{\mu\nu}W^{\mu\nu} = 4k^0k'^0\left(W_1\,2\,\sin^2\frac{\theta}{2} + W_2\,\cos^2\frac{\theta}{2}\right) . \tag{3.19}$$

For an EM interaction, the photon propagator is given by[4]

$$D_{\mu\nu} = -\mathbb{i}\frac{g_{\mu\nu}}{q^2 + \mathbb{i}\epsilon}\,, \tag{3.20}$$

and the coupling is the electron charge, $e = \sqrt{4\pi\alpha}$, with α the fine structure constant. Substituting the result of Eq. (3.19) and the expressions for the propagator and the coupling in the Eq. (3.9), we obtain

$$\frac{d\sigma}{dk'^0\,d\Omega} = \frac{\alpha^2}{4(k^0)^2\,\sin^4\frac{\theta}{2}}\left(W_1\,2\sin^2\frac{\theta}{2} + W_2\cos^2\frac{\theta}{2}\right) , \tag{3.21}$$

[4]We choose the Feynman gauge for simplicity.

in terms of $W_1(\omega, q^2)$ and $W_2(\omega, q^2)$, which depend on the particular target. This expression for the cross section is general for any EM interaction, and only the structure functions are specific of each case. In further sections we continue the description of the electron-hadron interaction for the cases of interest in this thesis.

3.2 Quasi-elastic scattering on the nucleon

As described in Sec. 2.4, for a lepton-nucleon scattering, Fig. 3.2, the hadronic current in momentum space reads

$$\left\langle N'(p')\right| J^\mu \left|N(p)\right\rangle = \overline{u}(p')\Gamma^\mu u(p) = \mathcal{V}^\mu - \mathcal{A}^\mu \,, \tag{3.22}$$

where the 4-vector is as a sum of operators with coefficients F_i, $\Gamma^\mu = \sum_i F_i \mathcal{O}_i^\mu$. These coefficients are the FFs which, in a given reaction, describe the spatial distributions of charge, and the current inside the nucleons. The FFs can be parametrized using empirical information extracted from the scattering of leptons with nucleons.

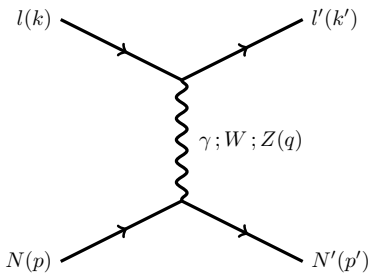

Figure 3.2: Diagram of a lepton-nucleon scattering.

For particles which obey the Dirac equation, the most general structure that can be written, after the use of Dirac algebra, for Γ^μ is given by

$$\Gamma^\mu = \gamma^\mu F_1 + \frac{\mathbb{i}}{2M_\mathrm{N}}\sigma^{\mu\nu}q_\nu F_2 + \frac{q^\mu}{M_\mathrm{N}}F_S - \gamma^\mu\gamma_5 F_A - \frac{\mathbb{i}}{2M_\mathrm{N}}\sigma^{\mu\nu}q_\nu\gamma_5 F_T - \frac{q^\mu}{M_\mathrm{N}}\gamma_5 F_P \,, \tag{3.23}$$

with M_N the nucleon mass, $\sigma^{\mu\nu} = \frac{\mathbb{i}}{2}\left[\gamma^\mu, \gamma^\nu\right]$ and $q = p' - p$. The FFs are functions of all independent scalars in the problem. In the QE case the condition $2(p\cdot q) + q^2 = 0$ is fulfilled and $F_i = F_i(q^2)$.

Some properties of the FFs can be extracted from the behaviour of the different components of the current under the discrete symmetries of the Dirac theory. Because the time reversal ($\mathcal{T}$) operator is antilinear, under this transformation the hadronic current behaves as

$$\mathcal{T}\left(\overline{u}\Gamma^{\mu}u\right)\mathcal{T}^{\dagger} = \sum_{i} F_i^{*}\overline{u}\left(\mathcal{O}_i\right)_{\mu} u\,. \tag{3.24}$$

The fact that the amplitude of the interaction, which is proportional to $l_{\mu}\overline{u}\Gamma^{\mu}u = \sum_i F_i l_{\mu}\overline{u}\mathcal{O}_i^{\mu}u$, does not change, keeping $\mathcal{T}$ invariance, implies that

$$\mathcal{T}\left(l_{\mu}\overline{u}\Gamma^{\mu}u\right)\mathcal{T}^{\dagger} = \sum_{i} F_i^{*} l_{\mu}\overline{u}\mathcal{O}_i^{\mu}u\,, \tag{3.25}$$

so the coefficients have to be real, $F_i^{*} = F_i$.

Looking now at how the different structures of Γ^{μ} transform under parity (P), we observe that the γ^{μ}, $\sigma^{\mu\nu}q_{\nu}$ and q^{μ} terms transform as vectors, while $\gamma^{\mu}\gamma_5$, $\sigma^{\mu\nu}q_{\nu}\gamma_5$ and $q^{\mu}\gamma_5$ do as axial vectors. This makes possible to identify the vector and axial vector parts of the current:

$$\begin{aligned}
\mathcal{V}^{\mu} &= \overline{u}(p')\left[\gamma^{\mu}F_1 + \frac{\mathbb{i}}{2M_{\mathrm{N}}}\sigma^{\mu\nu}q_{\nu}F_2 + \frac{q^{\mu}}{M_{\mathrm{N}}}F_S\right]u(p)\,,\\
\mathcal{A}^{\mu} &= \overline{u}(p')\left[\gamma^{\mu}\gamma_5 F_A + \frac{\mathbb{i}}{2M_{\mathrm{N}}}\sigma^{\mu\nu}q_{\nu}\gamma_5 F_T + \frac{q^{\mu}}{M_{\mathrm{N}}}\gamma_5 F_P\right]u(p)\,.
\end{aligned} \tag{3.26}$$

Making use of conservation of the vector current, $q_{\mu}\mathcal{V}^{\mu} = 0$, a relation between F_1 and F_S can be obtained because the piece $\sigma^{\mu\nu}q_{\mu}q_{\nu}$ vanishes by symmetry,

$$q_{\mu}\mathcal{V}^{\mu} = \overline{u}(p')\left[\left(\not{p}' - \not{p}\right)F_1 + \frac{q^2}{M_{\mathrm{N}}}F_S\right]u(p) = 0\,, \tag{3.27}$$

and hence

$$\mathcal{V}^{\mu} = \overline{u}(p')\left[\left(\gamma^{\mu} - \frac{\not{q}q^{\mu}}{q^2}\right)F_1 + \frac{\mathbb{i}}{2M_{\mathrm{N}}}\sigma^{\mu\nu}q_{\nu}F_2\right]u(p)\,. \tag{3.28}$$

If the masses of the two nucleons in the interaction are equal,[5] as the spinors fulfill the Dirac equation, $\overline{u}(p')\left(\not{p}' - M_{\mathrm{N}}\right) = \left(\not{p} - M_{\mathrm{N}}\right)u(p) = 0$, the term $\not{q}q^{\mu}/q^2$ in Eq. (3.28) is cancelled.

[5] In the case of CC interactions, this condition is satisfied in the isospin limit.

The charge conjugation (C) unitary linear operator transforms a particle in its corresponding antiparticle. Hence, the action of this operator on a fermionic field changes the sign of all of its quantum numbers, without affecting the spin and momentum. The combination of C with a rotation of π around the second axis of isospin space is defined as the G-parity (G), $G = \mathcal{C}e^{\mathrm{i}\pi\frac{\tau_2}{2}}$. Applying G to the currents we obtain

$$\begin{aligned} G\mathcal{V}^\mu G^\dagger &= \mathcal{V}^\mu \,, \\ G\mathcal{A}^\mu G^\dagger &= -\mathcal{A}^\mu \,, \end{aligned} \tag{3.29}$$

except for the term proportional to F_T, which transforms with the opposite sign of the rest in the axial current.[6] In absence of strong interactions, only the terms proportional to γ^μ and $\gamma^\mu\gamma_5$ are present in the vector and axial currents respectively. As G is a symmetry of strong interactions, we demand that all the terms in each current transform as these ones and, hence, $F_T = 0$.[7] Then, for the nucleon current we have the well-known result

$$\begin{aligned} \mathcal{V}^\mu &= \overline{u}(p')\left[\gamma^\mu F_1 + \frac{\mathrm{i}}{2M_\mathrm{N}}\sigma^{\mu\nu}q_\nu F_2\right]u(p) \,, \\ \mathcal{A}^\mu &= \overline{u}(p')\left[\gamma^\mu\gamma_5 F_A + \frac{q^\mu}{M_\mathrm{N}}\gamma_5 F_P\right]u(p) \,, \end{aligned} \tag{3.30}$$

where we have used that the initial and final nucleons have the same mass. The currents in Eq. (3.30) are written in terms of the Dirac (F_1), Pauli (F_2), axial (F_A) and pseudoscalar (F_P) FFs.

3.2.1 Isospin symmetry

In what follows, we explore the isospin symmetry for the nucleon matrix elements and the relations between the EM and the weak FFs are deduced. In Sec. 2.3 we described the isospin symmetry SU(2) for u and d quarks.

In the case of nucleons we assume the same SU(2) isospin symmetry. As it happens with the u and d quarks, under this symmetry the nucleons form a doublet with $I = 1/2$. The action of the isospin operators over the nucleon isospin states is described in Appendix A.2.

[6] The same would apply to the F_S term in the case we had not cancel it before.

[7] The terms of the vector and axial vector currents which transform as in Eq. (3.29) are the first class currents and the ones which transform with the opposite sign are classified as second class ones. From now on, we will ignore second class currents with $F_T \neq 0$ and $F_S \neq 0$.

In Sec. 2.3 the flavor structure of electroweak currents was presented. The nucleon transition currents can be written as

$$V_a^\mu = \mathcal{V}^\mu \frac{\tau_a}{2} \,, \tag{3.31}$$

$$A_a^\mu = \mathcal{A}^\mu \frac{\tau_a}{2} \,, \tag{3.32}$$

in terms of the isospin operators. The hypercharge current is

$$V_Y^\mu = \mathcal{V}_Y^\mu \mathbb{I} \,, \tag{3.33}$$

where $\mathbb{I}$ is the identity matrix. In the following, we use this to describe the flavor structure of EM and weak currents.

3.2.2 Electromagnetic form factors

The EM transitions between nucleons are given by

$$\langle p| V_{\mathrm{EM}}^\mu |p\rangle = \langle p| V_3^\mu + \frac{1}{2} V_Y^\mu |p\rangle = \frac{\mathcal{V}^\mu + \mathcal{V}_Y^\mu}{2} \equiv \mathcal{V}_p^\mu \,, \tag{3.34}$$

$$\langle n| V_{\mathrm{EM}}^\mu |n\rangle = \langle n| V_3^\mu + \frac{1}{2} V_Y^\mu |n\rangle = \frac{-\mathcal{V}^\mu + \mathcal{V}_Y^\mu}{2} \equiv \mathcal{V}_n^\mu \,, \tag{3.35}$$

with $\mathcal{V}_{p,n}^\mu$ in terms of the EM FFs, Eq. 3.30. It is common to use the Sachs electric and magnetic FFs, G_E and G_M, given by

$$\begin{aligned} G_E &= F_1 + \frac{q^2}{4M_{\mathrm{N}}^2} F_2 \,, \\ G_M &= F_1 + F_2 \,. \end{aligned} \tag{3.36}$$

In the Breit frame,[8] the three-dimensional Fourier integral of G_E plays a role analogous to the "classical" charge distribution. The Fourier transform of G_M would be interpreted as the magnetization density. See Ref. [42] for further details.

There are different parametrizations of the EM FFs that can be found in the literature, *e.g.* in Ref. [49].

[8] This is the frame where the incoming and the outgoing nucleons have momenta equal in magnitude but with opposite signs. In the case of elastic electron scattering, this frame coincides with the electron-nucleon center of mass (CM); the exchanged photon carries momentum $\vec{q}$ but no energy: the four-momentum transfer is $q^\mu = (0, \vec{q})$

EM form factors empirical parametrization

The nucleon FFs are extracted from scattering reactions of electrons on protons or electrons on deuterium, for neutrons. Here we present as an example the parametrization of Ref. [49]. In this functional form, the EM FFs are writen in terms of a dipole. For the proton we have

$$\begin{aligned} F_1^{(p)} &= \frac{\left[1+\tau\left(1+\lambda_p\right)\right] G}{(1+\tau)}\,, \\ F_2^{(p)} &= \frac{\lambda_p\, G}{(1+\tau)}\,, \\ \tau &= \frac{Q^2}{4M_{\mathrm{N}}^2}\,, \end{aligned} \tag{3.37}$$

with $Q^2 = -q^2$, $G = (1+4.97\tau)^{-2}$, and the anomalous momentum $\lambda_p = 1.793$ in units of nuclear magnetons. The neutron parametrization is given by

$$\begin{aligned} F_1^{(n)} &= \frac{\tau\lambda_n\left(1-\eta\right)\, G}{(1+\tau)}\,, \\ F_2^{(n)} &= \frac{\lambda_n\left(1+\tau\,\eta\right)\, G}{(1+\tau)}\,. \end{aligned} \tag{3.38}$$

In this case, the anomalous momentum is $\lambda_n = -1.913$ and $\eta = (1+5.6\tau)^{-1}$. Both FFs, for proton and neutron, are plotted in Fig. 3.3, 3.4 as functions of Q^2.

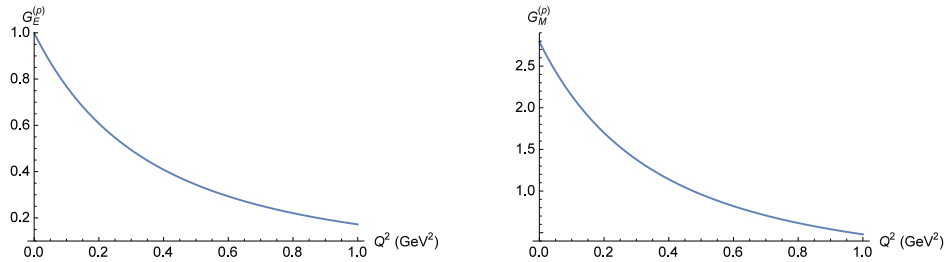

Figure 3.3: Sachs form factors of the proton as functions of Q^2.

3.2.3 Weak form factors

In the case of CC interactions the vector part of the transition of a neutron into proton is

$$\langle n|\, V_{\mathrm{CC}}^{\mu}\,|p\rangle = \langle n|\, V_1^{\mu} + \mathrm{i}V_2^{\mu}\,|p\rangle = \mathcal{V}^{\mu} = \mathcal{V}_p^{\mu} - \mathcal{V}_n^{\mu}\,. \tag{3.39}$$

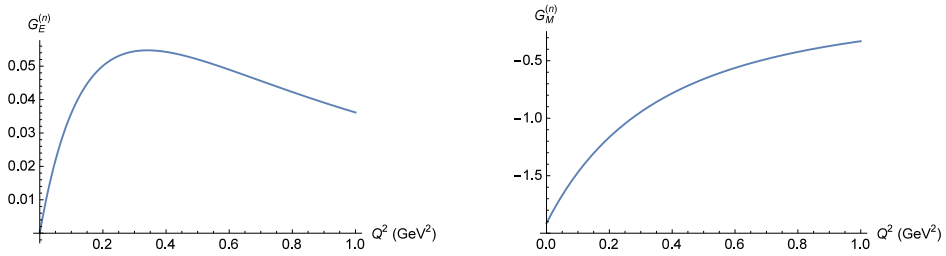

(a) (b)

Figure 3.4: Sachs form factors of the neutron as functions of Q^2.

Eq. 3.39 shows that the vector part of the CC can be expressed in terms of the EM one. The consequence for the CC vector FFs is the relation

$$F_{1,2}^{V} = F_{1,2}^{(p)} - F_{1,2}^{(n)} \,, \tag{3.40}$$

where $F_{1,2}^{(p,n)}$ are the EM FFs of the proton and the neutron.

The vector part of the NC transitions is given by

$$\begin{aligned}
\langle p|\, V_{\mathrm{NC}}^{\mu}\, |p\rangle &= \langle p|\, \left(1 - 2\sin^2\theta_W\right) V_3^{\mu} - \sin^2\theta_W V_Y^{\mu}\, |p\rangle \\
&= \left(\frac{1}{2} - \sin^2\theta_W\right) \mathcal{V}^{\mu} - \sin^2\theta_W \mathcal{V}_Y^{\mu} \\
&= \left(\frac{1}{2} - 2\sin^2\theta_W\right) \mathcal{V}_p^{\mu} - \frac{1}{2}\mathcal{V}_n^{\mu} \,, \\
\langle n|\, V_{\mathrm{NC}}^{\mu}\, |n\rangle &= -\left(\frac{1}{2} - \sin^2\theta_W\right) \mathcal{V}^{\mu} - \sin^2\theta_W \mathcal{V}_Y^{\mu} \\
&= \left(\frac{1}{2} - 2\sin^2\theta_W\right) \mathcal{V}_n^{\mu} - \frac{1}{2}\mathcal{V}_p^{\mu} \,.
\end{aligned} \tag{3.41}$$

Hence, the FFs for NC in terms of the EM ones are

$$\begin{aligned}
\tilde{F}_{1,2}^{(p)} &= \left(\frac{1}{2} - 2\sin^2\theta_W\right) F_{1,2}^{(p)} - \frac{1}{2} F_{1,2}^{(n)} \,, \\
\tilde{F}_{1,2}^{(n)} &= \left(\frac{1}{2} - 2\sin^2\theta_W\right) F_{1,2}^{(n)} - \frac{1}{2} F_{1,2}^{(p)} \,.
\end{aligned} \tag{3.42}$$

These relations between the weak vector FFs and the EM FFs, allow to use input from electron scattering experiments in neutrino cross sections, as consequence of isospin symmetry.

For the axial part of the current there is no EM counterpart. Still we can relate the axial part of the NC interactions with the one of the CC. For a transition of a neutron into a proton, the axial current is

$$\langle n|\, A^\mu_{\rm CC}\,|p\rangle = \langle n|\, A^\mu_1 + \mathbb{i} A^\mu_2\,|p\rangle = \mathcal{A}^\mu\,. \tag{3.43}$$

In the case of NCs we have

$$\begin{aligned}\langle p|\, A^\mu_{\rm NC}\,|p\rangle &= \langle p|\, A^\mu_3\,|p\rangle = \frac{1}{2}\mathcal{A}^\mu\,,\\ \langle n|\, A^\mu_{\rm NC}\,|n\rangle &= \langle n|\, A^\mu_3\,|n\rangle = -\frac{1}{2}\mathcal{A}^\mu\,.\end{aligned} \tag{3.44}$$

The consequence for the FFs is the relation

$$\begin{aligned}\tilde{F}^{(p)}_{A,P} &= \frac{1}{2}F_{A,P}\,,\\ \tilde{F}^{(n)}_{A,P} &= -\frac{1}{2}F_{A,P}\,,\end{aligned} \tag{3.45}$$

where $F_{A,P}\left(\tilde{F}_{A,P}\right)$ are the axial and pseudoscalar FFs for CC (NC) interactions. Eq. (3.45) shows that we only need one set of axial FFs to describe both kinds of weak nucleon transitions.

Back in Sec. 2.4, the lowest order chiral Lagrangian in the meson sector, Eq. (2.53), contains a direct coupling of the charged vector bosons to pions,

$$\mathcal{L}^{(2)}_M \supset \mathcal{L}_{W\phi} = \frac{f}{2}{\rm Tr}\left[l^{\rm CC}_\mu \partial^\mu \phi\right]\,. \tag{3.46}$$

Substituting Eqs. (2.45) and (2.50),

$$\begin{aligned}\mathcal{L}_{W\phi} = -f\frac{g}{2}\Big[&W^\dagger_\mu\left(V_{ud}\partial^\mu\pi^- + V_{us}\partial^\mu K^-\right)\\ &+W_\mu\left(V_{ud}\partial^\mu\pi^+ + V_{us}\partial^\mu K^+\right)\Big]\,.\end{aligned} \tag{3.47}$$

This implies that the Feynman diagram of Fig. 3.5 defines a pion-pole contribution to the axial current, Eq. (3.30),

$$\mathcal{A}^\mu_{\rm pp} = \overline{u}(p')\left[-\frac{G_{\pi N}(q^2)}{M_{\rm N}}\not{q}\gamma_5\frac{f\,q^\mu}{q^2-m^2_\pi}\right]u(p)\,, \tag{3.48}$$

where $G_{\pi N}$ stands for the πNN FF. Writing $q = p' - p$ and applying the Dirac equation,

$$\mathcal{A}^\mu_{\rm pp} = \overline{u}(p')\left[-G_{\pi N}(q^2)\frac{2f}{q^2-m^2_\pi}q^\mu\gamma_5\right]u(p)\,. \tag{3.49}$$

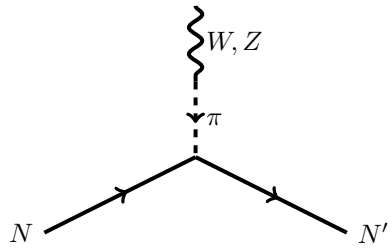

Figure 3.5: Diagram of the pion-pole contribution to the interaction between a vector boson and a nucleon.

Assuming that the pseudoscalar FF is dominated by the pion pole

$$F_P = \frac{2M_{\mathrm{N}} f}{Q^2 + m_\pi^2} G_{\pi N}(Q^2) \,, \tag{3.50}$$

with $Q^2 = -q^2$. In the chiral limit $q_\mu A^\mu = 0$, so that

$$F_A(Q^2) = \frac{f}{M_{\mathrm{N}}} G_{\pi N}(Q^2) \,. \tag{3.51}$$

At $Q^2 = 0$, this is the Goldberger-Treiman (GT) relation:

$$g_A = \frac{f}{M_{\mathrm{N}}} G_{\pi N}(0) \,. \tag{3.52}$$

Neglecting the corrections in Eq. (3.51) when going from the chiral limit to the phisical point, one can express F_P in terms of F_A,

$$F_P = F_A \frac{2M_{\mathrm{N}}^2}{Q^2 + m_\pi^2} \,, \tag{3.53}$$

See Refs. [41, 42] for further details. In the cross section F_P appears in terms proportional to $(m_l/M)^4$, which are neglected in NC interactions, where the outgoing lepton is a neutrino. The contribution of these terms to charged-current quasi-elastic (CCQE) scattering is also very small except for ν_τ interactions. However, F_P has been studied in muon capture $\mu^- p \to \nu_\mu n$ and found to be consistent with pion-pole dominance [50].

For the Q^2 dependence of the axial FF, the most common parametrization is the dipole ansatz,

$$F_A^{\mathrm{dipole}}(Q^2) = g_A \left(1 + \frac{Q^2}{M_A^2}\right)^{-2} \,, \tag{3.54}$$

in terms of a single parameter, the so-called axial mass M_A. The axial coupling $g_A = F_A(Q^2 = 0)$ is known rather precisely from the neutron β-decay asymmetry [40]:

$$g_A = 1.2723 \pm 0.0023\,, \tag{3.55}$$

although a more precise value can be obtained using recent measurements of the nucleon lifetime [51]. The limitations of this ansatz and other alternatives are covered in Chapter 5.

3.2.4 Electron-nucleon scattering

In this section we describe the EM interaction in the elastic scattering of an electron on a nucleon, $l(k) + N(p) \to l(k') + N(p')$, Fig. 3.2. The most general hadronic current for this reaction has the expression of the vector current in Eq. 3.30,

$$\langle N(p')|J^\mu|N(p)\rangle = \overline{u}(p')\left[\gamma^\mu F_1 + \frac{\mathbb{i}}{2M_\mathrm{N}}\sigma^{\mu\nu}q_\nu F_2\right]u(p)\,. \tag{3.56}$$

For the hadronic part of the process we can write:

$$\begin{aligned} H^{\mu\nu} = \frac{1}{2}\mathrm{Tr}\Bigg[&\left(\not{p}' + M_\mathrm{N}\right)\left(\gamma^\mu F_1 + \frac{F_2}{2M_\mathrm{N}}\left(2M_\mathrm{N}\,\gamma^\mu - \left(p'^\mu + p^\mu\right)\right)\right) \\ &\times\left(\not{p} + M_\mathrm{N}\right)\left(\gamma^\nu F_1 + \frac{F_2}{2M_\mathrm{N}}\left(2M_\mathrm{N}\,\gamma^\nu - \left(p'^\nu + p^\nu\right)\right)\right)\Bigg]\,, \end{aligned} \tag{3.57}$$

After performing the trace we have

$$\begin{aligned} H^{\mu\nu} = {}& 2F_1^2\left[p'^\mu p^\nu + p'^\nu p^\mu + g^{\mu\nu}\left(M_\mathrm{N}^2 - (p'\cdot p)\right)\right] \\ &+ 2F_1F_2\left[p'^\mu p^\nu + p'^\nu p^\mu - p'^\mu p'^\nu - p^\nu p^\mu + g^{\mu\nu}\left(M_\mathrm{N}^2 - (p'\cdot p)\right)\right] \\ &+ \frac{1}{2}F_2^2\Bigg[\left(p'^\mu p^\nu + p'^\nu p^\mu\right)\left(1 + \frac{(p'\cdot p)}{M_\mathrm{N}^2}\right) \\ &+ \left(p'^\mu p'^\nu + p^\nu p^\mu\right)\left(\frac{(p'\cdot p)}{M_\mathrm{N}^2} - 3\right) + 4g^{\mu\nu}\left(M_\mathrm{N}^2 - (p'\cdot p)\right)\Bigg]\,. \end{aligned} \tag{3.58}$$

There is only one final hadronic state for this scattering, hence, the hadronic tensor is given by

$$\begin{aligned} W^{\mu\nu} &= \frac{1}{2M_\mathrm{N}}\int\frac{d^3p'}{2E'}\delta^{(4)}\left(k + p - p' - k'\right)H^{\mu\nu} \\ &= \frac{1}{2M_\mathrm{N}\,E'}\delta\left(k^0 + E - E' - k'^0\right)H^{\mu\nu}\,. \end{aligned} \tag{3.59}$$

In an EM process like this one, the general structure of the hadronic tensor is given in Eq. (3.13). We now contract Eq. (3.59) with the metric tensor, $g_{\mu\nu}$ and with $p_\mu p_\nu$,

$$\begin{aligned} g_{\mu\nu}W^{\mu\nu} =& \frac{1}{4M_{\mathrm{N}}\,E'}\delta\left(k^0+E-k'^0-E'\right)\left[4F_1^2\left(M_{\mathrm{N}}^2-\frac{q^2}{2}\right)\right. \\ &\left.+6F_1F_2\,q^2+F_2^2\,q^2\left(2+\frac{q^2}{4M_{\mathrm{N}}^2}\right)\right], \end{aligned} \tag{3.60}$$

$$\begin{aligned} p_\mu p_\nu W^{\mu\nu} =& \frac{1}{4M_{\mathrm{N}}\,E'}\delta\left(k^0+E-k'^0-E'\right)\left[4F_1^2M_{\mathrm{N}}^2\left(M_{\mathrm{N}}^2-\frac{q^2}{2}\right)\right. \\ &\left.+2F_1F_2\,q^2\left(M_{\mathrm{N}}^2-\frac{q^2}{4}\right)+F_2^2\left(\left(M_{\mathrm{N}}^2-\frac{q^2}{4}\right)\frac{q^4}{4M_{\mathrm{N}}^2}\right)\right]. \end{aligned} \tag{3.61}$$

Then, we do the same contractions for Eq. (3.13),

$$g_{\mu\nu}W^{\mu\nu} = -3W_1+\frac{W_2}{M_{\mathrm{N}}^2}\left(M_{\mathrm{N}}^2-\frac{q^2}{4}\right), \tag{3.62}$$

$$p_\mu p_\nu W^{\mu\nu} = \left(M_{\mathrm{N}}^2-\frac{q^2}{4}\right)\left[-W_1+\frac{W_2}{M_{\mathrm{N}}^2}\left(M_{\mathrm{N}}^2-\frac{q^2}{4}\right)\right], \tag{3.63}$$

Comparing the results for both expressions of the hadronic tensor, we can obtain the structure functions W_1 and W_2.

$$W_1 = \frac{1}{4M_{\mathrm{N}}\,E'}\delta\left(k^0+E-k'^0-E'\right)\left(-q^2\right)\left(F_1+F_2\right)^2. \tag{3.64}$$

$$W_2 = \frac{1}{4M_{\mathrm{N}}\,E'}\delta\left(k^0+E-k'^0-E'\right)\left(4M_{\mathrm{N}}^2F_1^2-q^2F_2^2\right). \tag{3.65}$$

In terms of the Sachs FFs, Eq. (3.36), we can write

$$\begin{aligned} W_1 &= \frac{1}{4M_{\mathrm{N}}\,E'}\delta\left(k^0+E-k'^0-E'\right)\left(-q^2\right)G_M^2 \\ W_2 &= \frac{1}{4M_{\mathrm{N}}\,E'}\delta\left(k^0+E-k'^0-E'\right)\frac{4M_{\mathrm{N}}^2}{\left(1-\frac{q^2}{4M_{\mathrm{N}}^2}\right)}\left(G_E^2-\frac{q^2}{4M_{\mathrm{N}}^2}G_M^2\right). \end{aligned} \tag{3.66}$$

After substituting Eq. (3.66) in the expression for the differential cross section Eq. (3.21), we integrate the delta and we have

$$\frac{d\sigma}{d\Omega} = \frac{\alpha^2}{4(k^0)^2\,\sin^4\frac{\theta}{2}}\frac{\cos^2\frac{\theta}{2}}{1+\frac{2k^0}{M_{\mathrm{N}}}\sin^2\left(\frac{\theta}{2}\right)}\left[\frac{G_E^2+\tau\,G_M^2}{1+\tau}+2\,\tau\,G_M^2\tan^2\frac{\theta}{2}\right], \tag{3.67}$$

with $\tau = -\dfrac{q^2}{4M_{\mathrm{N}}}$. Finally we arrived to the same expression for the cross section that can be found in the literature, [42, 52].

3.3 Elastic scattering on a scalar nucleus

What characterizes a scalar nucleus is the value of it's spin, $J = 0$. The interest of this kind of nuclei, like ^{12}C, ^{16}O or ^{40}Ar, is their extended use in neutrino detectors. In this case, the most general structure for the current is

$$\langle A(p)|\, J^{\mu}\, |A(p')\rangle = \frac{F_1(q^2)}{M_A} p^{\mu} + \frac{F_2(q^2)}{M_A} q^{\mu}\,, \tag{3.68}$$

where M_A in the nucleus mass. As in the case of the QE scattering on nucleons, the FFs only depend on q^2, being the only independent scalar. The current can not carry any other kinematic dependence because the nucleus has spin zero and remains in its ground state after the interaction.

3.3.1 Electromagnetic form factor

The conservation of the EM current,

$$q_{\mu}\, \langle A(p)|\, J^{\mu}\, |A(p')\rangle = \frac{F_1(q^2)}{M_A}\,(q\cdot p) + \frac{F_2(q^2)}{M_A} q^2 = 0\,, \tag{3.69}$$

implies a relation between the two FFs,

$$F(q^2) \equiv F_2(q^2) = -F_1(q^2)\frac{(q\cdot p)}{q^2}\,. \tag{3.70}$$

As it happens in the case of the nucleon FFs, $F(q^2)$ has to be real due to the $\mathcal{T}$ invariance. After substituting Eq. (3.70), the current reads

$$\langle A(p)|\, J^{\mu}\, |A(p')\rangle = 2F(q^2)\left(p^{\mu} - \frac{(q\cdot p)}{q^2} q^{\mu}\right)\,, \tag{3.71}$$

in terms of the FF of the scalar nucleus. In the Breit frame, the incident lepton momentum is $\vec{k} = \vec{q}/2$ and it scatters with a nucleus which momentum is $\vec{p} = -\vec{q}/2$. The recoil of the nucleus is $\vec{p'} = \vec{q}/2$. The virtual mediator carries momentum but not energy: $q^{\mu} = (0, \vec{q})$. For an extended nucleus in this frame, the FF is the Fourier transform of the charge distribution, [53]

$$F(q^2) = \int d^3r\, e^{\mathrm{i}\vec{q}\cdot\vec{r}}\rho\,(\vec{r})\,. \tag{3.72}$$

In this relation, the spatial dependence has been integrated, hence the FF remains only as a function of q^2 once the density depends only on the absolute value of the spacial coordinate $|\vec{r}|$.

We choose the normalization of the charge density to be the nucleus electric charge, Z,

$$\int d^3r\, \rho\,(\vec{r}) = Z\,, \tag{3.73}$$

hence $F(0) = Z$. In the case of a point-like particle $F(q^2) = Z$, for any q^2. On the other hand, the nucleus charge density is well defined in the laboratory frame. In the approximation where we neglect the electron mass in comparison with the nucleus one, the Breit and the laboratory frame are the same. In other words, we neglect the boost effect between those two frames, for the charge density.

EM scalar nucleus form factor empirical parametrization

In the same way as for nucleons, the nuclear FFs are extracted from scattering experiments. In this case the sources are the electron-nucleus scattering experiments on different nuclei. In Fig. 3.6 it is shown the dipole parametrization from Ref. [54],

$$F(Q^2) = \frac{Z}{(1 + t/d)}, \tag{3.74}$$

where A is the mass number and $d = 0.164A^{-2/3}$ GeV^2. This parametrization is commonly used in the literature due to its simplicity for any nucleus and that it can be integrated analytically.

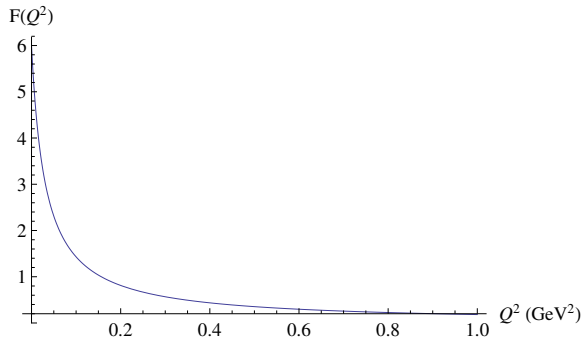

Figure 3.6: ^{12}C nucleus form factor, as a function of Q^2.

More realistic descriptions for several nuclei can be obtained from the charge density parametrizations of the Ref. [55]. In this reference the parametrizations are classified in model-dependent and model-independent categories. Among the latter, the one that can be written in terms of the Bessel spherical functions allows us to obtain an analytical expression for the FF. The charge density in this parametrization reads

$$\rho(r) = \begin{cases} \sum_{\nu=1}^{N} a_\nu j_0\left(\nu\pi\frac{r}{R}\right) & , r \leq R \\ 0 & , r \geq R \end{cases} , \tag{3.75}$$

where $j_0(x) = \dfrac{\sin x}{x}$ is the spherical Bessel function of zeroth order. The parameters of the charge density function are the coefficients of the series, a_ν, and the radius of the nucleus, R.

After the substitution of the charge density, Eq. (3.75), in Eq. (3.72), we perform the integral, obtaining the expression for the FF,

$$F(Q) = 4\pi \frac{\sin(Q\,r)}{Q\,r} \sum_{\nu=1}^{N} (-1)^{\nu+1} \frac{R^3\, a_\nu}{\pi^2\,\nu^2 - Q^2\,R^2} , \tag{3.76}$$

where $Q = \sqrt{-q^2}$. In Fig. 3.7 are shown the EM FFs for the ^{12}C and ^{40}Ar nuclei.

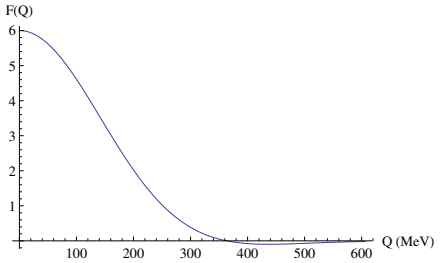

(a) ^{12}C form factor

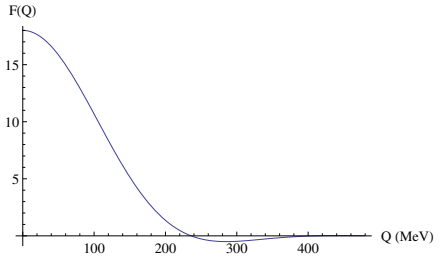

(b) ^{40}Ar form factor

Figure 3.7: Form factors from the model-independent analysis based on spherical Bessel functions, as a function of Q.

In Fig. 3.8 the comparison between both parametrizations for ^{12}C and ^{40}Ar nuclei is shown. We observe that the parametrization based on Bessel functions go down before the dipole one. This difference of behaviour has a small relevance in the total cross section, because the main contribution of the FF is the charge and, to a lesser extent, the mean square radius.

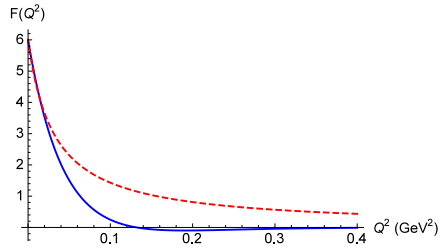

(a) ^{12}C form factor

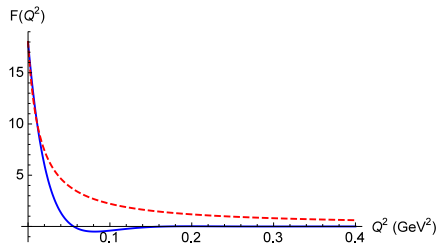

(b) ^{40}Ar form factor

Figure 3.8: Nuclear form factor as a function of $Q^2 = -q^2$. Discontinuous red line shows the dipole parametrization. The blue line is the model-independent parametrization of Ref. [55].

The mean square radius is defined as

$$\langle r^2 \rangle = \frac{1}{Z} \int d^3 r \rho(r) r^2 \,. \tag{3.77}$$

A power series expansion on Q^2 of the FF, Eq. (3.72), shows the the relation between the quadratic term and the mean square radius,

$$F(Q^2) = Z \left(1 - \frac{1}{6} \langle r^2 \rangle Q^2 + O(Q^4) \right) \,. \tag{3.78}$$

The values of the mean square radius in the dipole parametrization are $\langle r^2 \rangle^{1/2} = 2.728$ fm for ^{12}C and $\langle r^2 \rangle^{1/2} = 4.075$ fm for ^{40}Ar. In the case of the parametrization of Eq. (3.76), the values are $\langle r^2 \rangle^{1/2} = 2.463$ fm for ^{12}C and $\langle r^2 \rangle^{1/2} = 3.423$ fm for ^{40}Ar. We can see that, although the values in the second case is smaller, there are no significant differences. In a graphic way, the mean square radius corresponds to the slope of the curve at the origin.

3.3.2 Weak form factor

For NC interactions, the conservation of the vector current (CVC) gives the same relation of Eq. (3.70). Also, in the case of the scalar nucleus, Eq. (3.68) shows that there is no axial structure in the current. Therefore, like in the case of the EM interaction, there is only one FF for weak currents.

An atomic nucleus is composed by protons and nucleons and the weak FF must take into account this structure. While the proton is made of two

up-quarks and one down-quark, the content of the neutron is one up-quark and two down-quarks. From Eq. (2.21), we can extract the weak charge of each quark,

$$V^{\mu}_{\mathrm{NC}} = \overline{q}_u \gamma^{\mu} \left[\frac{1}{2} - \left(\frac{2}{3} \right) 2 \sin^2 \theta_W \right] q_u + \overline{q}_d \gamma^{\mu} \left[-\frac{1}{2} - \left(-\frac{1}{3} \right) 2 \sin^2 \theta_W \right] q_d + \overline{q}_s \gamma^{\mu} \left[-\frac{1}{2} - \left(-\frac{1}{3} \right) 2 \sin^2 \theta_W \right] q_s \, . \tag{3.79}$$

We define then,

$$\begin{aligned} Q^u_W &\equiv \frac{1}{2} - \left(\frac{2}{3} \right) 2 \sin^2 \theta_W \, , \\ Q^d_W &\equiv -\frac{1}{2} - \left(-\frac{1}{3} \right) 2 \sin^2 \theta_W \, . \end{aligned} \tag{3.80}$$

We can do the Fourier transform of the density distribution of both kinds of nucleons in the nucleus, obtaining

$$F_N(q^2) = \int d^3 r \, e^{\mathrm{i} \vec{q} \cdot \vec{r}} \rho_N \left(\vec{r} \right) \, , \qquad N = p, n \, . \tag{3.81}$$

The weak FF of the whole nucleus is given as the sum of the FF of each kind of nucleons, multiplied by their respective weak charges,

$$\begin{aligned} F_W(q^2) &= F_p(q^2) \left(2Q^u_W + Q^d_W \right) + F_n(q^2) \left(Q^u_W + 2Q^d_W \right) \\ &= F_p(q^2) \left(\frac{1}{2} - 2 \sin^2 \theta_W \right) - \frac{1}{2} F_n(q^2) \, . \end{aligned} \tag{3.82}$$

A good approximation is to use the electric charge distribution as input for the density of protons in the nucleus. Also we can approximate the distribution of neutrons to the protons one, taking the same parametrization for both distributions.

3.3.3 Scattering of electrons on scalar nuclei

In this section we come back to the electron-hadron scattering example. In this case we analyse the interaction between electrons and scalar nuclei. The hadronic current for an spinless nucleus is given in Eq. (3.71). The correspondent tensor is then

$$H^{\mu\nu} = 4 M_A^2 \, F(q^2) \left(p^{\mu} - \frac{(q \cdot p)}{q^2} q^{\mu} \right) \left(p^{\nu} - \frac{(q \cdot p)}{q^2} q^{\nu} \right) \, . \tag{3.83}$$

After substituting this expression in Eq. (3.10), the comparison with Eq. (3.13) gives

$$\begin{aligned} W_1(\omega, q^2) &= 0 \\ W_2(\omega, q^2) &= \frac{M_A}{E'} \delta\left(k^0 + E - k'^0 - E'\right) F^2(q^2) \,. \end{aligned} \tag{3.84}$$

In the same way than for nucleons, we substitute the expression of W_2 in Eq. (3.21) obtaining

$$\frac{d\sigma}{d\Omega} = \frac{\alpha^2}{4(k^0)^2 \, \sin^4 \frac{\theta}{2}} \, \frac{\cos^2 \frac{\theta}{2}}{1 + \frac{2k^0}{M_A} \sin^2\left(\frac{\theta}{2}\right)} \, F^2(q^2) \,, \tag{3.85}$$

in terms of the nuclear FF, see Sec. 3.3.

Part II

Analysis and Results

Chapter 4

Production and radiative decay of heavy neutrinos at the Booster Neutrino Beam

4.1 Introduction

The paradigm of three mixing neutrino flavors emerges from oscillation experiments with solar, atmospheric, reactor and accelerator neutrinos in which the square-mass differences and mixing angles have been determined with ever growing precision. Nevertheless, a number of anomalies that challenge this picture has been observed. One of them, reported by MiniBooNE, has found an excess of electron-like events over the predicted background in both ν and $\bar{\nu}$ modes [56, 57, 57, 58], Fig. 4.1. The excess is concentrated at $200 < E_\nu^{\mathrm{QE}} < 475$ MeV, where E_ν^{QE} is the neutrino energy reconstructed assuming a CCQE nature of the events.

Existing analyses struggle to accommodate this result together with world oscillation data, even in presence of one or more families of sterile neutrinos [59]. The effect of multinucleon interactions in E_ν reconstruction is insufficient to remove the tension in global analyses [60], pointing at an explanation that does not invoke oscillations. It was suggested that an underestimated background from photons emitted in NC interactions could account for the excess [61]. Indeed, the MiniBooNE detector does not distinguish between electrons and single photons. However, studies considering nuclear effects and acceptance corrections [3, 62], obtain a number of photon-induced electron-like events which is consistent with the MiniBooNE estimate.

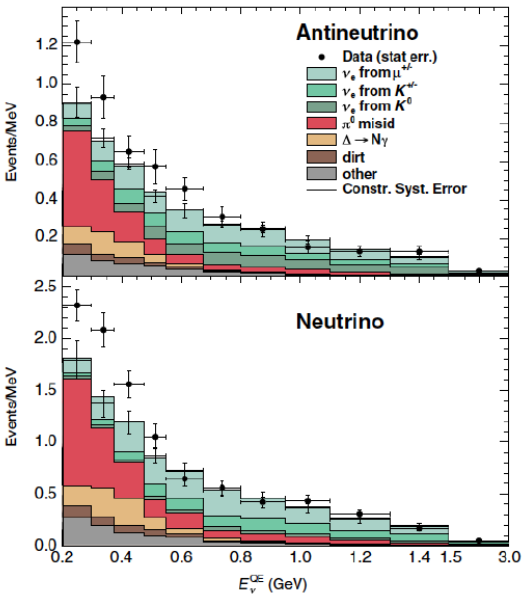

Figure 4.1: Results of the MiniBooNE experiment [57]. The distribution of electron-like events (oscillation candidates) as a function of the reconstructed (anti)neutrino energy. The upper figure corresponds to antineutrino mode, while the lower is for neutrino mode. In both modes an excess of events in the lower energy region is observed.

A variety of ideas to explain the MiniBooNE anomaly has been put forward, involving the production of heavy sterile/dark neutrinos and their subsequent decay into non-observable particles (such as active or other sterile neutrinos) and single photons or e^+e^- pairs [63, 64]. In one of the earlier studies, Gninenko proposed that additional photons could originate in the weak production of a heavy ($m_h \approx 50$ MeV) sterile neutrino slightly mixed with muon neutrinos, followed by its radiative decay [65] In Ref. [4] it was pointed out that the ν_h could also be electromagnetically produced, alleviating tensions in the original proposal with other data such as those from radiative muon capture measured at TRIUMF.

We have revisited the scenario presented in Ref. [4]. We compute coherent and incoherent ν_h production using present understanding of EM and weak interactions on nucleons and nuclei. For a more detailed analysis, we compare to the MiniBooNE excess of events in the originally measured electron energy and angle [66] (being the photon ones in our case) rather than

in $E_\nu^{\rm QE}$. We also take into account the experimental efficiency correction available from Ref. [66].[1]

Further insight on the nature of the MiniBooNE anomaly should be brought by the SBN program with the SBND, MicroBooNE (currently analyzing data) and ICARUS detectors, capable of distinguishing between electrons and photons. We have also computed the number of photon events from ν_h for the target (Argon) and geometry of the SBN detectors.

We have studied ν_h EM and weak production in the following processes

$$\nu_\mu\,,\bar{\nu}_\mu(k) + N(p) \;\to\; \nu_h\,,\bar{\nu}_h(k') + N(p')\,, \tag{4.1}$$

$$\nu_\mu\,,\bar{\nu}_\mu(k) + A(p) \;\to\; \nu_h,\bar{\nu}_h(k') + A(p')\,, \tag{4.2}$$

$$\nu_\mu\,,\bar{\nu}_\mu(k) + A(p) \;\to\; \nu_h,\bar{\nu}_h(k') + X(p')\,. \tag{4.3}$$

Reaction (4.2) is coherent while (4.3) is incoherent; excited states X include any number of knocked out nucleons but no meson production. The considered targets are $N = p$ and $A = {}^{12}$C for MiniBooNE (CH_2),and $A = {}^{40}$Ar for the SBN detectors.

4.2 Electromagnetic production of heavy neutrinos

Cherenkov detectors are not able to distinguish an electron from a photon, therefore the radiative decay of a heavy neutrino, Fig. 4.2, in such kind of detectors, would produce a signal which would be wrongly classified as a ν_e event. These heavy neutrinos would be produced by the interaction of muonic neutrinos of the beam directed to the detector and the detector's own material.

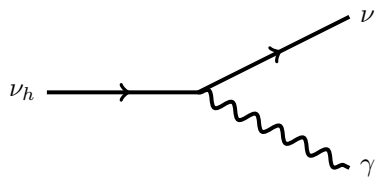

Figure 4.2: Decay of a heavy neutrino into a photon and a light neutrino.

[1] As we analyze both neutrino and antineutrino modes, in order to treat them on the same ground we stick to the original MiniBooNE results of Refs. [56, 57] and do not consider the more recent updates in antineutrino mode which are anyway consistent with the early findings.

The model presented in Ref. [4] is based on the idea proposed in Ref. [65], where a heavy neutrino is presented as a possible common explanation for the Liquid Scintillator Neutrino Detector (LSND) and MiniBooNE anomalies. The estimated mass of the ν_h in Ref. [4] is $m_h \approx 50$ MeV. It is assumed that the left-handed component of the ν_h has a slight mixing with ν_μ. In this section we describe the EM mechanism of ν_h production.

4.2.1 Electromagnetic interaction of heavy neutrinos

In the one-photon approximation, the electromagnetic interactions of a neutrino field $\nu(x)$ can be described by the effective interaction Hamiltonian [67]:

$$\mathcal{H}_{\text{eff}}(x) = \sum_{k,j=1}^{3} \overline{\nu_k}(x)\Lambda_\mu^{kj}\nu_j(x)A^\mu(x)\,, \tag{4.4}$$

where $A^\mu(x)$ is the electromagnetic field. Λ_μ^{kj} is a 4×4 matrix in spinor space, given by [67]

$$\begin{aligned}\Lambda_\mu^{h\alpha} = &\left(\gamma_\mu - q_\mu\frac{\not{q}}{q^2}\right)\left[f_Q^{h\alpha}(q^2) + f_A^{h\alpha}(q^2)q^2\gamma_5\right] \\ &- \mathbb{i}\sigma_{\mu\nu}q^\nu\left[f_M^{h\alpha}(q^2) + \mathbb{i}f_E^{h\alpha}(q^2)\gamma_5\right]\,.\end{aligned} \tag{4.5}$$

f_Q, f_M, f_E and f_A are the real charge, dipole magnetic and electric, and anapole neutrino FFs. In Ref. [67] it is shown that CP is conserved if f_Q, f_M and f_A, are real and symmetric and f_E is imaginary and antisymmetric.

In the case of an EM reaction, with an incoming light neutrino of flavor α and an outgoing heavy neutrino, we can write,

$$\mathcal{H}_{\text{eff}}(x) = \overline{\nu}_h(x)\Lambda_\mu^{h\alpha}\nu_\alpha(x)A^\mu(x)\,, \tag{4.6}$$

We follow the choice of Ref. [4], where $f_M = -\mathbb{i}f_E = \mu_{\text{tr}}^i/2$, in terms of the transition dipole magnetic moment for the process $\nu_h \to \nu_i\gamma$, μ_{tr}^i. The charge and anapole neutrino FFs are set to $f_Q = f_A = 0$, hence

$$\Lambda_\mu^{h\alpha} = -\frac{1}{2}\mathbb{i}\sigma_{\mu\nu}q^\nu\mu_{tr}^\alpha\left(1-\gamma_5\right)\,. \tag{4.7}$$

With these parameters, we recover the relevant terms in the effective Lagrangian used in Ref. [4],

$$\mathcal{L}_{\text{eff}} \supset \frac{1}{2}\mu_{\text{tr}}^i\left[\overline{\nu}_h\sigma_{\mu\nu}\left(1-\gamma_5\right)\nu_i + \overline{\nu}_i\sigma_{\mu\nu}\left(1+\gamma_5\right)\nu_h\right]\partial^\mu A^\nu\,. \tag{4.8}$$

In this scenario, the heavy neutrinos are Dirac particles with $m_{\nu_i} \ll m_{\nu_h}$.

We proceed now in analogy to the electron-hadron scattering scenario described in Chapter 3. We begin by calculating the cross section in terms of the structure functions for the inclusive process $\nu_i(k) + N(p) \to \nu_h(k') + X(p')$, fixing them afterwards for specific cases. As we are considering an EM interaction, mediated by a photon, its propagator is given by Eq. (3.20). Its coupling to the hadronic and leptonic currents are proportional to the electric charge and $\mu^i_{\rm tr}$, respectively. After substituting the couplings and the propagator in Eq. (3.9), we obtain

$$\frac{d\sigma}{dk'^0\, d\Omega} = \frac{\alpha\,(\mu^i_{\rm tr})^2}{16\,\pi\,q^4}\frac{|\vec{k'}|}{|\vec{k}|} L_{\mu\nu} W^{\mu\nu}\,, \tag{4.9}$$

with $d\Omega = d\cos\theta d\varphi$, the solid angle of the outgoing neutrino with respect to the direction of the incoming one. The hadronic tensor in this case is the same than in the electron-hadron interaction, Eq. (3.13), but the leptonic tensor is different from the SM one and reads

$$\begin{aligned} L^{\mu\nu} &= \mathrm{Tr}\left[(\not{k}' + m_h)\sigma^{\delta\mu}(1-\gamma_5)\not{k}\,\sigma^{\rho\nu}(1+\gamma_5)\right] q_\rho q_\delta \\ &= 8\left[(k'\cdot k)\left((k^\mu + k'^\mu)(k^\nu + k'^\nu) - m_h^2 g^{\mu\nu}\right)\right. \\ &\quad \left. -2m_h^2 k^\mu k^\nu + i\, m_h^2 \epsilon^{\mu\nu\sigma\rho} k'_\sigma k_\rho\right]\,, \end{aligned} \tag{4.10}$$

where we have neglected the light neutrino mass. The contraction of this tensor with the hadronic one of Eq. (3.13) is

$$\begin{aligned} L_{\mu\nu}W^{\mu\nu} = 8W_1 &\left[(k'\cdot k)\left(\frac{(k\cdot q + k'\cdot q)^2}{q^2} + 3m_h^2 - (k+k')^2\right)\right. \\ &\left. -2m_h^2\frac{(k\cdot q)^2}{q^2}\right] \\ &+ 8\frac{W_2}{M^2}\left[(k'\cdot k)\left(\left((p\cdot k + p\cdot k') - \frac{(p\cdot q)}{q^2}q^2(k+k')\right)^2\right.\right. \\ &\left.\left. -m_h^2\left(p - \frac{(p\cdot q)}{q^2}\right)^2\right) - 2m_h^2\left((k\cdot p) - \frac{(p\cdot q)}{q^2}(k\cdot q)\right)^2\right]. \end{aligned} \tag{4.11}$$

After some algebra we find that

$$\begin{aligned}\frac{d\sigma}{dk'^0\,dt} = \frac{\alpha\,(\mu^i_{\rm tr})^2}{4\,(k^0)^2\,t^2}\Big\{ & W_1\,\left(m_h^2 - t\right)\left(2m_h^2 + t\right) \\ & + \frac{W_2}{4M^2}\Big[-t\left(2s + t - M^2 - M_X^2\right)^2 - 4m_h^4\,M^2 \\ & - m_h^2\left(3M^4 - 2M^2\left(M_X^2 + 2s + t\right)\right. \\ & \left. - \left(M_X^2 - t\right)\left(M_X^2 - 4s - t\right)\right)\Big]\Big\}\,,\end{aligned} \tag{4.12}$$

in terms of the Mandelstam variables s and $t = q^2$. The mass of the hadronic target is denoted by M while the invariant mass of the final state is M_X. As there is not a φ dependence in the cross section, the integration over this variable only contributes with a factor 2π in Eq. (4.12). It is clear that due to the photon propagator low-t interactions are favoured in EM scattering.

To obtain the angular distribution is straightforward using

$$\frac{d\sigma}{dk'^0\,d\cos\theta} = 2k_0|\vec{k'}|\frac{d\sigma}{dk'^0\,dt}\,, \tag{4.13}$$

and the relation $t = m_h^2 - 2k_0\left(k'_0 - |\vec{k'}|\cos\theta\right)$.

4.2.2 Quasielastic scattering

When the initial and final hadronic states coincide, we refer to as quasielastic scattering. In this case, Eq. (4.12) is reduced to

$$\begin{aligned}\frac{d\sigma}{dk'^0\,dt} = & \frac{\alpha\,(\mu^i_{\rm tr})^2}{4\,(k^0)^2\,t^2}\Big[W_1\,\left(m_h^2 - t\right)\left(2m_h^2 + t\right) \\ & + \frac{W_2}{4M^2}\left(-t\left(2s + t - 2M^2\right)^2 + m_h^2\,t\,(4s + t) - 4m_h^4\,M^2\right)\Big]\,.\end{aligned} \tag{4.14}$$

In the following, we address the specific cases of quasielastic scattering on nucleons and scalar nuclei (coherent case).

Quasielastic scattering on nucleons

The structure functions $W_{1,2}$ in this case, the same as in electron-nucleon elastic scattering, are readily available in Eq. (3.66). Substituting them in Eq. (4.14) we find

$$\frac{d\sigma}{dk'^0\,dt} = \frac{\alpha\,(\mu^i_{\rm tr})^2}{4\,(k^0)^2\,t^2}\,\frac{1}{4M_{\rm N}E'}\,\delta(k^0 + E - k'^0 - E')\left(\widetilde{W}_1 + \frac{\widetilde{W}_2}{4M_{\rm N}^2}\right)\,, \tag{4.15}$$

where we have defined:

$$\begin{aligned}\widetilde{W}_1 \equiv& -t\,G_M^2\,\left(m_h^2-t\right)\left(2m_h^2+t\right)\\ \widetilde{W}_2 \equiv& \frac{\left(G_E^2-\frac{t}{4M_{\rm N}^2}G_M^2\right)}{1-\frac{t}{4M_{\rm N}^2}}\left[-t\left(2s+t-2M_{\rm N}^2\right)^2+m_h^2\,t\,(4s+t)-4m_h^4\,M_{\rm N}^2\right]\,.\end{aligned} \tag{4.16}$$

After the integration over k'^0, using that $2k^0\,M_{\rm N}=s-M_{\rm N}^2$, we get

$$\frac{d\sigma}{dt}=\frac{\alpha\,(\mu_{\rm tr}^i)^2}{4\,\left(s-M_{\rm N}^2\right)^2\,t^2}\,\frac{1}{1-\frac{t}{4M_{\rm N}^2}}\left(G_E^2\,R_E-G_M^2\,R_M\right), \tag{4.17}$$

where

$$\begin{aligned}R_E=&-t\left(2s+t-2M_{\rm N}^2\right)^2+m_h^2\,t\,(4s+t)-4m_h^4\,M_{\rm N}^2\\ R_M=&\frac{t}{4M_{\rm N}^2}\left[-4t\left(\left(M_{\rm N}^2-s\right)^2+s\,t\right)+2m_h^2\,t\left(2s+t-2M_{\rm N}^2\right)\right.\\ &\left.-2m_h^4\left(t-2M_{\rm N}^2\right)\right]\,.\end{aligned} \tag{4.18}$$

Setting $F_2=0$, $G_E=G_M=F_1$ we obtain the same expression for the differential cross section as in Ref. [4], where only one FF is used.

Coherent scattering on scalar nuclei

In this situation, the final nucleus remains in its ground state. Now the hadronic part of the EM process $\nu_i(k)+A(p)\to\nu_h(k')+A(p')$, on a nucleus without spin, is the same than for processes of electrons on scalar nuclei. Because of this, the structure functions are the same given in Eq. (3.84). Substituting them in Eq. (4.14), we obtain

$$\frac{d\sigma}{dt}=\frac{\alpha\,(\mu_{\rm tr}^i)^2}{4\,\left(s-M_A^2\right)^2\,t^2}\,F^2(q^2)\,R_E\,, \tag{4.19}$$

where R_E is given by the same expression as in Eq. (4.18) but replacing the nucleon mass, $M_{\rm N}$, by the nucleus one, M_A.

We now discuss how the choice of the parametrization for the nuclear FF influences the QE differential cross section. Keeping in mind that MiniBooNE and MicroBooNE detectors are composed mainly of ^{12}C and ^{40}Ar respectively, in Fig. 4.3 the coherent QE cross section is displayed for these two nuclei using the parametrizations of Eqs. (3.74) and (3.76). It can be seen in the plots that the distribution is very narrow in $Q^2=-t$ and quickly

falls as Q^2 increases. In the region of Q^2 where the cross section is not negligible, even the oversimplified dipole parametrization of Eq. (3.74) gives realistic results. This is because at such a low-Q^2, the cross section is only sensitive to the nucleus charge and mean squared radius squared, which is similar for both parametrizations. On the other hand, the model independent parametrization of Ref. [55] is more realistic and gives more information about the charge distribution in the nucleus.

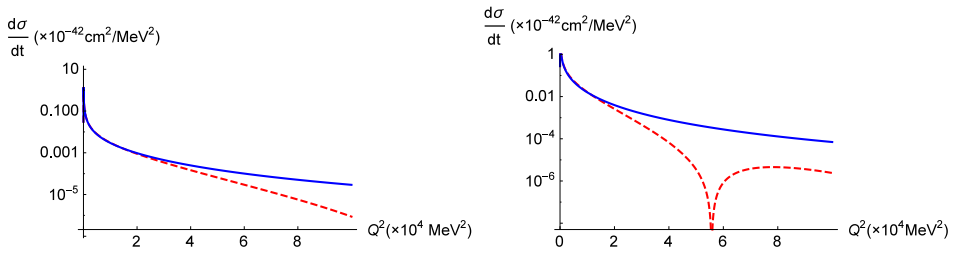

Figure 4.3: Differential cross section for coherent QE scattering process, Eq. (4.2) on ^{12}C (left) and ^{40}Ar (right) as a function of $Q^2 = -q^2 = -t$ for an incoming neutrino energy of 700 MeV. The calculations are performed with the dipole, Eq. 3.74, (blue) and Fourier-Bessel, Eq. 3.76, (red) parametrizations of the nuclear FF.

4.2.3 Incoherent scattering on nuclei

We now study the EM production of heavy neutrinos by incoherent scattering on nuclear targets, Fig. 4.4. We model this process within the impulse approximation, assuming that the interaction with all individual nucleons is only quasielastic. In this way we comply with the experimental scenario at the MiniBooNE measurement, which excludes mesons in the final state,[2]

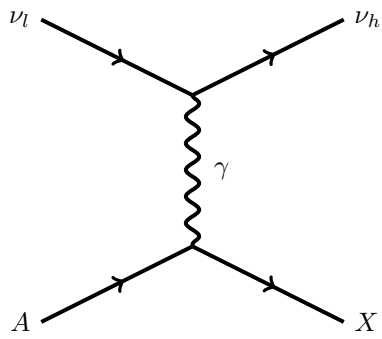

Figure 4.4: Incoherent process of heavy neutrino electromagnetic production.

In this calculation we follow the many body framework (MBF) of Refs. [68, 69] for neutrino propagation in nuclear matter adapted to (semi)inclusive processes on finite nuclei by means of the Local Density Approximation (LDA). The optical theorem relates the imaginary part of the self-energy, $\Sigma_r(k)$, of a neutrino, with four-momentum k to its decay rate in matter, Γ,

$$\Gamma(k) = -\frac{1}{k^0}\,\mathrm{Im}\,\Sigma(k)\,, \tag{4.20}$$

with k^0 given in the matter rest frame. Since the decay width in this context corresponds to the interaction probability per unit of time, the cross section per unit volume can be cast as [69]

$$d\sigma = \Gamma(k;\rho)dt\,dS = -\frac{1}{k^0}\,\mathrm{Im}\,\Sigma(k;\rho)dt\,dS = -\frac{1}{|\vec{k}|}\,\mathrm{Im}\,\Sigma(k;\rho)d^3r\,. \tag{4.21}$$

In the LDA, $\Sigma\,(k;\rho) = \Sigma\,(k;\rho(\vec{r}))$ and

$$\sigma = -\frac{1}{k^0}\int \mathrm{Im}\,\Sigma\,(k;\rho(\vec{r}))\,d^3r\,. \tag{4.22}$$

[2]Secondary pion production in the nucleus induced by knocked-out nucleons can be neglected at the energies of the Booster neutrinos.

We approximate both proton and neutron density profiles by the nuclear charge density, Eq. (3.75) re-scaled so that the normalizations are

$$\int d^3r \rho_p(r) = Z\,; \quad \int d^3r \rho_n(r) = A - Z\,, \tag{4.23}$$

where Z is the number of protons and A the total number of nucleons in the nucleus.

The relevant neutrino self-energy is shown in Fig. 4.5. The corresponding expression of the self-energy for a neutrino with helicity r is

$$\begin{aligned} -\mathbb{i}\Sigma_r\left(k;\rho\right) = \frac{\mathbb{i}(\mu^i_{\rm tr})^2}{4}\int \frac{d^4q}{(2\pi)^4}\overline{u}_r(k)\frac{\sigma_{\rho\eta}\left(1+\gamma_5\right)\left(\not{k}'+m_h\right)\sigma_{\delta\mu}\left(1-\gamma_5\right)}{k'^2-m_h^2+\mathbb{i}\epsilon} \\ \times u_r(k)\frac{q^\rho q^\delta}{\left(q^2+\mathbb{i}\epsilon\right)^2}\left(-\mathbb{i}\Pi^{\eta\mu}(q)\right)\,, \end{aligned} \tag{4.24}$$

in terms of the in-medium photon self-energy $\Pi^{\eta\mu}(q)$. Summing over the neutrino helicities we get

$$\Sigma\left(k;\rho\right) = \sum_r \Sigma_r\left(k;\rho\right) = \frac{\mathbb{i}(\mu^i_{\rm tr})^2}{4}\int \frac{d^4q}{(2\pi)^4}\frac{L_{\mu\eta}\Pi^{\eta\mu}(q)}{\left(q^2+\mathbb{i}\epsilon\right)^2}\frac{1}{\left(k'^2-m_h^2+\mathbb{i}\epsilon\right)}\,, \tag{4.25}$$

with $L_{\mu\eta}$ being the leptonic tensor introduced in Eq. 4.10.

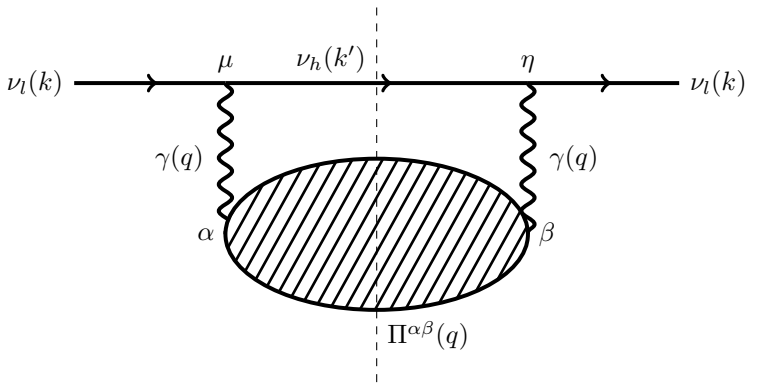

Figure 4.5: Diagram of the self-energy of a neutrino, with flavor $l = e, \mu, \tau$, in nuclear matter. $\Pi^{\alpha\beta}$ denotes the (virtual) photon self-energy in nuclear matter.

The imaginary part of Σ can be obtained applying Cutkosky's rules for

the cut shown in Fig. 4.5. Substituting

$$\begin{aligned}\Sigma(k;\rho) &\to 2\mathbb{i}\,\mathrm{Im}\,\Sigma(k;\rho)\Theta(k^0)\,,\\ \Xi(k') &\to 2\mathbb{i}\,\mathrm{Im}\,\Xi(k')\Theta(k'^0)\,,\\ \Pi^{\mu\nu}(q) &\to 2\mathbb{i}\,\mathrm{Im}\,\Pi^{\mu\nu}(q)\Theta(q^0)\,,\end{aligned} \tag{4.26}$$

where Θ is the Heaviside function, and

$$\Xi(k') = \frac{1}{k'^2 - m_h^2 + \mathbb{i}\epsilon}\,, \tag{4.27}$$

is the denominator of the heavy neutrino propagator, one obtains

$$\mathrm{Im}\,\Sigma(k;\rho) = \frac{(\mu^i_{\mathrm{tr}})^2}{4}\int \frac{d^3k'}{(2\pi)^3}\frac{1}{2\,|k'^0|\,q^4}\Theta(q^0)\,\mathrm{Im}\left\{\Pi^{\mu\nu}L_{\nu\mu}\right\}\,. \tag{4.28}$$

Both tensors in Eq. (4.28) can be written as a sum of symmetric and antisymmetric components,

$$L_{\mu\nu} = L^{(s)}_{\mu\nu} + \mathbb{i}L^{(a)}_{\mu\nu}\,, \tag{4.29}$$

$$\Pi^{\mu\nu} = \Pi^{\mu\nu}_{(s)} + \mathbb{i}\Pi^{\mu\nu}_{(a)}\,, \tag{4.30}$$

where the leptonic components, $L^{(s,a)}_{\mu\nu}$, are real but $\Pi^{\mu\nu}_{(s,a)}$ can be complex. Using that $\Pi^{\nu\mu} = \Pi^{\mu\nu}_{(s)} - \mathbb{i}\Pi^{\mu\nu}_{(a)}$ and Eq. (4.30) one has that

$$\begin{aligned}\Pi^{\mu\nu}_{(s)} &= \frac{\Pi^{\mu\nu} + \Pi^{\nu\mu}}{2}\,,\\ \mathbb{i}\Pi^{\mu\nu}_{(a)} &= \frac{\Pi^{\mu\nu} - \Pi^{\nu\mu}}{2}\,.\end{aligned} \tag{4.31}$$

The contraction can then be written then as

$$\mathrm{Im}\left\{\Pi^{\mu\nu}L_{\nu\mu}\right\} = \frac{1}{2}L_{\mu\nu}\left(\mathrm{Im}\left\{\Pi^{\mu\nu} + \Pi^{\nu\mu}\right\} + \mathbb{i}\,\mathrm{Re}\left\{\Pi^{\mu\nu} - \Pi^{\nu\mu}\right\}\right)\,. \tag{4.32}$$

Substituting Eqs. (4.28, 4.32) in Eq. (4.22) we find

$$\begin{aligned}\sigma = -\frac{(\mu^i_{\mathrm{tr}})^2}{8k^0}\int \frac{d^3r}{(2\pi)^3}\frac{d^3k'}{2|k'^0|}\frac{1}{q^4}L_{\mu\nu}\left(\mathrm{Im}\left\{\Pi^{\mu\nu} + \Pi^{\nu\mu}\right\}\right.\\ \left.+\mathbb{i}\,\mathrm{Re}\left\{\Pi^{\mu\nu} - \Pi^{\nu\mu}\right\}\right)\Theta(q^0)\,.\end{aligned} \tag{4.33}$$

On the other hand, recalling the general expression for the cross section, Eq. (4.9), one identifies the symmetric and asymmetric components of the hadron tensor

$$\begin{aligned} W^{\mu\nu}_{(s)} &= -\frac{1}{2\alpha}\int \frac{d^3r}{(2\pi)^2}\,\mathrm{Im}\left\{\Pi^{\mu\nu}+\Pi^{\nu\mu}\right\}\Theta(q^0)\,, \\ W^{\mu\nu}_{(a)} &= -\frac{1}{2\alpha}\int \frac{d^3r}{(2\pi)^2}\,\mathrm{Re}\left\{\Pi^{\mu\nu}-\Pi^{\nu\mu}\right\}\Theta(q^0)\,. \end{aligned} \tag{4.34}$$

Since we have an EM interaction, only the symmetric part of the hadronic tensor contributes,

$$W^{\mu\nu} = W^{\mu\nu}_{(s)} = -\frac{1}{\alpha}\int \frac{d^3r}{(2\pi)^2}\,\mathrm{Im}\left\{\Pi^{\mu\nu}_{(s)}\right\}\Theta(q^0)\,, \tag{4.35}$$

and hence, for the cross section we obtain

$$\sigma = -\frac{(\mu^i_{\mathrm{tr}})^2}{4k^0}\int \frac{d^3r}{(2\pi)^3}\frac{d^3k'}{2|k'^0|}\frac{1}{q^4}L_{\mu\nu}\,\mathrm{Im}\left\{\Pi^{\mu\nu}_{(s)}\right\}\Theta(q^0)\,. \tag{4.36}$$

Up to the lepton couplings and the specific structure of the leptonic tensor, this expression is general and valid for EM lepton-nucleus scattering within the present approach.

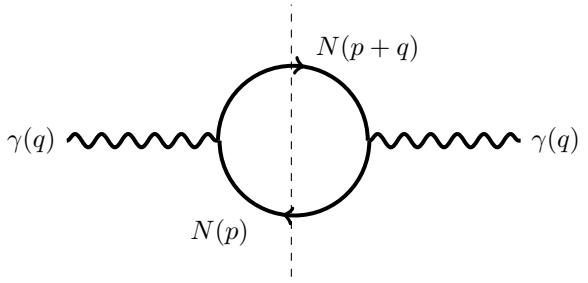

Figure 4.6: Diagram of the 1p1h contribution to the photon self-energy.

The photon self-energy can be obtained from a many body expansion, see Refs. [68, 69]. As pointed out earlier, we are interested in the QE contribution, which is given by one particle one hole (1p1h) nuclear excitations, Fig. 4.6.

The calculation of the 1p1h photon self-energy involves the nucleon propagator in the medium:

$$\begin{aligned} S\left(p;\rho\right) &= \left(\not{p}+M_{\mathrm{N}}\right)G\left(p;\rho\right)\,, \\ G\left(p;\rho\right) &= \frac{1}{p^2-M^2_{\mathrm{N}}+\mathrm{i}\epsilon}+\frac{2\pi\mathrm{i}}{2E(\vec{p})}\delta\left(p^0-E(\vec{p})\right)n(\vec{p})\,, \end{aligned} \tag{4.37}$$

with $E(\vec{p}) = \sqrt{M_{\rm N}^2 + \vec{p}^2}$; the occupation number $n(\vec{p}) = \Theta\left(k_F - |\vec{p}|\right)$ depends on the local Fermi momentum, k_F, which can be written as a function of the local density of nucleons,

$$k_F^{(p,n)}(r) = \left[3\pi^2 \rho_{(p,n)}(r)\right]^{1/3} . \tag{4.38}$$

Therefore, for the photon self-energy in nuclear matter we have

$$-\mathbb{i}\Pi^{\mu\nu} = -e^2 \int \frac{d^4p}{(2\pi)^4} G\left(p;\rho\right) G\left(p+q;\rho\right) 2H^{\mu\nu} , \tag{4.39}$$

with the nucleon tensor given by Eqs. (3.57 - 3.59). Applying again Cutkosky's rules, after some algebra, we obtain

$$\begin{aligned} -\mathbb{i}\,\mathrm{Im}\,\Pi^{\mu\nu}(q) = &-\mathbb{i}e^2 \int \frac{d^4p}{(2\pi)^2} 2H^{\mu\nu} \delta\left(p^0 + q^0 - E\left(\vec{p}+\vec{q}\right)\right) \\ &\times \frac{2n(\vec{p})n\left(\vec{p}+\vec{q}\right) - n(\vec{p}) - n\left(\vec{p}+\vec{q}\right)}{4p^0\left(p^0+q^0+E\left(\vec{p}+\vec{q}\right)\right)} \Theta(p^0)\Theta(p^0+q^0) . \end{aligned} \tag{4.40}$$

Substituting Eq. (4.40) in Eq. (4.35),

$$\begin{aligned} W^{\mu\nu} = &\int d^3r\, \theta(q^0) \int \frac{d^3p}{(2\pi)^3} H^{\mu\nu} \delta\left(p^0 + q^0 - E\left(\vec{p}+\vec{q}\right)\right) \\ &\times \frac{n(p)\left(1 - n\left(\vec{p}+\vec{q}\right)\right)}{p^0\left(p^0+q^0+E(\vec{p}+\vec{q})\right)} \theta(p^0) . \end{aligned} \tag{4.41}$$

With this result we can calculate the cross section, Eq. (4.9) with the help of the integrals listed in Appendix B. Equivalently, using Eqs. (3.62) and (3.63) one can obtain structure functions $W_{1,2}$ and plug them in Eq. (4.12) to readily obtain the cross section.

We have verified that after taking the low density limit ($k_F \to 0$) and for the initial nucleon at rest we recover the expressions previously reported for QE scattering on free nucleons.

4.3 Weak production of heavy neutrinos

In the previous section we described how heavy neutrinos are produced through EM mediated scattering of light neutrinos on nucleons and nuclei. Besides this mechanism, NC interactions also contribute to create heavy neutrinos. Following Refs. [4, 65], we now consider a slight mixing between the

heavy and the light neutrino. The interaction is then given by the SM Lagrangian, Eq. (2.2), but adding the mixing between light and heavy flavors, U_{lh}, to the neutrino current,

$$j^{\mu} = \frac{1}{2}\overline{\nu}_l \gamma^{\mu} \left(1 - \gamma_5\right) U_{lh} \nu_h \,. \tag{4.42}$$

We proceed in analogy to the previous section. In the first place, we derive a general expression for the cross section in terms of hadronic structure functions and afterwards consider the specific cases we are interested in. The NC interaction term in the Lagrangian is given in Eq. (2.2), while for the Z boson propagator we adopt the static approximation

$$D_{\mu\nu} = \frac{-g_{\mu\nu} + q_\mu q_\nu / M_Z^2}{q^2 - M_Z^2} \simeq \frac{g_{\mu\nu}}{M_Z^2} \,. \tag{4.43}$$

Hence, for the cross section we have

$$\frac{d\sigma}{dk'^0 \, d\Omega} = \frac{|U_{lh}|^2 G_F^2}{32\,\pi^2} \frac{|\vec{k'}|}{|\vec{k}|} L_{\mu\nu} W^{\mu\nu} \,, \tag{4.44}$$

which is the standard expression for NC interactions save for the presence of the mixing factor. The leptonic tensor is given by

$$\begin{aligned} L_{\mu\nu} &= \mathrm{Tr}\left\{ \left(\not{k}' + m_h\right) \gamma_\mu \left(1 - \gamma_5\right) \not{k} \gamma_\nu \left(1 - \gamma_5\right) \right\} \\ &= 8 \left[k'_\mu k_\nu + k'_\nu k_\mu - \left(k' \cdot k\right) g_{\mu\nu} + \mathbb{i} \epsilon_{\alpha\mu\beta\nu} k'^{\alpha} k^{\beta} \right] \,, \end{aligned} \tag{4.45}$$

with the $\epsilon_{\alpha\mu\beta\nu}$ definition given in Appendix A.1. This is the same expression obtained for SM light neutrinos as the tensor does not depend explicitly on the neutrino masses. Unlike the EM case the asymmetric part of the hadronic tensor, given in Eq. (3.11) is present. The contraction of both tensors gives

$$\begin{aligned} L_{\mu\nu} W^{\mu\nu} = 8 \Bigg\{ & 2W_1 \left(k' \cdot k\right) + \frac{W_2}{M^2} \left[2 \left(k' \cdot p\right) \left(k \cdot p\right) - \left(k' \cdot k\right) M^2 \right] \\ & + \frac{W_4}{M^2} \left[2 \left(k' \cdot q\right) \left(k \cdot q\right) - q^2 \left(k' \cdot k\right) \right] \\ & + \frac{2W_5}{M^2} \left[\left(k' \cdot p\right) \left(k \cdot q\right) + \left(k' \cdot q\right) \left(k \cdot p\right) - \left(k' \cdot k\right) \left(p \cdot q\right) \right] \\ & - \frac{2W_3}{4M^2} \left[\epsilon_{\mu\nu\sigma\rho} \epsilon^{\mu\nu\alpha\beta} k'^{\sigma} k^{\rho} p_\alpha q_\beta \right] + W_6 \left[2\mathbb{i} \epsilon_{\mu\nu\sigma\rho} k'^{\sigma} k^{\rho} p^{\mu} q^{\nu} \right] \Bigg\} \,. \end{aligned} \tag{4.46}$$

The term proportional to W_6 vanishes because $2\mathbb{i}\epsilon_{\mu\nu\sigma\rho}k'^{\sigma}k^{\rho}p^{\mu}\left(k^{\nu}-k'^{\nu}\right)=0$. The expression for the cross section is, then,

$$\begin{aligned}\frac{d\sigma}{dk'^{0}\,dt}=\frac{|U_{lh}|^{2}G_{F}^{2}}{32\,\pi\left(k^{0}\right)^{2}}8\Bigg\{&W_{1}\left(m_{h}^{2}-t\right)+\frac{W_{2}}{2M^{2}}\left[M^{2}\left(M_{X}^{2}-s\right)-m_{h}^{2}M^{2}\right.\\&\left.+s\left(s+t-M_{X}^{2}\right)\right]+\frac{W_{4}}{2M^{2}}m_{h}^{2}\left(m_{h}^{2}-t\right)+\frac{W_{5}}{M^{2}}m_{h}^{2}\left(M^{2}-s\right)\\&+\frac{W_{3}}{4M^{2}}\left[t\left(2s+t-M^{2}-M_{X}^{2}\right)-m_{h}^{2}\left(M^{2}-M_{X}^{2}+t\right)\right]\Bigg\}\,.\end{aligned}\tag{4.47}$$

In the case where the initial and final hadronic masses are equal, we can write Eq. 4.47 as

$$\begin{aligned}\frac{d\sigma}{dk'^{0}\,dt}=\frac{|U_{lh}|^{2}G_{F}^{2}}{4\,\pi\left(k^{0}\right)^{2}}\Big\{&W_{1}\left(m_{h}^{2}-t\right)\\&+\frac{W_{2}}{2M^{2}}\left[M^{4}-M^{2}\left(m_{h}^{2}+2s\right)+s\left(s+t\right)\right]\\&+\frac{W_{4}}{2M^{2}}m_{h}^{2}\left(m_{h}^{2}-t\right)+\frac{W_{5}}{M^{2}}m_{h}^{2}\left(M^{2}-s\right)\\&+\frac{W_{3}}{4M^{2}}t\left(2s+t-2M^{2}-m_{h}^{2}\right)\Big\}\,.\end{aligned}\tag{4.48}$$

Using Eq. (4.13) we can study the angular distribution. In contrast to the EM cross section, Eq. (4.12), in the NC case there is no enhancement in the low-Q^2 region because a heavy boson is exchanged. We will explore the impact of this difference.

4.3.1 Quasielastic scattering

As in the EM case, we address now the heavy neutrino production for identical initial and final hadronic states: quasielastic scattering on nucleons and scalar nuclei (coherent).

Quasielastic scattering on nucleons

The nucleon current is given in Eq. (3.30) and, unlike in the EM case, we now need both the axial and the vector parts of the current,

$$\begin{aligned}\langle N(p')|J^{\mu}|N(p)\rangle=\overline{u}(p')\Bigg[&\gamma^{\mu}F_{1}+\frac{\mathbb{i}}{2M_{\mathrm{N}}}\sigma^{\mu\nu}q_{\nu}F_{2}-\gamma^{\mu}\gamma_{5}F_{A}\\&-\frac{q^{\mu}}{M_{\mathrm{N}}}\gamma_{5}F_{P}\Bigg]u(p)\,.\end{aligned}\tag{4.49}$$

which is then substituted in Eq. (3.59) to obtain the hadronic tensor:

$$\begin{aligned} H^{\mu\nu} =& \frac{1}{2}\mathrm{Tr}\left[\left(\not{p}' + M_\mathrm{N}\right)\left(\gamma^\mu F_1 + \frac{\mathbb{i}}{2M_\mathrm{N}}\sigma^{\mu\alpha}q_\alpha F_2 - \gamma^\mu\gamma_5 F_A - \frac{q^\mu}{M_\mathrm{N}}\gamma_5 F_P\right)\right. \\ & \left.\times\left(\not{p} + M_\mathrm{N}\right)\left(\gamma^\nu F_1 - \frac{\mathbb{i}}{2M_\mathrm{N}}\sigma^{\nu\beta}q_\beta F_2 - \gamma^\nu\gamma_5 F_A + \frac{q^\nu}{M_\mathrm{N}}\gamma_5 F_P\right)\right] . \end{aligned} \tag{4.50}$$

Comparing the latter with the general expression, Eq. (3.11), the structure functions arise, in terms of the nucleon FF:

$$\begin{aligned} W_1 =& \frac{1}{2M_\mathrm{N}\,E'}\delta\left(k^0 + E - E' - k'^0\right)\left[4F_A^2 M_\mathrm{N}^2 - q^2\left(F_1 + F_2\right)^2 - q^2 F_A^2\right] , \\ W_2 =& \frac{1}{2M_\mathrm{N}\,E'}\delta\left(k^0 + E - E' - k'^0\right)\left[4M^2\left(F_1^2 + F_A^2\right) - q^2 F_2^2\right] , \\ W_3 =& \frac{1}{2M_\mathrm{N}\,E'}\delta\left(k^0 + E - E' - k'^0\right)\left[8F_A M^2\left(F_1 + F_2\right)\right] , \\ W_4 =& \frac{-1}{2M_\mathrm{N}\,E'}\delta\left(k^0 + E - E' - k'^0\right)\left[M^2\left(2F_1F_2 + F_2^2 + 4F_AF_P\right)\right. \\ & \left.+\frac{q^2}{4}\left(F_2^2 + 4F_P^2\right)\right] , \\ W_5 =& \frac{1}{2M_\mathrm{N}\,E'}\delta\left(k^0 + E - E' - k'^0\right)\left[2M^2\left(F_1^2 + F_A^2\right) - \frac{q^2}{2}F_2^2\right] . \end{aligned} \tag{4.51}$$

Substituting these structure functions in the cross section, Eq. (4.48) we find

$$\begin{aligned} \frac{d\sigma}{dt} =& \frac{|U_{\mu h}|^2\,G_F^2}{16\,\pi\,M^2\,k_0^2}\left[F_1^2\,R_1 + F_2^2\,R_2 + F_1F_2\,R_{1\,2} + F_A^2\,R_A + F_P^2 R_P\right. \\ & \left.+F_AF_1\,R_{A\,1} + F_AF_2\,R_{A\,2} + F_AF_P\,R_{A\,P}\right] , \end{aligned} \tag{4.52}$$

where $F_{1,2,A,P}$ are the NC FFs described in Chapter 3, and

$$\begin{aligned}
R_1 =& -m_h^2(2s+t) + 2(M^2-s)^2 + 2st + t^2\,,\\
R_2 =& \frac{1}{8M^2}\left[-4m_h^4M^2 + t^2(m_h^2+8M^2-4s) - t(m_h^2+2M^2-2s)^2\right]\,,\\
R_{1\,2} =& 2t^2 - m_h^2(m_h^2+t)\,,\\
R_A =& m_h^2(4M^2-2s-t) + 2M^4 - 4M^2(s+t) + 2s^2 + 2st + t^2\,,\\
R_P =& \frac{m_h^2\,t\,(t-m_h^2)}{2M^2}\,,\\
R_{A\,1} =& R_{A\,2} = 2t(2s+t-m_h^2-2M^2)\,,\\
R_{A\,P} =& 2m_h^2(t-m_h^2)\,.
\end{aligned} \tag{4.53}$$

Notice that we have kept the pseudoscalar form factor F_P because the mass of the outgoing neutrino is not negligible.

Coherent scattering on scalar nuclei

The hadronic current in the case of scattering on a scalar nucleus does not have axial component, Eq. (3.71). Hence, the same tensor of Eq. (3.83) is also valid for NC interactions. By comparison with Eq. (3.11) and using current conservation, $q_\mu J^\mu = 0$, it is easy to find that

$$\begin{aligned}
W_1 =& W_3 = W_6 = 0\,,\\
W_2 =& \frac{1}{4M_A\,E'}\delta\left(k^0+E-E'-k'^0\right)4M_AF^2\,,\\
W_4 =& \frac{1}{4M_A\,E'}\delta\left(k^0+E-E'-k'^0\right)M_AF^2\,,\\
W_5 =& \frac{1}{4M_A\,E'}\delta\left(k^0+E-E'-k'^0\right)2M_AF^2\,,
\end{aligned} \tag{4.54}$$

in terms of the weak nuclear FF, described in Chapter 3. Substituting this in Eq. (4.48) we obtain

$$\frac{d\sigma}{dt} = \frac{|U_{\mu h}|^2\,G_F^2}{32\,\pi\,M^2\,k_0^2}F^2\left[m_h^4 - m_h^2\,(4s+t) + 4\left(\left(M_A^2-s\right)^2 + st\right)\right]\,, \tag{4.55}$$

where we have performed the integral over k_0', making use of the Dirac delta. It is worth highlighting that, in the limit of $m_h \to 0$ and $U_{\mu h} \to 1$ one recovers the standard expression for coherent elastic neutrino-nucleus scattering (CEνNS) experimentally discovered a few years ago [70].

4.3.2 Incoherent scattering on nuclei

Our theoretical approach to neutrino-nucleus incoherent scattering in the case of NC interactions is analogous to the EM one covered in Sec.4.2. The diagrammatic representation of Fig. 4.5 still holds if one only replaces the exchanged photon by a Z boson. In this case, the neutrino self-energy is given by

$$\Sigma\left(k;\rho\right)=\frac{\mathbb{i}\left|U_{\mu h}\right|^{2}}{2M_{Z}^{2}}\frac{G_{F}}{\sqrt{2}}\int\frac{d^{4}q}{\left(2\pi\right)^{4}}\frac{L_{\mu\eta}\Pi^{\eta\mu}(q)}{\left(k'^{2}-m_{h}^{2}+\mathbb{i}\epsilon\right)}\,, \tag{4.56}$$

with

$$L_{\mu\eta}=\mathrm{Tr}\left[\not{k}\,\gamma_{\eta}(1-\gamma_{5})\left(\not{k}'+m_{h}\right)\gamma_{\mu}(1-\gamma_{5})\right]\,. \tag{4.57}$$

After applying the Cutkosky's rules, Eq. (4.26), we obtain

$$\mathrm{Im}\,\Sigma(k;\rho)=\frac{\left|U_{\mu h}\right|^{2}}{2M_{Z}^{2}}\frac{G_{F}}{\sqrt{2}}\int\frac{d^{3}k'}{\left(2\pi\right)^{3}}\frac{1}{2\left|k'^{0}\right|}\Theta(q^{0})\,\mathrm{Im}\left\{\Pi^{\mu\nu}L_{\nu\mu}\right\}\,. \tag{4.58}$$

Then, using Eq. (4.21) and the LDA one gets for the cross section

$$\begin{aligned}\sigma=-\frac{\left|U_{\mu h}\right|^{2}}{2k^{0}M_{Z}^{2}}\frac{G_{F}}{\sqrt{2}}\int\frac{d^{3}r}{\left(2\pi\right)^{3}}\frac{d^{3}k'}{4|k'^{0}|}L_{\mu\nu}\left(\mathrm{Im}\left\{\Pi^{\mu\nu}+\Pi^{\nu\mu}\right\}\right.\\ \left.+\mathbb{i}\,\mathrm{Re}\left\{\Pi^{\mu\nu}-\Pi^{\nu\mu}\right\}\right)\Theta(q^{0})\,.\end{aligned} \tag{4.59}$$

Comparing this result with Eq. (4.48) we find

$$\begin{aligned}W_{(s)}^{\mu\nu}&=-\frac{1}{\sqrt{2}M_{Z}^{2}G_{F}}\int\frac{d^{3}r}{2\pi}\,\mathrm{Im}\left\{\Pi^{\mu\nu}+\Pi^{\nu\mu}\right\}\Theta(q^{0})\,,\\ W_{(a)}^{\mu\nu}&=-\frac{1}{\sqrt{2}M_{Z}^{2}G_{F}}\int\frac{d^{3}r}{2\pi}\,\mathrm{Re}\left\{\Pi^{\mu\nu}-\Pi^{\nu\mu}\right\}\Theta(q^{0})\,,\end{aligned} \tag{4.60}$$

which can be also written in terms of the symmetric and antisymmetric parts of the Z boson self-energy, Eq. (4.31), as

$$W_{(s,a)}^{\mu\nu}=\mp\frac{\sqrt{2}}{M_{Z}^{2}G_{F}}\int\frac{d^{3}r}{2\pi}\,\mathrm{Im}\left\{\Pi_{(s,a)}^{\mu\nu}\right\}\Theta(q^{0})\,. \tag{4.61}$$

The contribution to the Z-boson self-energy given by 1p1h nuclear excitations, Fig. 4.6, with a Z boson instead of a photon, after applying Cutkosky's

rules, is given by

$$-\mathbb{i}\,\mathrm{Im}\,\Pi^{\mu\nu}(q) = -2\mathbb{i}M_Z^2\frac{G_F}{\sqrt{2}}\int\frac{d^4p}{(2\pi)^2}2H^{\mu\nu}\delta\left(p^0+q^0-E\left(\vec{p}+\vec{q}\right)\right) \times\frac{2n(\vec{p})n\left(\vec{p}+\vec{q}\right)-n(\vec{p})-n\left(\vec{p}+\vec{q}\right)}{4p^0\left(p^0+q^0+E\left(\vec{p}+\vec{q}\right)\right)}\Theta(p^0)\Theta(p^0+q^0)\,, \tag{4.62}$$

with $H^{\mu\nu}$ being the nucleon tensor of Eq. (4.50). In the same way, Eq. (4.41) also holds now with the corresponding $H^{\mu\nu}$ tensor of Eq. (4.50). Finally, to calculate the cross section we substitute this hadronic tensor in Eq. (4.44).

As in the EM case, if we consider the low density limit we recover the expressions for QE scattering on nucleons.

4.4 Interference of EM and NC processes

The scattering of light neutrinos on hadrons to produce heavy neutrinos can be mediated by EM or NC interactions, as we described in the previous sections. Once the two mechanisms involve the same initial and final states interference is present:

$$|\overline{\mathcal{M}}|^2 = |\overline{\mathcal{M}}^{(\mathrm{EM})}|^2 + |\overline{\mathcal{M}}^{(\mathrm{NC})}|^2 + \overline{\sum}2\,\mathrm{Re}\left\{\mathcal{M}^{(\mathrm{EM})}\cdot\left(\mathcal{M}^{(\mathrm{NC})}\right)^*\right\}\,. \tag{4.63}$$

The interference term of the amplitude squared is, then,

$$\overline{\mathcal{M}}^{(\mathrm{int})} \equiv \overline{\sum}2\,\mathrm{Re}\left\{\mathcal{M}^{(\mathrm{EM})}\cdot\left(\mathcal{M}^{(\mathrm{NC})}\right)^*\right\} = \mathbb{i}\frac{e\mu^i_{\mathrm{tr}}U_{ih}G_F}{\sqrt{2}q^2}\tilde{L}_{\mu\nu}\tilde{H}^{\mu\nu}\,, \tag{4.64}$$

with

$$\mathbb{i}\tilde{L}_{\mu\nu} = 8m_h\left[\left(k\cdot k'\right)g_{\mu\nu}+k_\mu\left(k_\nu-k'_\nu\right)-\mathbb{i}\epsilon_{\mu\nu\alpha\beta}k^\alpha k'^\beta\right]\,, \tag{4.65}$$

and

$$\tilde{H}^{\mu\nu} = \overline{\sum}\left\langle X\right|J^\mu_{\mathrm{EM}}\left|N\right\rangle\left\langle X\right|J^\nu_{\mathrm{NC}}\left|N\right\rangle^*\,. \tag{4.66}$$

Hence, the interference part of the cross section is

$$\frac{d\tilde{\sigma}}{dk'_0d\Omega} = \frac{eG_F}{16\pi^2\sqrt{2}q^2}\frac{|\vec{k'}|}{k_0}\,\mathrm{Re}\left\{\mu^i_{\mathrm{tr}}U^*_{ih}\left(\mathbb{i}L_{\mu\nu}\right)\tilde{W}^{\mu\nu}\right\}\,. \tag{4.67}$$

$\tilde{W}^{\mu\nu}$ shares the general form with the hadronic tensor of Eq. (3.11) in terms of $\tilde{W}_{1-6}$ structure functions Then

$$\begin{aligned}\left(\mathbb{i}\tilde{L}_{\mu\nu}\right)\tilde{W}^{\mu\nu} =& 8m_h\left\{\tilde{W}_1\frac{3}{2}\left(t-m_h^2\right)\right.\\ &+\frac{\tilde{W}_2}{4M^2}\left[M^4+M^2\left(2m_h^2-M_X^2-s-t\right)+s\left(M_X^2-t\right)\right]\\ &-\frac{\tilde{W}_3+2\tilde{W}_6}{4M^2}\left[M^2\left(m_h^2+t\right)+m_h^2\left(t-M_X^2\right)\right.\\ &\left.\left.+t\left(M_X^2-2s-t\right)\right]\right\}\ .\end{aligned} \tag{4.68}$$

From Eq. (4.66) it follows that $q_\mu H^{\mu\nu}=0$ due to EM current conservation. This condition gives relations between the structure functions, that simplifies Eq. (4.68). Finally,

$$\begin{aligned}\frac{d\tilde{\sigma}}{dk_0'dt} =& \frac{\sqrt{2\pi\alpha}G_F}{16\pi t k_0^2}\mu_{\rm tr}^i U_{ih}^* 8m_h\left(\tilde{W}_1\frac{3}{2}\left(t-m_h^2\right)\right.\\ &+\frac{\tilde{W}_2}{8M^2t}\left[(t-m_h)\left(M^4-2M^2\left(M_X^2+t\right)+\left(M_X^2-t\right)^2\right)\right]\\ &\left.-\frac{\tilde{W}_3+2\tilde{W}_6}{4M^2}\left[M^2\left(m_h^2+t\right)+m_h^2\left(t-M_X^2\right)+t\left(M_X^2-2s-t\right)\right]\right)\ .\end{aligned} \tag{4.69}$$

This interference term is proportional to the heavy neutrino mass ($\sim$ 50 MeV) and therefore small. Nevertheless, in the following we show the explicit expressions for all the cases under consideration.

4.4.1 Quasielastic scattering

Quasielastic scattering on nucleons

In the interference case, we have a mixing of both EM and NC currents. Therefore,

$$\begin{aligned}\tilde{H}^{\mu\nu} =& \frac{1}{2}\mathrm{Tr}\left[\left(\not{p}'+M_{\rm N}\right)\left(\gamma^\mu F_1^{\rm EM}+\frac{\mathbb{i}}{2M_{\rm N}}\sigma^{\mu\alpha}q_\alpha F_2^{\rm EM}\right)\left(\not{p}+M_{\rm N}\right)\right.\\ &\left.\times\left(\gamma^\nu F_1^{\rm NC}-\frac{\mathbb{i}}{2M_{\rm N}}\sigma^{\nu\beta}q_\beta F_2^{\rm NC}-\gamma^\nu\gamma_5 F_A^{\rm NC}+\frac{q^\nu}{M_{\rm N}}\gamma_5 F_P^{\rm NC}\right)\right]\ ,\end{aligned} \tag{4.70}$$

where $F_i^{\rm EM}$ and $F_i^{\rm NC}$, $i=1,2,A,P$ are the FFs for EM and NC interactions respectively. Using this expression in Eq. (3.59) and comparing with the

proper contractions, see Secs. 4.2 and 4.3, we find the structure functions,

$$\begin{aligned}
\tilde{W}_1 =& \frac{1}{2M_{\rm N}\,E'}\delta\left(k^0+E-E'-k'^0\right)\left[-t\left(F_1^{\rm EM}+F_2^{\rm EM}\right)\left(F_1^{\rm NC}+F_2^{\rm NC}\right)\right]\,,\\
\tilde{W}_2 =& \frac{1}{2M_{\rm N}\,E'}\delta\left(k^0+E-E'-k'^0\right)\left[4F_1^{\rm EM}F_1^{\rm NC}M_{\rm N}^2-tF_2^{\rm EM}F_2^{\rm NC}\right]\,,\\
\tilde{W}_3 =& \frac{1}{2M_{\rm N}\,E'}\delta\left(k^0+E-E'-k'^0\right)\left[4M_{\rm N}^2F_A^{\rm NC}\left(F_1^{\rm EM}+F_2^{\rm EM}\right)\right]\,,\\
\tilde{W}_6 =& 0\,,
\end{aligned} \tag{4.71}$$

that can be substituted in Eq.(4.69).

Coherent scattering on scalar nuclei

The hadronic current for a scalar nucleus is given in Eq. (3.71). Both EM and NC have the same functional form, only we have to change the nuclear FF by the appropriate one in each case. One gets that

$$\tilde{H}^{\mu\nu} = 4M_A^2\,F^{\rm EM}F^{\rm NC}\left(p^\mu-\frac{(q\cdot p)}{q^2}q^\mu\right)\left(p^\nu-\frac{(q\cdot p)}{q^2}q^\nu\right)\,. \tag{4.72}$$

Substituting this expression in Eq. (3.10) and comparing with Eq. (3.11) we find

$$\begin{aligned}
\tilde{W}_1 =& \tilde{W}_3=\tilde{W}_6=0\,,\\
\tilde{W}_2 =& \frac{1}{4M_A\,E'}\delta\left(k^0+E-E'-k'^0\right)\left[4M_A^2F^{\rm EM}F^{\rm NC}\right]\,.
\end{aligned} \tag{4.73}$$

Using this result in the Eq. (4.69), we obtain the following simple expression

$$\frac{d\tilde{\sigma}}{dk_0'dt} = \frac{\sqrt{2\pi\alpha}G_F}{16\pi t k_0^2 M_A}m_h\,{\rm Re}\left\{\mu_{\rm tr}^i U_{ih}^*\right\}F^{\rm EM}F^{\rm NC}\left(4M_A^2-t\right)\left(m_h^2-t\right)\,. \tag{4.74}$$

4.4.2 Incoherent scattering on nuclei

As for the purely EM and NC contribution to the cross section, Eq. (4.41) also holds for the interference but replacing $H^{\mu\nu}$ by $\tilde{H}^{\mu\nu}$ given by Eq. (4.70). Hence, we can calculate the interference part of the incoherent cross section by plugging the resulting tensor in Eq. (4.67).

4.5 Heavy antineutrino production

We address now the case where a light antineutrino scatters on a hadron producing a heavy antineutrino. In this case the only difference is in the leptonic tensor, whose antisymmetric part changes sign. In the case of EM interactions, this change does not have any effect, because the hadronic tensor is symmetric. In contrast, for NC now the leptonic tensor, given in Eq. 4.45, becomes

$$L_{\mu\nu} = \left[k'_\mu k_\nu + k'_\nu k_\mu - \left(k'\cdot k\right) g_{\mu\nu} - \mathbb{i}\epsilon_{\alpha\mu\beta\nu}k'^{\alpha}k^{\beta}\right] , \tag{4.75}$$

so that the cross section given by Eq. (4.47), turns into

$$\begin{aligned}\frac{d\sigma}{dk'^0\,dt} = \frac{|U_{lh}|^2 G_F^2}{32\,\pi\,(k^0)^2} 8 \Bigg\{ & W_1\left(m_h^2 - t\right) + \frac{W_2}{2M^2}\left[M^2\left(M_X^2 - s\right) - m_h^2 M^2\right. \\ & \left. + s\left(s + t - M_X^2\right)\right] + \frac{W_4}{2M^2} m_h^2\left(m_h^2 - t\right) + \frac{W_5}{M^2} m_h^2\left(M^2 - s\right) \\ & - \frac{W_3}{4M^2}\left[t\left(2s + t - M^2 - M_X^2\right) - m_h^2\left(M^2 - M_X^2 + t\right)\right]\Bigg\} ,\end{aligned} \tag{4.76}$$

where the term proportional to W_3 has changed sign. While the cross section for coherent scattering on scalar nuclei remains the same, as its hadronic tensor is symmetric, in the case of scattering on nucleons or incoherent scattering on nuclei the change is present, leading to a reduction in the cross section and different energy dependence.

Finally, the leptonic tensor of the interference between the EM and the NC interaction also change the sign of the antisymmetric term,

$$\mathbb{i}\tilde{L}_{\mu\nu} = 8 m_h \left[-\left(k\cdot k'\right) g_{\mu\nu} + k_\mu\left(k_\nu - k'_\nu\right) - \mathbb{i}\epsilon_{\mu\nu\alpha\beta}k^{\alpha}k'^{\beta}\right] . \tag{4.77}$$

This difference affects the expression for the contribution to the inclusive cross section, changing the signs of terms proportional to W_1, W_2 and W_6,

$$\begin{aligned}\frac{d\tilde{\sigma}}{dk'_0 dt} = \frac{\sqrt{2\pi\alpha}G_F}{16\pi t k_0^2}\,\mathrm{Re}\Bigg\{ & \mu^i_{\mathrm{tr}} U^*_{ih} 8 m_h \Bigg(-\tilde{W}_1 \frac{3}{2}\left(t - m_h^2\right) \\ & - \frac{\tilde{W}_2}{8M^2 t}\left[\left(t - m_h\right)\left(M^4 - 2M^2\left(M_X^2 + t\right) + \left(M_X^2 - t\right)^2\right)\right] \\ & - \frac{\tilde{W}_3 - 2\tilde{W}_6}{4M^2}\left[M^2\left(m_h^2 + t\right) + m_h^2\left(t - M_X^2\right)\right. \\ & \left.\left. + t\left(M_X^2 - 2s - t\right)\right]\right)\Bigg\} ,\end{aligned} \tag{4.78}$$

which corresponds to a global change of sign plus a change in the W_3 term, with respect to Eq. (4.69).

4.6 Photon event distributions in a detector

The radiative decay of a heavy neutrino would produce a photon, which, in a Cherenkov detector, could be misidentified as an electron. In this section we describe how to obtain the number of such events. In first place we study the radiative decay of the heavy neutrino. Afterwards, we calculate the probability that the neutrino decays inside the detector. Finally, we obtain the photon energy and angular distributions in the detector.

4.6.1 Radiative decay of heavy neutrinos

The general expression for a decay width is given in Eq. (C.2). For the process $\nu_h \to \nu_l + \gamma$ it reads

$$d\Gamma = \frac{1}{2m_h}(2\pi)^4 \delta^{(4)}\left(k' + q - k\right) \frac{d^3k'}{(2\pi)^3 2k'_0} \frac{d^3q}{(2\pi)^3 2q_0} |\overline{\mathcal{M}}|^2 \,. \tag{4.79}$$

The amplitude of this process is

$$\mathbb{i}\mathcal{M} = \mathbb{i}\frac{\mu^i_{\rm tr}}{2} \overline{u}(k')\sigma_{\mu\nu}\left(1+\gamma_5\right) q^\mu u(k) \epsilon^\nu(q) \,, \tag{4.80}$$

and

$$|\overline{\mathcal{M}}|^2 = \frac{\left(\mu^i_{\rm tr}\right)^2}{4} {\rm Tr}\left\{ \not{k}' \sigma_{\mu\nu}\left(1+\gamma_5\right) \frac{1}{2}\left(1+\gamma_5 \not{\epsilon}\right)\left(\not{k} + m_h\right) \sigma_{\beta\alpha}\left(1-\gamma_5\right) \right\} \times q^\mu q^\beta g^{\nu\alpha} \,, \tag{4.81}$$

where the projector, $\frac{1}{2}\left(1+\gamma_5\not{\epsilon}\right)$, has been introduced to take into account the heavy neutrino polarization. If we define θ_γ as the angle of the photon with respect to the heavy neutrino spin direction, we get

$$|\overline{\mathcal{M}}|^2 = \left(\mu^i_{\rm tr}\right)^2 m_h^4 \left(1 \mp \cos\theta_\gamma\right) \,, \tag{4.82}$$

where the negative (positive) sign corresponds to the decay of left (right)-handed heavy neutrino. Then, for the decay width

$$\frac{d\Gamma}{d\cos\theta_\gamma} = \frac{\left(\mu^i_{\rm tr}\right)^2 m_h^3}{32\pi}\left(1 \mp \cos\theta_\gamma\right) \,. \tag{4.83}$$

From this equation it is easy to see that, in the rest frame of the heavy neutrino, photons produced by left-handed heavy neutrinos are emitted preferably in the backward direction. On the contrary, right-handed heavy neutrinos emit photons predominantly in the forward direction.

With the same procedure we obtain for antineutrinos

$$\frac{d\Gamma}{d\cos\theta_\gamma}\left(\overline{\nu}_h \to \overline{\nu}_l + \gamma\right) = \frac{\left(\mu^i_{\rm tr}\right)^2 m_h^3}{32\pi}\left(1 \pm \cos\theta_\gamma\right) \ . \tag{4.84}$$

In this case, photons produced by left and right-handed antineutrinos are emitted in the forward and backward directions, respectively.

Using the left and right chiral projectors, given in Appendix A.1, we can write the EM interaction Lagrangian, Eq. 4.8 in terms of left and right fields

$$\begin{aligned}\mathcal{L}_{\rm eff} &= \mu^i_{\rm tr}\left[\overline{\nu}_h \sigma_{\mu\nu} P_L \nu_i + \overline{\nu}_i \sigma_{\mu\nu} P_R \nu_h\right]\partial^\mu A^\nu \\ &= \mu^i_{\rm tr}\left[\overline{\nu}_{h,R} \sigma_{\mu\nu} \nu_{i,L} + \overline{\nu}_{i,L} \sigma_{\mu\nu} \nu_{h,R}\right]\partial^\mu A^\nu \ .\end{aligned} \tag{4.85}$$

Although heavy neutrinos are massive particles, their mass is quite small compared to the energies of the order of 1 GeV of accelerator neutrinos at the Booster beam in Fermilab. This allows to approximate their helicity by their chirality. From this Lagrangian it is apparent that the EM interaction flips chirality. Hence, the heavy neutrinos (antineutrinos) produced by this type of scattering would be right(left)-handed particles. If we do the same exercise for the NC interaction, from Eqs. (2.2, 4.42) we can write

$$\begin{aligned}\mathcal{L}_I &= -\frac{g}{2\cos\theta_W}\left(\frac{1}{2}\overline{\nu}_l \gamma^\mu \left(1-\gamma_5\right) U_{lh} \nu_h\right) Z_\mu \\ &= -\frac{g}{2\cos\theta_W} U_{lh}\left(\overline{\nu}_{l,L} \gamma^\mu \nu_{h,L}\right) Z_\mu \ .\end{aligned} \tag{4.86}$$

Therefore, NC interactions preserve chirality so that heavy neutrinos or antineutrinos produced by this interaction would have the same polarization as the light ones.

4.6.2 Number of photons emitted inside the detector

In neutrino experiments, a flux of light neutrinos illuminates the detector. The neutrino flux directed to the detector would produce the heavy neutrinos, which decay emitting photons, as described previously. We intend to determine how many of these photons are generated inside the detector.

For this purpose we first calculate the total number of heavy neutrinos produced in the detector, N_h. For a given flux, $\phi(k_0)$, normalized to a number of protons on target (POT),[3] N_{POT}, directed to a detector with mass, M_D,

$$\begin{aligned} N_h = N_{\text{POT}} M_D N_A \sum_i f_i \int dk_0 \phi(k_0) \\ \times \int dk_0' d\cos d\theta_h d\varphi_h \frac{d\sigma\left(k_0, k_0', \cos\theta_h, \varphi_h\right)}{dk_0' d\cos d\theta_h d\varphi_h} , \end{aligned} \tag{4.87}$$

where the number of hadronic targets per unit of mass is given by the Avogadro constant, N_A, and the fraction, f_i. This quantity is the ratio between the specific target, i, and the molecular mass of the detector material. The scattering angles of the heavy neutrino with respect to the light neutrino are θ_h and φ_h.

After a heavy neutrino is produced, it can decay emitting photon. This means that their number decreases exponentially with time:

$$N_h(t) = N_{h,0} e^{-t/\tau} , \tag{4.88}$$

where τ is the mean lifetime. In terms of the distance the heavy neutrino can travel inside the detector, Δl,

$$N_h(t) = N_{h,0} e^{-\Delta l/\lambda} , \tag{4.89}$$

with $\lambda = \tau v$, a function of the mean lifetime and the velocity of the particle, v, in the laboratory frame. The functional form of Δl, which depends on the specific geometry of each detector, is a function of the interaction point, characterized by position vector $\vec{r}$ with angles θ and φ. Then, the probability of a photon to be emitted inside the detector can be cast as

$$P\left(k_0', r, \theta, \varphi, \theta_h, \varphi_h\right) = 1 - e^{-\Delta l/\lambda} \tag{4.90}$$

In terms of the mean lifetime in the rest frame of the heavy neutrino, τ_0

$$\lambda = \frac{\tau_0}{\sqrt{1-v^2}} v = \tau_0 \frac{k_0'}{m_h} \sqrt{1 - \frac{m_h^2}{\left(k_0'\right)^2}} , \tag{4.91}$$

In the ν_h rest frame the mean lifetime is given by its decay width,

$$\tau_0 = \frac{1}{\Gamma} , \tag{4.92}$$

[3]The normalization comes from the primary proton beam in the accelerator. In next sections some details about the neutrino flux are provided.

derived above.

The number of photons inside the detector depends, then, on the number of heavy neutrinos produced and the probability they emit photons,

$$\begin{aligned} N_\gamma =& \frac{M_D}{V} N_{\rm POT} N_A \sum_i f_i \int dk_0 \phi(k_0) \int dk_0' d\cos d\theta_h d\varphi_h \\ & \times \frac{d\sigma\left(k_0, k_0', \cos\theta_h, \varphi_h\right)}{dk_0' d\cos d\theta_h d\varphi_h} \int d^3 r P\left(k_0', r, \theta, \varphi, \theta_h, \varphi_h\right) \ , \end{aligned} \tag{4.93}$$

where V is the active volume in the detector. We define now a factor which contains the information about the detector geometry,

$$A\left(k_0', r, \theta, \varphi, \theta_h, \varphi_h\right) \equiv 1 - \frac{1}{V} \int d^3 r e^{-\Delta l/\lambda} \ , \tag{4.94}$$

to rewrite Eq. (4.93) as

$$\begin{aligned} N_\gamma =& M_D N_{\rm POT} N_A \sum_i f_i \int dk_0 \phi(k_0) \int dk_0' d\cos d\theta_h d\varphi_h \\ & \times \frac{d\sigma\left(k_0, k_0', \cos\theta_h, \varphi_h\right)}{dk_0' d\cos d\theta_h d\varphi_h} A\left(k_0', r, \theta, \varphi, \theta_h, \varphi_h\right) \ . \end{aligned} \tag{4.95}$$

4.6.3 Photon distributions

We now calculate the energy and angular distributions of the emitted photons inside the detector. They can be obtained from the information of the heavy neutrino decay in its rest frame by performing a boost to the laboratory frame. From the decay width, Eq. (4.83), we can obtain the probability of a photon to be emitted with an angle $\cos\theta_\gamma^{\rm CM}$, in the heavy neutrino rest frame, with respect to the direction of its spin,

$$P\left(\cos\theta_\gamma^{\rm CM}\right) = \frac{1}{\Gamma} \frac{d\Gamma}{d\cos\theta_\gamma^{\rm CM}} = \frac{1 \mp \cos\theta_\gamma^{\rm CM}}{2} \ . \tag{4.96}$$

Boost to laboratory frame

In the laboratory frame we choose the incoming light neutrino as the z-direction. Then, the heavy neutrino spin direction, $\vec{l}$, which we can approximated to the one of its momentum, is

$$\vec{l} = \left(\sin\theta_h \cos\varphi_h, \sin\theta_h \sin\varphi_h, \cos\theta_h\right) \ . \tag{4.97}$$

If we define the scattering plane choosing $\varphi_h = 0$,

$$\vec{l} = (\sin\theta_h, 0, \cos\theta_h) \ . \tag{4.98}$$

In the laboratory frame, we can define a new coordinate system as a rotation of the scattering one, O_R. This system is a rotation by angle θ_h over the y-axis, where $\vec{l} = (0, 0, 1)$, Fig. 4.7.

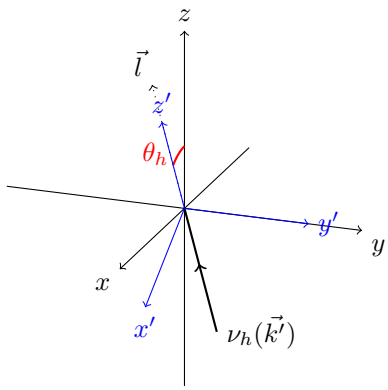

Figure 4.7: Diagram of the reference systems in the laboratory frame. Axes in black correspond to the scattering plane. The axes of the rotated coordinate system, O_R, are in blue.

The emitted photon has a momentum in any direction in the heavy neutrino rest frame,

$$\vec{p}_\gamma^{\,\mathrm{CM}} = |\vec{p}_\gamma^{\,\mathrm{CM}}| \left(\sin\theta_\gamma^{\mathrm{CM}} \cos\varphi_\gamma^{\mathrm{CM}}, \sin\theta_\gamma^{\mathrm{CM}} \sin\varphi_\gamma^{\mathrm{CM}}, \cos\theta_\gamma^{\mathrm{CM}}\right) \ , \tag{4.99}$$

where $|\vec{p}_\gamma^{\,\mathrm{CM}}| = E_\gamma^{\mathrm{CM}} = m_h/2$. The boost to the laboratory frame, in the $\vec{l}$ direction, is a function of the heavy neutrino velocity, $\vec{v}$. After the Lorentz transformation, in the O_R coordinate system, the energy and momentum of the photon are

$$E_\gamma^{\mathrm{lab}} = \frac{k'_0}{2}\left(1 + \frac{|\vec{k'}|}{k'_0}\cos\theta_\gamma^{\mathrm{CM}}\right) \ , \tag{4.100}$$

$$\left(\vec{p}_\gamma^{\,\mathrm{lab}}\right)_\parallel = \frac{k'_0}{2}\left(\frac{|\vec{k'}|}{k'_0} + \cos\theta_\gamma^{\mathrm{CM}}\right) \ , \tag{4.101}$$

where $(\vec{p}_\gamma)_\parallel$ denotes the momentum component in the $\vec{l}$ direction. The momentum components orthogonal to this direction are not affected by the

boost. Hence, in the laboratory frame with the coordinate system defined by the scattering plane the momentum component in the z-direction is

$$\left(\vec{p}_\gamma^{\,\mathrm{lab}}\right)_z = -\frac{m_h}{2}\sin\theta_\gamma^{\mathrm{CM}}\cos\varphi_\gamma^{\mathrm{CM}}\sin\theta_h + \frac{k_0'}{2}\left(\frac{|\vec{k'}|}{k_0'} + \cos\theta_\gamma^{\mathrm{CM}}\right)\cos\theta_h\,, \tag{4.102}$$

and, then,

$$\cos\theta_\gamma^{\mathrm{lab}} = \frac{\left(\vec{p}_\gamma^{\,\mathrm{lab}}\right)_z}{E_\gamma^{\mathrm{lab}}} = \frac{\left(|\vec{k'}| + k_0'\cos\theta_\gamma^{\mathrm{CM}}\right)\cos\theta_h - m_h\sin\theta_\gamma^{\mathrm{CM}}\cos\varphi_\gamma^{\mathrm{CM}}\sin\theta_h}{k_0' + |\vec{k'}|\cos\theta_\gamma^{\mathrm{CM}}}. \tag{4.103}$$

Energy and angular distributions

With the information about the energy and momentum of photons in laboratory frame, we can write the differential number of photons as

$$\begin{aligned}\frac{dN_\gamma}{dE_\gamma\, d\cos\theta_\gamma} = \int dk_0 \frac{dN_\gamma}{dk_0}\int d\cos\theta_\gamma^{\mathrm{CM}}\, d\varphi_\gamma^{\mathrm{CM}}\,\frac{1\mp\cos\theta_\gamma^{\mathrm{CM}}}{2}\,\frac{1}{2\pi} \\ \times\,\delta\left(E_\gamma - E_\gamma^{\mathrm{lab}}\right)\delta\left(\cos\theta_\gamma - \cos\theta_\gamma^{\mathrm{lab}}\right)\,,\end{aligned} \tag{4.104}$$

where E_γ^{lab} and $\cos\theta_\gamma^{\mathrm{lab}}$ are given in Eqs. (4.100) and (4.103) respectively. The expression for $\frac{dN_\gamma}{dk_0}$ is given in Eq. (4.95).

To obtain the energy distribution of photons we use the relation of Eq. (4.100) to integrate the energy δ-function in Eq. (4.104) getting

$$\begin{aligned}\frac{dN_\gamma}{dE_\gamma} =& M_D N_{\mathrm{POT}} N_A \sum_i f_i \int dk_0\phi(k_0)\int dk_0' d\cos d\theta_h d\varphi_h \\ &\times\frac{d\sigma\left(k_0, k_0', \cos\theta_h, \varphi_h\right)}{dk_0' d\cos d\theta_h d\varphi_h} A\left(k_0', r, \theta, \varphi, \theta_h, \varphi_h\right) \\ &\times\frac{\sqrt{(k_0')^2 - m_h^2} - 2E_\gamma + k_0'}{(k_0')^2 - m_h^2}\,.\end{aligned} \tag{4.105}$$

To calculate the angular distribution of photons we have to invert Eq. (4.103), and use it to integrate over $\cos\theta_\gamma^{\mathrm{CM}}$. Squaring this equation introduces spurious solutions that are non-physical. To avoid this problem, we can find some bounds from the limit cases. The angular δ-function in Eq. (4.104) gives the restriction

$$\cos\theta_\gamma - \cos\theta_\gamma^{\mathrm{lab}} = 0\,. \tag{4.106}$$

From this condition we find that if $\cos\varphi_\gamma^{\rm CM} = 0$,

$$\cos\theta_\gamma^{\rm CM} = \zeta \,, \tag{4.107}$$

where, we have defined

$$\zeta \equiv \frac{k_0' \cos\theta_\gamma - |\vec{k'}|\cos\theta_h}{k_0' \cos\theta_h - |\vec{k'}|\cos\theta_\gamma} \,. \tag{4.108}$$

In the case of $\cos\varphi_\gamma^{\rm CM} > 0$, we can distinguish two situations:

$$k_0' \cos\theta_h - |\vec{k'}|\cos\theta_\gamma \geq 0 \quad \rightarrow \quad \cos\theta_\gamma^{\rm CM} \geq \zeta \,, \tag{4.109}$$

$$k_0' \cos\theta_h - |\vec{k'}|\cos\theta_\gamma \leq 0 \quad \rightarrow \quad \cos\theta_\gamma^{\rm CM} \leq \zeta \,. \tag{4.110}$$

And for $\cos\varphi_\gamma^{\rm CM} < 0$, we have:

$$k_0' \cos\theta_h - |\vec{k'}|\cos\theta_\gamma \geq 0 \quad \rightarrow \quad \cos\theta_\gamma^{\rm CM} \leq \zeta \,, \tag{4.111}$$

$$k_0' \cos\theta_h - |\vec{k'}|\cos\theta_\gamma \leq 0 \quad \rightarrow \quad \cos\theta_\gamma^{\rm CM} \geq \zeta \,. \tag{4.112}$$

Finally, for the angular distribution of photons we use Eq. (4.103) to integrate the angular δ-function and get

$$\begin{aligned}
\frac{dN_\gamma}{d\cos\theta_\gamma} = {} & M_D N_{\rm POT} N_A \sum_i f_i \int dk_0 \phi(k_0) \int dk_0' d\cos d\theta_h d\varphi_h \\
& \times \frac{d\sigma\left(k_0, k_0', \cos\theta_h, \varphi_h\right)}{dk_0' d\cos d\theta_h d\varphi_h} A\left(k_0', r, \theta, \varphi, \theta_h, \varphi_h\right) \\
& \times \int d\varphi_\gamma^{\rm CM} \frac{1 \mp \cos\theta_\gamma^{\rm CM,(0)}}{4\pi} \\
& \times \left| \frac{k_0' + |\vec{k'}|\cos\theta_\gamma^{\rm CM,(0)}}{k_0'\cos\theta_h + m_h \cos\varphi_\gamma^{\rm CM} \sin\theta_h \frac{\cos\theta_\gamma^{\rm CM,(0)}}{\sin\theta_\gamma^{\rm CM,(0)}} - |\vec{k'}|\cos\theta_\gamma} \right| \,,
\end{aligned} \tag{4.113}$$

where

$$\cos\theta_\gamma^{\rm CM,(0)} = \frac{\left(k_0'\cos\theta_h - |\vec{k'}|\cos\theta_\gamma\right)\left(k_0'\cos\theta_\gamma - |\vec{k'}|\cos\theta_h\right) + \Delta_\pm}{\left(k_0'\cos\theta_h - |\vec{k'}|\cos\theta_\gamma\right)^2 + m_h^2 \sin^2\theta_h \cos^2\varphi_\gamma^{\rm CM}} \,, \tag{4.114}$$

with

$$\Delta_\pm \equiv \pm m_h^2 \left|\sin\theta_h \cos\varphi_\gamma^{\rm CM}\right| \sqrt{\cos^2\theta_h - \cos^2\theta_\gamma + \sin^2\theta_h \cos^2\varphi_\gamma^{\rm CM}} \,. \tag{4.115}$$

The sign of $\Delta_\pm$ depends on each of the cases given in Eqs. (4.107 - 4.112).

4.7 Event estimation for MiniBooNE

4.7.1 MiniBooNE

The MiniBooNE experiment [71] at Fermilab, was designed to detect electron (anti)neutrinos in a muon (anti)neutrino beam with the goal of testing an earlier result by the LSND experiment, that could be attributed to short baseline neutrino oscillations [72]. MiniBooNE is a 12.2 m diameter Cherenkov spherical detector filled with 806 tons of mineral oil, CH_2. Two separate regions can be distinguished: the inner one with 1280 photomultiplier tubes (PMTs) of 8 inches each, which collects the light of the processes inside the detector, and the outer region, with 240 PMTs, that is the veto zone. This last one, is used to identify cosmic rays.

The neutrino flux directed to MiniBooNE is produced from a proton 8 GeV beam, generated in the Fermi National Accelerator Laboratory (FNAL), which is 149 m diameter synchrotron. The proton beam is directed to a beryllium target, where the secondary meson beam is produced. Using magnetic fields, one of the components of the meson beam can be selected to obtain a beam of predominantly neutrinos or antineutrinos. For example, by keeping the π^+ muonic neutrinos as favored by their decay, $\pi^+ \rightarrow \mu^+ + \nu_\mu$.. The distance between the beryllium target and the detector is 541 m length. In Fig. 4.8 is schematically represented. MiniBooNE collected data for 6.46×10^{20} POT, which is the number of protons directed to the beryllium target, in neutrino mode. In antineutrino mode it took data for 11.27×10^{20} POT[4] The largest, ν_μ and $\bar{\nu}_\mu$ components of the fluxes at the MiniBooNE

[4]Data has been further collected collected in antineutrino mode [57, 58] confirming the original results.

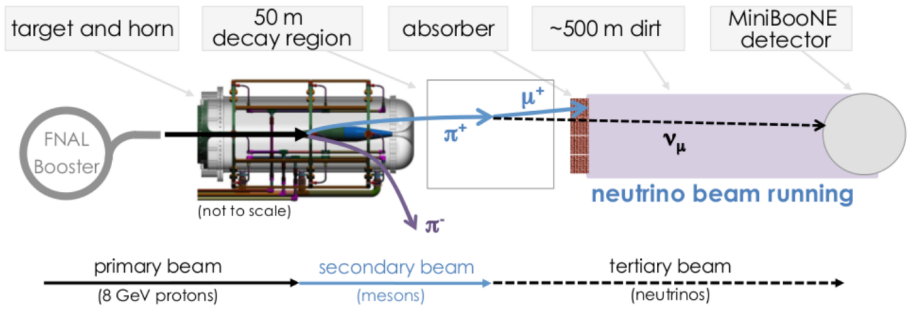

Figure 4.8: The MiniBooNE experiment [71].

detector in both neutrino and antineutrino modes, are shown in Fig. 4.9.

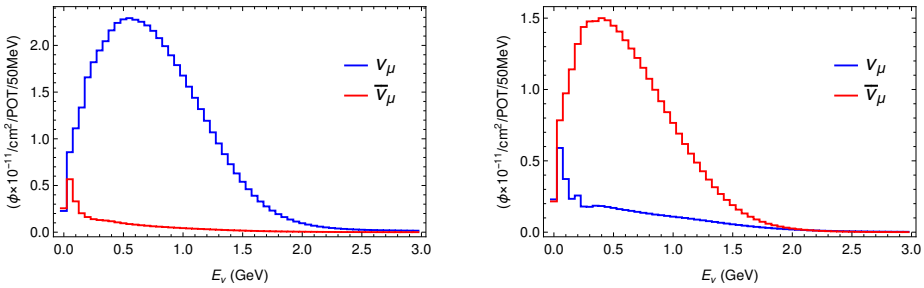

(a) Flux in neutrino mode.

(b) Flux in antineutrino mode.

Figure 4.9: Fluxes used in MiniBooNE experiment [73].

Another critical and often forgotten factor to consider is the detection efficiency. As there are technical limitations for any machine, not every event in the detector produces a signal. Figure 4.10 shows a plot of the MiniBooNE detector efficiency. It can be seen that it is rather low, being at its maximum about 14%, and strongly energy dependent. This efficiency should be taken into account in order to predict a signal in the detector.

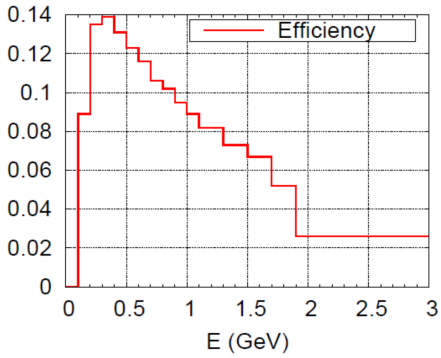

Figure 4.10: MiniBooNE detection efficiency as a function of the produced electron-like particle energy [66].

4.7.2 Heavy neutrino propagation inside MiniBooNE

In Sec. 4.6 it was described how we compute the photon energy and angular distributions of photons in a detector. It was pointed out that only the photons produced inside the detector would produce a signal, Fig. 4.11.

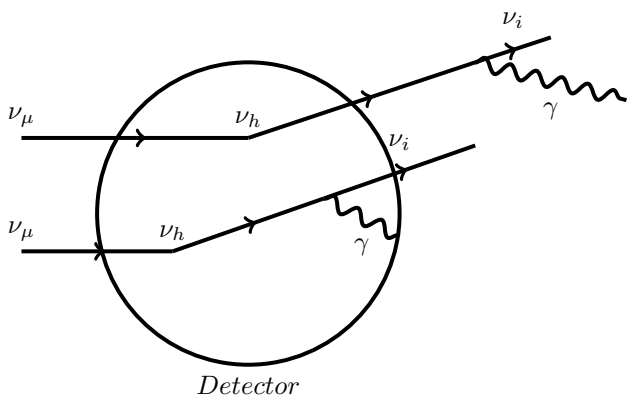

Figure 4.11: Heavy neutrinos decaying inside and outside the detector. Only the photon produced in the detector would produce a signal.

The path length that the heavy neutrino can travel inside the detector, Δl, is contained in the A factor, Eq. (4.94) in Eqs. (4.95, 4.105 and 4.113). In the case of MiniBooNE we have an spherical geometry, where we choose the center of coordinates to be in the sphere's geometrical center, Fig. 4.12. We take the z-axis parallel to the incoming light neutrino momentum. Each of the heavy neutrinos can be produced at any point inside the detector, and the scattering plane would have a different orientation in each case. the path length can be written as

$$\Delta l = \sqrt{R^2 - r^2\left(1-\alpha^2\right)} - r\alpha\,. \tag{4.116}$$

where R is the radius of the detector, and

$$\alpha = \sin\theta_h \sin\theta\cos\varphi_h + \cos\theta_h\cos\theta\,. \tag{4.117}$$

4.7.3 Results

Our model includes the production of heavy neutrinos through EM and NC processes, followed by their EM decay, leading to photons. It is determined by four parameters: the heavy neutrino mass, m_h; the mixing angle between the light and heavy neutrino, U_{lh}; the heavy neutrino mean lifetime, τ_h, which determines the magnetic dipole moment through Eqs. (4.83, 4.92); and the branching ratio of the ν_h decay to a light neutrino of flavor i, which depends on the corresponding transition magnetic moments,

$$\mathrm{BR}_i = \frac{\left(\mu^i_{\mathrm{tr}}\right)^2}{\sum_i \left(\mu^i_{\mathrm{tr}}\right)^2}\,. \tag{4.118}$$

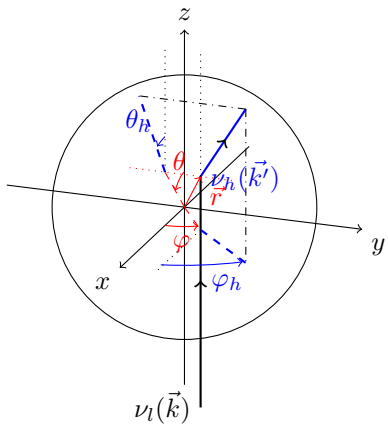

Figure 4.12: Diagram of the geometry at the MiniBooNE detector. The incoming neutrino momentum is parallel to the z-axis. The angles of the position vector of the interaction point are shown in red. The scattering angles of the produced heavy neutrino appear in blue.

The choice for these parameters adopted in Ref. [4] is

$$\begin{aligned} m_h &= 50\,\text{MeV}\,, \\ |U_{\mu h}|^2 &= 3\times 10^{-3}\,, \\ \tau_h &= 5\times 10^{-9}\,\text{s}\,, \\ BR_\mu &= 10^{-2}\,. \end{aligned} \tag{4.119}$$

The main difference between the EM and NC types of ν_h production is how coherent and incoherent scattering contribute in each case. Our results for the integrated cross sections on protons and ^{12}C, obtained with the parameters of Eq. (4.119), are given in Fig. 4.13. The EM cross section on ^{12}C is dominated by the coherent mechanism while the incoherent one is suppressed by Pauli blocking at low q^2, where it is enhanced by the photon propagator Eq. (4.9). On the contrary, the incoherent reaction is the largest contribution to the weak cross section. Similar features are observed for ^{40}Ar target and also for antineutrino beams.

The resulting event distributions at the MiniBooNE detector, ignoring the detection efficiency, are shown in Fig. 4.14. The contribution from the two protons in the CH_2 target, coherent and incoherent scattering on ^{12}C are separately shown. We observe in this plot that the calculated number of events is much higher than the measured excess of events, Ref. [66].

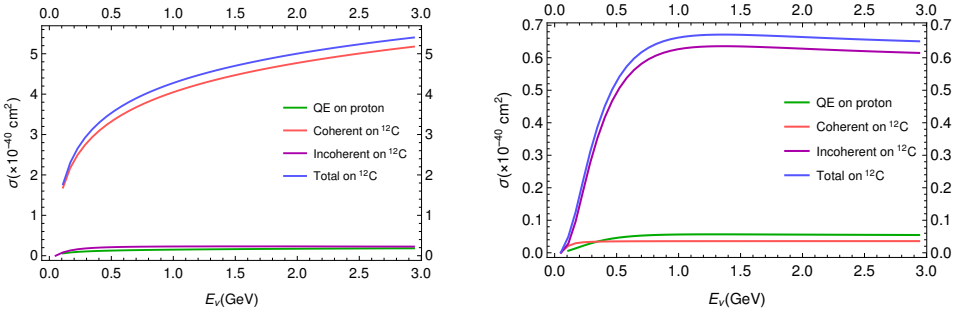

Figure 4.13: Integrated cross sections for ν_h production in ν_μ-nucleus scattering by EM (left) and weak (right) interactions as a function of the incident neutrino energy.

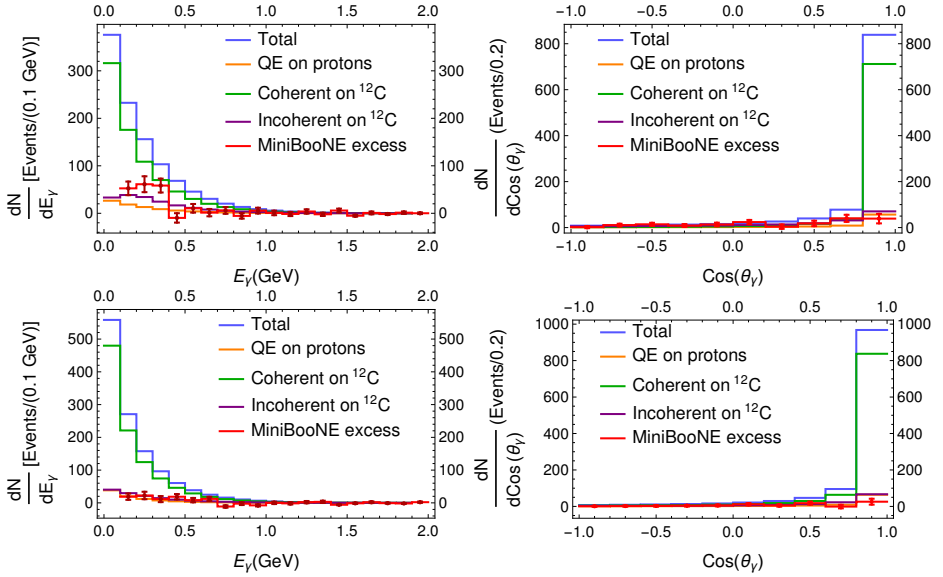

Figure 4.14: Photon events from radiative decay of ν_h, $\overline{\nu}_h$ at the MiniBooNE detector in neutrino mode (top) and antineutrino mode (bottom). Theoretical results, obtained with the ν_h properties of Ref. [4], Eq. (4.119), without taking detector efficiency into account, are compared to the MiniBooNE excess, Ref. [66].

Being the detector efficiency energy dependent and low, Fig. 4.10, its impact on the number of events is significant. The results we obtained when the efficiency is incorporated to the calculation are shown in Fig. 4.15. Although these results are much closer than the previous ones to the MiniBooNE excess and the agreement is good in $\overline{\nu}$-mode, discrepancies clearly show up. The number of low energy events is underestimated in ν-mode while the predominantly EM coherent contribution is strongly forward peaked.This leads to a very narrow angular distribution not observed in the experiment. This result is in line with the findings of Ref.[74]. The combined $\chi^2/\text{DoF} = 127/54$ is too high to consider this scenario, with the parameter values chosen in Ref. [4], as a valid explanation of the MiniBooNE excess[5].

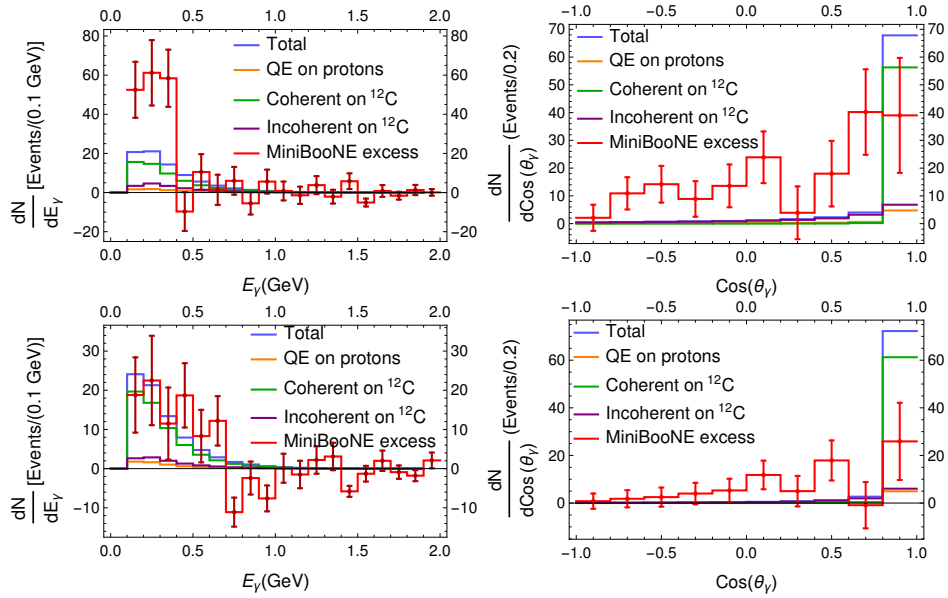

Figure 4.15: Photon events from radiative decay of ν_h, $\overline{\nu}_h$ at the MiniBooNE detector in neutrino mode (top) and antineutrino mode (bottom). Theoretical results, obtained with the ν_h properties of Ref. [4], taking into account the efficiency of the detector, are compared to the MiniBooNE excess, Ref. [66].

Fitted parameters

In Ref. [5] the author estimates the limits for the model parameters that are compatible with the LSND anomaly and other constrains. For the heavy

[5] Although we are ignoring correlations in the data set.

neutrino mass there is a lower bound of 40 MeV from the KArlsruhe Rutherford Medium Energy Neutrino experiment (KARMEN) experiment, which did not observed the same anomaly as MiniBooNE. As the flux in this experiment is lower than 40 MeV, a heavy neutrino with a mass lower than this bound would be observed in this experiment. On the other hand, for a ν_h mass higher than 80 MeV the production in LSND is suppressed by the phase space factor, resulting in an upper bound for this mass. Furthermore, for the mentioned range of masses, the estimate for the mixing is in the range [5]

$$10^{-3} \lesssim |U_{\mu h}|^2 \lesssim 10^{-2} \,. \tag{4.120}$$

The lifetime is restricted to $\tau_h \lesssim 10^{-8}$, to be compatible with the LSND results [5].

We have performed a fit of the signal predicted by the model to the MiniBooNE excess of events, respecting the given bounds. After the minimization, we obtain a $\chi^2/\text{DoF} = 102/54$, corresponding to the values

$$\begin{aligned} m_h &= 70^{+10}_{-30}\,\text{MeV}\,, \\ |U_{\mu h}|^2 &= 10^{-2}\,, \\ \tau_h &= 2.5^{+0.6}_{-1.2} \times 10^{-9}\,\text{s}\,, \\ BR_\mu &= 9^{+31}_{-9} \times 10^{-4}\,. \end{aligned} \tag{4.121}$$

Although we found a minimum value for the mass, changing this parameter in the given range does not seem to have any significant effect in the results. As consequence, the error covers the entire allowed range. This is illustrated in Fig. 4.16, where the distributions in neutrino mode are shown for three different values covering the allowed range while fixing the rest of the parameters to the best-fit values. Similar results are observed in antineutrino mode. In the light of these results, from now on we treat m_h as a constant parameter, not propagating its uncertainty. We also notice that the best agreement of the theoretical distribution to the experimental data occurs when the mixing $|U_{\mu h}|^2$ value is set to its upper limit. The minimization process clearly reveals that this limit prevents from obtaining a more satisfactory description of the data. For this reason, we have fixed this parameter to its maximum allowed value, without error bars. Besides, the quality of the data, with large error bars is reflected in the large uncertainty in the determination of the remaining parameters.

The MiniBooNE excess of events is now better described, particularly the angular distributions, as can be seen in Fig. 4.18. The better agreement is obtained at the price of reducing the EM strength, while increasing the NC

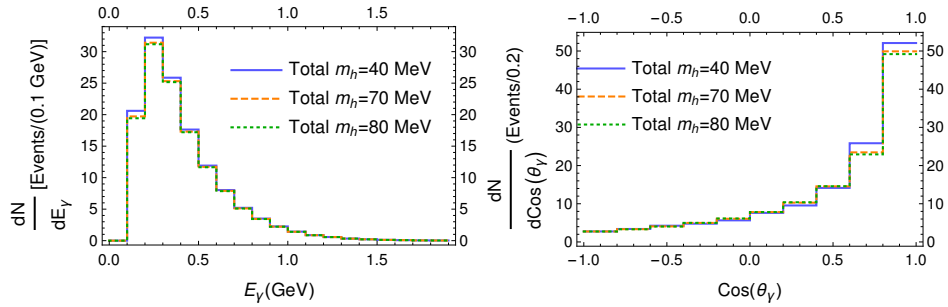

Figure 4.16: Photon events from radiative decay of ν_h, $\overline{\nu}_h$ at the MiniBooNE detector in neutrino mode. The results are obtained for different values of the ν_h mass, with the fitted values of Eq. (4.121) for the rest of parameters.

one by setting $|U_{\mu h}|^2$ to its maximal allowed value, as mentioned above. This can be clearly perceived from Fig. 4.18, where the different contributions are explicitly given, taking the central values for all the parameters.

Fitted parameters with radiative muon capture bounds

On the other hand, there are other bounds for the mixing, $U_{\mu h}$. In particular, according to the study of Ref. [6] a more restrictive constraint than the one in Eq. (4.120) emerges from radiative muon capture: $\mu^- p \to n \nu \gamma$, experimentally investigated at TRIUMF. The mixing upper bound from Ref. [6] is a decreasing function of m_h in the range under consideration (see Fig. 4 of Ref. [6]). Once the fit results are largely independent on the mass and improve for larger values of $U_{\mu h}$, we have fixed the mass to its allowed minimum of 40 MeV in order to have a larger upper bound in the mixing. The fit with this new restriction gives a value of $\chi^2/\text{DoF} = 104/54$, only slightly above the previous one, for the set of parameters:

$$\begin{aligned} m_h &= 40\,\text{MeV}\,, \\ |U_{\mu h}|^2 &= 8.4 \times 10^{-3}\,, \\ \tau_h &= 9.1^{+1.1}_{-1.5} \times 10^{-10}\,\text{s}\,, \\ BR_\mu &= 1.7^{+2.4}_{-1.4} \times 10^{-5}\,. \end{aligned} \tag{4.122}$$

Still, these results describe better the MiniBooNE excess than the calculations done with the parameters of Ref. [4]. The different contributions to heavy neutrino production, taking the central value for the parameters, are plotted in Fig. 4.20. It can be noticed that the EM drive coherent mechanism is further reduced in comparison to the previous fits.

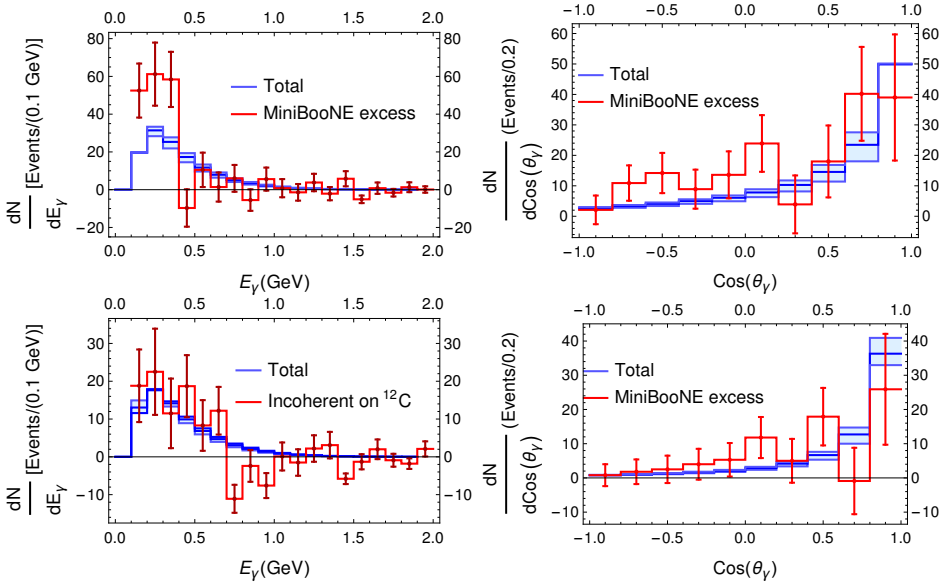

Figure 4.17: Photon events from radiative decay of ν_h, $\overline{\nu}_h$ at the MiniBooNE detector in neutrino mode (top) and antineutrino mode (bottom). Theoretical results, obtained with the fitted ν_h properties, Eq. (4.121), taking into account the efficiency of the detector, are compared to the MiniBooNE excess, Ref. [66].

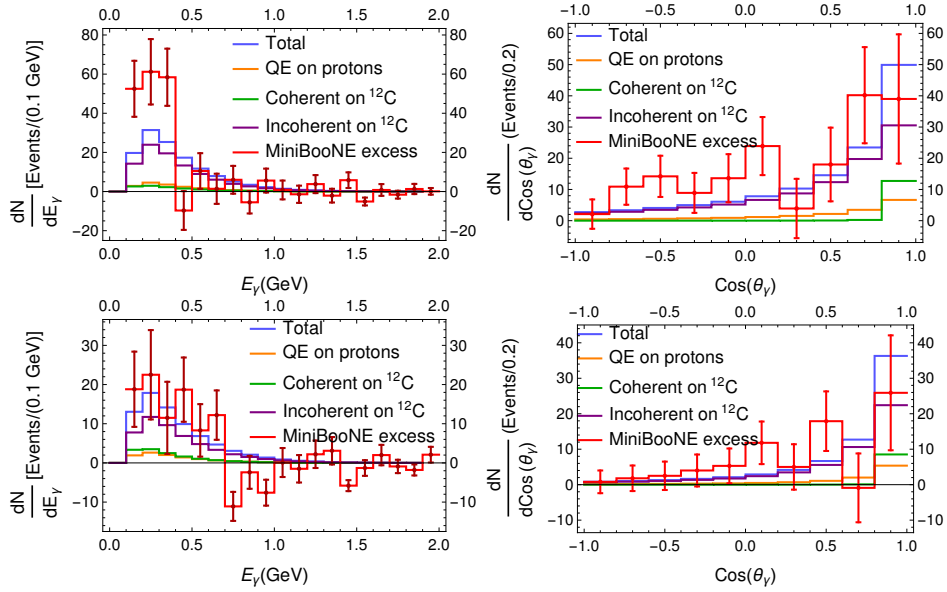

Figure 4.18: Photon events from radiative decay of ν_h, $\overline{\nu}_h$ at the MiniBooNE detector in neutrino mode (top) and antineutrino mode (bottom). Theoretical results, obtained with the fitted ν_h properties, Eq. (4.121), are compared to the MiniBooNE excess, Ref. [66]. The contributions from different ν_h production mechanisms are shown.

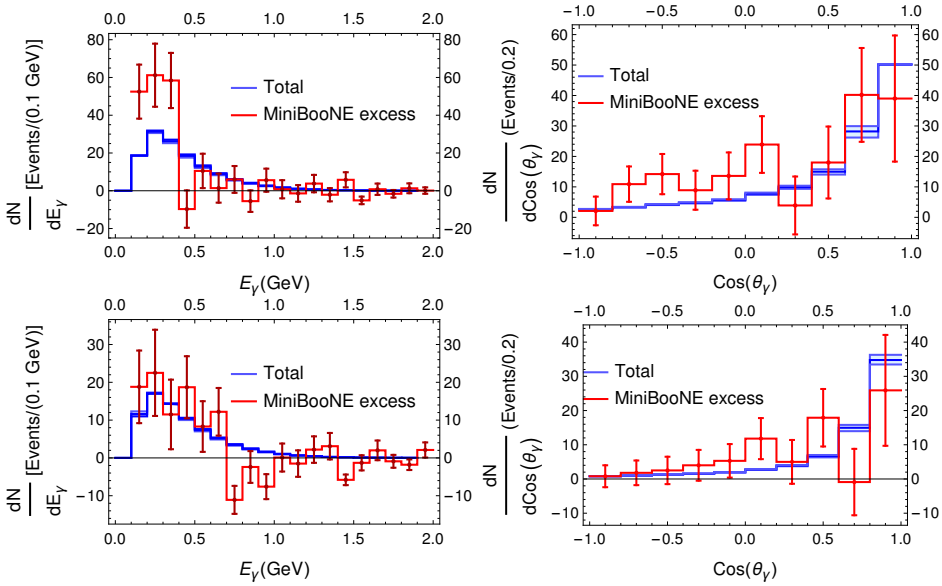

Figure 4.19: Photon events from radiative decay of ν_h, $\overline{\nu}_h$ at the MiniBooNE detector in neutrino mode (top) and antineutrino mode (bottom). The theoretical results take into account the radiative muon capture restrictions of Ref. [6], Eq. (4.122).

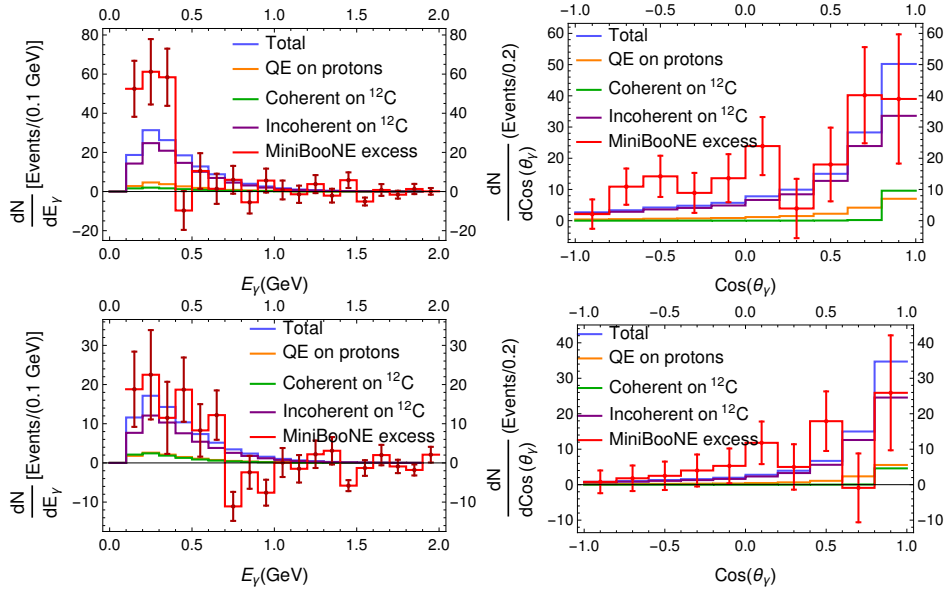

Figure 4.20: Photon events from radiative decay of ν_h, $\overline{\nu}_h$ at the MiniBooNE detector in neutrino mode (top) and antineutrino mode (bottom). The theoretical results take into account radiative muon capture restrictions, Eq. (4.122). The contributions of different ν_h production mechanisms are shown.

The present study shows that the hypothesis of Refs. [4, 65] cannot satisfactorily explain the MiniBooNE anomaly. In particular, we have shown that there are clear difficulties to simultaneously describe the energy and the angular distributions of the electron-like events. Nevertheless, based on MiniBooNE data, radiative decay of heavy neutrinos cannot be fully excluded at least as a partial source of the excess. It is worth studying it further in the new generation of experiments at the Booster Neutrino Beam, which should be able to distinguish photons from electrons. In the next sections we show the signal predictions at MicroBooNE, SBND and Icarus detectors.

4.8 Event estimation for SBN

The SBN program at Fermilab consists of three collaborations in a large project dedicated to the experimental study of neutrino oscillations. This project was designed to address the possible existence of 1 eV mass-scale sterile neutrinos, motivated by the LSND and MiniBooNE anomalies. The idea is to use three different detectors, located in the same beam line at different lengths, to perform sensitive searches for ν_e appearance and ν_μ disappearance in the Booster Neutrino Beam, see Fig. 4.21. The detectors

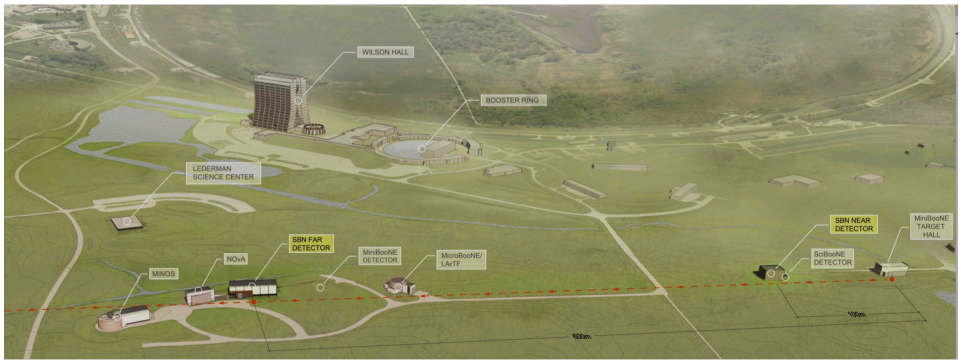

Figure 4.21: SBN program outline [75].

of this program are three liquid argon time projection chambers (LArTPCs), named as SBND, MicroBooNE and ICARUS. Additional details about this program can be found in its proposal, Ref. [75].

4.8.1 Heavy neutrino propagation inside the detectors

As done in the previous section for MiniBooNE, in order to obtain the number of photon events, we need the path length that the heavy neutrino travels inside the detector as a function of the production point. In this case, all three detectors, SBND, MicroBooNE and ICARUS have a square cuboid parallelepiped geometry. The only differences we consider between them are their dimension of length, a, width, b, and height, c. In Fig. 4.22 a detector with this geometry is diagrammatically depicted. We define $\vec{r}_0 = (x_0, y_0, z_0)$, as the position where the heavy neutrino is produced. Its momentum direction is given by Eq. (4.97). Then, the equation of the line which defines the

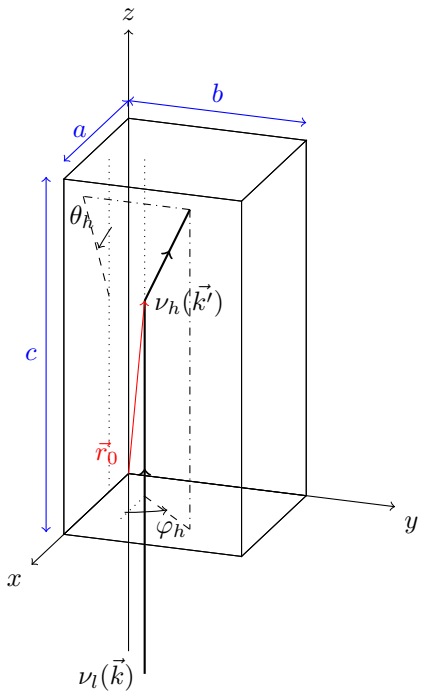

Figure 4.22: Diagram of a parallelepiped geometry detector. The light neutrino momentum is parallel to the z-axis of the detector.

trajectory of the particle can be cast as

$$\vec{r} = \begin{cases} x_0 + \Delta l \sin\theta_h \cos\varphi_h \\ y_0 + \Delta l \sin\theta_h \sin\varphi_h \\ z_0 + \Delta l \cos\theta_h \end{cases} . \tag{4.123}$$

As we integrate over $\vec{r}$, we obtain the value of Δl at each point, given the ν_h scattering angles, in order to calculate the probability that it decays inside the detector; Δl to obtain the photon distributions as previously described.

4.8.2 MicroBooNE

MicroBooNE was the first of the SBN detectors to be operative. One of its advantages over MiniBooNE is that it is able to distinguish electron signals from the photon ones, which will help to establish the origin of the MiniBooNE anomaly. For this reason, it was constructed with the approximate same L/E than MiniBooNE, trying to recreate its conditions. This detector

is placed at 470 m of the beryllium target. MicroBooNE is a cylindrical tank which contains 170 tons of liquid argon, Fig. 4.23. Inside the tank there is a 2.3 m $\times$ 2.6 m $\times$ 10.4 m time projection chamber (TPC).

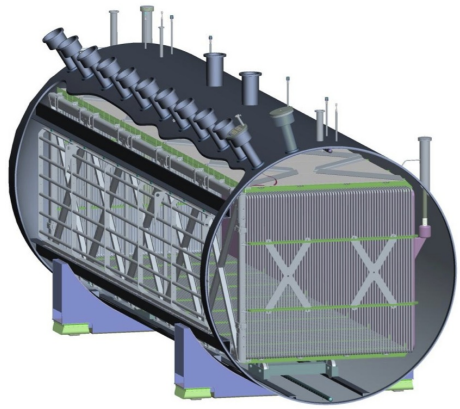

Figure 4.23: Transverse section of MicroBooNE detector [76].

As in the case of MiniBooNE, the neutrino flux for the SBN is generated by the FNAL synchrotron, using the same technology. The predicted flux of MicroBooNE, in neutrino mode, is shown in Fig. 4.24. This experiment has a run plan of 6.6×10^{20} POT. In this case we do not have any information about the flux in antineutrino mode, neither about its detection efficiency.

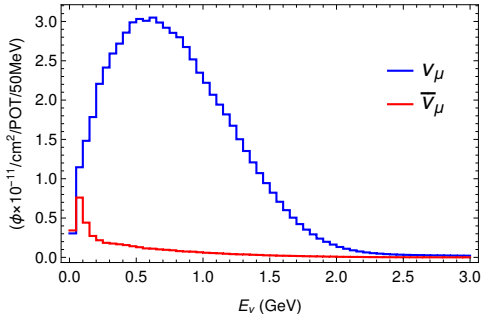

Figure 4.24: Predicted flux for MicroBooNE experiment, provided by [77].

In the case of MicroBooNE, and the rest of the SBN detectors, we have studied the neutrino interactions with the scalar nucleus ^{40}Ar. In Fig. 4.25 we show our results for the predicted number of events in the MicroBooNE detector. This plot has been produced using the parameters of Ref. [4],

Eq. (4.119). For the sake of the estimate, we have assumed that the flux in antineutrino mode corresponds to the one in neutrino one.

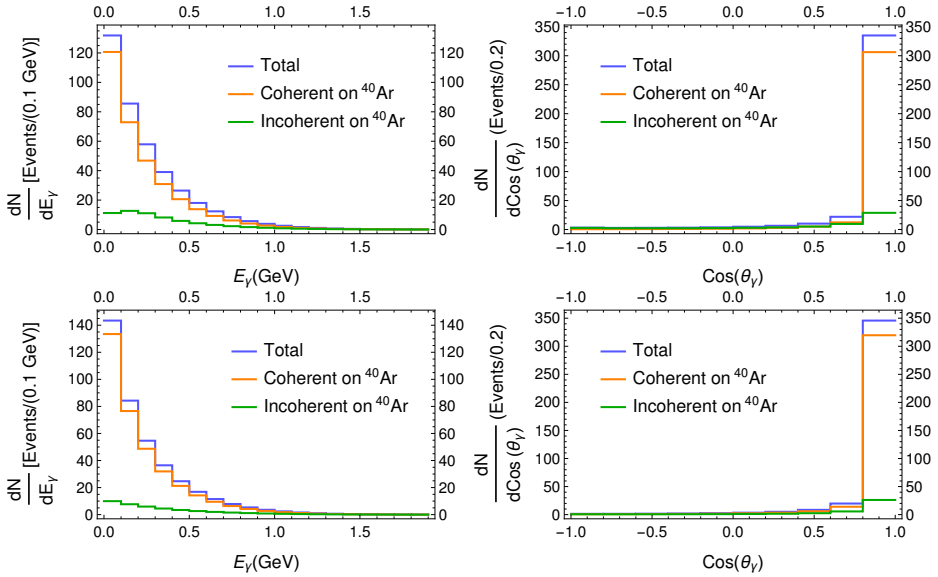

Figure 4.25: Prediction of photon events from radiative decay of ν_h, $\overline{\nu}_h$ at the MicroBooNE detector in neutrino mode (top) and antineutrino mode (bottom). Theoretical results obtained with the parameters of Ref. [4].

In this case, as for MiniBooNE, with the parameters of Ref. [4], the coherent EM contribution clearly dominates the distributions. Because of this, the angular distribution is very forward peaked. Instead, if we use our fitted parameters, Eq. (4.121), we obtain a wider distribution, Fig. 4.26. The individual contribution of the different channels is shown in Fig.4.27.

The results for the fit done with the restrictions imposed by Ref. [6] are shown in Fig. 4.28. The contributions from different mechanisms are given in Fig.4.29.

These distributions can be compared with predictions made for other mechanisms of photon production in MicroBooNE. For example, in Ref. [3] the photon emission from the process $\Delta(1232) \to n\gamma$ was calculated. Their results are shown in Fig. 4.30. The number of events and the shape of these distributions are different than our predictions, for any combination of parameters. This would make possible to distinguish the origin of the photon signal in the detector.

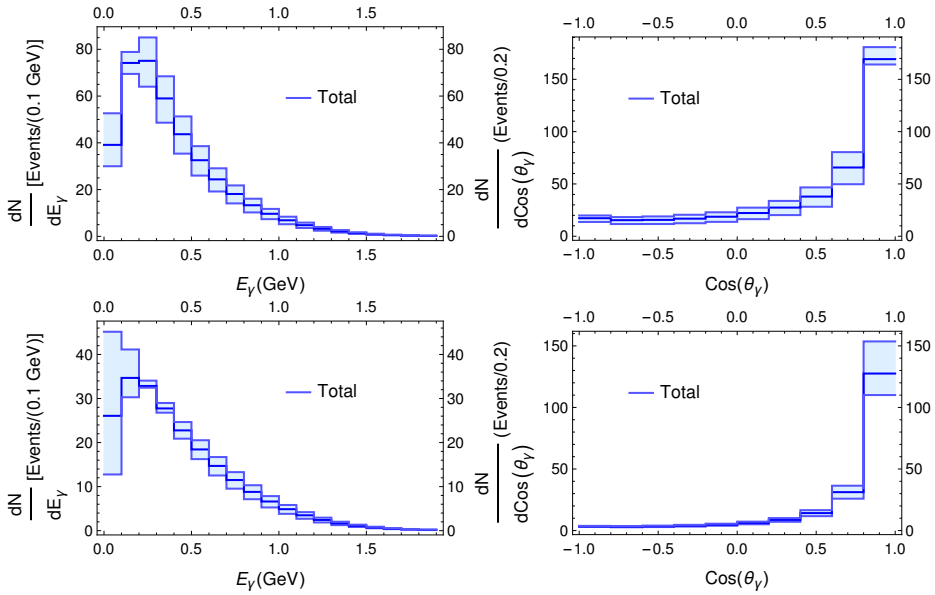

Figure 4.26: Prediction of photon events from radiative decay of ν_h, $\overline{\nu}_h$ at the MicroBooNE detector in neutrino mode (top) and antineutrino mode (bottom). Theoretical results obtained with the fitted parameters of Eq. (4.121).

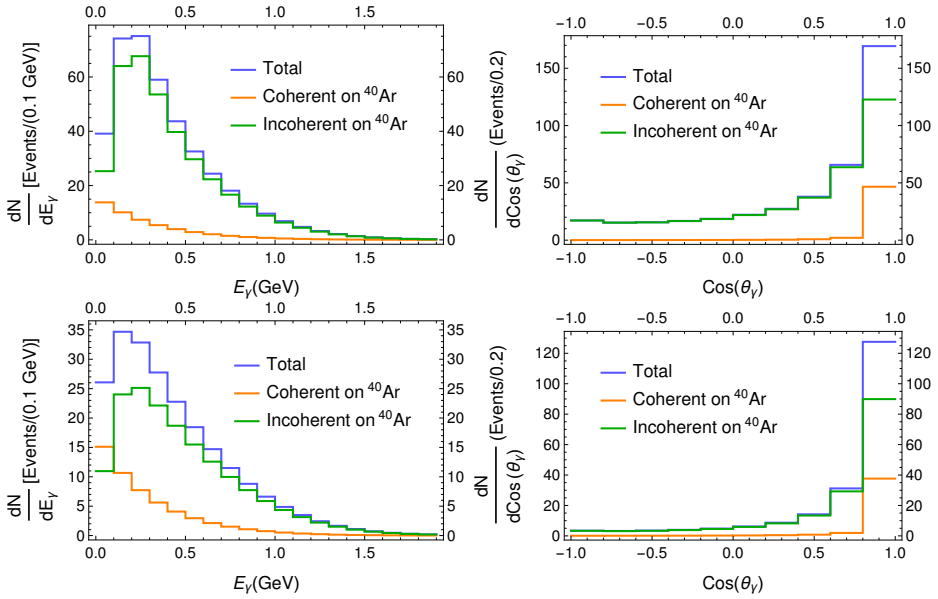

Figure 4.27: Prediction of photon events from radiative decay of ν_h, $\overline{\nu}_h$ at the MicroBooNE detector in neutrino mode (top) and antineutrino mode (bottom). Theoretical results obtained with the fitted parameters of Eq. (4.121). The contributions from different ν_h production mechanisms are shown.

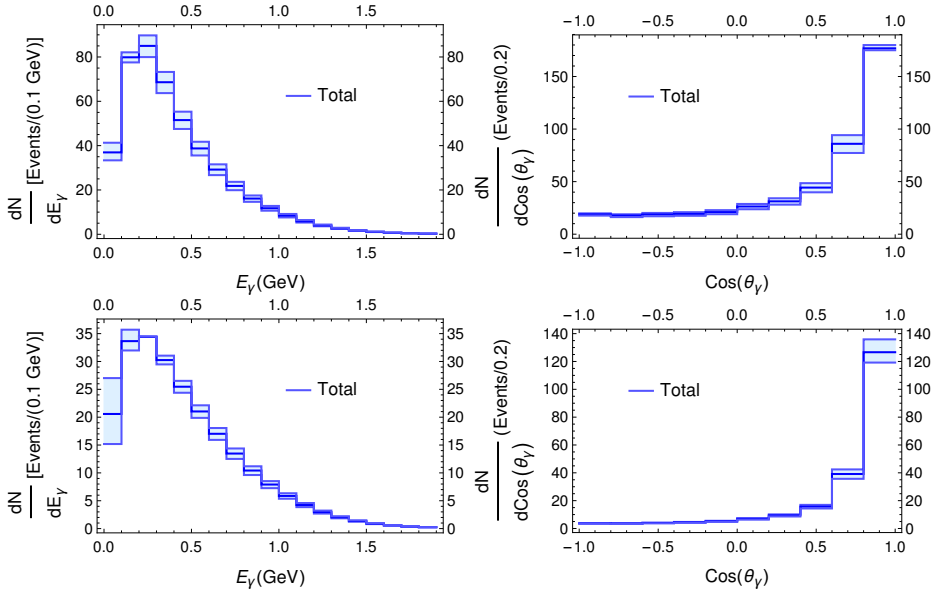

Figure 4.28: Photon events prediction from radiative decay of ν_h, $\overline{\nu}_h$ at the MicroBooNE detector in neutrino mode (top) and antineutrino mode (bottom). Theoretical results obtained using the muon capture restrictions of Ref. [6], Eq. (4.122).

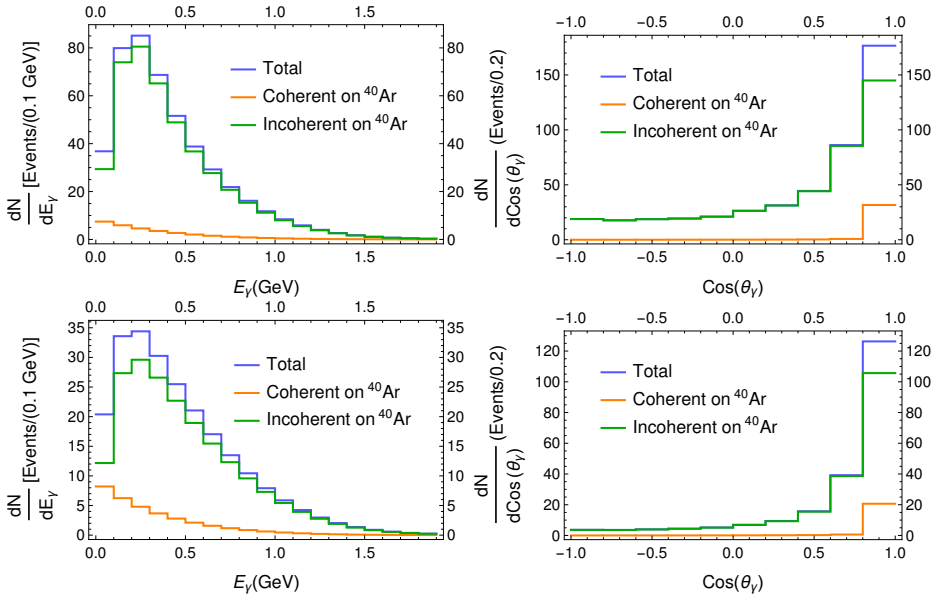

Figure 4.29: prediction of photon events from radiative decay of ν_h, $\overline{\nu}_h$ at the MicroBooNE detector in neutrino mode (top) and antineutrino mode (bottom). Theoretical results obtained using the muon capture restrictions of Ref. [6], Eq. (4.122).

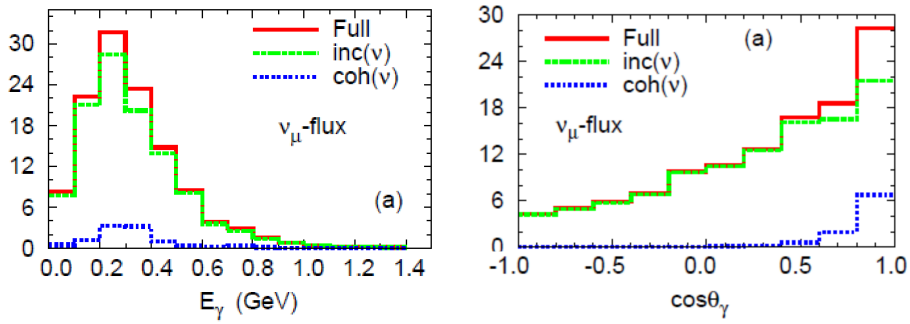

Figure 4.30: Prediction for SM predominant photon emission from $\Delta(1232) \to n\gamma$, Ref. [3].

4.8.3 SBND

SBND is the closest detector to the source of the beam of the SBN program. In this case, the dimensions of the TPC are 5 m × 4 m × 4 m, containing an active mass of 112 tons. With the same run plan than MicroBooNE, the flux is plotted in Fig. 4.31.

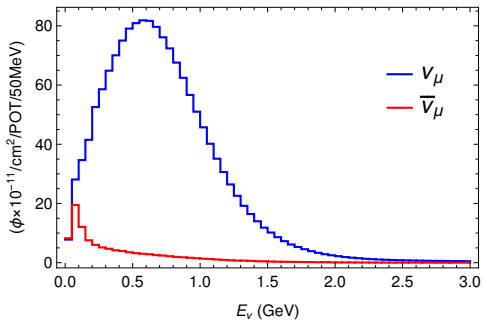

Figure 4.31: Predicted flux for SBND experiment, provided by [77].

Our results with the Ref. [4] parameters are shown if Fig. 4.32. Like in the previous cases we obtain a narrow angular distribution peaked in the forward direction. The angular distribution with the fitted parameters of Eq. (4.121), Fig. 4.33, is wider, as expected. In Fig.4.34 the contribution from all mechanisms is shown.

The predictions for the more restrictive fit of Eq. (4.122) is given in Fig. 4.35, while the contribution of each ν_h production mechanism is displayed in Fig. 4.36.

As one would have easily guessed the shapes of the event distributions and relative contributions from different reaction mechanisms are essentially the same as in MicroBooNE. The distinctive feature apparent in all plots is the very large statistics achievable with this detector, which shall be particularly helpful to study processes with small cross sections as the present one.

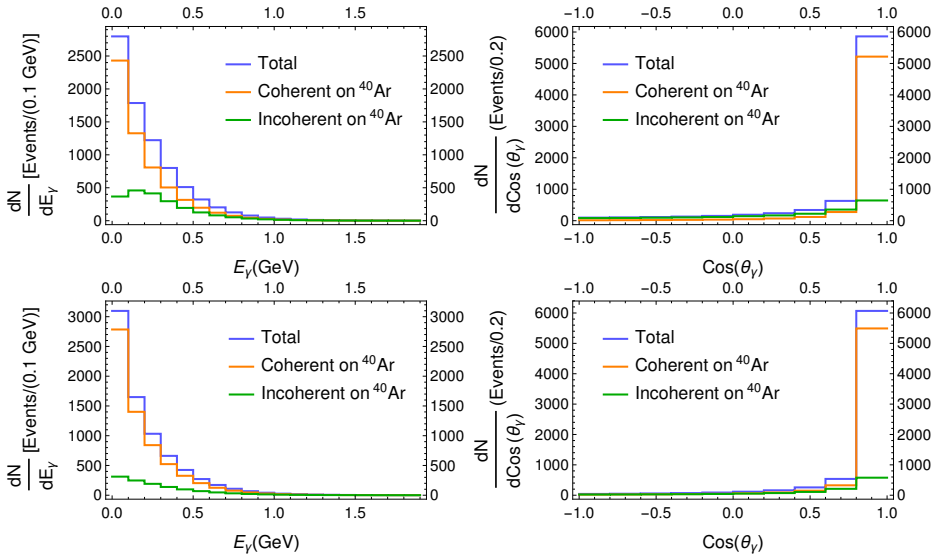

Figure 4.32: Prediction of photon events from radiative decay of ν_h, $\overline{\nu}_h$ at the SBND detector in neutrino mode (top) and antineutrino mode (bottom). Theoretical results obtained with the parameters of Ref. [4].

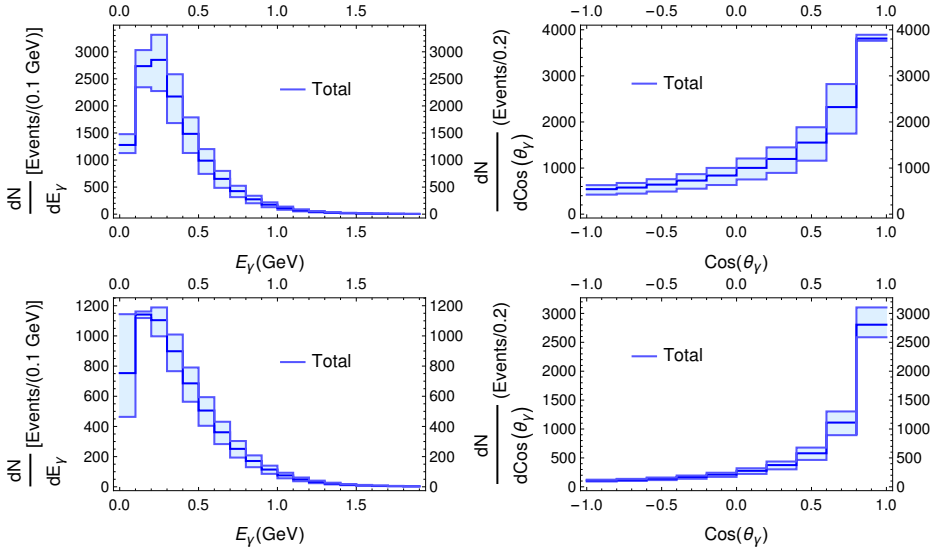

Figure 4.33: Prediction of photon events from radiative decay of ν_h, $\overline{\nu}_h$ at the SBND detector in neutrino mode (top) and antineutrino mode (bottom). Theoretical results obtained with the fitted parameters of Eq. (4.121).

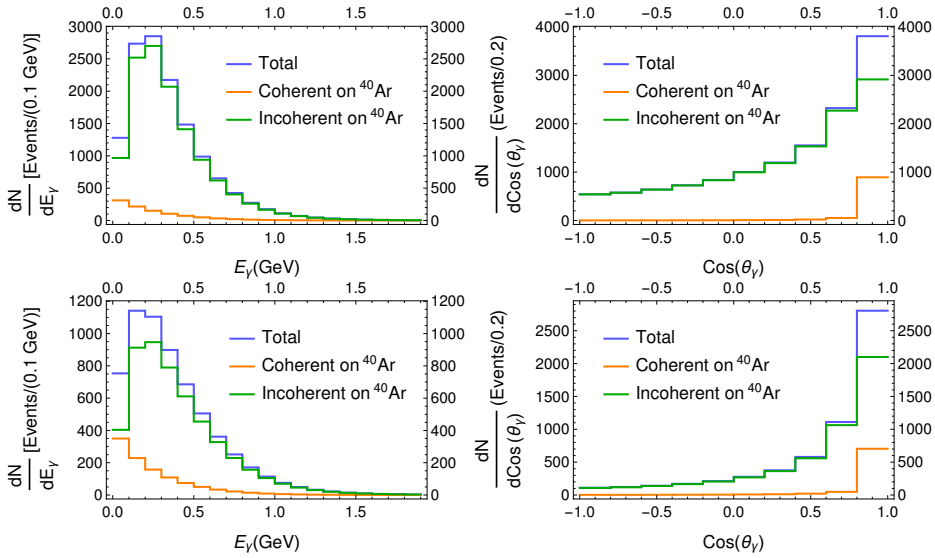

Figure 4.34: Photon events prediction from radiative decay of ν_h, $\overline{\nu}_h$ at the SBND detector in neutrino mode (top) and antineutrino mode (bottom). Theoretical results obtained with the fitted parameters of Eq. (4.121). The contributions of different ν_h production mechanism are shown.

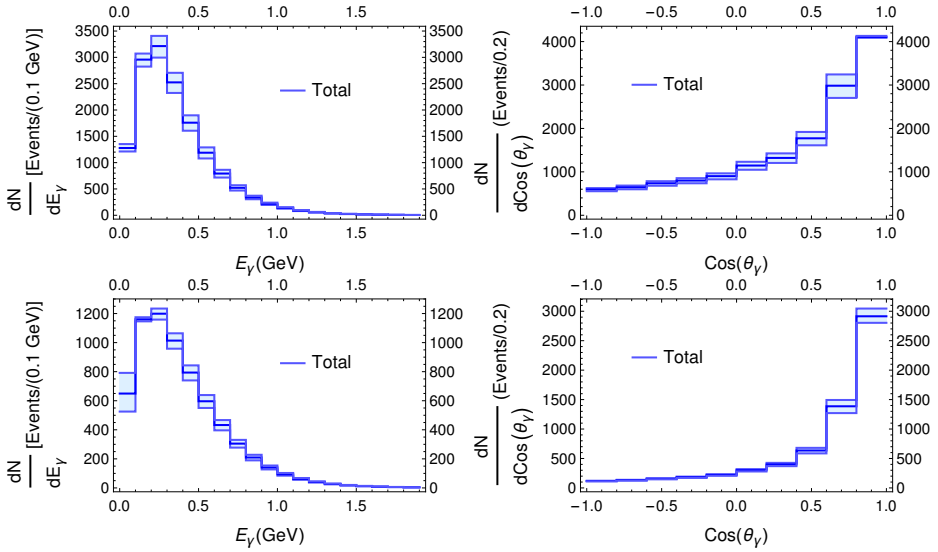

Figure 4.35: Prediction of photon events prediction from radiative decay of ν_h, $\overline{\nu}_h$ at the SBND detector in neutrino mode (top) and antineutrino mode (bottom). Theoretical results obtained using the muon capture restrictions of Ref. [6], Eq. (4.122).

4.8.4 ICARUS

The farthest to the beam source and largest detector in the SBN program is ICARUS. It has a 3 m × 2 m × 18 m TPC, with an active mass of 238 tons. The neutrino flux at its position is plotted in Fig. 4.37.

In the same way as in the previous cases, the predicted distributions with the Ref. [4] parameters, Fig. 4.38, exhibit a forward peaked angular distribution. For the fitted parameters of Eq. (4.121) we found a wider distribution, as before, ig. 4.39. The different contributions to the distributions are shown in Fig.4.40.

Finally, the distributions using the more restrictive fit of Eq. (4.122) are plotted in Fig. 4.41. Fig. 4.42 shows the contribution of each different channel.

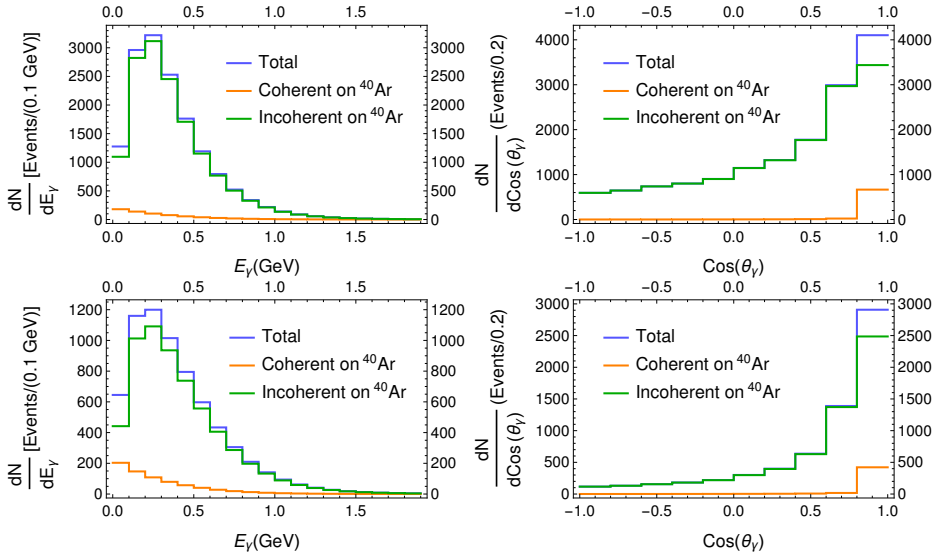

Figure 4.36: Prediction of photon events from radiative decay of ν_h, $\overline{\nu}_h$ at the SBND detector in neutrino mode (top) and antineutrino mode (bottom). Theoretical results obtained using the muon capture restrictions of Ref. [6], Eq. (4.122). The contributions of different ν_h production mechanism are shown.

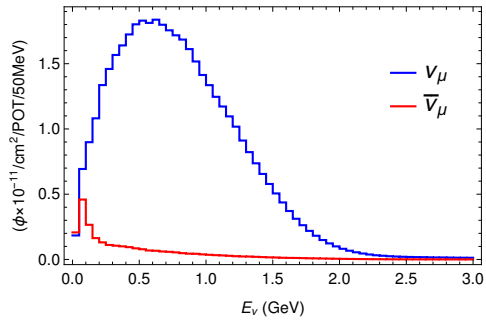

Figure 4.37: Predicted flux for ICARUS experiment, provided by [77].

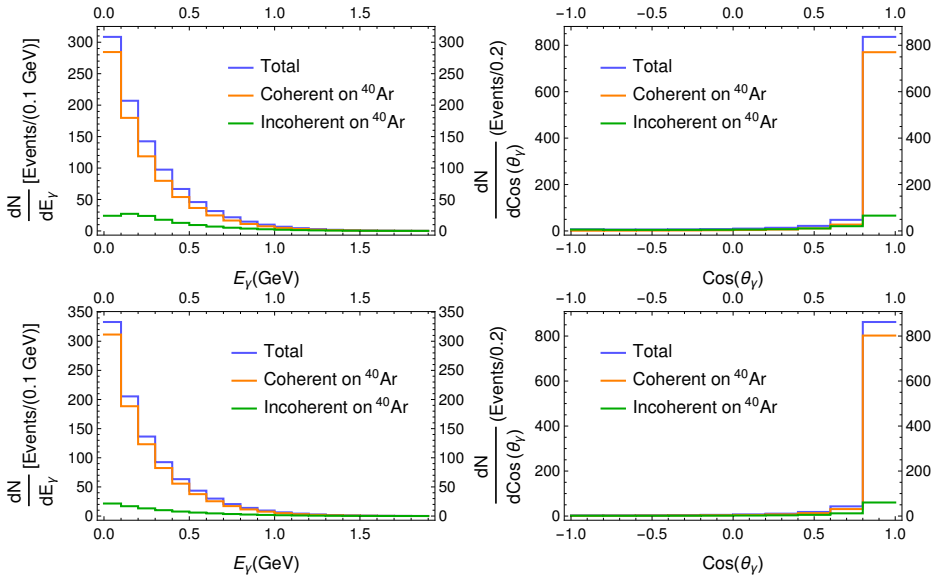

Figure 4.38: Prediction of photon events from radiative decay of ν_h, $\overline{\nu}_h$ at the ICARUS detector in neutrino mode (top) and antineutrino mode (bottom). Theoretical results obtained with the parameters of Ref. [4].

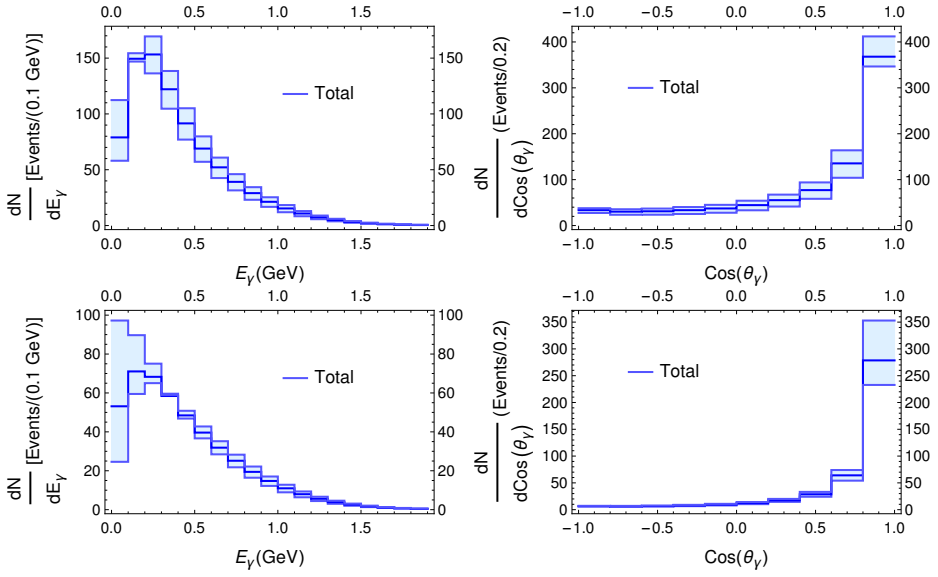

Figure 4.39: Photon events prediction from radiative decay of ν_h, $\overline{\nu}_h$ at the ICARUS detector in neutrino mode (top) and antineutrino mode (bottom). Theoretical results obtained with the fitted parameters of Eq. (4.121).

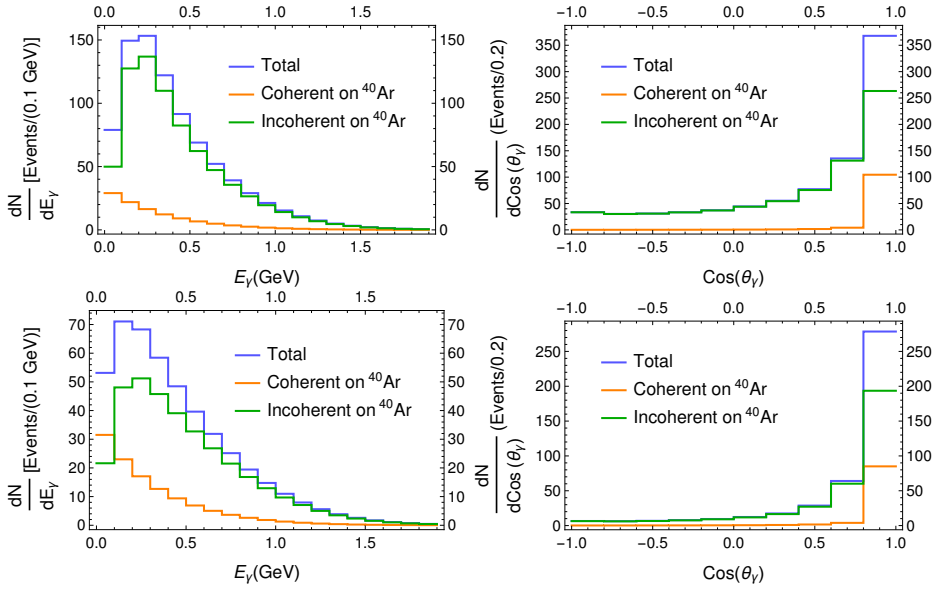

Figure 4.40: Prediction of photon events from radiative decay of ν_h, $\overline{\nu}_h$ at the ICARUS detector in neutrino mode (top) and antineutrino mode (bottom). Theoretical results obtained with the fitted parameters of Eq. (4.121). The contributions of the different ν_h production mechanisms are shown.

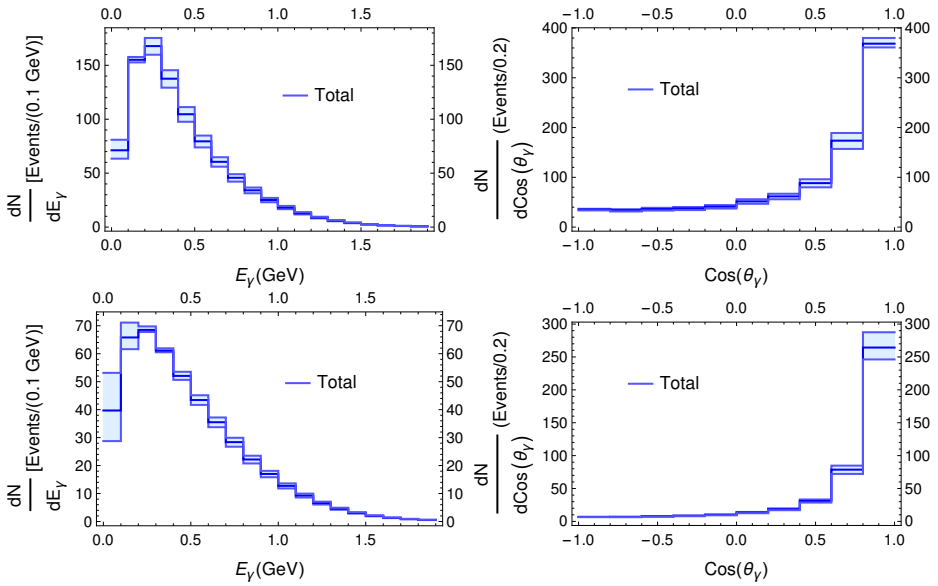

Figure 4.41: Prediction of photon events prediction from radiative decay of ν_h, $\overline{\nu}_h$ at the ICARUS detector in neutrino mode (top) and antineutrino mode (bottom). Theoretical results obtained using the muon capture restrictions of Ref. [6], Eq. (4.122).

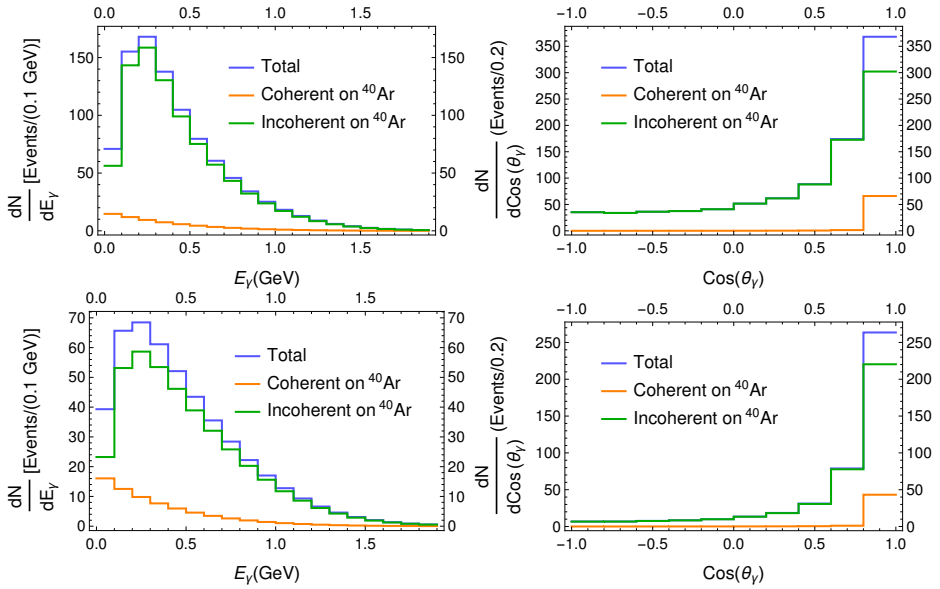

Figure 4.42: Prediction of photon events prediction from radiative decay of ν_h, $\overline{\nu}_h$ at the ICARUS detector in neutrino mode (top) and antineutrino mode (bottom). Theoretical results obtained using the muon capture restrictions of Ref. [6], Eq. (4.122). The contributions of the different ν_h production mechanisms are shown.

4.9 Summary

The answer to the question about the origin of the neutrino excess at MiniBooNE is not yet clear. Different possibilities range from bad modeling of backgrounds to Beyond Standard Model (BSM) theories. Among all these hypotheses, in this work we have studied an idea that implies the existence of a new family of heavy sterile neutrinos. In addition, it incorporates the electromagnetic interaction for neutrinos, induced by a magnetic dipole transition moment.

In order to determine the number of events at MiniBooNE, we have calculated the cross section of the processes given by this model with heavy neutrinos. We have done it for their production through the interaction of light neutrinos with the components of the detectors, including coherent and incoherent reactions on nuclear targets. We have taken into account both the EM and the weak production mediated by NC of these heavy neutrinos. We considered then the decay of a heavy neutrino inside the detector, taking into account its geometry. With these expressions, using the flux and detection efficiency in the MiniBooNE detector as input, we were able to calculate the corresponding energy and angular theoretical distributions of photons. We compared these distributions to the excess, showing that this model, as presented in Ref. [4], is not able to provide a good description of the data. We have changed the values of the model parameters, minimizing them in a fit to the experimental data, respecting the constrains given in Ref. [5]. The results of the model with these fitted parameters provide a much better description of the data but they are not yet able to fully explain the MiniBooNE excess. In particular, the model is hardly able to describe the energy and angular distributions of the electron-like events. When we consider the more restrictive limits of Ref. [6] from radiative muon capture the description slightly worsen but is still better than the one with the original set of parameters of Ref. [4]. All in all, at the moment this model can not be fully discarded as a sizable partial contribution to the excess.

The SBN is the natural successor of the MiniBooNE experiment. The three detectors of the program, with a different detection technology, are able to distinguish photons from electrons. This will allow the scrutiny of this model in the future. Following the same procedure than for MiniBooNE, we have made predictions of the photon distributions for all the three detectors. We have seen that the comparison of the number of events and the shape of the distributions with the standard single-photon production would allow to distinguish the heavy neutrino radiative decay mechanism.

Chapter 5

Extraction of the nucleon axial form factor from neutrino scattering data

5.1 Introduction

In this chapter, based on the work done in Ref. [78], we resume the discussion about the axial FF, introduced in Chapter 3. This quantity is a source of uncertainty in the neutrino scattering amplitudes and the corresponding cross sections. As previously mentioned, the dipole parametrization, Eq. 3.54, is commonly used in the literature. This parametrization has been utilized to describe also the electric and magnetic FFs of the nucleon. In the Breit frame and for small momenta, this Q^2 dependence implies that the axial-charge distribution is an exponentially decreasing function of the radial coordinate. This can be seen performing a Fourier transform of the dipole expression of the axial FF. Both the electric and the magnetic FFs of the nucleon deviate from the dipole parametrization, for a review see Ref. [7]. It seems then natural to expect similar deviations for the axial one.

In Chapter 3 it is explained that empirical parametrizations are obtained from data of lepton scattering on nucleons. As EM interactions are blind to the axial part of the current, in the case of the axial FF, F_A, the information must be extracted from weak interactions. The CCQE reaction, $\nu_l\, n \to l^-\, p$ is a rather simple process which is particularly sensitive to F_A. However, modern neutrino cross-section measurements have been performed on heavy nuclear targets (mostly ^{12}C) where the determination of F_A becomes unreliable due to the presence of not well-constrained nuclear corrections and the

difficulties in isolating the CCQE channel in a model-independent way. A detailed discussion of this problem can be found, for instance, in Sec. III of Ref. [8]. A more direct and, in principle, less model dependent determination of F_A relies on bubble-chamber data on deuterium. Global analyses of the Argonne National Laboratory (ANL), Refs. [9–11], Brookhaven National Laboratory (BNL), Refs. [12, 13], FNAL, Ref. [14], and European Organization for Nuclear Research (CERN), Ref. [15], data with updated vector from factors based on modern electron-scattering data have been performed by Bodek and collaborators. A reference value of $M_A = 1.016 \pm 0.026$ GeV with a small (2.5%) error has been obtained in Ref. [16].

On the other hand, as pointed out in Refs. [79, 80], the anzatz of Eq. (3.54) is not theoretically well founded. A new extraction of F_A has been recently undertaken using a functional representation of the FF based on conformal mapping (z expansion), Ref. [17]. The function is only constrained by the analytic structure and asymptotic behavior dictated by QCD. The resulting FF is consistent with the dipole one but with a much larger error, Fig. 7 of Ref. [17]. In particular, the axial radius, [1]

$$r_A^2 \equiv -\frac{6}{g_A}\left.\frac{dF_A}{dQ^2}\right|_{Q^2=0} , \tag{5.1}$$

obtained is $r_A^2 = 0.46 \pm 0.22$ fm^2, which agrees with the dipole one, $r_A^2 = 12/M_A^2$, but with an ~ 20 times larger error. This result might have implications for oscillation studies and calls for a new measurement of neutrino-nucleon cross sections, which is in any case desirable. The axial radius can also be extracted from muon capture by protons. A recent analysis, Ref. [18], using the z expansion obtains $r_A^2 = 0.43 \pm 0.24$ fm^2, in agreement with the neutrino-scattering result.

A promising source of information about $F_A(Q^2)$ is lattice QCD. Although the experimental value of g_A has been recurrently underpredicted in lattice QCD studies, the use of improved algorithms has recently lead to consistent results, Refs. [19–21, 81, 82]. A global analysis of the low-Q^2 and light-quark mass dependence of the results of Refs. [19–21] using baryon chiral perturbation theory has found $g_A = 1.237 \pm 0.074$ and $r_A^2 = 0.263 \pm 0.038$, Ref. [22]. The central value of r_A^2 is considerably lower than those from empirical determinations but within the (large) error bars of the z expansion results.

The choice of a specific functional form of F_A may bias the results of the analysis. Moreover, the choice of the number of parameters within a

[1] See also Eq. (3.78).

given parametrization is a delicate question. Too few parameters may not give enough versatility. As the number of parameters increase, the χ^2 value of the fits can be reduced, but at some point the fit tends to reproduce statistical fluctuations of the experimental data , see Ref. [23]. A reduction of the model-dependence of the results can be obtained within the methods of neural networks. This approach has been used to obtain nucleon parton distribution functions from deep-inelastic scattering data by the neural network parton distribution function (NNPDF) collaboration in Ref. [24].

In this chapter, we demonstrate that model-independent information about F_A can be obtained from a semi-parametric analysis of ν-deuteron scattering data[2]. In contrast to the parametric approach in which a particular parametrization of F_A is adopted based on physics assumptions, semi-parametric ones are not motivated by physics; they allow to construct a statistical model in terms of an ensemble of probability densities that are used to do statistical inference *i.e.* to determine the quantities of interest and their uncertainties (see Chapter 2 of Ref. [83]). The lack of physics motivation may prevent the results from being extrapolated outside the fit region (positive Q^2 in our case). On the other hand, given the generality of the approach, the results may contain new physics beyond the underlying assumptions of a given model or be affected by theoretical mismodeling and/or deficiencies in a data set.

To perform this semiparametric analysis, we make use of feed-forward neural networks,[3] a class of functions with unlimited adaptive abilities [25]. With this choice, we can eliminate any bias in the result introduced by the functional form of the fit function. Depending on the number of adaptive parameters, one can get different variants of the statistical model (fit). In this context, Bayesian statistics has proved to be a very effective tool, see Ref. [26]. Its methods allow to make comparisons between different models and control the number of parameters in the fit. Bayesian methods are successfully used in different branches of physics. For instance, in hadron and nuclear physics, they have been applied to the study of the resonance content of the $p(\gamma, K^+)\Lambda$ reaction, Ref. [84], and to constrain the nuclear energy-density functional from nuclear-mass measurements, Ref. [85]. We consider the Bayesian framework for neural networks formulated by MacKay in Ref. [27]. It has been adapted to model electric and magnetic form fac-

[2]See Sec. 5.2 for more detailed descriptions of parametric and semiparametric techniques.

[3]Semiparametric analyses of experimental data can also rely on other families of functions, such as polynomials or radial-basis functions [83].

tors in Ref. [28]. It was also used in the investigation of the two-photon exchange phenomenon in elastic electron-proton scattering, Refs. [86–88]. Furthermore, this approach has proved valuable to gain insight into the proton radius puzzle and, in particular, to study the model dependence in the extraction of the proton radius from the electron-scattering data, Refs. [23, 89].

5.2 Neural networks

Our aim is to obtain a statistical model which has the ability to generate $F_A(Q^2)$ values together with uncertainties. In practice, to construct such a model, a number of probability densities must be estimated. This can be achieved within three general methods, Ref. [83]: (i) non-parametric, (ii) parametric, and (iii) semiparametric. In the first approach, no particular functional model is assumed, and the probabilities are determined only by the data. However, if the size of the data is large, the method requires introduction of many internal parameters. Additionally, this approach is computationally expensive. In the parametric method, a specific functional form of the model is assumed. In this case, it is relatively easy to find the optimal configuration of the model parameters. However, a particular choice of the parametrization limits the ability of the model for an accurate description of the data.[4] In this case, the uncertainties for the model prediction are either overestimated or underestimated. The semiparametric method takes the best features from both (i) and (ii) approaches. In this method, instead of a single specific functional model, a broad class of functions is considered. The optimal model is chosen among them. The neural-network approach is a realization of the semiparametric method. In particular, the feedforward neutral networks form a class of functions with unlimited adaptative abilities.

5.2.1 Perceptron

Within the field of artificial intelligence we find neural networks, which encompass a family of algorithms designed to emulate intelligent behavior. Inspired by their biological counterparts, these networks are made up of small, linked processing units called single neurons or perceptrons. This unit receives n different inputs, x_n, and returns an output, y. One of the

[4] Fitting the axial FF with the dipole parametrization is an example of the parametric approach.

simplest functions that can be used in a perceptron to process the inputs is a linear map,

$$y = w_0 + \sum_{i=1}^{n} w_i x_i \,, \tag{5.2}$$

where the w_i coefficients are the weights of the input signals and w_0 is the bias. In this case we can fit our parameters to a dataset, using a linear regression algorithm. By doing so we would be able to perform a basic linear description of the dataset, and predict the values of the function for new inputs, not included in the original dataset.

With a neuron defined, we can think of linking several perceptrons in a neural network, to do more complex work. The problem here is that it can be proved that the sum of linear fits its equivalent to a single one. The solution to this problem is to modify the function of each perceptron in a non-linear way. Using the weighted sum of inputs as the argument of an activation function would introduce the non-linear distortion we need. There are different activation functions that can be used in a neuron, being the simplest one the step function, which returns 0 if the value of its argument is negative and 1 otherwise. One of the problems with the step function is that it has 0 gradient everywhere except 0, which does not allow to use gradient descent to minimize the parameters. Instead, there are several alternatives for the activation function that have a better behaviour and are easily found in the literature. As it is explained below, between them we will focus on the sigmoid function given by

$$f(x) = \frac{1}{1 + e^{-x}} \,, \tag{5.3}$$

which has a smooth gradient. Fig. 5.1 shows a plot of this function.

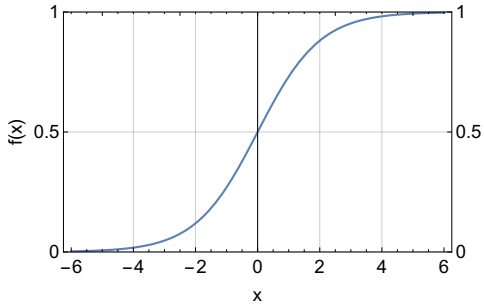

Figure 5.1: Sigmoid function

5.2.2 Multilayer perceptron

The concept of multilayer perceptron (MLP) comes from neuroscience, see Ref. [90]. A given MLP is a nonlinear map from the input space of dimension n_i to the output space of dimension n_o,

$$\mathcal{N} : \mathbb{R}^{n_i} \mapsto \mathbb{R}^{n_o}. \tag{5.4}$$

The MLP map can be represented by a graph which consists of several layers of units: the input layer with n_i units, one or more hidden layers with hidden units, and the output layer which has n_o units. In the input and in every hidden layer, there is an additional bias unit. The units from the consecutive layers are all connected, but the bias unit is connected only to the following layer. As an example, the graphical representation of the MLP: $\mathcal{N}$: $\mathbb{R} \mapsto \mathbb{R}$ is given in Fig. 5.2. Every edge (connection line) in the graph represents one parameter of the function, called latter a weight.

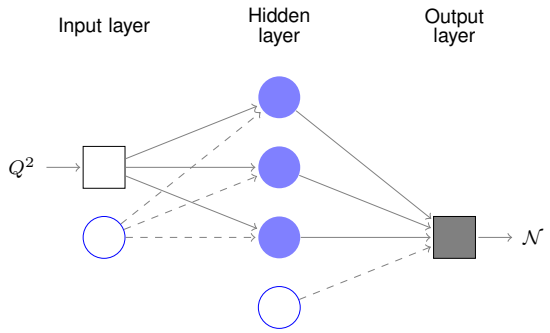

Figure 5.2: Feedforward neural network in an MLP configuration, $\mathcal{N}$: $\mathbb{R} \mapsto \mathbb{R}$. It consists of: (i) an input layer with one input unit Q^2 (open square); (ii) one hidden layer with three hidden $M = 3$ units (filled blue circles); (iii) an output layer consisting of one output unit (black square). Each line denotes a weight parameter w_j. The bias weights are denoted by dashed lines, whereas the bias units are represented by open blue circles.

To every unit (blue circles in Fig. 5.2), a real single-valued activation function, f, is associated; its argument is the weighted sum of the activation function values received from the connected units. In the feedforward case, the ith unit in the kth layer is given in terms of the input from the $(k-1)$th

layer by

$$y_{i,k} = f^{i,k}\left(\sum_{u\in\text{previous layer}} w_u^{i,k} y_{u,k-1}\right) . \tag{5.5}$$

A graphical representation of the above function is given in Fig. 5.3. The weights $w_u^{i,k}$ are real parameters. Their optimal values are established by the network training for which we adopt the Bayesian framework explained below.

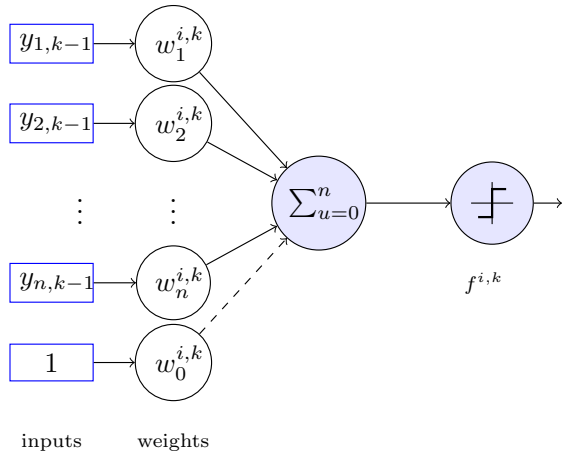

Figure 5.3: The ith unit in the kth layer, Eq. (5.5).

Note that for the bias unit $f^{i,k}(x) = 1$. Furthermore, it is assumed that in the output layer the activation functions are linear $f(x) = x$. In order to simplify and speed up the performance of the numerical analyses MLPs with only one hidden layer of units are considered. In Fig. 5.2, there is an example of such an MLP with $M = 3$ hidden units.

Let us introduce the MLP $\mathcal{N}_M : \mathbb{R} \mapsto \mathbb{R}$, with a single hidden layer and M units, which has the following functional form:

$$\mathcal{N}_M(Q^2;\{w_j\}) = \sum_{n=1}^{M} w_{2M+n}\, f\left(w_n \frac{Q^2}{Q_0^2} + w_{M+n}\right) + w_{3M+1} , \tag{5.6}$$

where $Q_0^2 \equiv 1$ GeV^2. This function depends on $W = 3M + 1$ weights and Q^2.

It has been proved (Cybenko theorem), Refs. [25, 91–96], that, if M is sufficiently large, feedforward neural networks with sigmoidal and linear

activation functions in the (single) hidden and output layers, respectively, form a dense subset in the set of continuous functions. This implies that a map of the form of Eq. (5.6) can approximate arbitrarily well any continuous function and its derivative. As required by the theorem, in our numerical analysis, the activation functions in the hidden layer are given by sigmoids, Eq. (5.3).

5.2.3 Axial form factor

We seek for a model-independent parametrization of F_A that best represents the available data without any input from theory. It should be quite general but, nonetheless, constrained by the following general properties:

(I) $F_A(Q^2)$ is assumed to be a continuous function of Q^2 in its validity domain;

(II) the domain of F_A is restricted to the $Q^2 \in (0, 3)$ GeV^2 where the ANL data are present;

(III) $F_A(Q^2 = 0)$ is constrained by the g_A experimental value, Eq. 3.55;

(IV) as $F_A(Q^2)$ is bounded, there must be a $C > 1$: $F_A(Q^2) < CF_A^{\text{dipole}}(Q^2)$ in the whole Q^2 interval of $(0, 3)$ GeV^2.

The feedforward neural network of Eq. (5.6) can fulfill these properties; for a more detailed discussion see Sec. 5.3.1. In order to speed up the numerical computations, we rescale the output of the MLP, Eq. (5.6), by normalizing it to the dipole ansatz. As the result, the axial FF is represented by

$$F_A(Q^2) = F_A^{\text{dipole}}(Q^2) \times \mathcal{N}_M(Q^2; \{w_i\}) \,, \tag{5.7}$$

where F_A^{dipole} is given in Eq. (3.54) with $M_A = 1$ GeV. In this way, the neural-network response gives the deviation of the axial FFr from the dipole parametrization. The value of g_A is allowed to change within the Particle Data Group (PDG) uncertainty Eq. (3.55).

5.3 Bayesian framework for neural networks

As described above, a MLP is a nonlinear map defined by some number of the adaptive parameters. The increase in the number of hidden units improves MLP's ability to reproduce the data. However, when the number of units (weights) is too large, the model tends to overfit the data, and it

reproduces the statistical noise. As a result, its predictive power is lost. On the other hand, if the network is too small, then the data are underfitted. This competition between two extreme cases is know in statistics as the bias-variance trade-off, Ref. [97]. Certainly, the optimal model is a compromise between both extreme situations.

Bayesian statistics provides methods to face the bias-variance trade-off dilemma. Indeed, the Bayesian approach naturally embodies Occam's razor, see for example Refs. [26, 27, 98, 99], *i.e.* complex models, defined by a large number of parameters, are naturally penalized, whereas simple fits with a small number of parameters, are preferred. Moreover, the Bayesian approach allows one to make comparisons between different statistical descriptions of the data and to indicate the model which is favored by the measurements. An example of such analysis can be found in Ref. [23] where a large number of different fits of the electric and magnetic FFs were obtained from electron-proton scattering data. For each model, the value of the proton radius r_p^E has been calculated. It turned out that, depending on the model, r_p^E ranges from 0.8 to 1.0 fm. A considerable fraction of the results agreed with the muonic-atom measurement $r_p^E = 0.84184(67)$ fm, Ref. [100], but the Bayesian algorithm preferred a model with $r_p^E = 0.899 \pm 0.003$ fm, which is in contradiction with the muonic-atom result but in agreement with some other non-Bayesian *ep* scattering data analysis. A critical review of various approaches to proton radius extraction can be found in Ref. [101] and references therein.

We adopt the Bayesian framework for the feedforward neural network formulated by MacKay in Ref. [102, 103]. This section reviews this approach and its adaptation to the problem of the extraction of the nucleon axial FF that best represents a given set of data. The proposed framework is quite general: it does not rely on physics assumptions about the functional form of $F_A(Q^2)$ and is independent of the experimental conditions from which the data originate. In this way, the present approach not only complements those based on physically motivated parametrizations, but also has the potential to disclose new physics effects as well as deficiencies in the theoretical modeling or in the data.

The general idea is the following: given a data set a statistical model is built. The model is characterized by a number of probability densities, which are obtained using feed-forward neural networks. A detailed account of the different ingredients of the approach is given in this section. The specific application to ANL CCQE neutrino-deuteron scattering data is left for the subsequent sections.

5.3.1 Bayesian framework for multilayer perceptron

Given two different events, *e.g.* in an experiment, we define their respective probabilities to occur as $\mathcal{P}(A)$ and $\mathcal{P}(B)$. Bayes' theorem is a direct consequence of the symmetry of the combined probability of A and B, $\mathcal{P}(A \cap B) = \mathcal{P}(B \cap A)$, which implies the following relation between conditional probabilities (see Appendix. D)

$$\mathcal{P}(A \mid B) = \frac{\mathcal{P}(B \mid A)\mathcal{P}(A)}{\mathcal{P}(B)} \,, \tag{5.8}$$

with $P(B) \neq 0$.

Let us consider a group of M models, $\mathcal{N}_W$ with $W = 1, \ldots, N$, where the model $\mathcal{N}_W$ contains W parameters, $\vec{w} = (w_1, \ldots, w_W)$, and a set of data $\mathcal{D}$. In this case, for a specific model, Eq. (5.8) reads

$$\mathcal{P}(\mathcal{N} \mid \mathcal{D}) = \frac{\mathcal{P}(\mathcal{D} \mid \mathcal{N})\mathcal{P}(\mathcal{N})}{\mathcal{P}(\mathcal{D})} \,, \tag{5.9}$$

where $P(\mathcal{D})$ is the normalization constant. We dropped the index W to simplify the notation.

In our case the models correspond to the set of neural networks,

$$\mathcal{N}_1, \mathcal{N}_2, \ldots, \mathcal{N}_M \,, \tag{5.10}$$

where M denotes the number of units in the hidden layer. To each of the models $\mathcal{N}$, one associates a prior probability denoted $\mathcal{P}(\mathcal{N})$. Our task is to obtain two posterior conditional probabilities: $\mathcal{P}(\mathcal{N} \mid \mathcal{D})$ and $\mathcal{P}(\rho \mid \mathcal{D}, \mathcal{N})$; ρ denotes the set of model parameters, which encompasses the neural network weights $\rho = \{\{w_j\}, \ldots\}$. The first probability density allows us to choose among many network types the one which is favorable by the data, whereas the second one is necessary to make model predictions.

If one assumes, at the beginning of the analysis, that all MLP configurations are equally suited for describing the data, then the following relations between prior probabilities hold

$$\mathcal{P}(\mathcal{N}_1) = \mathcal{P}(\mathcal{N}_2) = \cdots = \mathcal{P}(\mathcal{N}_M) \,, \tag{5.11}$$

therefore

$$\mathcal{P}(\mathcal{N} \mid \mathcal{D}) \sim \mathcal{P}(\mathcal{D} \mid \mathcal{N}) \,, \tag{5.12}$$

and $P(\mathcal{D} \mid \mathcal{N})$ can be used to distinguish between models: the larger $P(\mathcal{D} \mid \mathcal{N})$ the better.

On the other hand, the posterior probability for the weights of a given MLP reads

$$\mathcal{P}(\rho \mid \mathcal{D}, \mathcal{N}) = \frac{\mathcal{P}(\mathcal{D} \mid \rho, \mathcal{N})\mathcal{P}(\rho \mid \mathcal{N})}{\mathcal{P}(\mathcal{D} \mid \mathcal{N})} , \tag{5.13}$$

where $\mathcal{P}(\mathcal{D} \mid \rho, \mathcal{N})$ is the likelihood whereas the density $\mathcal{P}(\rho \mid \mathcal{N})$ is the prior describing the initial assumptions about the parameters. If the posterior is properly normalized, $\int d\rho\, \mathcal{P}(\rho \mid \mathcal{D}, \mathcal{N}) = 1$, by integrating both sides of Eq. (5.13), one gets the evidence for the model,

$$\mathcal{P}(\mathcal{D} \mid \mathcal{N}) = \int d\rho\, \mathcal{P}(\mathcal{D} \mid \rho, \mathcal{N})\mathcal{P}(\rho \mid \mathcal{N}) . \tag{5.14}$$

Occasionally, one can be interested in integrating out some variables of the model to determine the marginal contribution of another, sometimes this is called 'integrating out the nuisance variables'. For example, for a model with dependence on the set of parameters given by $\rho = (\alpha, \vec{w})$, we can integrate all but the α parameter,

$$\mathcal{P}(\mathcal{D} \mid \alpha, \mathcal{N}) = \int d\vec{w}\mathcal{P}(\mathcal{D} \mid \rho, \mathcal{N})\mathcal{P}(\rho \mid \mathcal{N}) . \tag{5.15}$$

In what follows we apply these results derived from Bayes' theorem to the case of models given by the MLP.

Likelihood

In order to calculate the posterior we assume that the likelihood is given in terms of the χ^2 function,

$$\mathcal{P}(\mathcal{D} \mid \{w_j\}, \mathcal{N}) = \frac{1}{N_L} \exp(-\chi^2) , \tag{5.16}$$

where N_L is the normalization constant, which does not depend on the model parameters. The general expression for the χ^2 function is

$$\chi^2(\{w_j\}) = \sum_{i=1}^{N} \frac{(\delta_i - f_i(\{w_j\}))^2}{\sigma_i^2} , \tag{5.17}$$

where $\delta_i \pm \sigma_i$ are the experimental points in the dataset and $f_i(\vec{w})$ are the predicted values for the model at each point.[5]

[5] While the specific expression for the χ^2 function for the present work is defined in Sec. 5.4.2 [see Eq. (5.50)], we make use of this general form below when describing the evidence approximation.

Prior distributions

It is assumed that the initial values of the weights are Gaussian distributed

$$\mathcal{P}(\{w_j\},\mathcal{N}) = \left(\frac{\alpha}{2\pi}\right)^{W/2} e^{-\alpha\, E_w(\{w_j\})}\,, \tag{5.18}$$

where α is a positive hyperparameter (regularizer) introduced to deal with the overfitting problem and

$$E_w(\{w_j\}) = \frac{1}{2}\sum_{i=1}^{W} w_i^2\,. \tag{5.19}$$

The regularizer α plays a crucial role in model optimization and should be properly determined. Indeed, if α is large then the term of Eq. (5.19) dominates in the posterior Eq. (5.13), so it is very likely that the model underfits the data. On the contrary, if α is too small, the likelihood dominates, and the model tends to overfit the data. Note that α is another parameter of the model, hence, $\rho = \{\{w_j\},\alpha\}$.

The prior distribution of the weights, Eqs. (5.18 and 5.19), is justified by the following properties of the adopted feed-forward neural network in the MLP configuration and of the problem under study:

(P1) internal symmetry: the exchange of any two units in the hidden layer does not change the functional form of the network and its output values;

(P2) the sigmoid activation function $f(x)$ Eq. (5.3) saturates and can be effectively assumed to be constant outside the interval $-a \le x \le a$ with $a \sim 10$;

(P3) $f(-x) = 1 - f(x)$;

(P4) the ANL data are concentrated in the region $Q^2 \in (0,3)$ GeV^2 – constraint (II) in Sec. 5.2.3;

(P5) $F_A(Q^2)/F_A^{\text{dipole}}(Q^2) < C$, where $C > 1$ – constraint (IV) in Sec. 5.2.3.

Properties (P4) and (P2) constrain the weights $w_1, ..., w_{2M}$ in function of Eq. (5.6). Indeed, from (P2) one sees that for a full performance of the activation function $f(x)$ in Eq. (5.6) it is enough to have $x \in (-a,a)$. Let us consider then the function $f(w_i Q^2 + w_{M+i})$, $i = 1\ldots, M$, which is one of the elements of the sum in Eq. (5.6). To efficiently cover all possible

outputs, achieving a good performance of the network, it is enough that the arguments of $f(...)$ belong to $(-a, a)$ for all values of Q^2 under consideration. Then, one gets limits for the weights, namely, $|w_{M+i}| < a$ [6] from which one also gets the constraint $|w_i| < 2/3a < a$ for $Q^2 \in (0, 3)$ GeV^2.

Note that both negative and positive values of weights w_i and w_{M+i} are equally possible according to (P3). Therefore, without losing generality, the prior density should be symmetric in weights $w_{1\text{-}2M}$ and cover the hypercube $(-a, a)^{2M}$.

The limits for the weights in the linear layer are less obvious. Property (P5) provides a constraint on the weights in the linear output layer w_{2M+i}, $i = 1, \ldots, M + 1$, namely,

$$\left| \sum_{i=1}^{M} w_{2M+i} f(\ldots) + w_{3M+1} \right| < C \,. \tag{5.20}$$

The main role of the weights in the linear layer is to control the range of the neural-network output. In our case, at any Q^2, the absolute value of the output should be smaller than C. Hence, for a reliable performance of the network, it is enough to assume that the weights in the linear layer are $|w_{2M+i}| < C \sim a$, $i = 1, \cdots, M + 1$. In analogy to the reasoning in the paragraph above, one can argue that these weights could equally take positive and negative values.

We, therefore, conclude that the prior density for the weights should cover the hypercube $(-a, a)^{3M+1}$ and be symmetric in w_i. This is a rough estimate of the bounds for the model parameters, but the functional form of the prior densities is still arbitrary. In the present analysis, we have considered the Gaussian distribution, Eq. (5.18). Such a density profile maximizes the entropy of the system, see Ref. [104]. However, our choice is also supported by further arguments from neural-network computations. In particular, as we describe below, prior , Eq.(5.18), modifies the error function, Eq.(5.45), through the contribution of Eq. (5.19). Such a penalty term has been considered in non-Bayesian approaches, Ref. [105], to the feed forward neural networks. Bayesian statistics provides a probabilistic justification for Eq. (5.19). Moreover, the Bayesian approach allows to consistently obtain the optimal value of the α. We recall that in the numerical analysis, the initial value of α is set to $\alpha_0 = 0.001$. Then, the prior Gaussian distribution has a width of $\sqrt{1/\alpha} \approx 30$, which fully covers the region of the parameter space allowed by the constraints.

[6] At $Q^2 = 0$ we have $f(w_{M+i})$, so it is enough that $|w_{M+i}| < a$.

Eventually, let us remark that the most general Gaussian prior has the form

$$P(\{w_i\} \mid \mathcal{N}) = e^{-\sum_{i=1}^{3M+1} \frac{\alpha_i}{2} w_i^2}, \tag{5.21}$$

where every weight w_i has its own regularizer α_i. However, the internal symmetry of the network (P1) allows to reduce the number of regularizers to only four – each for every class of parameters (w_i, w_{M+i}, w_{2M+i}, w_{3M+1}) with $i = 1 - M$. In Ref. [28], it was verified that the inclusion of more regularizers has a negligible impact on the results but slows down the numerical procedures. Hence, in the present analysis, we consider the simplest and practically very effective scenario.

Evidence approximation

In principle, to get the evidence $\mathcal{P}(\mathcal{D} \mid \mathcal{N})$ on which model discrimination is based, the integration in Eq. (5.14) over the whole space of parameters ρ should be performed.

$$\mathcal{P}(\mathcal{D} \mid \mathcal{N}) = \frac{1}{N_L} \int d\rho \left(\frac{\alpha}{2\pi}\right)^{W/2} e^{-\chi^2(\{w_j\}) - \alpha E_w(\{w_j\})}. \tag{5.22}$$

This is, however, numerically difficult to perform. Therefore, in our analysis, we consider another method, the so-called evidence approximation [102, 103].

The evidence framework divides the inference into distinct levels [102]:

- Infer the parameters $\{w_j\}$ for a given value of α,

$$\mathcal{P}(\{w_j\} \mid D, \alpha, \mathcal{N}) = \frac{\mathcal{P}(D \mid \{w_j\}, \alpha, \mathcal{N})\, \mathcal{P}(\{w_j\} \mid \alpha, \mathcal{N})}{\mathcal{P}(D \mid \alpha, \mathcal{N})}. \tag{5.23}$$

- Infer α,

$$\mathcal{P}(\alpha \mid D, \mathcal{N}) = \frac{\mathcal{P}(D \mid \alpha, \mathcal{N})\, \mathcal{P}(\alpha \mid \mathcal{N})}{\mathcal{P}(D \mid \mathcal{N})}. \tag{5.24}$$

- Compare models by their evidence, $\mathcal{P}(D \mid \mathcal{N})$, see Eqs. (5.9, 5.12).

Eqs. (5.23, 5.24) are the posterior probabilities for the weights and the regularizer respectively, see Eq. (5.13).

In the adopted approach it is assumed that the posterior distributions have a Gaussian shape. Hence, to get the necessary information about Eq. (5.13), it is enough to obtain the configuration of the parameters $\rho_{\mathrm{MP}} = (\{w_j\}_{\mathrm{MP}}, \alpha_{\mathrm{MP}})$ at which the posterior distribution is at its maximum and the

covariance matrix for the model.[7] The latter is necessary to provide the uncertainties for the model predictions. Within the present approximation, the evidence for a given model can be obtained in an analytical form. For this purpose, the exponent of the posterior, given in Eq. (5.22), is first expanded around $\vec{w}_{\rm MP} = \{w_j\}_{\rm MP}$ up to quadratic terms

$$\begin{aligned}\chi^2(\{w_j\}) + \alpha\, E_w(\{w_j\}) \simeq & \chi^2\left(\{w_j\}_{\rm MP}\right) + \alpha\, E_w(\{w_j\}_{\rm MP}) \\ & + \frac{1}{2}\sum_{k,l}^{W}\left(\left.\frac{\partial^2\chi^2}{\partial w_k \partial w_l}\right|_{\vec{w}=\vec{w}_{\rm MP}} + \alpha\delta_{k,l}\right)\left(w_k - w_{{\rm MP},k}\right)\left(w_l - w_{{\rm MP},l}\right) \\ = & \chi^2\left(\{w_j\}_{\rm MP}\right) + \alpha\, E_w(\{w_j\}_{\rm MP}) + \frac{1}{2}\vec{w}_{\rm MP}^{\,T}\mathbf{A}_\chi\vec{w}_{\rm MP} + \frac{1}{2}\vec{w}_{\rm MP}^{\,T}\mathbf{B}\vec{w}{\rm MP}\,,\end{aligned} \tag{5.25}$$

where $\mathbf{A}_\chi$ is the Hessian matrix of the χ^2 function while the matrix elements of $\mathbf{B}$ are defined as $B_{ij} \equiv \alpha\,\delta_{ij}$. Linear terms in the expansion of Eq. (5.25) vanish because at the most probable values for the weights we are in a maximum of the function. Then, using the Gaussian integrals of Appendix B.1, after the integration of Eq. (5.23) over the weights, we obtain

$$\mathcal{P}(\mathcal{D}\mid\alpha,\mathcal{N}) = \frac{1}{N_L}\left(\frac{\alpha}{2\pi}\right)^{W/2}\sqrt{\frac{(2\pi)^W}{|\mathbf{A}|}}e^{-\chi^2(\{w_j\}_{\rm MP})-\alpha\,E_w(\{w_j\}_{\rm MP})}\,, \tag{5.26}$$

where $\mathbf{A} = \mathbf{A}_\chi + \mathbf{B}$ and $|\mathbf{A}|$ denotes the determinant of $\mathbf{A}$. Taking logarithms, we have

$$\begin{aligned}\ln\left(\mathcal{P}(\mathcal{D}\mid\alpha,\mathcal{N})\right) = & -\chi^2\left(\{w_j\}_{\rm MP}\right) - \alpha\, E_w(\{w_j\}_{\rm MP}) - \ln\left(N_L\right) \\ & - \frac{1}{2}\ln|\mathbf{A}| + \frac{W}{2}\ln\left(\alpha\right)\,.\end{aligned} \tag{5.27}$$

Let λ_i be the eigenvalues of $\mathbf{A}_\chi$, then

$$\begin{aligned}\ln\left(\mathcal{P}(\mathcal{D}\mid\alpha,\mathcal{N})\right) = & -\chi^2\left(\{w_j\}_{\rm MP}\right) - \alpha\, E_w(\{w_j\}_{\rm MP}) - \ln\left(N_L\right) \\ & - \frac{1}{2}\sum_{i=1}^{W}\ln\left(\lambda_i+\alpha\right) + \frac{W}{2}\ln\left(\alpha\right)\,.\end{aligned} \tag{5.28}$$

As the first derivative of the evidence at the maximum fulfills the condition

$$\left.\frac{\partial}{\partial\alpha}\mathcal{P}(\mathcal{D}\mid\alpha,\mathcal{N})\right|_{\alpha=\alpha_{\rm MP}} = 0\,. \tag{5.29}$$

[7] The optimal values for the parameters are stabilised in the training process. See next section.

we can write

$$\begin{aligned}\frac{\partial}{\partial\alpha}\mathcal{P}(\mathcal{D}\mid\alpha,\mathcal{N}) =&\mathcal{P}(\mathcal{D}\mid\alpha,\mathcal{N})\frac{\partial}{\partial\alpha}\ln\left(\mathcal{P}(\mathcal{D}\mid\alpha,\mathcal{N})\right)\\ =&\mathcal{P}(\mathcal{D}\mid\alpha,\mathcal{N})\left[-E_w(\{w_j\}_{\mathrm{MP}})-\frac{1}{2}\sum_{i=1}^{W}\frac{1}{\lambda_i+\alpha}+\frac{W}{2\alpha}\right],\end{aligned} \tag{5.30}$$

to find the relation

$$2\alpha_{\mathrm{MP}}\,E_w(\{w_j\}_{\mathrm{MP}}) = W-\alpha\,\mathrm{Tr}\left(\mathbf{A}^{-1}\right)=\sum_{i=1}^{W}\frac{\lambda_i}{\lambda_i+\alpha_{\mathrm{MP}}}\equiv\gamma\,, \tag{5.31}$$

where we have used that the eigenvalues of $\mathbf{A}^{-1}$ are $(\lambda_i+\alpha)^{-1}$. This result tacitly assumes that the eigenvalues λ_i do not themselves depend on α. Furthermore, only for a quadratic function of the weights is this relation exact. Otherwise it is an approximation that omits terms proportional $\partial\lambda_i/\partial\alpha$ (see Ref. [103]). The terms in the left part of Eq. (5.31) measure how much the fitted parameters differ from their null value. The rank of values for γ is from 0 to W. This parameter measures the effective number of weights, whose values are controlled by the data [83]. Equation 5.31 to get the proper α_{MP} is solved iteratively during the training process, *i.e.*

$$\alpha_{k+1}=\frac{\gamma(\alpha_k)}{2E_w(\{w_j\})}\,, \tag{5.32}$$

where k is the order of iteration. The iteration procedure fixes in the optimal way the α parameter. In Ref. [28] it is shown that the choice of the initial α value has a small impact on the final results.

Having found the value of α which minimizes the evidence, we can construct a Gaussian approximation for the evidence $\mathcal{P}(\mathcal{D}\mid\ln\alpha,\mathcal{N})$, as a function of $\ln\alpha$, centered on this maximum value [28, 83, 102]. The choice of $\ln\alpha$ as the new variable to perform the minimization has two advantages: it ensures that α remains positive and discourages pathological solutions with $\alpha\to 0$. Performing a power expansion of $\ln\left(\mathcal{P}(\mathcal{D}\mid\ln\alpha,\mathcal{N})\right)$ around $\ln\alpha_{\mathrm{MP}}$, we obtain

$$\begin{aligned}\ln\left(\mathcal{P}(\mathcal{D}\mid\ln\alpha,\mathcal{N})\right)\simeq&\ln\left(\mathcal{P}(\mathcal{D}\mid\ln\alpha_{\mathrm{MP}},\mathcal{N})\right)\\ &+\frac{1}{2}\,\frac{\partial^2}{\partial\left(\ln\alpha\right)^2}\ln\left(\mathcal{P}(\mathcal{D}\mid\ln\alpha,\mathcal{N})\right)\Big|_{\ln\alpha=\ln\alpha_{\mathrm{MP}}}\\ &\times\left(\ln\alpha-\ln\alpha_{\mathrm{MP}}\right)^2\,.\end{aligned} \tag{5.33}$$

From Eq. (5.33) it follows that

$$\mathcal{P}(\mathcal{D} \mid \ln \alpha, \mathcal{N}) = \mathcal{P}(\mathcal{D} \mid \ln \alpha_{\text{MP}}, \mathcal{N}) e^{-\frac{(\ln \alpha - \ln \alpha_{\text{MP}})^2}{2\sigma^2_{\ln \alpha}}} . \tag{5.34}$$

with

$$\frac{1}{\sigma^2_{\ln \alpha}} = -\alpha \frac{\partial}{\partial \alpha} \left(\alpha \frac{\partial}{\partial \alpha} \ln \left(\mathcal{P}(\mathcal{D} \mid \ln \alpha, \mathcal{N}) \right) \right) . \tag{5.35}$$

Substituting Eq. (5.28) in Eq. (5.35), we find that

$$\frac{1}{\sigma^2_{\ln \alpha}} = \alpha \, E_w(\{w_j\}_{\text{MP}}) + \frac{1}{2} \sum_{i=1}^{W} \frac{\alpha \, \lambda_i}{(\alpha + \lambda_i)^2} , \tag{5.36}$$

and using Eq. (5.31)

$$\frac{1}{\sigma^2_{\ln \alpha}} = \frac{\gamma}{2} + \frac{1}{2} \sum_{i=1}^{W} \frac{\alpha \, \lambda_i}{(\alpha + \lambda_i)^2} . \tag{5.37}$$

If $\lambda_i \ll \alpha$ the terms in the sum reduce to $\lambda_i/\alpha \ll 1$, while if $\lambda_i \gg \alpha$ they reduce to $\alpha/\lambda_i \ll 1$. Significant contributions arise only if $\lambda_i \simeq \alpha$. Since there will typically be few such eigenvalues, we see that the second term in Eq. (5.37) can be neglected. Therefore, following Ref. [83] we adopt

$$\frac{1}{\sigma^2_{\ln \alpha}} = \frac{\gamma}{2} . \tag{5.38}$$

With the approximation of Eq. (5.33), we then obtain

$$\begin{aligned} \mathcal{P}(\mathcal{D} \mid \alpha, \mathcal{N}) = & \frac{1}{N_L} e^{-\chi^2(\{w_j\}_{\text{MP}}) - \alpha_{\text{MP}} E_w(\{w_j\}_{\text{MP}}) - \frac{1}{2} \ln |\mathbf{A}| + \frac{W}{2} \ln(\alpha_{\text{MP}})} \\ & \times e^{-\frac{(\ln \alpha - \ln \alpha_{\text{MP}})^2}{2\sigma^2_{\ln \alpha}}} . \end{aligned} \tag{5.39}$$

We substitute now Eq. (5.39) in Eq. (5.24). At this point we need to define a prior, $\mathcal{P}(\alpha \mid \mathcal{N})$, in order to perform the integral. As we do not have information about the value of α, we should choose a prior which in some sense gives the same weights to all possible values. Such priors are called *non-informative* and often have the characteristic that they cannot be normalized since the integral of the prior diverges, in this case they are called *improper*. For scale parameters as our regularizer, α, this kind of priors are generally chosen to be uniform on a logarithmic scale. Further discussion on this topic

can be found in Ref. [83]. Hence, the prior $\mathcal{P}(\alpha \mid \mathcal{N})$ should be expressed in logarithmic scale. Thus, we can choose an improper prior of the form $\mathcal{P}(\ln \alpha \mid \mathcal{N}) = 1$, which imply

$$\mathcal{P}(\alpha \mid \mathcal{N}) = \frac{1}{\alpha} \,. \tag{5.40}$$

The integral over α in Eq. (5.24) leads to an analytic result

$$\mathcal{P}(\mathcal{D} \mid \mathcal{N}) = \frac{\sqrt{2\pi}\sigma_{\ln \alpha}}{N_L} e^{-\chi^2(\{w_j\}_{\mathrm{MP}}) - \alpha_{\mathrm{MP}} E_w(\{w_j\}_{\mathrm{MP}}) - \frac{1}{2}\ln|\mathbf{A}| + \frac{W}{2}\ln(\alpha_{\mathrm{MP}})} \,. \tag{5.41}$$

Taking logarithms we can write

$$\begin{aligned} \ln\left(\mathcal{P}(\mathcal{D} \mid \mathcal{N})\right) = & -\chi^2\left(\{w_j\}_{\mathrm{MP}}\right) - \alpha_{\mathrm{MP}} E_w(\{w_j\}_{\mathrm{MP}}) - \frac{1}{2}\ln|\mathbf{A}| \\ & + \frac{W}{2}\ln\left(\alpha_{\mathrm{MP}}\right) + \frac{1}{2}\ln\left(2\pi\right) + \frac{1}{2}\ln\left(\sigma^2_{\ln \alpha}\right) - \ln\left(N_L\right) \,. \end{aligned} \tag{5.42}$$

On the other hand, we should keep in mind that the models are neural networks with a hidden layer containing M units, given by Eq. (5.6). Each unit has a sigmoid, Eq. (5.3), as activation function. By the symmetry of these kind of activation functions, it can be shown that for M hidden units any given weight vector will be one of a set 2^M equivalent weight vectors. This is proved in Ref.[83] from the results of Ref. [106] with activation functions of the kind $f(x) = \tanh(x)$. In Ref. [107], it is shown that these results can be generalized to the sigmoid functions used in our calculations, Eq. (5.3).

We have a set of weights and a bias corresponding to each unit in the hidden layer of the neural network. As all units have the same activation function, there would not be any change in the final output after the interchange of the sets of values for two of these units. Given this symmetry, for M hidden units, any given weight vector will have $M!$ equivalent weight vectors, corresponding to the different orderings of the hidden units [83, 106]. The network will therefore have an overall weight-space symmetry factor of $M!\,2^M$, thus we must include this extra factor in Eq. (5.42). Finally, omitting normalization factors common to all models, the logarithm of the

evidence reads

$$\ln\left(\mathcal{P}(\mathcal{D}\mid\mathcal{N})\right) \approx -\chi^2\left(\{w_j\}_{\rm MP}\right) - \alpha_{\rm MP}\, E_w(\{w_j\}_{\rm MP}) \tag{5.43}$$

$$- \frac{1}{2}\ln|\mathbf{A}| + \frac{W}{2}\ln\left(\alpha_{\rm MP}\right) - \frac{1}{2}\ln\frac{\gamma(\alpha_{MP})}{2}$$

$$+ \ln\left(M!\right) + M\ln\left(2\right)\ , \tag{5.44}$$

where Eq. (5.38) has been used.

The evidence contains two contributions: Occam's factor [Eq. (5.44) plus the $\alpha_{\rm MP}E_w$ term of Eq. (5.43)], which is large for models with many parameters and the misfit [χ^2 term in Eq. (5.43)], which could be large if the model is too simple. Therefore, the model which maximizes the evidence is the one which solves the bias-variance dilemma. As an illustration from the present analysis (details can be found in the following section), in Fig. 5.4 we plot the values of the error,

$$\mathcal{E} = \chi^2 + \alpha E_w, \tag{5.45}$$

and the evidence for MLP fits. The best model with the highest evidence is not the one which has the smallest value of the error function $\mathcal{E}$, in variance with more conventional approaches based on the minimization of the χ^2 per degree of freedom.

5.4 Analysis of ANL neutrino-deuteron scattering data

5.4.1 Theoretical framework

The neutrino-induced CCQE,

$$\nu_\mu(k) + n(p) \to \mu^-(k') + p(p')\ , \tag{5.46}$$

differential cross section, in terms of the standard Mandelstam variables $s = (k+p)^2$, $u = (p-k')^2$, and $t = (k-k')^2 = -Q^2$, can be cast as [108]

$$\frac{d\sigma}{dQ^2} = \frac{G_F^2 m_N^2}{8\pi E_\nu^2}\left[A(Q^2) + B(Q^2)\frac{(s-u)}{m_N^2} + C(Q^2)\frac{(s-u)^2}{m_N^4}\right]\ , \tag{5.47}$$

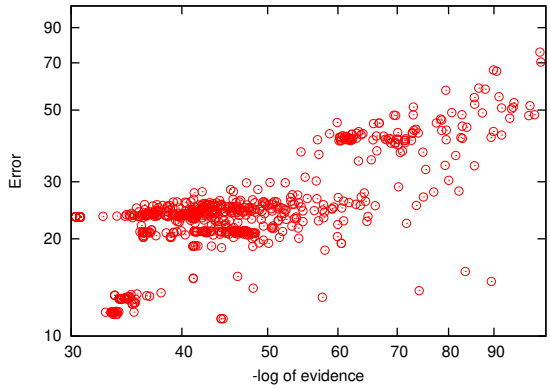

Figure 5.4: The error Eq. (5.45) as a function of the logarithm of the evidence Eqs. ((5.43) and 5.44). Each point denotes the result obtained for one MLP fit to the BIN1 data, including deuteron corrections (see Sec. 5.4 for details). The fits with a logarithm of the evidence smaller than -100 are not shown in the figure.

where

$$
\begin{aligned}
A &= \frac{(m^2+Q^2)}{M^2}\left[(1+\eta)\,F_A^2-(1-\eta)\,F_1^2+\eta\,(1-\eta)\,F_2^2+4\eta F_1F_2\right.\\
&\quad\left.-\frac{m^2}{4M^2}\left((F_1+F_2)^2+(F_A+2F_P)^2-\left(\frac{Q^2}{M^2}+4\right)F_P^2\right)\right]\,,\\
B &= \frac{Q^2}{M^2}F_A(F_1+F_2)\,,\\
C &= \frac{1}{4}\left(F_A^2+F_1^2+\eta F_2^2\right)\,,
\end{aligned}
\tag{5.48}
$$

in terms of the nucleon FF and $\eta = Q^2/(4M^2)$.[8] In the present chapter we have taken these electromagnetic FFs from Refs. [49, 69]. With this simple choice we disregard deviations from the dipole shape because the accuracy of the neutrino-deuteron data is insufficient to be sensitive to them, particularly at the rather low $Q^2 \lesssim 1$ GeV^2 probed in the ANL experiment.

Deuterium-filled bubble-chamber experiments actually measured $\nu_\mu + d \to \mu^- + p + p$. The cross section for this process differs from the one on free

[8] See Chapter 3 for complete description of FF.

neutrons due to the momentum distribution of the neutron in the nucleus, Pauli principle, final-state interactions, and meson-exchange currents. In the literature, it has been commonly assumed that Eq. (5.47) can be corrected for these effects by a multiplicative function of Q^2 alone $R(Q^2)$ and such that $R \to 1$ at large Q^2. For the present calculation, we adopt $R(Q^2)$ from the Ref. [109], Fig. 5.5.

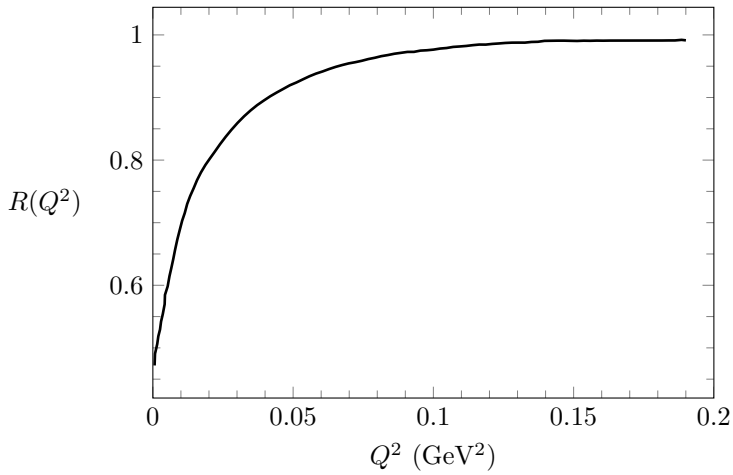

Figure 5.5: Estimation of the deuteron correction effect on the differential cross section, including meson exchange currents, at $E_\nu = 1$ GeV, Ref. [109].

5.4.2 χ^2 function for the ANL experiment

In the ANL experiment, the interactions of muon neutrinos in a 12-ft bubble chamber filled with liquid deuterium were studied, Refs. [9–11, 110]. The neutrino flux peaked at $E_\nu \sim 0.5$ GeV and has fallen by an order of magnitude at $E_\nu = 2$ GeV, Refs. [10, 11]. For the statistical analysis, we consider the Q^2 distribution of CCQE events. Some of the originally published bins were combined together to have a number of events larger than five in every bin. Therefore, the number of bins is $n_{\text{ANL}} = 25$, where bins from 1 to 23 have a width of 0.05 GeV^2, whereas bins 24 and 25 have widths of 0.65 GeV^2. The total number of measured two- and three-prong events adds to $N_{\text{ANL}} = 1792$, Ref. [11]. One-prong events were not included in the ANL selection. To account for their loss, the region of $Q^2 = 0.05$ GeV^2 was excluded.

The predicted number of events in each bin is calculated similarly as in

Ref. [17],

$$N_i^{th} = p \int_0^\infty dE_\nu \frac{\frac{d\sigma}{dQ^2}(E_\nu, F_A, Q_i^2)}{\sigma(E_\nu, F_A)} \frac{dN}{dE_\nu}\,, \tag{5.49}$$

where $p(dN/dE_\nu)/\sigma(E_\nu, F_A)$ is the neutrino energy flux, given in terms of the experimental energy distribution of observed events dN/dE_ν taken from Ref. [110].

As stated in the previous section, the likelihood, Eq. (5.16), is built using the χ^2 function, which we cast as

$$\chi^2 = \chi^2_{\rm ANL} + \chi^2_{g_A}, \tag{5.50}$$

where $\chi^2_{g_A}$ is introduced to constrain the value of the axial FF at $Q^2 = 0$,

$$\chi^2_{g_A} = \left(\frac{F_A(0) - g_A}{\Delta g_A}\right)^2; \tag{5.51}$$

g_A and Δg_A are fixed by the present PDG central value and its uncertainty, respectively, Eq. (3.55). For $\chi^2_{\rm ANL}$, we take

$$\chi^2_{\rm ANL} = \sum_{i=k}^{n_{\rm ANL}} \frac{\left(N_i - N_i^{th}\right)^2}{N_i} + \left(\frac{1-p}{\Delta p}\right)^2, \tag{5.52}$$

where N_i denotes the number of events in the bin. The last term takes into account the systematic uncertainty in the total number of events, inherited from the flux-normalization uncertainty, Ref. [111]. Similarly as in the analysis of single pion production data of Ref. [112], it is assumed that $\Delta p = 0.20$.[9] At the beginning of the analysis, $p = 1$ is set. Then, during the training of the network, p is iteratively updated. This algorithm is described in Ref. [86].

It is known that the low-Q^2 data are characterized by a lower efficiency (see, for instance, Fig. 1 of Ref. [11]). Moreover, in this kinematic domain deuteron structure corrections must be carefully discussed. In order to study this problem we consider three variants of the ANL data:

(i) $\chi^2_{\rm ANL} \to \chi^2_{\rm BIN0}$: All ANL bins included;

(ii) $\chi^2_{\rm ANL} \to \chi^2_{{\rm BIN}k}$: where $k = 1$ or $k = 2$: ANL bins without the first k bins.

Additionally, for each data set, we consider the cross-section model both with and without $[R(Q^2) \equiv 1]$ deuteron corrections.

[9] This is a more conservative value of the flux-normalization uncertainty than the ANL estimate of 15% [11].

5.4.3 Numerical algorithm

We consider a MLP with $M = 1 - 4$ hidden units in a single hidden layer. For $M > 4$, the number of parameters in the fit starts to be comparable with number of bins. The numerical algorithm for getting the optimal fit is summarized by the following list of steps:

(i) Consider a MLP with a fixed number of hidden units $M = 1$;

(ii) using the Bayesian learning algorithm, perform the network training and find the optimal values for the weights and the regularizer α;

- set the initial value of $\alpha \equiv \alpha_0 = 0.001$;
- initialize randomly the values of the weights;
- perform training until the maximum of the posterior is reached; at each iteration step update the values of weights and α.

(iii) Calculate the evidence for each of the obtained MLP fits;

(iv) repeat steps (i) (iii) for various initial configurations of $\{w_j\}$;

(v) among all registered fits choose the best one according to the evidence;

(vi) repeat steps (i) (iv) for $M = 2 - 4$;

(vii) among the best fits, obtained for $\mathcal{N}_{1-4}$ MLPs, choose the model with the highest evidence.

The optimal configuration of parameters is obtained using the Levenberg-Marquardt algorithm, described in Refs. [113, 114].

5.5 Numerical results

The analysis of the BIN0, BIN1, and BIN2 data sets has been independently performed. For each set, both cross-section models with and without deuteron corrections have been studied. For the default analyses, Δg_A has been taken from the PDG as in Eq. (3.55), but the impact of a larger uncertainty $\Delta g_A/g_A = 10\%$ has been investigated and is discussed below. We have also performed analyses with normalization uncertainties smaller ($\Delta p = 0.10$) and larger ($\Delta p = 0.30$) than the default $\Delta p = 0.20$, but it turned out that decreasing or increasing Δp does not significantly affect the final results. All in all, about 17000 fits have been collected. Among them,

for each type of analysis, the best model has been chosen according to the objective Bayesian criterion described in Sec. 5.3.

In order to compare quantitatively different analyses, one needs to take into account the relative data normalization $\mathcal{P}(\mathcal{D})$. This density is not evaluated within the adopted approach. Hence, we can not quantitatively compare the results of, *e.g.*, BIN0 and BIN1 analyses. Nonetheless, for a given data set, quantitative comparisons between the results obtained with the two versions of the cross-section model can be made.

As described in Sec. 5.4.3 for each type of analysis (data set plus cross section model), to find the optimal fit, MLPs with: $M = 1, 2, 3$ and 4, hidden units have been trained. The best model within each MLP type is the one with the maximal value of the evidence, Eqs. (5.43 and 5.44).

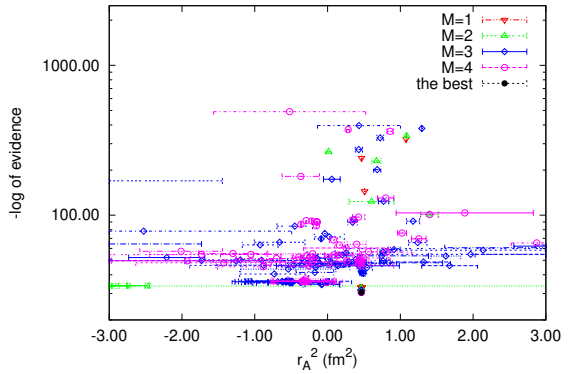

Figure 5.6: The dependence of r_A^2, defined in Eq. (5.1), on the logarithm of the evidence, Eqs. (5.43 and 5.44). Results for the MLP fits to BIN1 data (without the deuteron correction). The MLPs consist of $M = 1 - 4$ hidden units.

In order to illustrate the performance of the training algorithm, in Fig. 5.6 we present the dependence of the resulting axial-radius squared, r_A^2, values on the evidence for the BIN1 data set. The best fit with the highest evidence, obtained with $M = 4$, gives $r_A^2 \approx 0.464$ fm^2.

Note that all the best models within each MLP type reproduce well the ANL data. This is illustrated in Fig. 5.7, which presents the distribution of the ANL events and the best fits.

Our main results, *i.e.*, the best fits to BIN0, BIN1, and BIN2 data for the model with and without the deuteron correction with Δg_A from Eq. (3.55)

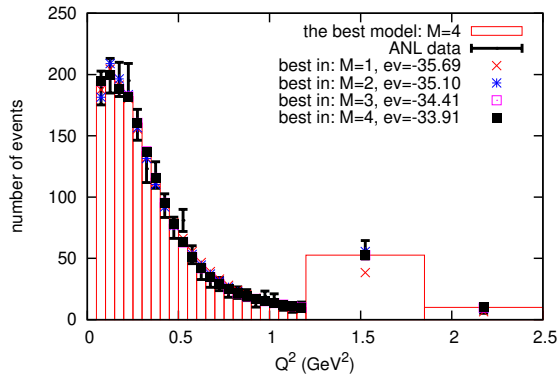

Figure 5.7: Distribution of the ANL number of events and the best fits obtained for MLPs with $M = 1 - 4$ hidden units. The figure shows the results of the analysis of BIN0 data (deuteron corrections included). For each fit, the value of the logarithm of evidence (ev) is given.

are summarized in Table 5.1. The corresponding $F_A(Q^2)$ functions and their error bands are shown in Fig. 5.8.

Deuteron	M	$\ln \mathcal{P}(\mathcal{D}, \mathcal{N})$	χ^2	p	$\mathcal{E}$	r_A^2 (fm^2)
BIN0						
No	4	-34.72	11.97	1.1	14.14	-0.394 ± 0.278
Yes	4	-33.91	11.73	1.08	13.95	-0.161 ± 0.240
BIN1						
No	4	-30.57	24.84	1.16	25.41	0.464 ± 0.014
Yes	3	-29.6	22.90	1.12	23.43	0.471 ± 0.015
BIN2						
No	2	-30.15	22.62	1.18	23.16	0.476 ± 0.017
Yes	4	-27.67	21.94	1.13	22.62	0.478 ± 0.017

Table 5.1: The best MLP fits, obtained for the analysis of the BIN0, BIN1 and BIN2 data with and without deuteron corrections; Δg_A is taken from Eq. (3.55).

Both fits for the BIN0 data set, which contains all the data from the original ANL measurement, with and without deuteron corrections show a Q^2 behavior of F_A with a rapid increase followed by a decrease after a local

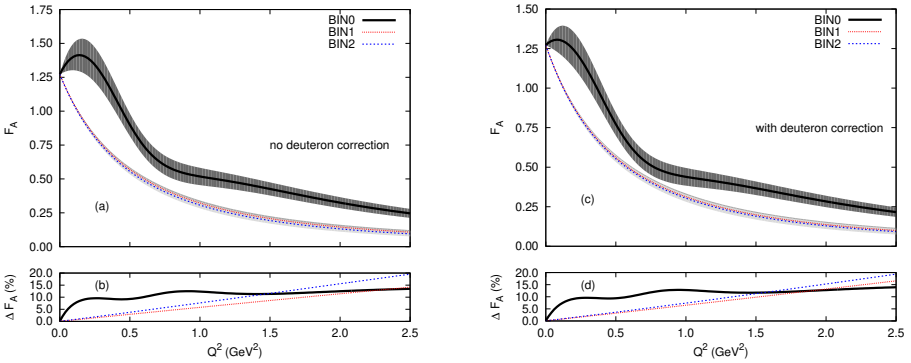

Figure 5.8: Best fits of the axial form factor obtained from the analysis of the BIN0, BIN1 and BIN2 data sets. The top (bottom) panel presents the results obtained without (with) deuteron corrections. The shaded areas denote 1σ uncertainties. Additionally, the relative uncertainty $\Delta F_A/F_A$ is plotted.

maximum. As a result, r_A^2 has a negative sign,[10] which is at odds with all available determinations. We also observe that the Q^2 dependence of the FF disagrees with the one obtained from the same data set using the z expansion {the coefficients from the ANL fit are given in Eq. (19) of Ref. [17]}. We have obtained the z expansion coefficients for the BIN0 best fit, finding that their values grow with the expansion order to values that are too large compared to phenomenological expectations, Ref. [79]. This is an indication that the fit that best represents BIN0 data is inconsistent with the QCD assumptions implicit in the z expansion.

The height of the F_A maximum is reduced once the deuteron correction is included in the analysis, and it disappears when the first bin is removed from the ANL data (BIN1 data set).[11] Hence, the presence of the local maximum of F_A appears to be caused by low-Q^2 effects. Furthermore, the coefficients of the z expansion for the fits to BIN1 and BIN2 data sets are fully consistent with the expectations from QCD.

There are several possible sources of this unexpected behavior of the fits to the BIN0 set, namely, (i) an improper description of the nuclear corrections; (ii) a low quality of the measurements at low-Q^2 due to low and

[10] Although the large uncertainty does not exclude positive values.

[11] It is worth mentioning that fits with a negative slope of F_A at low Q^2, resembling the best result for BIN0 data, have also been obtained in this case, but they are not preferred by the Bayesian algorithm.

not well understood efficiency; (iii) constraints coming from the uncertainty of g_A; (iv) because of the lack of very low-Q^2 data, the actual value of r_A^2 might not be properly estimated: For instance, if F_A has first a local minimum and then a local maximum.[12] In the later scenario, the ANL data (and the available bubble-chamber data, in general) are not precise enough to reveal this behavior.

In the low-Q^2 kinematic domain, deuteron effects are sizable and may play a crucial role. On the other hand the inclusion of deuteron corrections in the analysis of the BIN1 and BIN2 data sets has a minor impact on the functional dependence of the final results, *i.e.*, there is small difference between $F_A(Q^2)$ obtained with and without deuteron corrections as can be seen in Fig. 5.9. It is also interesting to highlight that the inclusion of the deuteron-structure corrections in the cross-section model increases the value of the evidence for each type of the analysis, see Table 5.1.

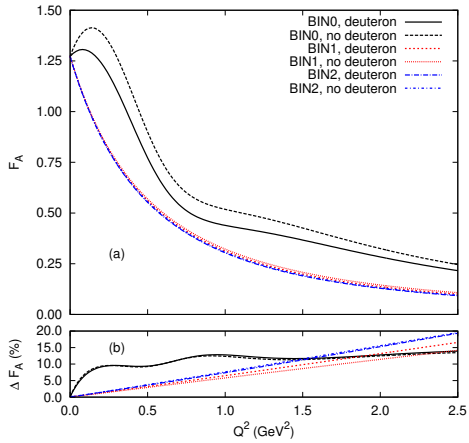

Figure 5.9: Impact of the deuteron corrections on the axial form factor fits. Results of the best fits to the BIN0, BIN1, and BIN2 data sets with and without the deuteron correction together with relative uncertainties. All curves for the BIN1 and BIN2 cases nearly overlap.

In Fig. 5.10, we plot values of r_A^2 against the evidence. It is clearly seen that the fits including deuteron corrections are favored by the ANL data. The impact of the sensitivity of the results on the deuteron structure revealed in the present chapter calls for a more accurate account of this ingredient

[12] The magnetic FFs of the nucleon at very low-Q^2 (about 0.01 GeV^2) when normalized to a dipole have an oscillatory Q^2 dependence, Ref.[28].

of the cross section models, beyond the $R(Q^2)$ function from Ref. [109] employed so far. Recent studies of CC νd scattering in the QE regime (without pions in the final state) include the non-relativistic calculation of the inclusive cross section, incorporating two-body amplitudes, of Ref. [115]. For the kinematics of the ANL and other bubble-chamber experiments, it is important to employ a relativistic framework as in Ref. [116]. Furthermore, the consideration of the semi-inclusive rather than the inclusive cross section will allow taking into account the detection threshold for outgoing protons, which, in the ANL case, is 100 MeV, Ref. [10]. One should nonetheless bear in mind that even with the best model for the deuteron there is no guarantee that the low-Q^2 region is successfully described because of the difficulties in the measurement and with efficiency estimates at this kinematics.

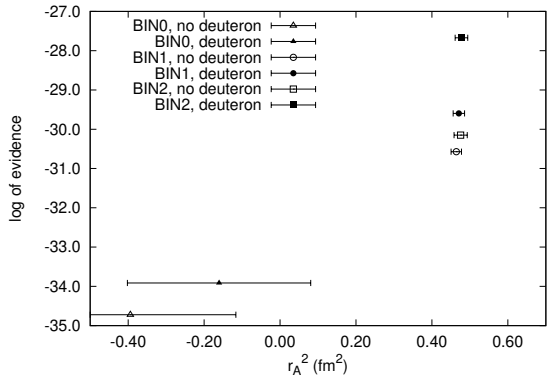

Figure 5.10: Dependence of r_A^2 on the evidence. Open and full triangles denote (the best) fits to the BIN0 data without and with the deuteron corrections, respectively. Analogously, the fits to the BIN1 and BIN2 data are denoted by circles and squares, respectively.

The impact of Δg_A on the results can be easily investigated. Indeed if one increases the Δg_A uncertainty from $\Delta g_A/g_A \approx 0.1\%$, as in Eq. (3.55) to 10%, then the local maximum of F_A disappears. However, the fit uncertainty rapidly grows from $\Delta F_A/F_A$ lower than 0.01% to $\Delta F_A/F_A \approx 7\%$ at $Q^2 = 0$. This analysis is shown in Fig. 5.11.

In order to compare the Bayesian neural-network results with the traditional approach, we have performed a conventional analysis of the ANL data assuming the dipole parametrization for the axial FF Eq. (3.54). The best

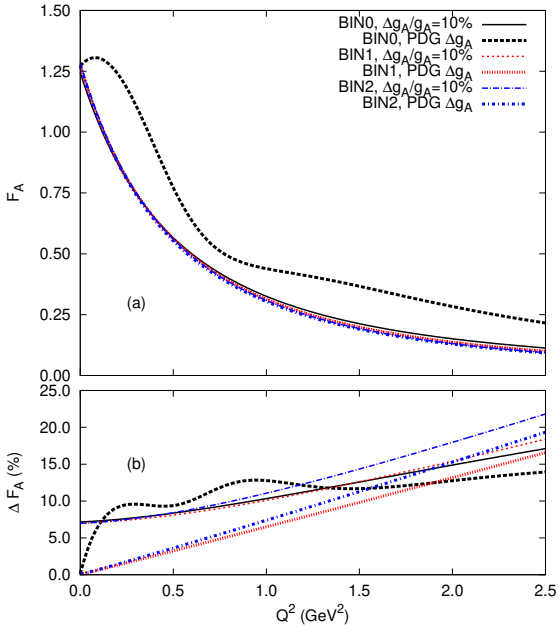

Figure 5.11: Impact of the Δg_A uncertainty on the extraction of the axial form factor. The best fits to BIN0, BIN1 and BIN2 data (with deuteron correction). The thin lines denote results obtained assuming a 10% uncertainty for g_A, whereas the thick lines denote fits with the PDG uncertainty.

fit minimizes the $\chi^2_{\rm ANL}$ function, Eq. (5.52).[13] These results are summarized in Table 5.2, whereas the comparison between dipole fits and neural-network analyses are displayed in Fig. 5.12.

Let us stress that the r_A^2 and normalization parameter p for the fits of BIN0 data are comparable to the z expansion results, Ref. [17], even though in the latter case, a different error function was utilized. Certainly, with a dipole fit to BIN0 data one can not obtain the local maximum of F_A at low Q^2. On the other hand, the dipole fits to the BIN1 and the BIN2 data have very similar functional Q^2 dependence as the best MLP fits. For these data sets, the evidence, which contains Occam's factor penalizing overfitting parametrizations with large error bars, establishes the preference for a rather structureless neural network that departs very little from the normal-

[13]For these analyses, the MINUIT package of ROOT has been utilized.

χ^2 analyses				
	χ^2	p	M_A (MeV)	r_A^2 (fm^2)
BIN0				
No deuteron	33.3	1.12 ± 0.03	1110 ± 60	0.38 ± 0.04
Deuteron	28.0	1.09 ± 0.03	1050 ± 60	0.43 ± 0.05
BIN1				
	χ^2	p	M_A (MeV)	r_A^2 (fm^2)
No deuteron	24.4	1.17 ± 0.03	1000 ± 70	0.47 ± 0.07
Deuteron	22.3	1.13 ± 0.03	950 ± 70	0.52 ± 0.08
BIN2				
	χ^2	p	M_A (MeV)	r_A^2 (fm^2)
No deuteron	20.8	1.22 ± 0.05	890 ± 100	0.59 ± 0.13
Deuteron	19.8	1.18 ± 0.05	850 ± 110	0.65 ± 0.16

Table 5.2: Fits of the dipole axial form factor, Eq. (3.54), to the BIN0, BIN1 and BIN2 data sets.

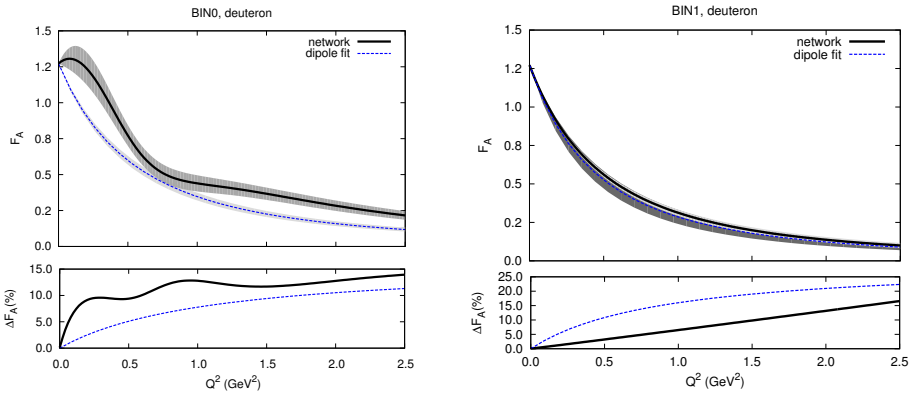

Figure 5.12: Comparison of the dipole with the neural network fits to the BIN0 and BIN1 data, the deuteron corrections included. The shaded areas denote 1σ uncertainties of F_A.

ization values, given by Eq. (3.54) with $M_A = 1$ GeV, and has small errors. Furthermore, the uncertainties in the neural-network fits are systematically smaller than in the dipole χ^2 ones. In Appendix. E are given the explicit

numerical results for the BIN0 and BIN1 fits, as well as the correspondent covariance matrices.

5.6 Summary

The first Bayesian neural-network analysis of the neutrino-deuteron scattering data has been performed. The reported study has been oriented to the extraction of the axial FF from the ANL CCQE data, searching for deviations from the dipole form. With the full ANL data set, the analysis leads to an axial FF which has a positive slope at $Q^2 = 0$ and a local maximum at low Q^2. The inclusion of the deuteron correction reduces the peak in F_A. Only after removing the lowest available Q^2 region ($0.05 < Q^2 < 0.10$ GeV^2) from the data, a value of the axial radius consistent with available determinations could be obtained. This suggests that corrections from the deuteron structure play a crucial role at low Q^2 but it could also be the case that the experimental errors in this kinematic region were underestimated. Analyses without the low-Q^2 data do not show any significant deviation from previous determinations. Furthermore, our neural-network fits are characterized by smaller uncertainties than the dipole ones.

New more precise measurements of the neutrino cross sections on hydrogen and deuterium are needed to unravel the axial structure of the nucleon. Techniques, such as the one applied in the present chapter will prove valuable in such a scenario.

Chapter 6

Weak Kaon Production off the nucleon and Watson's theorem

6.1 Introduction

When pursuing the goal of reducing systematic uncertainties in oscillation experiments, much attention has been paid to quasi-elastic scattering and weak pion production. On the other hand, with better statistics and higher precision goals, other, largely unexplored, processes with smaller cross sections may play a significant role. Kaon and strangeness production in general belongs to this category.

The charged-kaon production ($\nu_\mu \mathrm{CH} \rightarrow \mu^- K^+ X$) measurement at MINER$\nu$A [29] experiment opens a new window to study the weak strangeness production mechanisms in detail. The weak processes that could lead to kaons in the final state are either initiated by strangeness conserving ($\Delta S = 0$) or strangeness changing ($\Delta S = 1$) mechanisms. Although the $\Delta S = 1$ reactions ($1K$) are Cabibbo suppressed compared to $\Delta S = 0$ ones (YK), the latter involve the production of massive strange hyperons (Y), which pushes the reaction thresholds higher in neutrino energies. Therefore, below 2 GeV of incoming neutrino energies, the $1K$ reaction is favoured [29, 30]. In nuclei, final state interactions of the produced kaon are not very strong because of the absence of baryon resonances. However, kaons can also be produced in secondary collisions, rendering the extraction of information about the elementary $1K$-production amplitudes in experiments with nuclear targets rather difficult [117].

Theoretical work on weak production of meson-baryon pairs with open and hidden strangeness was performed in the early days of neutrino

physics [118–121], and resumed only recently with studies in the $\Delta S = 0$ [122, 123], $\Delta S = -1$ [124, 125] and $\Delta S = 1$ [30] sectors. The first calculation of the $\nu_l N \to l^- K N'$ amplitudes using leading-order SU(3) ChPT was performed by Alam et. al. [30]. The threshold cross section was predicted in a model independent way in terms of only three precisely-known quantities f_π, D and F. To extend the validity of the study to higher energies, the hadronic currents were multiplied by a phenomenological global dipole FF. However, as it is based on tree-level diagrams, this model neither respects the unitarity of the S matrix, nor it satisfies the related Watson's theorem [126],[1] according to which, the phase of the amplitude is determined by the strong meson-baryon interaction (KN in this case).

In this chapter, we address this issue and partially restore unitarity, by imposing Watson's theorem. This is achieved by introducing relative phases in the amplitudes derived in Ref. [30], as suggested by Olsson in [127] for pion photoproduction. In Refs. [31, 128], the same strategy has been successfully applied to the weak pion production model of Ref. [129].

In the next sections we present the model for $\Delta S = 1$ K-production, derive Watson's theorem and present Watson's prescription to approximately restore unitarity. Then, we discuss the impact of this improvement on observable quantities.

6.2 Single kaon production model

The allowed neutrino-induced $\Delta S = 1$ single-kaon production reaction channels on nucleons are

$$\begin{aligned} \nu_l + p &\to l^- + p + K^+ \,, \\ \nu_l + n &\to l^- + p + K^0 \,, \\ \nu_l + n &\to l^- + n + K^+ \,. \end{aligned} \tag{6.1}$$

The differential cross section for the processes of Eq. (6.1) is given by

$$\frac{d\sigma}{dW\, dQ^2 d\Omega_K^*} = \frac{|\vec{p}_K^{\,*}|}{64(2\pi)^4 E_\nu^2 M_{\rm N}^2} |\overline{\mathcal{M}}|^2 \,, \tag{6.2}$$

in terms of the squared modulus of the amplitude of the interaction.[2] $W = \sqrt{s}$ is the invariant mass of the outgoing kaon-nucleon pair. As in previous chapters, $Q^2 = -q^2$ stands for minus the square of the four momentum

[1] A consequence of unitarity of $S-$matrix and time reversal symmetry.

[2] The cross section expression can be obtained from Eq.(3.8), for the specific case of three outgoing particles.

transfer $q = k - k'$, with k and k' the four momenta of the incoming neutrino and outgoing lepton respectively. We fix the lepton kinematics and target nucleon the Laboratory frame, in which E_ν denotes the incoming neutrino energy ($E_\nu = k^0$). The outgoing KN system is treated in the rest frame of the pair, referred as the hadronic center-of-mass (HCM) frame. We represent HCM quantities with a '$*$' superscript. In Eq. 6.2, the kaon momentum ($\vec{p}^{\,*}_K$) and solid-angle (Ω^*_K) are indeed in the HCM frame.

Given the coupling of CC interactions, Eq. (2.2), and the $W^\pm$ boson propagator,

$$D_{\mu\nu} = \frac{-g_{\mu\nu} + q_\mu q_\nu / M_W^2}{q^2 - M_W^2} \simeq \frac{g_{\mu\nu}}{M_W^2} \,, \tag{6.3}$$

for the squared modulus of the amplitude, Eq. (3.5), we have

$$|\overline{\mathcal{M}}|^2 = \frac{1}{2} G_F^2 |V_{us}|^2 L^{\mu\nu} H_{\mu\nu} \,, \tag{6.4}$$

where $L^{\mu\nu}$ ($H_{\mu\nu}$) is the leptonic (hadronic) tensor. The numerical values of the Fermi coupling constant (G_F) and the CKM matrix element, $|V_{us}|$, are given in Appendix. A.3. The leptonic tensor may be written as,[3]

$$L_{\mu\nu} = 8 \left[k'_\mu \, k_\nu + k'_\nu \, k_\mu - g_{\mu\nu} (k' \cdot k) + i \epsilon^{\mu\nu\sigma\rho} k'_\sigma k_\rho \right] \,. \tag{6.5}$$

The tensor $H^{\mu\nu}$ can be expressed in terms of the $WN \to KN'$ hadronic current J^μ as

$$H^{\mu\nu} = \sum_{\text{spins}} J^\mu \, (J^\nu)^\dagger \,, \tag{6.6}$$

where the sum is performed over the spin projections of the incoming and outgoing nucleons.

The complete set of diagrams that contribute to J^μ for the processes in Eq. (6.1) are shown in Fig. 6.1. The hadronic current is obtained from the expansion of the SU(3) chiral Lagrangian at its lowest order, plus next-to-leading contributions to weak magnetism, described in Sec. 2.4. The

[3] Note that the leptonic tensor in these processes has the same functional form than the one presented in Eq. (4.45) of Chapter 4, in terms of the momenta of the incoming and outgoing leptons.

corresponding contributions to the hadronic current are

$$
\begin{aligned}
J^{\mu}\big|_{\mathrm{CT}} &= -\mathbb{i} A_{\mathrm{CT}} V_{us} \frac{\sqrt{2}}{2 f_{\pi}} \bar{N}(p')(\gamma^{\mu} + \gamma^{\mu}\gamma^{5} B_{\mathrm{CT}}) N(p) \,, \\
J^{\mu}\big|_{Cr\Sigma} &= \mathbb{i} A_{Cr\Sigma} V_{us} \frac{\sqrt{2}}{2 f_{\pi}} \bar{N}(p') \left(\gamma^{\mu} + \mathbb{i} \frac{\mu_p + 2\mu_n}{2 M_{\mathrm{N}}} \sigma^{\mu\nu} q_{\nu} \right. \\
&\quad \left. + (D - F)(\gamma^{\mu} - \frac{q^{\mu}}{q^2 - M_k^2} \not{q}) \gamma^5 \right) \frac{\not{p} - \not{p}_k + M_{\Sigma}}{(p - p_k)^2 - M_{\Sigma}^2} \not{p}_k \gamma^5 N(p) \,, \\
J^{\mu}\big|_{Cr\Lambda} &= \mathbb{i} A_{Cr\Lambda} V_{us} \frac{\sqrt{2}}{4 f_{\pi}} \bar{N}(p') \left(\gamma^{\mu} + \mathbb{i} \frac{\mu_p}{2 M_{\mathrm{N}}} \sigma^{\mu\nu} q_{\nu} \right. \\
&\quad \left. - \frac{D + 3F}{3} (\gamma^{\mu} - \frac{q^{\mu}}{q^2 - M_k^2} \not{q}) \gamma^5 \right) \frac{\not{p} - \not{p}_k + M_{\Lambda}}{(p - p_k)^2 - M_{\Lambda}^2} \not{p}_k \gamma^5 N(p) \,, \\
J^{\mu}\big|_{\mathrm{KP}} &= \mathbb{i} A_{\mathrm{KP}} V_{us} \frac{\sqrt{2}}{4 f_{\pi}} \bar{N}(p')(\not{q} + \not{p}_k) N(p) \frac{1}{q^2 - M_k^2} q^{\mu} \,, \\
J^{\mu}\big|_{\pi} &= \mathbb{i} A_{\pi P} V_{us} (D + F) \frac{\sqrt{2}}{2 f_{\pi}} \frac{M_{\mathrm{N}}}{(q - p_k)^2 - M_{\pi}^2} \bar{N}(p') \gamma^5 . (q^{\mu} - 2 {p_k}^{\mu}) N(p) \,, \\
J^{\mu}\big|_{\eta} &= \mathbb{i} A_{\eta P} V_{us} (D - 3F) \frac{\sqrt{2}}{2 f_{\pi}} \frac{M_{\mathrm{N}}}{(q - p_k)^2 - M_{\eta}^2} \bar{N}(p') \gamma^5 . (q^{\mu} - 2 {p_k}^{\mu}) N(p) \,.
\end{aligned}
\tag{6.7}
$$

The values of A_i, where i labels the corresponding diagram in Fig. 6.1, depend on the reaction channel and are listed in Table 6.1. Finally, to extend the kinematic range of the calculation, a global dipole FF has been introduced, with a dipole mass of 1 ± 0.1 GeV, accounting for the finite hadronic structure and its uncertainty.

Process	A_{CT}	B_{CT}	$A_{Cr\Sigma}$	$A_{Cr\Lambda}$	A_{KP}	$A_{\pi P}$	$A_{\eta P}$
$\nu n \to l K n$	1	$D - F$	$-(D - F)$	0	1	1	1
$\nu p \to l K p$	2	$-F$	$-(D - F)/2$	$(D + 3F)$	2	-1	1
$\nu n \to l K p$	1	$-D - F$	$(D - F)/2$	$(D + 3F)$	1	-2	0

Table 6.1: List of the hadronic current parameter values for each process [30].

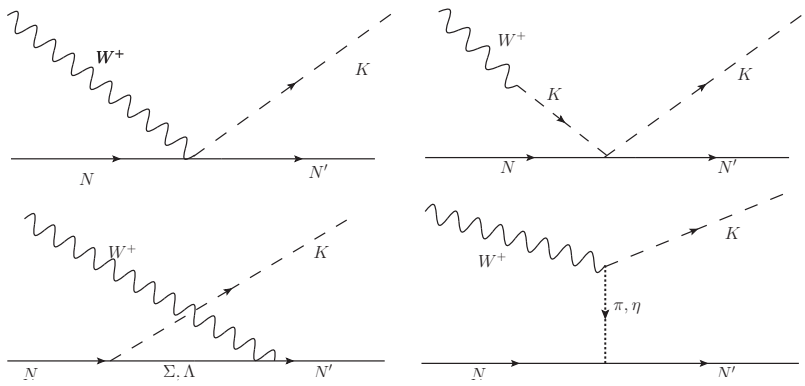

Figure 6.1: Feynman diagrams for the hadronic current $W^+N \to KN'$. From the upper left corner in clockwise order: contact (CT), kaon pole (KP), π and η in flight (πP, ηP) and u-channel hyperon exchange (CrΣ, CrΛ) terms.

6.3 Center of Mass two-particle helicity states

In preparation for our goal of imposing constrains from Watson's theorem on weak kaon production observables, we introduce the formalism of two-particle helicity states following closely Ref. [130]. In the first place we define the helicity state of a single particle. The state of such a particle, with mass m, momentum $\vec{p}$ and spin j, can be represented by

$$|m, j; \vec{p}, \lambda\rangle = R(\theta, \phi)\, Z_p\, |m, j; \vec{p} = 0, \lambda\rangle \ , \tag{6.8}$$

where Z_p is a boost along the positive direction of the z-axis and $p = |\vec{p}|$. The rotation $R(\theta, \phi)$ brings this axis into the direction of the momentum; it is defined as

$$R(\theta, \phi) \equiv R(\phi, \theta, -\phi) = e^{-\mathbb{i}\phi J_z} e^{-\mathbb{i}\theta J_y} e^{\mathbb{i}\phi J_z} \ , \tag{6.9}$$

in terms of the polar angles of $\vec{p}, (0 \leq \theta \leq \pi,\ 0 \leq \phi \leq 2\pi)$. The three dimensional rotation group generators are $J_i, i = 1, 2, 3$. The eigenvalue of J_3 is denoted by λ, the spin Then, λ is the component of spin along the z-direction in the rest frame of the particle. As λ is not affected neither by a Z_p boost nor by a rotation, it can be interpreted as the spin component along the direction of motion and, hence, the helicity of the particle. The normalization of the states is given by

$$\langle m, j; \vec{p}, \lambda \mid m, j; \vec{p}\,', \lambda'\rangle = (2\pi)^3\, 2E(\vec{p})\, \delta^{(3)}\left(\vec{p} - \vec{p}\,'\right) \delta_{\lambda\lambda'} \ , \tag{6.10}$$

with $E(\vec{p}) = \sqrt{m^2 + \vec{p}^2}$.

The state of two non-interacting particles can be cast as

$$|m_1, j_1; \vec{p_1}, \lambda_1\rangle \otimes |m_2, j_2; \vec{p_2}, \lambda_2\rangle \equiv |\vec{p_1}, \vec{p_2}, \lambda_1, \lambda_2; \gamma\rangle \ , \tag{6.11}$$

where γ includes all other quantum numbers of the system. In the CM frame, $\vec{p_1} = -\vec{p_2} \equiv \vec{p}$ so that the invariant mass is given by

$$W = \sqrt{m_1^2 + p^2} + \sqrt{m_2^2 + p^2} \, . \tag{6.12}$$

In this frame, we use the vector $|m_1, j_1; \vec{p_1}, \lambda_1\rangle$, with the structure given by Eq. (6.8), to represent the state of the particle with momentum $\vec{p}$. Then, for the particle with momentum $-\vec{p}$, we can use the same rotation operator,

$$\overline{|m_2, j_2; -\vec{p}, \lambda_2\rangle} = R(\theta, \phi) \, \overline{|m_2, j_2; -p_z, \lambda_2\rangle} \, , \tag{6.13}$$

where p_z is the component of the momentum in the z-direction. The bar state is defined as

$$\overline{|m_2, j_2; -p_z, \lambda_2\rangle} = (-1)^{j_2 - \lambda_2} \, R(\pi, 0) \, |m_2, j_2; p_z, \lambda_2\rangle \ , \tag{6.14}$$

with

$$|m_2, j_2; p_z, \lambda_2\rangle = Z_p \, |m_2, j_2; \vec{p} = 0, \lambda_2\rangle \ . \tag{6.15}$$

The phase factor $(-1)^{j_2 - \lambda_2}$ is introduced so that as $p_z \to 0$

$$\overline{|m_2, j_2; -p_z = 0, \lambda_2\rangle} = |m_2, j_2; \vec{p} = 0, -\lambda_2\rangle \ . \tag{6.16}$$

An equivalent definition for two particle CM states can be written as

$$|p, 0, 0; \lambda_1, \lambda_2; \gamma\rangle = |m_1, j_1; p_z, \lambda_1\rangle \otimes \overline{|m_2, j_2; -p_z, \lambda_2\rangle} \, , \tag{6.17}$$

and

$$|p, \theta, \phi; \lambda_1, \lambda_2; \gamma\rangle = R(\theta, \phi) \, |p, 0, 0; \lambda_1, \lambda_2; \gamma\rangle \ . \tag{6.18}$$

One can define two different vectors, corresponding to two particle helicity states in an arbitrary frame,

$$\begin{aligned} |I\rangle &= \left|p_1', p_2'; \lambda_1', \lambda_2'; \gamma'\right\rangle \ , \\ |F\rangle &= |p_1, p_2; \lambda_1, \lambda_2; \gamma\rangle \ . \end{aligned} \tag{6.19}$$

The normalization is given then by

$$\langle F \mid I\rangle = (2\pi)^6 \, 2E_1 2E_2 \delta^{(3)}\left(\vec{p_1}' - \vec{p_1}\right) \delta^{(3)}\left(\vec{p_2}' - \vec{p_2}\right) \delta_{\lambda_1' \lambda_1} \delta_{\lambda_2' \lambda_2} \delta_{\gamma' \gamma} \, . \tag{6.20}$$

These states are eigenstates of the total four-momentum of the system, $P^\mu = p_1^\mu + p_2^\mu$. Thus, we can write

$$\begin{aligned} |I\rangle &= |P_\mu\rangle \otimes |\alpha\rangle \ , \\ |F\rangle &= \left|P'_\mu\right\rangle \otimes \left|\alpha'\right\rangle \ , \end{aligned} \tag{6.21}$$

and

$$\langle P'_\mu \mid P_\mu\rangle = (2\pi)^4\, \delta^{(4)}\left(P'_\mu - P_\mu\right) \ . \tag{6.22}$$

In the CM frame $\vec{P} = 0$ and $P^0 = W$; it then follows that

$$\langle \alpha' \mid \alpha\rangle = (2\pi)^2\, \frac{4W}{p} \delta\left(\Omega' - \Omega\right) \delta_{\lambda'_1\lambda_1}\delta_{\lambda'_2\lambda_2}\delta_{\gamma'\gamma} \ , \tag{6.23}$$

with $d\Omega = d\cos\theta d\phi$. To remove the dependence on P_μ of $|\alpha\rangle$, we introduce the vectors

$$|\theta, \phi; \lambda_1, \lambda_2; \gamma\rangle = \sqrt{\frac{p}{4W}}\, |\alpha\rangle \ , \tag{6.24}$$

with normalization given by

$$\langle \theta', \phi'; \lambda'_1, \lambda'_2; \gamma' \mid \theta, \phi; \lambda_1, \lambda_2; \gamma\rangle = \delta\left(\Omega' - \Omega\right) \delta_{\lambda'_1\lambda_1}\delta_{\lambda'_2\lambda_2}\delta_{\gamma'\gamma} \ . \tag{6.25}$$

Hence the CM state vectors of Eq. (6.18) can be written as

$$|p, \theta, \phi; \lambda_1, \lambda_2; \gamma\rangle = \sqrt{\frac{4W}{p}}\, |P_\mu\rangle \otimes |\theta, \phi; \lambda_1, \lambda_2; \gamma\rangle \ . \tag{6.26}$$

On the other hand, the CM states can be expressed in terms of states with well-defined total angular momentum J,

$$|p, J, M; \lambda_1, \lambda_2; \gamma\rangle = \sqrt{\frac{4W}{p}}\, |P_\mu\rangle \otimes |J, M; \lambda_1, \lambda_2; \gamma\rangle \ , \tag{6.27}$$

where M is the eigenvalue the third component of J and

$$\langle J', M'; \lambda'_1, \lambda'_2; \gamma' \mid J, M; \lambda_1, \lambda_2; \gamma\rangle = \delta_{JJ'}\delta_{MM'}\delta_{\lambda'_1\lambda_1}\delta_{\lambda'_2\lambda_2}\delta_{\gamma'\gamma} \ . \tag{6.28}$$

The transformation properties of these vectors under a rotation $R\,(\alpha, \beta, \gamma)$ are

$$|p, J, M; \lambda_1, \lambda_2; \gamma\rangle \to \mathcal{D}^{(J)}_{MM'}\,(\alpha, \beta, \gamma)\, |p, J, M; \lambda_1, \lambda_2; \gamma\rangle \ , \tag{6.29}$$

where $\mathcal{D}^{(J)}_{MM'}(\alpha,\beta,\gamma)$ is the matrix representation of a rotation operator $R(\alpha,\beta,\gamma)$ in an irreducible representation of the rotation group labeled by J,

$$\mathcal{D}^{(J)}_{MM'}(\alpha,\beta,\gamma) \equiv \left\langle JM' \right| R(\alpha,\beta,\gamma) \left| JM \right\rangle \ . \tag{6.30}$$

We can write

$$\begin{aligned} \mathcal{D}^{(J)}_{MM'}(\alpha,\beta,\gamma) &= e^{-\mathbb{i}\alpha M'} d^{J}_{M'M}(\beta) e^{-\mathbb{i}\gamma M} \ , \\ d^{J}_{M'M}(\beta) &= \left\langle J, M' \right| e^{-\mathbb{i}\beta J_y} \left| J, M \right\rangle \ . \end{aligned} \tag{6.31}$$

This matrices fulfils the orthogonality relations [130]

$$\int d\Omega\, \mathcal{D}^{(J)*}_{M_1M_2}(\phi,\theta,-\phi)\, \mathcal{D}^{(J')}_{M_1'M_2'}(\phi,\theta,-\phi) = \frac{4\pi}{2J+1}\delta_{JJ'}\delta_{M_1M_1'}\delta_{M_2M_2'} \ . \tag{6.32}$$

The vectors of Eq. (6.26) can be written as an expansion in the base given by the vectors of Eq.(6.27),

$$\left|p,\theta,\phi;\lambda_1,\lambda_2;\gamma\right\rangle = \sum_{J,M} C_{JM}(p,\theta,\phi;\lambda_1,\lambda_2;\gamma) \left|p,J,M;\lambda_1,\lambda_2;\gamma\right\rangle \ , \tag{6.33}$$

with coefficients C_{JM}. The state $|p,0,0;\lambda_1,\lambda_2;\gamma\rangle$ is an eigenstate of J_z with eigenvalue $\lambda = \lambda_1 - \lambda_2$, then

$$\left|p,0,0;\lambda_1,\lambda_2;\gamma\right\rangle = \sum_{J} C_{J\lambda}(p,0,0;\lambda_1,\lambda_2;\gamma) \left|p,J,\lambda;\lambda_1,\lambda_2;\gamma\right\rangle \ . \tag{6.34}$$

Applying the rotation $R(\theta,\phi)$ in both sides of of this equation we obtain

$$\left|p,\theta,\phi;\lambda_1,\lambda_2;\gamma\right\rangle = \sum_{J,M} C_J \mathcal{D}^{(J)}_{M\lambda}(\phi,\theta,-\phi) \left|p,J,M;\lambda_1,\lambda_2;\gamma\right\rangle \ , \tag{6.35}$$

with $C_J \equiv C_{J\lambda}(p,0,0;\lambda_1,\lambda_2;\gamma)$. Substituting the result of Eq. (6.35) in Eqs. (6.26, 6.27) and with the orthogonality relations of Eq. (6.32) we find

$$\left|J,M;\lambda_1,\lambda_2;\gamma\right\rangle = \frac{2J+1}{4\pi C_J} \int d\Omega\, \mathcal{D}^{(J)*}_{M\lambda}(\phi,\theta,-\phi) \left|\theta,\phi;\lambda_1,\lambda_2;\gamma\right\rangle \ . \tag{6.36}$$

From this result and the normalization of the $|J,M;\lambda_1,\lambda_2;\gamma\rangle$ states we can determine the constant C_J,

$$C_J = \sqrt{\frac{2J+1}{4\pi}} \ , \tag{6.37}$$

where we have chosen the phase of C_J, which is not determined, to be zero, taking the positive square root, and, hence,

$$|J, M; \lambda_1, \lambda_2; \gamma\rangle = \sqrt{\frac{2J+1}{4\pi}} \int d\Omega \, \mathcal{D}^{(J)*}_{M\lambda} (\phi, \theta, -\phi) \, |\theta, \phi; \lambda_1, \lambda_2; \gamma\rangle \ . \quad (6.38)$$

An alternative basis, with well-defined total spin, $S = j_1 \oplus j_2$, and relative orbital angular momentum, $L = J \oplus S$, of the two particles, is given by the vectors $|J, M; L, S; \gamma\rangle$. These vectors can be expressed as a linear combination of states of relative angular momentum L, M_L with spin components m_1, m_2 along the z-axis,

$$\begin{aligned} |J, M; L, S; \gamma\rangle = & \sum_{m_1, m_2} (L, S, J \mid M_L, M_S, M) \, (j_1, j_2, S \mid m_1, m_2, M_S) \\ & \times |L, M_L; m_1, m_2; \gamma\rangle \ , \end{aligned} \quad (6.39)$$

where $(L, S, J \mid M_L, M_S, M)$ are the Clebsch-Gordan coefficients. In turn, these states can be written in terms of plane wave states in which the particle spins are quantized along the z-axis [130]

$$|L, M_L; m_1, m_2; \gamma\rangle = \sqrt{\frac{2L+1}{4\pi}} \int d\Omega \, \mathcal{D}^{(L)*}_{M_L 0} (\phi, \theta, -\phi) \, |\theta, \phi; m_1, m_2; \gamma\rangle \quad (6.40)$$

The $|J, M; L, S; \gamma\rangle$ states can be related to the helicity states $|J, M; \lambda_1, \lambda_2; \gamma\rangle$, by the relation, for a single particle helicity state,

$$|\vec{p}, \lambda\rangle = \sum_{m_s} \mathcal{D}^{(j)}_{m_s, \lambda} (\phi, \theta, -\phi) \, |\vec{p}, m_s\rangle \ , \quad (6.41)$$

where m_s is the spin component along the z-axis, and the property [130]

$$\mathcal{D}^{(j_1)}_{m_1', m_1} \mathcal{D}^{(j_2)}_{m_2', m_2} = \sum_J (j_1, j_2, J \mid m_1, m_2, M) \left(j_1, j_2, J \mid m_1', m_2', M'\right) \mathcal{D}^{(J)}_{M' M} \ . \quad (6.42)$$

Therefore, for the helicity states we can write

$$\begin{aligned} |J, M; \lambda_1, \lambda_2; \gamma\rangle = & \sum_{L, S} \sqrt{\frac{2L+1}{2J+1}} \, (L, S, J \mid 0, \lambda, \lambda) \, (j_1, j_2, S \mid \lambda_1, -\lambda_2, \lambda) \\ & \times |J, M; L, S; \gamma\rangle \ , \end{aligned} \quad (6.43)$$

and

$$|J,M;L,S;\gamma\rangle = \sum_{\lambda_1,\lambda_2} \sqrt{\frac{2L+1}{2J+1}}\,(L,S,J \mid 0,\lambda,\lambda)\,(j_1,j_2,S \mid \lambda_1,-\lambda_2,\lambda) \times |J,M;\lambda_1,\lambda_2;\gamma\rangle \ . \tag{6.44}$$

6.4 Watson's theorem

In this section we highlight the main points of the Watson's theorem formulation, following the derivation presented in Ref. [31]. The transition amplitude between the asymptotically defined *in* and *out* states of definite momentum is given in terms of the unitary operator called the S-matrix. The structure of this operator contains two parts, the identity operator, which corresponds to the case where the particles do not interact at all, and the T-matrix, which is the interaction term,

$$S = \mathbb{I} - \mathrm{i}T \ . \tag{6.45}$$

The unitarity of the S-matrix, $SS^\dagger = S^\dagger S = \mathbb{I}$, implies that

$$\begin{aligned} S^\dagger S = \mathbb{I} - \mathrm{i}T + \mathrm{i}T^\dagger + T^\dagger T &= \mathbb{I} \ , \\ \mathrm{i}\left(T - T^\dagger\right) &= T^\dagger T \ , \\ \mathrm{i}\left(\langle F|\,T\,|I\rangle - \langle F|\,T^\dagger\,|I\rangle\right) &= \langle F|\,T^\dagger T\,|I\rangle \\ &= \sum_N \langle F|\,T^\dagger\,|N\rangle\,\langle N|\,T\,|I\rangle \\ &= \sum_N \langle N|\,T\,|F\rangle^*\,\langle N|\,T\,|I\rangle \ , \end{aligned} \tag{6.46}$$

where $|I\rangle$ and $|F\rangle$ are the initial and final asymptotic states. On the other hand, for a system which is invariant under time reversal, $\mathcal{T}^\dagger T^\dagger \mathcal{T} = T$, as the $\mathcal{T}$ operator is antiunitary, with $\mathcal{T}^2 = \pm 1$, we have

$$\langle F|\,T^\dagger\,|I\rangle = \langle I|\,T\,|F\rangle^* = \langle I|\,\mathcal{T}^\dagger T^\dagger \mathcal{T}\,|F\rangle^* = \langle I_\mathcal{T}|\,T^\dagger\,|F_\mathcal{T}\rangle = \langle F_\mathcal{T}|\,T\,|I_\mathcal{T}\rangle^* \ . \tag{6.47}$$

Substituting the result of Eq.(6.47) in Eq. (6.46) we find that

$$\mathrm{i}\left(\langle F|\,T\,|I\rangle - \langle F_\mathcal{T}|\,T\,|I_\mathcal{T}\rangle^*\right) = \sum_N \langle N|\,T\,|F\rangle^*\,\langle N|\,T\,|I\rangle \ . \tag{6.48}$$

If $\langle F|\,T\,|I\rangle = \langle F_{\mathcal{T}}|\,T\,|I_{\mathcal{T}}\rangle$ and there is only one relevant intermediate state in the sum of Eq. (6.48), one obtains that

$$\langle N|\,T\,|F\rangle^{*}\,\langle N|\,T\,|I\rangle = -2\mathrm{Im}\,\langle F|\,T\,|I\rangle \in \mathbb{R}\,, \tag{6.49}$$

which is the Watson's theorem [126] on the effect of final state interactions on reaction cross sections.

6.4.1 Watson's theorem for weak kaon production

Let us consider matrix elements of the transition (T) scattering operator between two-body states with well defined total angular momentum J and particle helicities (λ) in the HCM frame. Following the derivation of Sec. II.A of Ref. [31] for weak pion production, the $S-$matrix unitarity and time reversal symmetry imply that

$$\begin{aligned}\sum_{\lambda_{K''}\lambda_{N''}} &\langle J,M;\lambda_{K''},\lambda_{N''}\,|T(s)|J,M;\lambda_K,\lambda_{N'}\,\rangle^{*} \\ &\times\,\langle J,M;\lambda_{K''},\lambda_{N''}\,|T(s)|J,M;\lambda_W,\lambda_N\,\rangle \in \mathbb{R}\,,\end{aligned} \tag{6.50}$$

for the $W^{+}N \to KN'$ transition. We remind here that $\sqrt{s}$ is the center-of-mass energy of the kaon-nucleon pair, and we limit its range in this work such that, the only relevant strong process in the sum over intermediate states implicit in the derivation of Eq. (6.50) in [31], is the $K''N'' \to KN'$ reaction. This equation, Watson's theorem, relates the phases of the strong $K''N'' \to KN'$ amplitudes with the electroweak $WN \to K''N''$ ones. The later, up to a real normalization constant

$$\langle K''N''|T|WN\rangle \propto -iJ_{\mu}\epsilon^{\mu}\,, \tag{6.51}$$

in terms of the hadronic current J^{μ}, introduced earlier in the chapter, and the polarization vector of the W boson. [4] The W-boson offshellness does not affect the present argument [31]. We consider only KN intermediate states, restricting the validity of the approach to invariant masses of the KN pair below the KKY threshold. We further neglect the influence of $K\pi N$ intermediate states. This assumption relies on the observation that in the KN partial waves under consideration (details are given below), inelasticities are either sharply or very close to one for invariant masses below 2.1 GeV [131].

[4] Notice that the gauge coupling has been factored out and absorbed in the Fermi constant of Eq. (6.4).

To be more specific, in Eq. (6.50) after setting the kaon helicities to zero, we denote as r the helicity of the W gauge boson, and as λ, λ', ρ the corresponding ones of the initial, final and intermediate nucleons. Furthermore, assigning the z direction ($\theta = \varphi = 0$) to the WN incoming pair, one can write

$$|\theta = 0, \varphi = 0; r, \lambda\rangle = \sum_J \sqrt{\frac{2J+1}{4\pi}}\, |J, M = r - \lambda; r\, \lambda\rangle \ , \tag{6.52}$$

which follows from Eq. (6.38). By taking into account that T is a scalar and therefore diagonal in J, Eq. (6.50) can be cast as ($M = r - \lambda$)

$$\begin{aligned} \sum_\rho \langle J, M; \underbrace{0, \rho}_{KN} |T(s)| J, M; \underbrace{0, \lambda'}_{KN}\rangle^* \\ \times \langle J, M; \underbrace{0, \rho}_{KN} |T(s)| \theta, \varphi = 0; \underbrace{r, \lambda}_{WN}\rangle \in \mathbb{R} \, . \end{aligned} \tag{6.53}$$

Introducing states with well-defined orbital angular momentum L and spin S, and using their transformation properties given in Sec. 6.3 one finds that

$$\begin{aligned} \sum_L \sum_\rho \frac{2L+1}{2J+1} (L, 1/2, J|0, -\lambda', -\lambda')(L, 1/2, J|0, -\rho, -\rho) \\ \times \underbrace{\langle J, M; L, 1/2|T(s)|J, M; L, 1/2\rangle^*}_{KN \to KN} \\ \times \underbrace{\langle J, M; 0, \rho|T(s)|\theta, \varphi = 0; r, \lambda\rangle}_{WN \to KN} \in \mathbb{R} \, , \end{aligned} \tag{6.54}$$

given that parity is conserved by the strong $KN \to KN$ amplitudes. Here $(L, S, J|M_L, M_S, M_J)$ are Clebsch-Gordan coefficients.

Based on kaon-nucleon scattering phenomenology and the behavior of weak kaon production amplitudes close to threshold, it is reasonable to assume that the process under study is dominated by the s partial wave ($L = 0$). This implies that $S = J = 1/2$, the nucleon spin. Eq. 6.54 takes then the form

$$\chi_{r,\lambda}(s) \langle 1/2, r - \lambda; 0, 1/2|T(s)|1/2, r - \lambda; 0, 1/2\rangle^* \in \mathbb{R} \, , \tag{6.55}$$

where the shorthand notation

$$\chi_{r,\lambda}(s) = \sum_\rho \langle 1/2, r - \lambda; 0, \rho|T(s)|\theta, \varphi = 0; r, \lambda\rangle \tag{6.56}$$

has been introduced. Up to an irrelevant constant, these functions can be written as

$$\chi_{r,\lambda}(s) = \sum_{\rho} \int d\Omega \; \mathcal{D}^{(1/2)}_{M\ -\rho}(\varphi,\theta,-\varphi)\, \langle \theta,\varphi;0,\rho|T(s)|\theta,\varphi=0;r,\lambda\rangle \ , \quad (6.57)$$

where $\mathcal{D}^{(1/2)}_{M\ -\rho}$ are Wigner D-matrices (see Eq. (6.38) in Sec. 6.3). The integral is performed over the solid angle of the outgoing kaon in the HCM frame.

Owing to the $V-A$ nature of the weak interaction, T in Eq. (6.56) can be expressed as $T_V - T_A$, $T_{V(A)}$ being even (odd) under parity inversion. Therefore, it is convenient to write $\chi_{r,\lambda} = \chi^V_{r,\lambda} - \chi^A_{r,\lambda}$. In terms of two-particle helicity states with well defined angular momentum J ($= 1/2$ in our case)

$$\chi^{V,A}_{r,\lambda} = \sum_{\rho} \langle 1/2, M; 0, \rho|\, T^{V,A}\, |1/2, M; r, \lambda\rangle \ . \quad (6.58)$$

Under parity inversion, these states are transformed as (Eq. (5.28) of Ref. [130])

$$P\,|J, M; \mu_1, \mu_2\rangle = \eta_1\eta_2(-1)^{J-s_1-s_2}\,|J, M; -\mu_1, -\mu_2\rangle \ , \quad (6.59)$$

in terms of the two particles' intrinsic parities $\eta_{1,2}$ and spins $s_{1,2}$. Therefore

$$\begin{aligned} P\,|1/2, M; r, \lambda\rangle &= \ \ \eta_N\eta_W(-1)^{1/2-1/2-1}\,|1/2, M; -r, -\lambda\rangle \ , \\ P\,|1/2, M; 0, \rho\rangle &= \ \ \eta_N\eta_K(-1)^{1/2-1/2-0}\,|1/2, M; -r, -\lambda\rangle \ . \end{aligned} \quad (6.60)$$

Therefore

$$\chi^{V,A}_{-r,-\lambda} = -\sum_{\rho} \langle 1/2, M; 0, \rho|\, P^{-1}T^{V,A}P\, |1/2, M; r, \lambda\rangle \ ,$$

where we have taken into account that these matrix elements do not depend on M because T is a scalar under rotations. Once $P^{-1}T^{V,A}P = \pm T^{V,A}$

$$\chi^{V,A}_{-r,-\lambda} = \mp\chi^{V,A}_{r,\lambda} \ , \quad (6.61)$$

from where

$$\begin{aligned} \chi^V_{r,\lambda} &= \frac{1}{2}\left(\chi_{r,\lambda} - \chi_{-r,-\lambda}\right) \ , \\ \chi^A_{r,\lambda} &= -\frac{1}{2}\left(\chi_{r,\lambda} + \chi_{-r,-\lambda}\right) \ . \end{aligned} \quad (6.62)$$

They allow to reduce the number of independent functions from four vector (axial) ones to two [31] for each of the reaction channels listed in Eq. (6.1).[5]

Finally, we project onto states with well defined isospins (I) and introduce isospin amplitudes, and hence the $\chi^{(I=0,1)}$ functions,

$$\begin{aligned}\chi^{(1)} &= \chi(W^+ p \to K^+ p) \\ \chi^{(0)} &= \chi(W^+ n \to K^+ n) - \chi(W^+ n \to K^0 p)\,.\end{aligned} \tag{6.63}$$

Other indices have been dropped for simplicity. These identities let us to write the χ for all three processes in terms of only two with $I = 0, 1$.

We proceed by identifying the dominant contributions to the amplitude. From the analysis of Ref. [30] we know that contact term (CT) is the largest one for all processes of Eq. (6.1). We find convenient to split the T matrix as $T = T_{CT} + T_B$, where T_{CT} denotes the CT term, while the rest of the diagrams of Fig. 6.1 are included in T_B. Next, we compute all the independent $\chi^{V,A\,(I=0,1)}_{r,1/2}$ with $r = 0, 1$ (eight in total), calculated from the CT Feynman diagram. As illustrated in Fig. 6.2 for a fixed Q^2, we identify $\chi^{A(0)}_{0,1/2}$ and $\chi^{V(1)}_{0,1/2}$ as dominant and select them to determine the Olsson's phases introduced next.

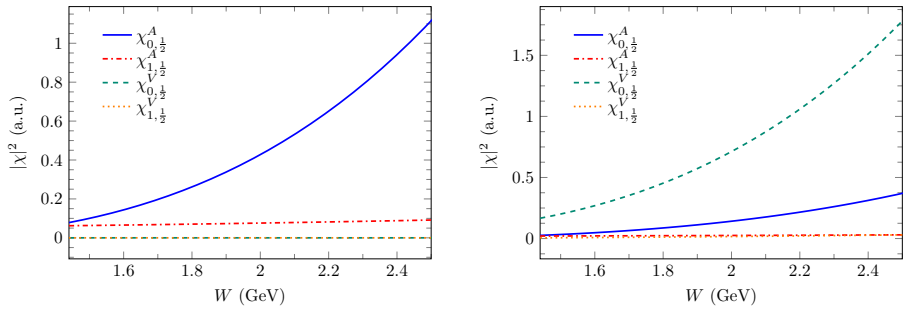

Figure 6.2: Absolute value squared of $\chi^{V,A}_{r,\lambda}$ defined using Eqs. (6.56), (6.62) and (6.63) as a function of the KN invariant mass (W) for a fixed $Q^2 = 0.1$ GeV^2. Left and right panels stands for isospin $I = 0$ and $I = 1$ respectively.

In order to implement Watson's theorem to partially restore unitarity, we follow the prescription given by Olsson [127]. Namely, we introduce phases $\Psi_{V,A}$ in both vector and axial CT terms, such that the modified amplitude

[5] Combinations with $|r - \lambda| = 3/2$ are excluded because $J = 1/2$.

reads as

$$\langle \theta, \varphi; 0, \rho | T(s) | \theta, \varphi = 0; r, \lambda \rangle = \epsilon_{r\mu} T^{V\mu}_{\mathrm{B}\lambda\rho}(\theta, \varphi) - \epsilon_{r\mu} T^{A\mu}_{\mathrm{B}\lambda\rho}(\theta, \varphi) + \epsilon_{r\mu} T^{V\mu}_{\mathrm{CT}\lambda\rho}(\theta, \varphi)\, e^{i\Psi_V} - \epsilon_{r\mu} T^{A\mu}_{\mathrm{CT}\lambda\rho}(\theta, \varphi)\, e^{i\Psi_A} \,. \tag{6.64}$$

where $\epsilon_{(r,r')\mu}$, $r = 0, \pm 1$, is the $W-$boson polarization vector. Thanks to Watson's theorem these unknown phases can be determined using the available experimental information about KN scattering phase shifts. We impose that

$$\mathrm{Im}\left\{ \chi^{V(1)}_{0,1/2}(s)\, e^{-\mathrm{i}\delta_{S_{11}}} \right\} = 0 \,, \tag{6.65}$$

$$\mathrm{Im}\left\{ \chi^{A(0)}_{0,1/2}(s)\, e^{-\mathrm{i}\delta_{S_{01}}} \right\} = 0 \,, \tag{6.66}$$

where the KN phase shift $\delta_{L_{I,2J}}$ are taken from the Scattering Analyses Interactive Dialin (SAID) database of the INS Data Analysis Center [131]. The Eqs. (6.65) and (6.66) can be used to determine the Olsson phases $\Psi_{V,A}$, which are two-dimension functions of W and Q^2.

6.5 Results and discussion

The $\Psi_{V,A}(W, Q^2)$ solutions of Eqs. (6.65), (6.66) plugged in Eq. (6.64) correct the relative phase between the CT term and the rest of mechanisms. As discussed in [31], there exist two solutions for the vector Eq. (6.65) [axial Eq. (6.66)], which correspond to $\chi^{V(1)}_{0,1/2}(s)$ [$\chi^{A(0)}_{0,1/2}(s)$] having phases $\delta_{S_{11}}$ [$\delta_{S_{01}}$] or $(\delta_{S_{11}} + \pi)$ [$(\delta_{S_{01}} + \pi)$], since the KN phase shift is defined up to a π factor. We label *Sol.1* or *Sol.2*, the solutions with the smallest or largest phases, respectively. In Fig. 6.3, the integrated cross sections obtained with these two set of solutions are shown, together with the reference calculation of Ref. [30], which did not include the Olsson's phases. One immediately notices that, while the partial unitarization with *Sol.1* provides small effects, *Sol. 2* leads to large variations. For example, in $\nu_\mu n \to \mu^- p K^0$, we find that around $E_\nu = 2$ GeV, the cross section obtained with *Sol.2* is four times larger than that predicted in Ref. [30]. In Ref. [31], where a similar approach was undertaken for weak pion production, the preference for small Olsson's phases was clearly validated by pion photoproduction data (see Fig. 2 of that paper). In the present case, there are no equivalent electromagnetic single kaon production data that could serve for validation purposes. Future data for weak single kaon production at low energies obtained, for example

with SBND [132] at Fermilab, that will collect data with high statistics, or in a future neutrino experiment on hydrogen and/or deuterium shall have the potential to distinguish between the two solutions. Nonetheless, given the weakness (for strong forces) of the KN interactions, one is seriously inclined to expect *Sol.1* with small phases to be the physical one. In this case, Olsson's phases have a small effect, with the largest one, observed in $\nu_\mu n \to \mu^- p K^0$, amounting to about an 18% increase with respect to the reference predictions of Ref. [30] at $E_\nu = 2$ GeV. It is therefore plausible that, in the energy region in which the present model is applicable, the size of unitarity corrections is within the model uncertainties effectively accounted by the 10 % uncertainty assumed for the dipole mass, at least for the total cross section.

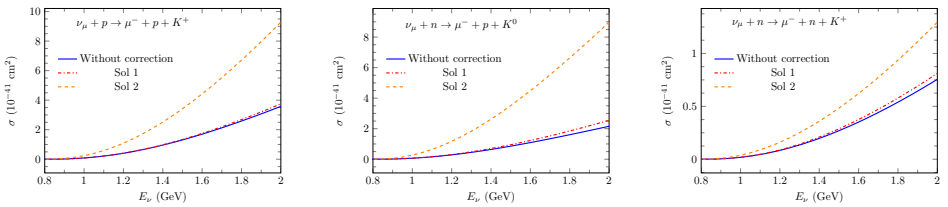

Figure 6.3: Total cross section $\sigma(E_\nu)$ as a function of the muon-neutrino energy (E_ν) for the processes of Eq. (6.1). The solid curve stand for the original results of Ref. [30], while the predictions obtained after the Watson's corrections are shown with dashed and dashed dotted lines for (*Sol 1*) and (*Sol 2*) sets of Olsson's phases, respectively.

In order to perform a more detailed analysis of the impact of unitarity corrections we rely on the following representation of the differential cross section, Eq. (6.2),

$$\frac{d\sigma}{dW\, dQ^2 d\Omega_K^*} = \frac{G_F^2 W}{4\pi M_N |\vec{k}|^2} \left(A + B\cos\phi_K^* + C\cos 2\phi_K^* \right. \\ \left. + D\sin\phi_K^* + E\sin 2\phi_K^*\right) , \tag{6.67}$$

where the dependence on the HCM kaon azimuthal angle has been singled out [129, 133, 134]. The structure functions $A - E$ are real and depend on the scalars Q^2, $p \cdot q$, $p_K \cdot q$ and $p_K \cdot p$. We have obtained these structure functions for weak kaon production for the first time. They are displayed in Figs. 6.4, 6.5, and 6.6 for each of the possible reaction channels as a function of $\cos\theta_K^*$ for fixed E_ν, W and Q^2. Large differences for results with *Sol. 2* are apparent, while those with *Sol. 1* are close to the uncorrected ones as

expected. Particularly noticeable are the larger values and stronger angular dependence found for A in the *Sol. 2* case. So is also the different sign of the *Sol. 2* prediction of B and C in $\nu_\mu + n \to \mu^- + n + K^+$. Remarkably, the D and E structure functions, responsible for parity violation in kaon production (and weak meson production in general [134]), which are zero in the tree-level model with real amplitudes, acquire nonzero although small values due to unitarization.

6.6 Summary

We have improved the theoretical description of single kaon production in neutrino-nucleon collisions below the KKY threshold by partially accounting for unitarity. For this purpose we have introduced Olsson's phases for the largest (contact) term of the amplitude in the dominant vector and axial multipoles. These phases take the values required to fulfill Watson's theorem. Experiment should ultimately discriminate among the two mathematical solutions found for the Olsson's phases but one of them is a firm candidate to be the non-physical one due to the large changes in the observables that it drives, which are unlikely to be caused by the rather weak KN interaction. The alternative solution, instead, leads to small corrections in the cross section, as expected because of the absence of baryon resonances, and which in addition are within the uncertainties of the model. This would validate the reference tree-level model, built upon leading the order chiral Lagrangian, in the kinematic region under consideration. Finally, we have investigated the behavior of the structure functions that characterize the cross-section dependence on the kaon azimuthal angle, finding also clear difference between solutions. The impact of unitarization is visible in the fact that the parity-violating structure functions depart from zero.

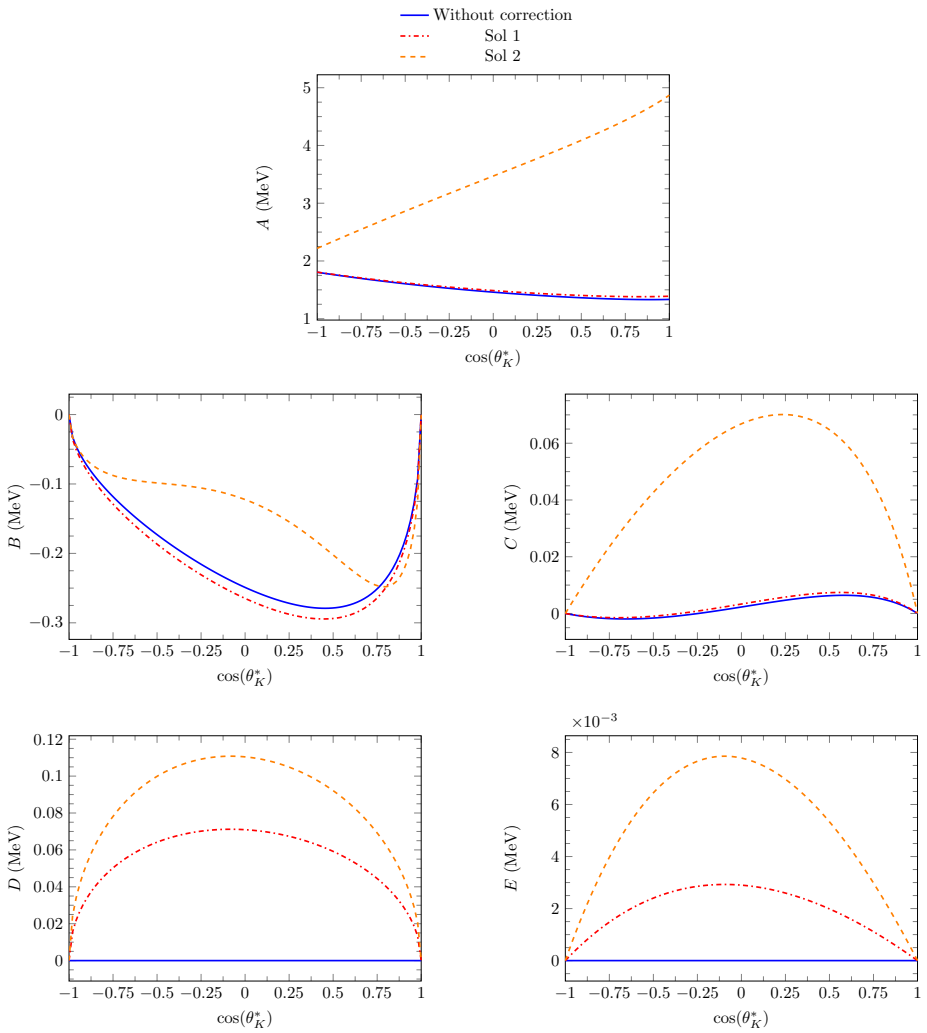

Figure 6.4: A, B, C, D, E structure functions for $\nu_\mu + p \to \mu^- + p + K^+$ as a function of the cosine of the polar kaon angle in the HCM frame (θ^*_K) for fixed $E_\nu = 2$ GeV, $W = 1.5$ GeV, $Q^2 = 0.2$ GeV^2. Line styles are as in Fig. 6.3.

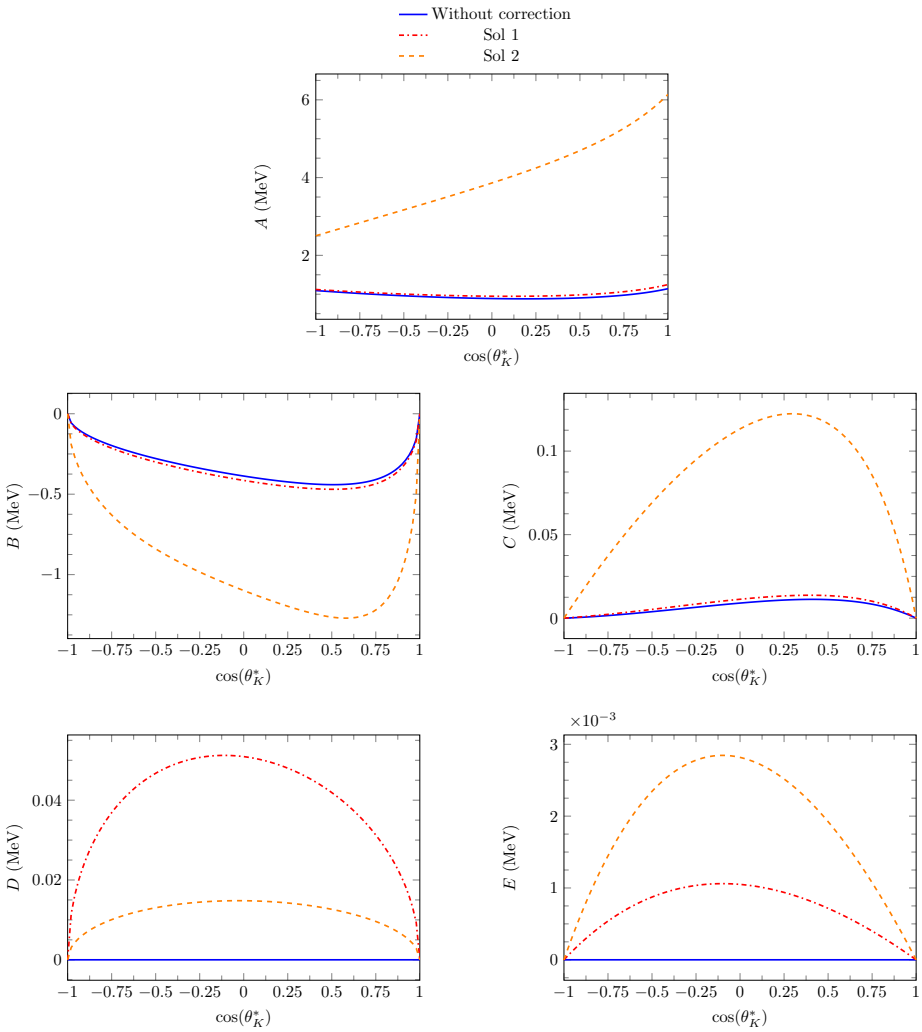

Figure 6.5: Same as Fig. 6.4, but for the $\nu_\mu + n \to \mu^- + p + K^0$ reaction.

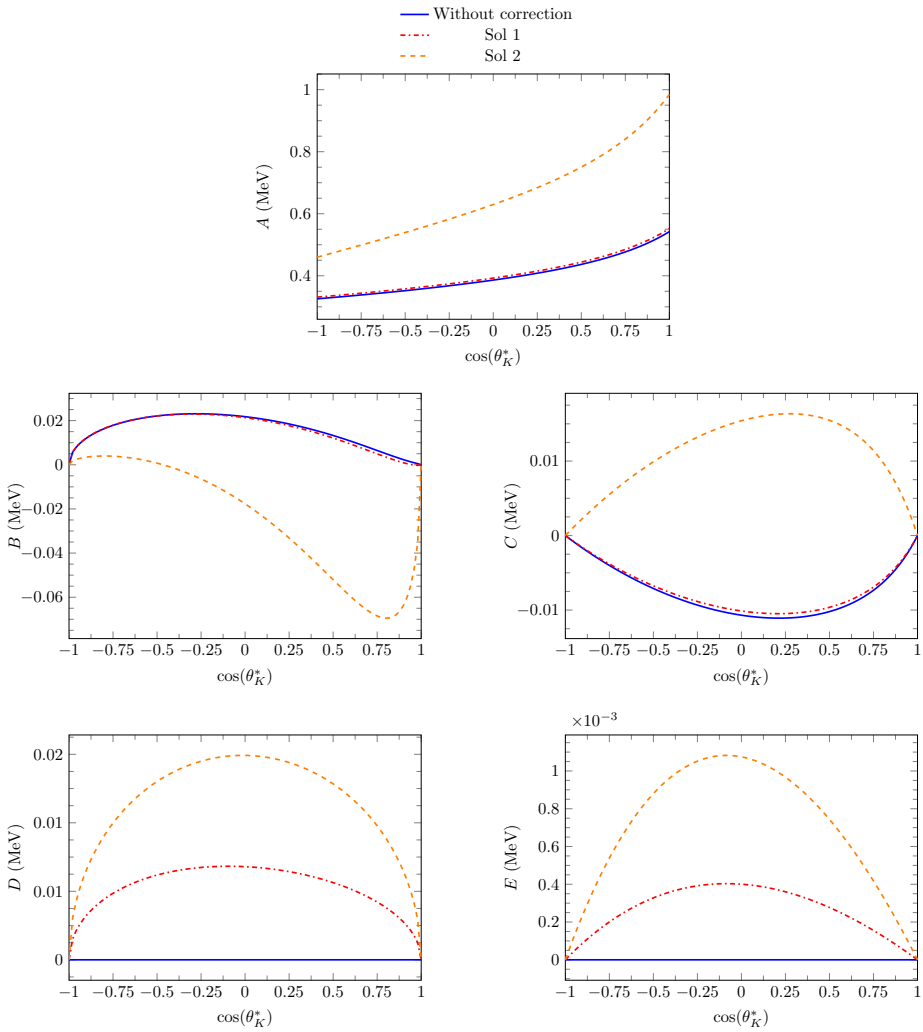

Figure 6.6: Same as Fig. 6.4, but for the $\nu_\mu + n \to \mu^- + n + K^+$ reaction.

Chapter 7

Coherent photon emission in neutral-current interactions

7.1 Introduction

Coherent scattering refers to processes in which the final-state nucleus is left in its ground state, rather than in an excited one. Coherent production of mesons and photons are relevant for neutrino oscillation experiments as a source of backgrounds. For this reason, they have received special attention both experimentally and theoretically, see Ref. [135] and references therein. Most efforts have been devoted to coherent pion production $\nu_l A \to l^{\mp}\pi^{\pm}A$ (CC$\pi^{\pm}$) and $\nu_l A \to \nu_l \pi^0 A$ (NCπ^0). For some detection techniques, NCπ^0 events can mimic $e^{\pm}$ from ν_e CC interactions, influencing therefore ν_e appearance measurements. Theoretically, PCAC allows to relate the coherent pion production cross section to pion-nucleus elastic scattering, Refs. [136, 137], for which some experimental data are available. Microscopic models, which start from particle production models on nucleons and perform a coherent sum over all nucleonic currents, have also been extensively developed (for example Refs. [138, 139]). In this chapter we study coherent photon emission $\nu_l A \to \nu_l \gamma A$ (NCγ).

Although smaller than the NCπ^0 one, the NCγ background remains irreducible in Cherenkov detectors. Moreover, in some proposed explanations of the anomalous excess of events observed at MiniBooNE [56–58, 140], heavy sterile neutrinos decay to active neutrinos and single photons or e^+e^- pairs [63]. Coherent NCγ production appears as a background to the proposed signature, which can be tested with liquid Argon (LAr) experiments such as MicroBooNE and SBND. Furthermore, in some experiments, single

showers induced by coherent NCγ emission can hardly be distinguished from those coming from neutrino-electron elastic scattering, which is a reference process in neutrino physics. At the MINERνA experiment, alongside with the $\nu - e$ sample [141], a sizable and distinctive fraction of NCγ events might be present, opening the possibility to identify and characterize this reaction channel using suitable kinematic variables and energy deposition (dE/dx) information [142].

Theoretically, PCAC has also been applied to relate the axial-vector contribution to coherent NCγ to the $\pi^0 A \to \gamma A$ differential cross section, Ref. [36], but this amounts only to the small longitudinal contribution. The majority of the cross section has to be calculated using model assumptions. In Refs. [32–34], the coherent NCγ reaction has been studied in microscopic model including non-resonant contributions as well as the excitation and subsequent radiative decay the $\Delta(1232)3/2^+$ resonance. In Ref. [34] the lightest $N^*(1440)1/2^+$, $N^*(1520)3/2^-$ and $N^*(1535)1/2^-$ baryonic states were also added.

In this chapter, we present an extension of the model of Ref. [34] including heavier baryon resonances to make it more suitable for MINERνA energies. In addition, we perform and validate a simplified treatment of the $\Delta(1232)3/2^+$ in-medium modification that allows to factorize the nuclear form factor. In this way, we succeed in speeding up significantly the computation, making its implementation in GENIE possible.

We first briefly describe the microscopic interaction model, following Ref. [34]. Then we present our approximations for the $\Delta(1232)$ modification in nuclei. Next we extend the model by adding N^* and Δ resonances with invariant masses up to 2 GeV. Finally, we show our results for the photon energy and angular distributions corresponding to a selected sample of incoming neutrino energies.

7.2 Coherent photon production cross section

We begin by introducing the cross section for the photon production by the coherent scattering of neutrinos[1] on nuclei mediated by neutral currents. In the reaction

$$\overset{(-)}{\nu}(k) + A(P) \to \overset{(-)}{\nu}(k') + A(P') + \gamma(p_\gamma)\,, \tag{7.1}$$

diagrammatically illustrated in Fig. 7.1, a neutrino with four-momentum $k \equiv (E_\nu, \vec{k})$ interacts with a nucleus of four-momentum $P \equiv \left(E, \vec{P}\right)$.

[1] With the term neutrino we refer also to its antiparticle.

After the interaction, the nucleus remains in the ground state, changing only its four-momentum to $P' \equiv \left(E', \vec{P}\,'\right)$, while the neutrino does to $k' \equiv (E'_\nu, \vec{k}\,')$. The four-momentum of the emitted photon is $p_\gamma \equiv (E_\gamma, \vec{p}_\gamma)$ and the one transferred by the neutrino is $q = k - k'$. In the Laboratory frame $P = (M_A, 0)$, where M_A denotes the target mass. Under the assumption that the recoil kinetic energy of the outgoing nucleus $(E' - M_A) \ll M_A$, energy conservation implies that $q_0 = E_\gamma$.

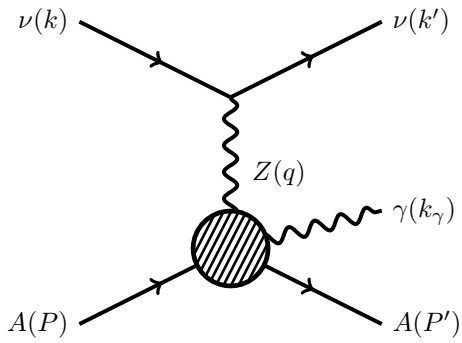

Figure 7.1: Diagram for coherent photon emission induced by neutral currents.

The framework adopted here closely follows Ref. [34] and is adapted from Refs. [138, 143] for neutrino-induced coherent pion production reactions. One has that

$$\frac{d\sigma}{dE_\gamma d\Omega_\gamma d\Omega_{k'}} = \frac{1}{8}\frac{1}{(2\pi)^5}\frac{E'_\nu E_\gamma}{E_\nu}|\overline{\mathcal{M}}|^2 \,, \tag{7.2}$$

where Ω_γ and $\Omega_{k'}$ are the solid angles of the photon and the outgoing neutrino with respect to the direction of the incoming neutrino. This differential cross section is equivalent to the one presented in Eq. (6.2) with a change of variables.[2] The amplitude, Eq. (3.4), takes the form

$$\mathrm{i}\mathcal{M} = \frac{G_F}{\sqrt{2}} \langle \nu | \, j_\mu \, | \nu \rangle \, \langle A \, \gamma | \, J^\mu_{\mathrm{coh}} \, | A \rangle \,, \tag{7.3}$$

with the leptonic current for neutral currents, given by

$$\langle \nu | \, j_\mu \, | \nu \rangle = \overline{\nu}(k') \gamma_\alpha \left(1 - \gamma_5\right) \nu(k) \,. \tag{7.4}$$

[2] It can also be obtained from Eq. (3.8).

Owing to the coherence of the process, the nucleon wave function inside the nucleus remains unchanged. Hence, after summing the elementary $ZN \to N\gamma$ amplitudes over all nucleons, one obtains the nuclear density distributions of protons and neutrons, $\rho_p(r)$ and $\rho_n(r)$ respectively. The hadronic matrix element in Eq. (7.3) then becomes

$$\begin{aligned}\langle A\,\gamma|\, J^{\mu}_{\text{coh}}\,|A\rangle &= \mathbb{i}\, e\, \epsilon^{*}_{\alpha}\left(k_{\gamma}\right) \int d^3 r e^{\mathbb{i}(\vec{q}-\vec{k}_{\gamma})\vec{r}} \\ &\quad \times \frac{1}{2}\text{Tr}\left[\overline{u}(p')\left(\rho_p(r)\Gamma^{\mu\alpha}_{p} + \rho_n(r)\Gamma^{\mu\alpha}_{n}\right)u(p)\right]\frac{M_{\text{N}}}{E_p} \\ &\equiv \mathbb{i}\, e\, \epsilon^{*}_{\alpha}\left(k_{\gamma}\right) R^{\mu\alpha}\,,\end{aligned} \tag{7.5}$$

where we have defined the amputated amplitudes $\Gamma^{\mu\alpha}_{N}$ corresponding to the Z boson interaction with each nucleon, N, as

$$\langle N\gamma|\, J^{\mu}_{\text{NC}\gamma}\,|ZN\rangle = \overline{u}\left(p'\right)\Gamma^{\mu\alpha}_{N} u\left(p\right)\epsilon^{*}_{\alpha}\left(k_{\gamma}\right)\,, \tag{7.6}$$

with $\epsilon_{\alpha}(k_{\gamma})$ the polarization of the outgoing photon. In the following section we define the content of these amplitudes. Using the Fourier transform property of Eq. (B.13), we have that

$$R^{\mu\alpha} = \frac{2\pi}{\left|\vec{q}-\vec{k}_{\gamma}\right|}\int dr\, r \sin\left(\left|\vec{q}-\vec{k}_{\gamma}\right| r\right)\text{Tr}\left[\overline{u}(p')\left(\rho_p\Gamma^{\mu\alpha}_{p} + \rho_n\Gamma^{\mu\alpha}_{n}\right)u(p)\right]\frac{M_{\text{N}}}{E_p}\,. \tag{7.7}$$

For the so far undefined nucleon momenta, we assume that the momentum transferred to the nucleus is equally shared by initial and final on-shell nucleons [138]:

$$\vec{p} = \frac{\vec{k}_{\gamma}-\vec{q}}{2}\,, \tag{7.8}$$

with the corresponding energy is $E_p = \sqrt{M^2_{\text{N}} + \vec{p}^{\,2}}$, and then

$$\begin{aligned} p &= (E_p, \vec{p})\,, \\ p' &= (E_p, -\vec{p})\,. \end{aligned} \tag{7.9}$$

This prescription is based on the fact that, for Gaussian nuclear wave functions, it leads to an exact treatment of the terms in the elementary amplitude that are linear in momentum. Therefore, we have

$$\begin{aligned} R^{\mu\alpha} &= \frac{2\pi}{\left|\vec{q}-\vec{k}_{\gamma}\right|}\int dr\, r \sin\left(\left|\vec{q}-\vec{k}_{\gamma}\right| r\right) \\ &\quad \times \text{Tr}\left[\frac{\not{p}+M_{\text{N}}}{2M_{\text{N}}}\gamma_0\left(\rho_p\Gamma^{\mu\alpha}_{p} + \rho_n\Gamma^{\mu\alpha}_{n}\right)\right]\frac{M_{\text{N}}}{E_p}\,. \end{aligned} \tag{7.10}$$

In the case where there is no density dependence in the amputated amplitudes, one can factorize the density. Then, relying on the definition of Eq. (3.72), we have

$$R^{\mu\alpha} = \sum_{N=p,n} \frac{1}{2}\mathrm{Tr}\left[\frac{\not{p}+M_{\mathrm{N}}}{2M_{\mathrm{N}}}\gamma_0\Gamma_N^{\mu\alpha}\right]\frac{M_{\mathrm{N}}}{E_p}F_N\left(\left|\vec{q}-\vec{k}_\gamma\right|\right)\,, \tag{7.11}$$

where, for the nuclear FF, we take the parametrization given in Eq. (3.76). We further discuss the applicability of this factorization when treating the nuclear corrections in next section.

Finally, for the modulus of the amplitude squared we can write

$$|\overline{\mathcal{M}}|^2 = -\frac{G_F^2}{2}e^2 L_{\alpha\beta}\, g_{\mu\nu}\,(R^{\mu\alpha})^\dagger\, R^{\nu\beta}\,, \tag{7.12}$$

where we have performed the average over initial spins and the sum over the final ones. From Eq. (7.4) we obtain the same expression for the leptonic tensor than in Eq. (6.5),

$$L_{\mu\nu} = 8\left[k'_\mu\, k_\nu + k'_\nu\, k_\mu - g_{\mu\nu}(k'\cdot k) \pm i\epsilon^{\mu\nu\sigma\rho}k'_\sigma k_\rho\right]\,, \tag{7.13}$$

where the upper (lower) sign stands for (anti)neutrinos.

7.3 Elementary amplitudes

The elementary $ZN \to N\gamma$ amplitude, described in earlier publications [32, 34, 144], include nucleon and baryon-resonance pole terms (direct and crossed), as well as anomaly-driven t-channel meson (π, ρ, ω) exchange. In the case of the coherent process, nucleon-pole contributions are negligible because a cancellation between direct and crossed terms is favored by kinematics. π and ρ exchange terms are not only small but, in the coherent case, vanish exactly for isospin symmetric nuclei. The ω exchange contribution, instead, does not vanish for symmetric nuclei because amplitudes on protons and neutrons add up rather than cancel. This mechanism was found subdominant at $E\nu \sim 1$ GeV. Its relevance at higher energies is highly uncertain due to a high sensitivity to unknown form factors and unitarity constraints but cannot be discarded due to its strong energy dependence [33] and deserves future studies. Here we focus on the contribution from baryon-resonance (N^*, and Δ) intermediate states, Fig. 7.2. The calculation of Ref. [34] considered $\Delta(1232)$, $N(1440)$, $N(1520)$ and $N(1535)$ diagrams. From these results it is clear that the contribution of the $\Delta(1232)$-pole term

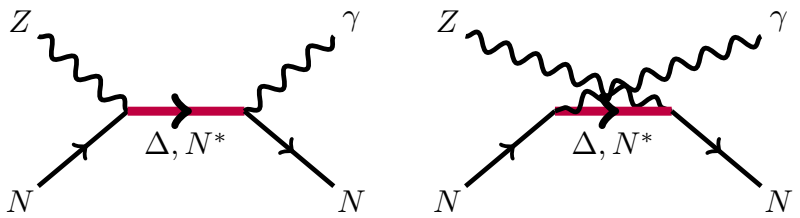

Figure 7.2: Feynman diagrams for photon emission off the nucleon mediated by baryon resonances.

is dominant at neutrino energies of the order of 1 GeV. Keeping in mind that there are experiments which work with higher energy fluxes, like MINERνA, where the medium-energy flux peaks at around 6 GeV and can detect photons with energies above 500 MeV, we extend the validity of the model to this domain. This is done by adding new resonant diagrams to the amplitude.

7.3.1 Resonance properties

We consider in our calculation all N^* and Δ states listed in Table 7.1, which correspond to all four-star (according to the PDG [40] classification) resonances with invariant masses $W < 2$ GeV whose electromagnetic properties were investigated with the Mainz Unitary Isobar model (MAID) [145, 146].

While most properties of the isolated $\Delta(1232)$ are rather well known, there are large uncertainties and model dependence in our understanding of heavier excited states of the nucleon. To reflect this situation, in the present study we consider two sets of resonance properties (Breit Wigner mass and total width and $R \to \pi N$ branching ratio). In the first one, labeled MAID, the parameters are taken from the SAID partial wave analysis [147] while the second, labeled PDG, adopts the estimates of the Particle Data Group [40]. The list of Table 7.1 contains the values for both sets. As discussed later in the section to each of the sets we associate a different treatment of the W dependence of the resonance width.

Electromagnetic properties of the nucleon-to-resonance transitions are a critical input for our study. Not only they determine the electromagnetic couplings that characterize the resonance radiative decays but also fix the vector part of the weak transition nuclear currents by means of isospin rotations. Transition EM properties are encoded in helicity amplitudes, which

	J	P	L	M_R [GeV]		Γ_0 [GeV]		b_R	
$\Delta(1232)$	3/2	+	P	1.232	1.232	0.118	0.117	1.00	1.00
$N(1440)$	1/2	+	P	1.462	1.440	0.391	0.350	0.69	0.65
$N(1520)$	3/2	−	D	1.524	1.515	0.124	0.110	0.59	0.60
$N(1535)$	1/2	−	S	1.534	1.530	0.151	0.150	0.51	0.42
$\Delta(1620)$	1/2	−	S	1.672	1.610	0.154	0.130	0.09	0.30
$N(1650)$	1/2	−	S	1.659	1.650	0.173	0.125	0.89	0.60
$N(1675)$	5/2	−	D	1.676	1.675	0.159	0.145	0.47	0.40
$N(1680)$	5/2	+	F	1.684	1.685	0.139	0.120	0.70	0.65
$\Delta(1700)$	3/2	−	D	1.762	1.710	0.599	0.300	0.14	0.15
$N(1720)$	3/2	+	P	1.717	1.720	0.383	0.250	0.13	0.11
$\Delta(1905)$	5/2	+	F	1.881	1.880	0.327	0.330	0.12	0.12
$\Delta(1910)$	1/2	+	P	1.882	1.900	0.239	0.300	0.23	0.20
$\Delta(1950)$	7/2	+	F	1.945	1.930	0.300	0.285	0.38	0.40

Table 7.1: Properties of the baryon resonances included in the model. N resonances have $I = 1/2$ and Δ resonances $I = 3/2$. This list includes spin, parity, πN partial wave, Breit-Wigner mass, total decay width and branching ratio into πN. The first column for each parameter corresponds to the analysis of Ref. [147], while the second column was extracted from Ref. [40].

we introduce in the next section before describing how we ascribe specific values to the two sets of parameters.

7.3.2 Helicity amplitudes

We have taken the parametrizations for these helicity amplitudes from the MAID analysis of Refs. [145, 146], where they are defined as[3]

$$\begin{aligned}
A^N_{1/2} &= \sqrt{\frac{2\pi\alpha}{k_R}}\,\langle R, J_z = 1/2|\,\epsilon^+_\mu J^\mu_{\rm EM}\,|N, J_z = -1/2\rangle\,\frac{1}{\sqrt{2M_{\rm N}}\sqrt{2M_R}}\,,\\
A^N_{3/2} &= \sqrt{\frac{2\pi\alpha}{k_R}}\,\langle R, J_z = 3/2|\,\epsilon^+_\mu J^\mu_{\rm EM}\,|N, J_z = 1/2\rangle\,\frac{1}{\sqrt{2M_{\rm N}}\sqrt{2M_R}}\,,\\
S^N_{1/2} &= -\sqrt{\frac{2\pi\alpha}{k_R}}\,\frac{|\vec{k}|}{\sqrt{Q^2}}\,\langle R, J_z = 1/2|\,\epsilon^0_\mu J^\mu_{\rm EM}\,|N, J_z = 1/2\rangle\,\frac{1}{\sqrt{2M_{\rm N}}\sqrt{2M_R}}\,,
\end{aligned} \tag{7.14}$$

in the resonance rest frame. J_z denotes the spin projection onto the z-axis. In this definition the z-axis is taken parallel to the photon momentum, then

$$\begin{aligned}
k^\mu &= \left(k^0, 0, 0, |\vec{k}|\right)\,,\\
p^\mu &= \left(\sqrt{M^2_{\rm N} + \vec{k}^{\,2}}, 0, 0, -|\vec{k}|\right)\,,\\
p^\mu_R &= p^\mu + k^\mu = (M_R, 0, 0, 0)\,,
\end{aligned} \tag{7.15}$$

are the virtual photon, nucleon and resonance four-momenta. Furthermore, in Eq. (7.14) $Q^2 = -k^2$, and

$$k_R = \frac{M^2_R - M^2_{\rm N}}{2M_R}\,. \tag{7.16}$$

The photon polarization vectors are given by

$$\begin{aligned}
\epsilon^\mu_{(\pm)} &= \mp\frac{1}{\sqrt{2}}\,(0, 1, \pm\mathrm{i}, 0)\,,\\
\epsilon^\mu_{(0)} &= \frac{1}{\sqrt{Q^2}}\left(|\vec{k}|, 0, 0, k^0\right)\,.
\end{aligned} \tag{7.17}$$

For both the MAID and PDG sets, we adopt the MAID parametrizations [145, 146] for the q^2 dependence of the amplitudes but in the PDG set,

[3] Factor $\frac{1}{\sqrt{2M_{\rm N}}\sqrt{2M_R}}$ in the definition of the helicity amplitudes comes from the adopted normalization of Dirac spinors.

$A^N_{1/2}(0)$ and $A^N_{3/2}(0)$ values at the photon point are replaced by the PDG estimates. These values are given in Table 7.2. Our results for coherent photon emission turn out to be quite sensitive to these values.

		$A_{1/2}(0)$		$A_{3/2}(0)$		$S_{1/2}(0)$
$\Delta(1232)$		-140.4	-135.0	-265.3	-255.0	17.5
$N(1440)$	(p)	-61.4	-65.0	–	–	4.2
	(n)	54.1	45.0	–	–	-41.5
$N(1520)$	(p)	-27.0	-25.0	160.6	140.0	-63.6
	(n)	-76.5	-50.0	-154.0	-115.0	13.6
$N(1535)$	(p)	66.0	105.0	–	–	-2.0
	(n)	-50.7	-75.0	–	–	28.5
$\Delta(1620)$		65.6	50.0	–	–	16.2
$N(1650)$	(p)	33.3	45.0	–	–	-3.5
	(n)	9.3	-10.0	–	–	10.1
$N(1675)$	(p)	15.3	18.0	21.6	22.0	1.1
	(n)	-61.7	-60.0	-83.7	-85.0	0
$N(1680)$	(p)	-25.1	-10.0	134.3	135.0	-44.0
	(n)	-27.9	30.0	-38.4	-35.0	0
$\Delta(1700)$		226.0	130.0	210.0	130.0	2.1
$N(1720)$	(p)	73.0	100.0	-11.5	28.0	-53.0
	(n)	-2.9	-64.0	-31.0	-4.0	0
$\Delta(1905)$		18.0	22.0	-28.0	-45.0	0
$\Delta(1910)$		18.0	20.0	–	–	0
$\Delta(1950)$		-94.0	-70.0	-121.0	-90.0	0

Table 7.2: Helicity couplings in units of 10^{-3} GeV$^{-1/2}$. The first column for each parameter corresponds to the analysis of Ref. [147], while the second column was extracted from Ref. [40].

7.3.3 Amputated amplitudes

The expression of each amputated amplitude depends on which resonance mediates the interaction. Indeed, we must distinguish the different resonances not only by their spin but also by their isospin and parity quantum numbers. In this calculation, following Ref. [148], resonances of spin higher than 3/2 are treated using the same formalism as spin 3/2 ones. The amputated amplitude for each intermediate state includes, in turn, the contri-

bution from the direct, $\Gamma^{\mu\alpha}_D$, and crossed diagram, $\Gamma^{\mu\alpha}_C$, in Fig. 7.2.

Spin 1/2 resonances

In this case

$$\Gamma^{\mu\alpha}_{1/2} = \Gamma^{\mu\alpha}_{1/2,D} + \Gamma^{\mu\alpha}_{1/2,C} = \jmath^{\mu}_{\mathrm{EM}}(-k_\gamma)\frac{\not{p} + \not{q} + M_R}{(p+q)^2 - M_R^2 + \mathrm{i}M_R\Gamma_R}\jmath^{\alpha}_{\mathrm{NC}}(q) + \jmath^{\alpha}_{\mathrm{NC}}(q)\frac{\not{p}' + \not{q} + M_R}{(p'-q)^2 - M_R^2 + \mathrm{i}\epsilon}\jmath^{\mu}_{\mathrm{EM}}(-k_\gamma)\,, \tag{7.18}$$

where M_R is the mass of the resonance and Γ_R its W-dependent decay width, discussed below. We have introduced amputated currents as

$$\langle R(p_2)|\, J^\mu\, |N(p_1)\rangle = \overline{u}(p_2)\jmath^\mu u(p_1)\,, \tag{7.19}$$

where

$$\begin{aligned}
\jmath^{\mu}_{\mathrm{EM},\pm}(q) &= \left[\frac{F_1(q^2)}{(2M_{\mathrm{N}})^2}\left(\not{q}q^\mu - q^2\gamma^\mu\right) + \frac{F_2(q^2)}{2M_{\mathrm{N}}}\mathrm{i}\sigma^{\mu\nu}q_\nu\right]\begin{pmatrix}\mathbb{I}\\ \gamma_5\end{pmatrix}\,,\\
\jmath^{\alpha}_{\mathrm{NC},\pm}(q) &= \left[\frac{\tilde{F}_1(q^2)}{(2M_{\mathrm{N}})^2}\left(\not{q}q^\mu - q^2\gamma^\mu\right) + \frac{\tilde{F}_2(q^2)}{2M_{\mathrm{N}}}\mathrm{i}\sigma^{\mu\nu}q_\nu\right]\begin{pmatrix}\mathbb{I}\\ \gamma_5\end{pmatrix}\\
&\quad + \tilde{F}_A(q^2)\gamma^\alpha\begin{pmatrix}\gamma_5\\ \mathbb{I}\end{pmatrix}\,,
\end{aligned} \tag{7.20}$$

where the first (second) row corresponds to resonances with positive (negative) parity. We have not considered a term proportional to the pseudoscalar FF in the above equation because it leads to terms in the cross section proportional to the outgoing neutrino mass and therefore negligible. In the above equation, $F_i(q^2)$ and $\tilde{F}_i(q^2)$, $i = 1, 2, A$, are the EM and NC transition FFs respectively. These FFs are specific for the transition between nucleon and each different resonance. Notice that the EM current in Eq. (7.18) is evaluated at the photon point $k_\gamma^2 = 0$.

As mentioned above, in order to obtain $F_i(q^2)$ we rely on the MAID global analysis of pion electroproduction [145, 146] data, where $\gamma^* N \to R$ transitions are described and parametrized in terms of helicity amplitudes. Substituting the EM currents of Eq. (7.20) in the definition of the helicity amplitudes of Eq. (7.14), we obtain the equations connecting them to the

EM FFs for $J = 1/2$ resonances,

$$
\begin{aligned}
A^{(p,n)}_{1/2,\pm} &= \sqrt{\frac{\pi\alpha\left[(M_R \mp M_\mathrm{N})^2 + Q^2\right]}{2M_\mathrm{N}\left(M_R^2 - M_\mathrm{N}^2\right)}}\left[\frac{Q^2}{2M_\mathrm{N}^2}F_1^{(p,n)} + \frac{M_R \pm M_\mathrm{N}}{M_\mathrm{N}}F_2^{(p,n)}\right] , \\
S^{(p,n)}_{1/2,\pm} &= \mp\sqrt{\frac{\pi\alpha\left[(M_R \pm M_\mathrm{N})^2 + Q^2\right]}{2M_\mathrm{N}\left(M_R^2 - M_\mathrm{N}^2\right)}}\frac{(M_R \mp M_\mathrm{N})^2 + Q^2}{4M_\mathrm{N}M_R} \\
&\quad \times \left[\frac{M_R \pm M_\mathrm{N}}{2M_\mathrm{N}}F_1^{(p,n)} - F_2^{(p,n)}\right] ,
\end{aligned}
\tag{7.21}
$$

where the upper (lower) sign corresponds to positive (negative) parity resonances. By inverting these equations one obtains the EM FFs in terms of the helicity amplitudes.

Isospin symmetry allows to relate NC vector FFs to the EM ones. For $I = 1/2$ resonances (N^*) these relations are the same as for nucleons:

$$
\begin{aligned}
2\tilde{F}^{(p)}_{1,2} &= \left(1 - 4\sin^2\theta_W\right)F^{(p)}_{1,2} - F^{(n)}_{1,2} - F^{(s)}_{1,2} , \\
2\tilde{F}^{(n)}_{1,2} &= \left(1 - 4\sin^2\theta_W\right)F^{(n)}_{1,2} - F^{(p)}_{1,2} - F^{(s)}_{1,2} , \\
&\quad ,
\end{aligned}
\tag{7.22}
$$

For the purely isovector transitions to resonances with $I = 3/2$ (Δ)

$$
\tilde{F}_{1,2} = \left(1 - 2\sin^2\theta_W\right)F_{1,2} , \tag{7.23}
$$

for both protons and neutrons.

In the same way, isospin rotations relate axial NC FFs to the CC ones. For $I = 1/2$ resonances

$$
2\tilde{F}^{(p,n)}_A = \pm F_A + F^{(s)}_A , \tag{7.24}
$$

while for $I = 3/2$

$$
\tilde{F}_A = -F_A . \tag{7.25}
$$

For the axial couplings $F_A(0)$ one can derive off-diagonal GT relations as shown in Sec. 7.3.4. In contrast, there is no experimental information that could guide our choice for the q^2 dependence of F_A. Then, we simply adopt a dipole ansatz

$$
F_A = F_A(0)\left(1 - \frac{q^2}{M_A^{*2}}\right)^{-2} , \tag{7.26}
$$

with $M_A^* = 1$ GeV, so that the axial transition radius has the right order of magnitude.

Finally, we set to zero the strange vector and axial-vector FFs that are present in the $I = 1/2$ case, for which no experimental information is available but likely have a negligible impact on the observables.

Spin 3/2 resonances

In the case of transitions from a nucleon to a resonance with $J = 3/2$, the amputated amplitude reads

$$\begin{aligned}\Gamma^{\mu\alpha}_{3/2} &= \Gamma^{\mu\alpha}_{3/2,D} + \Gamma^{\mu\alpha}_{3/2,C} \\ &= \mathbb{i}\, e\, \gamma^0 \left[\mathcal{J}^{\beta\alpha}_{\mathrm{EM}}\left(p', k_\gamma\right)\right]^\dagger \gamma^0 \frac{P_{\beta\rho}\left(p+q\right)}{\left(p+q\right)^2 - M_R^2 + \mathbb{i} M_R \Gamma_R} \mathcal{J}^{\rho\mu}_{\mathrm{NC}}(p,q) \\ &\quad + \mathbb{i}\, e\, \gamma^0 \left[\mathcal{J}^{\beta\alpha}_{\mathrm{NC}}\left(p', -q\right)\right]^\dagger \gamma^0 \frac{P_{\beta\rho}\left(p'-q\right)}{\left(p'-q\right)^2 - M_R^2 + \mathbb{i}\epsilon} \mathcal{J}^{\rho\mu}_{\mathrm{EM}}(p, -k_\gamma)\,,\end{aligned} \tag{7.27}$$

where $P_{\beta\rho}(p)$ is the spin 3/2 projector operator, which reads

$$P_{\mu\nu}(p) = -\left(\not{p} + M_R\right)\left[g^{\mu\nu} - \frac{1}{3}\gamma^\mu\gamma^\nu - \frac{2}{3}\frac{p^\mu p^\nu}{M_R^2} + \frac{1}{3}\frac{p^\mu\gamma^\nu - p^\nu\gamma^\mu}{M_R}\right], \tag{7.28}$$

and

$$\begin{aligned}\mathcal{J}^{\delta\mu}_{\mathrm{EM},\pm}(p,q) = &\left[\frac{C_3^V(q^2)}{M_{\mathrm{N}}}\left(g^{\delta\mu}\not{q} - q^\delta\gamma^\mu\right) + \frac{C_4^V(q^2)}{M_{\mathrm{N}}^2}\left(g^{\delta\mu}q\cdot p_R - q^\delta p_R^\mu\right)\right. \\ &\left. + \frac{C_5^V(q^2)}{M_{\mathrm{N}}^2}\left(g^{\delta\mu}q\cdot p - q^\delta p^\mu\right)\right]\begin{pmatrix}\gamma_5\\ \mathbb{I}\end{pmatrix}, \\ \mathcal{J}^{\sigma\alpha}_{\mathrm{NC},\pm}(p,q) = &\left[\frac{\tilde{C}_3^V\left(q^2\right)}{M_{\mathrm{N}}}\left(g^{\sigma\alpha}\not{q} - q^\sigma\gamma^\alpha\right) + \frac{\tilde{C}_4^V\left(q^2\right)}{M_{\mathrm{N}}^2}\left(g^{\sigma\alpha}q\cdot p_R - q^\sigma p_R^\alpha\right)\right. \\ &\left. + \frac{\tilde{C}_5^V\left(q^2\right)}{M_{\mathrm{N}}^2}\left(g^{\sigma\alpha}q\cdot p - q^\sigma p^\alpha\right)\right]\begin{pmatrix}\gamma_5\\ \mathbb{I}\end{pmatrix} \\ &+ \left[\frac{\tilde{C}_3^A\left(q^2\right)}{M_{\mathrm{N}}}\left(g^{\sigma\alpha}\not{q} - q^\sigma\gamma^\alpha\right) + \frac{\tilde{C}_4^A\left(q^2\right)}{M_{\mathrm{N}}^2}\left(g^{\sigma\alpha}q\cdot p_R - q^\sigma p_R^\alpha\right)\right. \\ &\left. + \tilde{C}_5^A\left(q^2\right)g^{\sigma\alpha}\right]\begin{pmatrix}\mathbb{I}\\ \gamma_5\end{pmatrix},\end{aligned} \tag{7.29}$$

with $p_R = p+q$. In both cases, the upper (lower) sign correspond to positive (negative) parity resonances. As for $S = 1/2$ resonances and for exactly the same reasons, pseudoscalar terms have been omitted.

Analogously to the spin 1/2 case, substituting Eq. (7.29) in the helicity amplitudes, Eq. (7.14), we obtain

$$\begin{aligned}
A^{(p,n)}_{1/2,\pm} &= \sqrt{\frac{\pi\alpha\left[(M_R \mp M_\mathrm{N})^2 + Q^2\right]}{3M_\mathrm{N}\left(M_R^2 - M_\mathrm{N}^2\right)}}\left[\frac{M_\mathrm{N}^2 \pm M_\mathrm{N}M_R + Q^2}{M_\mathrm{N}M_R}C_3^{V(p,n)}\right. \\
&\quad \left. - \frac{-M_R - M_\mathrm{N}^2 - Q^2}{2M_\mathrm{N}^2}C_4^{V(p,n)} - \frac{M_R^2 - M_\mathrm{N}^2 + Q^2}{2M_\mathrm{N}^2}C_5^{V(p,n)}\right], \\
A^{(p,n)}_{3/2,\pm} &= \sqrt{\frac{\pi\alpha\left[(M_R \mp M_\mathrm{N})^2 + Q^2\right]}{M_\mathrm{N}\left(M_R^2 - M_\mathrm{N}^2\right)}}\left[\frac{M_\mathrm{N} \pm M_R}{M_\mathrm{N}}C_3^{V(p,n)}\right. \\
&\quad \left. + \frac{-M_R - M_\mathrm{N}^2 - Q^2}{2M_\mathrm{N}^2}C_4^{V(p,n)} + \frac{M_R^2 - M_\mathrm{N}^2 + Q^2}{2M_\mathrm{N}^2}C_5^{V(p,n)}\right], \\
S^{(p,n)}_{1/2,\pm} &= \pm\sqrt{\frac{\pi\alpha\left[(M_R \pm M_\mathrm{N})^2 + Q^2\right]}{6M_\mathrm{N}\left(M_R^2 - M_\mathrm{N}^2\right)}\frac{(M_R \mp M_\mathrm{N})^2 + Q^2}{M_R^2}} \\
&\quad \times\left[\frac{M_R}{M_\mathrm{N}}C_3^{V(p,n)} + \frac{M_R^2}{M_\mathrm{N}^2}C_4^{V(p,n)} + \frac{M_R^2 + M_\mathrm{N}^2 + Q^2}{2M_\mathrm{N}^2}C_5^{V(p,n)}\right],
\end{aligned} \tag{7.30}$$

where the upper and lower signs correspond to positive and negative parity resonances respectively. With these equations, the EM FFs are obtained as functions of the helicity amplitudes.

For $I = 1/2$ resonances we have again the same isospin symmetry than for nucleons, then the vector NC FFs can be written in terms of the just deduced EM FFs

$$\begin{aligned}
\tilde{C}_i^{V,(p)} &= \left(\frac{1}{2} - 2\sin\theta_W\right)C_i^{(p)} - \frac{1}{2}C_i^{(n)} - \frac{1}{2}C_i^{sV}, \\
\tilde{C}_i^{V,(n)} &= \left(\frac{1}{2} - 2\sin\theta_W\right)C_i^{(n)} - \frac{1}{2}C_i^{(p)} - \frac{1}{2}C_i^{sV},
\end{aligned} \tag{7.31}$$

with $i = 3, 5$, while for $I = 3/2$ resonances we have

$$\tilde{C}_i^{V} = \left(1 - 2\sin^2\theta_W\right)C_i^{V}. \tag{7.32}$$

In this case $C_i^V = C_i^{V(p)} = C_i^{V(n)}$.

For the $\Delta(1232)$ we can take advantage of the clear dominance of the M1 multipole for the EM transition and simplify the expressions taking

$$\begin{aligned} C^V_{5,\Delta(1232)} &= 0\,, \\ C^V_{4,\Delta(1232)} &= -\frac{M_{\rm N}}{M_{\Delta(1232)}} C^V_{3,\Delta(1232)}\,. \end{aligned} \tag{7.33}$$

Then, in this scenario, $C^V_{3,\Delta(1232)}$ can be written as a simple function of $A_{3/2}$, as follows Eq. (7.30).

In the axial sector, isospin relations lead to

$$\tilde{C}_i^{A,(p,n)} = \pm\frac{1}{2} C_i^A + \frac{1}{2} C_i^{s_A}\,, \tag{7.34}$$

for $I = 1/2$ resonances while for $I = 3/2$ resonances we have

$$\tilde{C}_i^A = -C_i^A\,, \tag{7.35}$$

For the dominant axial FF, we assume a dipole q^2 dependence,

$$C_5^A(q^2) = C_5^A(0)\left(1 - \frac{q^2}{M_A^2}\right)^{-2}\,, \tag{7.36}$$

with $M_A = 1$ GeV. The coupling $C_5^A(0)$ is determined via GT relations as explained below. As for the q^2 dependence of $C_5^A(0)$, there is no experimental information to constrain the remaining axial FFs. We simply set them $\tilde{C}_3^A(q^2) = \tilde{C}_4^A(q^2) = 0$ owing to the fact that their contribution to the amplitude squared contain higher powers of q^2 and, then, their contributions should be small. This is specially true in coherent scattering, where high values of q^2 are suppressed. The only exception of this prescription corresponds to the $N - \Delta(1232)$ transition, for which some information is available from ANL and BNL bubble chamber experiments on deuterium due to the prominent role it plays in pion production. Following the analysis of Ref. [149], we keep the dipole ansatz but with $M_A = 0.93$ GeV, while adopting the so-called Adler model [150, 151]

$$\begin{aligned} \tilde{C}^A_{3,\Delta(1232)}(q^2) &= 0\,, \\ \tilde{C}^A_{4,\Delta(1232)}(q^2) &= -\frac{\tilde{C}^A_{5,\Delta(1232)}(q^2)}{4}\,, \end{aligned} \tag{7.37}$$

for the rest of axial FFs.

As for $S = 1/2$ resonances, we set to zero the strange vector and axial-vector FFs that are present in the $I = 1/2$ case.

7.3.4 Resonance decay widths and axial couplings

For the invariant mass dependence of the resonance decay width we follow to different strategies. In the case of the MAID set, as in the MAID model [152], all the width that does not come from the πN decay is ascribed to the two-pion channel:

$$\Gamma_R(W) = \Gamma_{R\to\pi N}(W) + (1 - b_R)\,\Gamma_{R\to\pi\pi N}(W)\,, \tag{7.38}$$

where b_R is the πN branching ratio. The only exception is the $N(1535)$, for which the decay to nucleon and η is also treated separately. Then, instead of Eq. (7.38) we have

$$\begin{aligned}\Gamma_{N1535}(W) =&\Gamma_{N1535\to\pi N}(W) + \Gamma_{N1535\to\eta N}(W)\\ &+ (1 - b_{N1535\to\pi N} - b_{N1535\to\eta N})\,\Gamma_{N1535\to\pi\pi N}(W)\,.\end{aligned} \tag{7.39}$$

The two-pion decay partial decay width is parametrized as in Ref. [153][4]

$$\Gamma_{R\to\pi\pi N}(W) = \Gamma_0 \left(\frac{|\vec{q}_{2\pi}|(W)}{|\vec{q}_{2\pi}|(M_R)}\right)^{2L+4} \left(\frac{M_R}{W}\right)\,, \tag{7.40}$$

where Γ_0 is the total decay width in the vacuum and L the angular momentum of the πN partial wave; the CM momentum of the 2π compound is approximated as [153]

$$|\vec{q}_{2\pi}|(W) = \frac{\sqrt{\left[W^2 - (M_{\rm N} + 2m_\pi)^2\right]\left[W^2 - (M_{\rm N} - 2m_\pi)^2\right]}}{2W}\,. \tag{7.41}$$

In Table 7.1 we have listed the mass, total decay width , partial wave and πN branching ratio for the resonances under consideration. For the calculations corresponding to the MAID parametrization, we use the parameter values of the first column in the table.

In the case of the PDG set, besides the πN channel, we take into account the most relevant decay channels according to the PDG estimate, with branching ratios within the PDG ranges. They are listed in Table. 7.3. Often, the decay products are unstable mesons or baryon resonances. We then use [154]

$$\Gamma_{R\to ab}(W) = \Gamma_{R\to ab}(M_R)\frac{\rho_{ab}(W)}{\rho_{ab}(M_R)}\,, \tag{7.42}$$

[4]Except for the barrier-penetration factor since we do not incorporate such factors in this study.

where ρ_{ab} is given by

$$\begin{aligned}\rho_{ab}(W) = &\int d\left(p_a^2\right) d\left(p_b^2\right) \mathcal{A}\left(p_a^2\right) \mathcal{A}\left(p_b^2\right) \frac{|\vec{q}_{\rm cm}|^{2L+1}\left(W^2, p_a^2, p_b^2\right)}{W} \\ &\times \Theta\left(W - \sqrt{p_a^2} - \sqrt{p_b^2}\right) ,\end{aligned} \tag{7.43}$$

and the CM momentum of the final state products is

$$|\vec{q}_{\rm cm}| = \frac{\lambda^{1/2}\left(W^2, p_a^2, p_b^2\right)}{2W} , \tag{7.44}$$

with λ, the Källén function defined in Appendix C.2. The vacuum spectral function reads

$$\mathcal{A}(p_a^2) = -\frac{1}{\pi} \operatorname{Im}\left\{\frac{1}{p_a^2 - M_a^2 + \mathrm{i} M_a \Gamma_a(p_a^2)}\right\} . \tag{7.45}$$

If one of the decay products is a stable particle, then for that particle $\Gamma_a = 0$ and

$$\mathcal{A}(p_a^2) = \delta\left(p_a^2 - M_a^2\right) , \tag{7.46}$$

hence

$$\begin{aligned}\rho_{ab}(W) = &\frac{M_b}{\pi W} \int d(p_b^2) \frac{\Gamma_b(p_b^2)}{\left(p_b^2 - M_b^2\right)^2 + M_b^2 \Gamma_b^2(p_b^2)} \\ &\times |\vec{q}_{\rm cm}|^{2L+1}\left(W^2, p_a^2, p_b^2\right) \Theta\left(W - M_a - \sqrt{p_b^2}\right) .\end{aligned} \tag{7.47}$$

The one-pion channel is not only prominent for most resonances but often it is also the best understood. Furthermore, it is particularly relevant here because the strength of the resonance coupling to πN can be used to obtain the leading transition axial couplings thanks to the off-diagonal GT relations. In the following we give a more detailed description of how the πN channel is modeled in the present work.[5]

Spin 1/2 resonances

The effective Lagrangian describing the $R_{1/2} N \pi$ coupling can be cast as

$$\mathcal{L}_{R_{1/2}N\pi} = \frac{f^*_{1/2}}{m_\pi} \overline{\Psi} \left\{ \begin{array}{c} \gamma^\mu \gamma_5 \\ \gamma^\mu \end{array} \right\} \left(\partial_\mu \vec{\pi} \cdot \vec{t}\right) \Psi_{R_{1/2}} + \text{H.c.} , \tag{7.48}$$

[5] The treatment of the $N(1535)$ decay to ηN is analogous to the πN one, as described below.

$N(1440)$	br$[\Delta(1232)\pi]$		L		br$[N\sigma]$		L	
	0.17		P		0.18		S	
$N(1520)$	br$[\Delta(1232)\pi]$		L		br$[\Delta(1232)\pi]$		L	
	0.27		S		0.13		D	
$N(1535)$	br$[N\eta]$		L		br$[N\sigma]$		L	
	0.48		S		0.03		P	
	br$[N(1440)\pi]$		L		br$[\Delta(1232)\pi]$		L	
	0.05		S		0.02		D	
$\Delta(1620)$	br$[\Delta(1232)\pi]$		L		br$[N(1440)\pi]$		L	
	0.64		D		0.06		S	
$N(1650)$	br$[N\eta]$	L	br$[\Lambda K]$	L	br$[\Delta(1232)\pi]$		L	
	0.14	S	0.05	S	0.07		D	
	br$[N\sigma]$		L		br$[N(1440)\pi]$		L	
	0.05		P		0.09		S	
$N(1675)$	br$[\Delta(1232)\pi]$		L		br$[N\sigma]$		L	
	0.51		D		0.09		F	
$N(1680)$	br$[\Delta(1232)\pi]$	L	br$[\Delta(1232)\pi]$	L	br$[N\sigma]$		L	
	0.09	P	0.09	F	0.17		D	
$\Delta(1700)$	br$[\Delta(1232)\pi]$	L	br$[\Delta(1232)\pi]$	L	br$[N(1520)\pi]$		L	
	0.45	S	0.22	D	0.06		P	
	br$[N(1535)\pi]$		L		br$[\Delta(1232)\eta]$		L	
	0.02		P		0.10		S	
$N(1720)$	br$[N\eta]$	L	br$[N\omega]$	L	br$[\Lambda K]$		L	
	0.03	P	0.21	P	0.04		P	
	br$[\Delta(1232)\pi]$	L	br$[N\sigma]$	L	br$[N(1520)\pi]$		L	
	0.51	P	0.07	D	0.03		S	
$\Delta(1905)$	br$[\Delta(1232)\pi]$		L		br$[\Delta(1232)\pi]$		L	
	0.26		P		0.50		F	
	br$[N(1680)\pi]$		L		br$[\Delta(1232)\eta]$		L	
	0.09		P		0.03		P	
$\Delta(1910)$	br$[\sigma K]$	L	br$[\Delta(1232)\pi]$	L	br$[N(1440)\pi]$		L	
	0.10	P	0.54	P	0.06		P	
$\Delta(1950)$	br$[\Delta(1232)\pi]$		L		br$[N(1680)\pi]$		L	
	0.27		F		0.33		P	

Table 7.3: List of resonance decay channels, excluding πN, extracted from Ref. [40]. L stands for the relative angular momenta of the decay particles.

where the upper and lower rows correspond to positive and negative parity resonances respectively. Ψ and $\Psi_{R_{1/2}}$ are the nucleon and resonance fields. The pion field is denoted by $\vec{\pi}$. In the case of $I = 1/2$ resonances, $\vec{t} = \vec{\tau}$, the vector made of Pauli matrices. For $I = 3/2$ resonances we have the isospin $1/2 \to 3/2$ transition operator, $\vec{t} = \vec{T}$, defined by the matrix of the spherical components of $\vec{T}^\dagger$ [155]

$$T^\dagger_{\pm 1} \equiv \mp \frac{T^\dagger_1 \pm \mathrm{i} T^\dagger_2}{\sqrt{2}} \; ; \quad T^\dagger_0 \equiv T^\dagger_3 \; . \tag{7.49}$$

Namely,

$$\left\langle \frac{3}{2}, M_R \middle| T^\dagger_\lambda \middle| \frac{1}{2}, M_\mathrm{N} \right\rangle = \left(\frac{1}{2}, 1, \frac{3}{2} \middle| M_\mathrm{N}, \lambda, M_R \right) \; . \tag{7.50}$$

where $\left(\frac{1}{2}, 1, \frac{3}{2} \,\middle|\, M_\mathrm{N}, \lambda, M_R\right)$ is a Clebsch-Gordan coefficient.

From the Lagrangian of Eq. (7.48) we can obtain the $R_{1/2} \to \pi N$ decay width in the resonance rest frame, in terms of the invariant mass of the system,

$$\begin{aligned} \Gamma_{R_{1/2,\pm} \to \pi N}(W) = \frac{c_I}{4\pi} \left(\frac{f^*_{1/2}}{m_\pi} \right)^2 (W \pm M_\mathrm{N})^2 \\ \times \frac{E' \mp M_\mathrm{N}}{W} \, |\vec{q}_\mathrm{cm}| \, \Theta \left(W - M - m_\pi \right) \; , \end{aligned} \tag{7.51}$$

where Θ is the step function, $c_I = 3$ for $I = 1/2$ and $c_I = 1$ for $I = 3/2$. The upper and lower signs hold for positive and negative parity, respectively. The momentum and the energy of the outgoing nucleon are given in this frame by

$$\begin{aligned} |\vec{q}_\mathrm{cm}| &= \frac{\sqrt{\left(W^2 - m_\pi^2 - M_\mathrm{N}^2 \right)^2 - 4 m_\pi^2 M_\mathrm{N}^2}}{2W} \; , \\ E' &= \frac{W^2 + M_\mathrm{N}^2 - m_\pi^2}{2W} \; . \end{aligned} \tag{7.52}$$

Using the values for the Breit-Wigner mass, total width and branching ratio tabulated in Table 7.1, from

$$\Gamma_{R \to \pi N}(M_R) = \Gamma_0 \, b_R \; , \tag{7.53}$$

in Eq. (7.51) we obtain the coupling $f^*_{1/2}$.

On the other hand, proceeding in an analogous way as for the diagonal (nucleon) case, Sec. 3.2, we can get the off-diagonal GT relation and write

the axial coupling in terms of $f^*_{1/2}$,

$$F_A(0) = -c_{\rm iso}\sqrt{2}\frac{f^*_{1/2}}{m_\pi}f_\pi \,, \tag{7.54}$$

with the isospin factor $c_{\rm iso} = \sqrt{2}$ and $c_{\rm iso} = -\sqrt{1/3}$ for $I = 1/2$ and $I = 3/2$ resonances, respectively.

Finally, in analogy to the $N(1535) \to \pi N$ decay, for the $N(1535) \to \eta N$ we can write

$$\begin{aligned}\Gamma_{N(1535)\to\eta N}(W) = \frac{1}{4\pi}\left(\frac{\tilde{f}^*_{1/2}}{m_\eta}\right)^2 (W - M_{\rm N})^2 \\ \times \frac{E' + M_{\rm N}}{W}\,|\vec{q}_{\rm cm}|\,\Theta\left(W - M - m_\eta\right) \,,\end{aligned} \tag{7.55}$$

where $\tilde{f}^*_{1/2}$ is the coupling to this channel, that can be obtained from the corresponding branching ratio, which in the case of MAID we set to $b_{N(1535)\to\eta N} = 0.42$ [156], and the analogous one for PDG is given in Table 7.3.

Spin 3/2 resonances

In the case of resonances with spin 3/2 the $R_{3/2}N\pi$ coupling is given by the Lagrangian

$$\mathcal{L}_{R_{3/2}N\pi} = \frac{f^*_{3/2}}{m_\pi}\overline{\Psi}\left\{\begin{array}{c}\mathbb{I}\\ \gamma_5\end{array}\right\}\left(\partial_\mu\vec{\phi}\cdot\vec{t}\right)\Psi^\mu_{R_{3/2}} + \text{H.c.}\,, \tag{7.56}$$

where the upper and lower rows hold for positive and negative resonances respectively; $\Psi^\mu_{R_{3/2}}$ is a Rarita-Schwinger field. The correspondent decay width is given by

$$\Gamma_{R_{3/2,\pm}\to\pi N}(W) = \frac{c_I}{6\pi}\left(\frac{f^*_{3/2}}{m_\pi}\right)^2 \frac{E' \pm M_{\rm N}}{2W}|\vec{q}_{\rm cm}|^3\,\Theta\left(W - M - m_\pi\right) \,, \tag{7.57}$$

with the upper (lower) sign standing for the positive (negative) resonances. The off-diagonal GT relation has an analogous form to Eq. (7.54),

$$C_5^A(0) = -c_{\rm iso}\sqrt{2}\frac{f^*_{3/2}}{m_\pi}f_\pi \,. \tag{7.58}$$

7.3.5 Nuclear medium corrections

In our model for NC coherent photon emission, as discussed above, the elementary process is mediated by resonances, which are produced inside the nucleus. Therefore, the nuclear medium, can alter the resonance properties. We must, then, consider these effects. We specifically do it for the $\Delta(1232)$ resonance, which dominates the cross section and is known to be strongly modified in this medium, see Refs. [157–163]. For the rest of the baryon states, less information is available about a medium modification of states which are already broader and less isolated than the $\Delta(1232)$. Furthermore, their contribution to the cross section is small so we choose to neglect this correction.

The denominator of the $\Delta(1232)$ propagator in vacuum reads

$$D_R(p^2) = \frac{1}{p_R^2 - M_R^2 + \mathbb{i} M_R \Gamma_R(p^2)} \,, \tag{7.59}$$

with $\Gamma_R(p^2)$ given by the $\Delta \to N\pi$ decay, Eq. (7.57).[6] The propagator is then modified in the nucleus as $D_R \to \tilde{D}_R$, with

$$\begin{aligned} \tilde{D}_R(p^2, \rho(r)) = \Big[& p_R^2 - (M_R + \mathrm{Re}\{\Sigma_R\})^2 \\ & + \mathbb{i} \left(M_R + \mathrm{Re}\{\Sigma_R\}\right) \left(\tilde{\Gamma}_R - 2\,\mathrm{Im}\{\Sigma_R\}\right) \Big]^{-1} \,, \end{aligned} \tag{7.60}$$

where $\tilde{\Gamma}_R$ is the vacuum decay width corrected by the Pauli blocking of the final nucleon in the $\Delta \to N\pi$ decay. Adopting the approximation of Ref. [164] we have

$$\tilde{\Gamma}_R\left(p^2, \rho(r)\right) \approx \Gamma_R(p^2) I\left(p^2, \rho(r)\right) \,, \tag{7.61}$$

where

$$\begin{aligned} I\left(p^2, \rho(r)\right) = 1 & + \theta\left(\tilde{q} - 1\right) \left(-\frac{2}{5}\frac{1}{\tilde{q}^2} + \frac{9}{35}\frac{1}{\tilde{q}^4} - \frac{2}{21}\frac{1}{\tilde{q}^6} \right) \\ & + \theta\left(1 - \tilde{q}\right) \left(\frac{34}{35}\tilde{q} - \frac{22}{105}\tilde{q}^3 - 1 \right) \,, \end{aligned} \tag{7.62}$$

with

$$\tilde{q} = \frac{|\vec{q}_{\mathrm{cm}}|}{k_F\left(r\right)} \,, \tag{7.63}$$

[6] The coupling, obtained with the method previously described, is $f^*_{\Delta(1232)} = 2.14$.

and the Fermi momentum[7]

$$k_F\left(r\right) = \left(3\pi^2 \frac{\rho(r)}{2}\right)^{1/3} . \tag{7.64}$$

The nucleon density, $\rho(r) = \rho_p(r) + \rho_n(r)$ is normalized as in Eq. (4.23). In Ref. [34], as well as in earlier studies of coherent pion production the $\Delta(1232)$ self-energy has been taken from the many-body calculation of Ref. [160]. Here, instead, the simpler approximation of a central spreading potential has been adopted:

$$\begin{aligned} \mathrm{Re}\{\Sigma_\Delta\} &\approx 0 \,, \\ \mathrm{Im}\{\Sigma_\Delta\} &\approx 2V_0 \frac{\rho(r)}{\rho(0)} \,, \end{aligned} \tag{7.65}$$

with $V_0 \approx 80$ MeV [165]. We have checked that with this self-energy we get results that are consistent with those obtained with the more sophisticated self-energy of Ref. [160].

This broadening of the $\Delta(1232)$ resonance propagator only applies to the scattering direct diagram in Fig. 7.2. Therefore, for the rest of the cases, as the amputated amplitudes do not have any dependence on the density, we can use Eq. (7.11). For the direct diagram of the $\Delta(1232)$, we can write

$$\tilde{\Gamma}^{\mu\alpha}_{R,\,\mathrm{Dir}}\left(\left(p+q\right)^2, \rho(r)\right) = G^{\mu\alpha}\tilde{D}_R\left(\left(p+q\right)^2, \rho(r)\right) \,, \tag{7.66}$$

where

$$G^{\mu\alpha} = \mathbb{i}\, e\, \gamma^0 \left[\jmath^{\beta\alpha}_{\mathrm{EM}}\left(p', k_\gamma\right)\right]^\dagger \gamma^0 P_{\beta\rho}\left(p+q\right) \jmath^{\rho\mu}_{\mathrm{NC}}(p,q) \,. \tag{7.67}$$

As $G^{\mu\alpha}$ does not depend on the density, we have

$$R^{\mu\alpha} = \sum_{N=p,n} \frac{1}{2}\mathrm{Tr}\left[\frac{\not{p} + M_{\mathrm{N}}}{2M_{\mathrm{N}}}\gamma_0 G^{\mu\alpha}_N\right] \frac{M_{\mathrm{N}}}{E_p}\tilde{\mathcal{F}}_N \,, \tag{7.68}$$

with

$$\tilde{\mathcal{F}}_N = \frac{4\pi}{\left|\vec{q} - \vec{k}_\gamma\right|} \int dr\, r \sin\left(\left|\vec{q} - \vec{k}_\gamma\right| r\right) \rho_N(r) \tilde{D}_R\left(\left(p+q\right)^2, \rho_N(r)\right) \,. \tag{7.69}$$

In the case of the $\Delta(1232)$, since $G^{\mu\alpha}_{(p)} = G^{\mu\alpha}_{(n)} = G^{\mu\alpha}$,

$$R^{\mu\alpha} = \frac{1}{2}\mathrm{Tr}\left[\frac{\not{p} + M_{\mathrm{N}}}{2M_{\mathrm{N}}}\gamma_0 G^{\mu\alpha}\right] \frac{M_{\mathrm{N}}}{E_p}\left(\tilde{\mathcal{F}}_{(p)} + \tilde{\mathcal{F}}_{(n)}\right) \,, \tag{7.70}$$

[7] In this case we do not distinguish between both types of nucleons, which leads to a difference of 2 due to isospin with respect to Eq. (4.38).

Performing this integral can be computationally expensive.[8] Therefore we evaluate the propagator at the average nuclear density, $\overline{\rho}$,

$$\tilde{\mathcal{F}}_N = \tilde{D}_R\left((p+q)^2, \overline{\rho}\right) F_N\left(\left|\vec{q} - \vec{k}_\gamma\right|\right) , \tag{7.71}$$

with $\overline{\rho}$ calculated as

$$\overline{\rho} = \frac{A}{\frac{4}{3}\pi R^3} , \tag{7.72}$$

where $R = (1.2 \text{ fm})A^{1/3}$. Then, the average density has a constant value of $\overline{\rho} = 0.138 \text{ fm}^{-3}$. In Fig.7.3 we compare this approximate result with the calculation without the factorization of the density integral in the case of the $\Delta(1232)$ resonance alone and for a ^{12}C target. In this figure we also show the difference between using the Eq. (7.65) potential and the Ref. [160] self-energy. Although in our calculations we choose the nuclear FF parametrization of Eq. (3.76), in Fig. 7.3 for this comparison the harmonic oscillator parametrization, that can be found in Ref. [55], has been taken. These intermediate results are also used in next section to compare our approximations to the results of Ref. [34], where the harmonic oscillator density profile was used for ^{12}C. In Fig. 7.3 only a small difference between

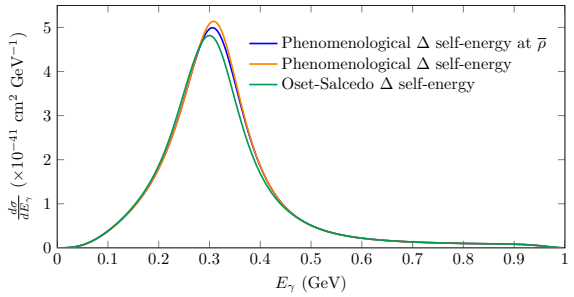

Figure 7.3: Differential cross section for the coherent NCγ reaction as a function of the outgoing photon energy in the Laboratory frame. Results are shown for ^{12}C, with incoming neutrino energy of 1 GeV and the harmonic oscillator nuclear density profile of Ref. [55]. Orange and green curves have been calculated by performing the integration over density, taking the approximation of Eq. (7.65) and the self-energy of Ref. [160], respectively. The blue line is obtained with the factorization of the nuclear form factor, using the average nuclear density (7.71) and the approximated self-energy.

[8] The computing time becomes relevant when considering the implementation of this model in Monte Carlo event generators like GENIE or NuWro.

the curves in the peak region can be noticed. At higher energies of the incoming neutrino we observe similar effects. As such a sensitivity is not at reach for future experimental measurements of this process, the approximations previously described are justified and, therefore, used in the rest of the work.

7.4 Results

We begin this section by comparing our results with those of Ref. [34], taking only the $\Delta(1232)$, $N(1440)$, $N(1520)$ and $N(1535)$ resonances into account. In Fig. 7.4 we show our results, using the MAID set for both energy and angular distributions, in neutrino mode, together with the corresponding curves from Ref. [34]. The difference observed between the two results (blue vs green curves) can be chiefly attributed to the difference in the $N-\Delta(1232)$ axial coupling value. Indeed, in Ref. [34] a value of $C^A_{5,\Delta(1232)}(0) = 1.0$ was used, as well as a harmonic oscillator density profile. Taking the same $C^A_{5,\Delta(1232)}(0)$ and nuclear FF parametrization, our results get much closer to those of the Ref. [34]. The small remaining difference is mainly due to the density factorization approximation and the phenomenological in-medium $\Delta(1232)$ self-energy. In antineutrino mode we observe similar effects.

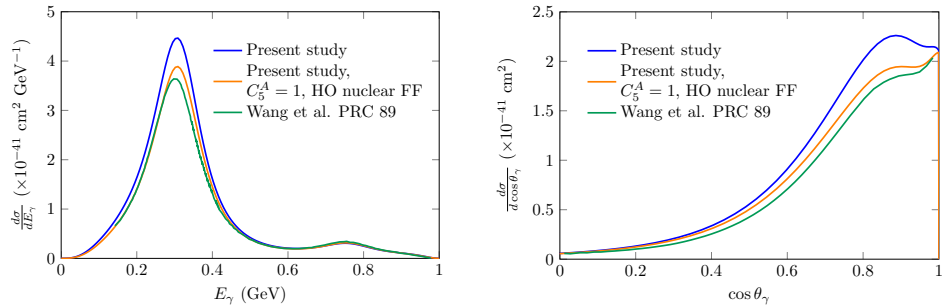

Figure 7.4: Energy (left) and angular (right) distributions for coherent NCγ on ^{12}C, for 1 GeV incoming neutrinos. Results from Ref. [34] (green curve) are compared to those of the present work using only the $\Delta(1232)$, $N(1440)$, $N(1520)$ and $N(1535)$ resonances (blue curve). Changing the value of C_5^A and the nuclear FF to match those in Ref. [34] we obtain the orange curve.

7.4.1 Extension of the model to higher energies

As the neutrino energy increases, new excitation channels for the nucleon open and the inclusion of heavier resonances becomes necessary. In the present work we incorporated all the N^* and Δ resonances listed in Table 7.1. A simple estimate of the E_γ in the Laboratory frame that corresponds to a resonance peak can be obtained from

$$\left(k_\gamma + p'\right)^2 = M_R^2 \,, \tag{7.73}$$

Taking p' from Eqs. (7.8, 7.9) and for $\vec{k}_\gamma \approx \vec{q}$, which is favored by the nuclear FF we obtain

$$E_\gamma = \frac{M_R^2 - M_{\rm N}^2}{2M_{\rm N}} \,. \tag{7.74}$$

This estimate also allows us to gauge the validity range of the model in E_γ: given the resonance content of our model and the width of the states one can see for $E_\gamma \gtrsim 2.5$ GeV the invariant masses probed are too high for the model to be reliable. We therefore restrict $E_\gamma < 2.5$ GeV in all the forthcoming results.

As expected from Eq. (7.74) and phase space considerations, the addition of heavier resonances has a very small effect for neutrinos of energy around 1 GeV. This can be realized by comparing the full calculation with the results where only the lightest four states are taken into account, Fig. 7.5. At this energy the contribution of the $\Delta(1232)$ dominates the distribution, together with a small peak that comes from the $N(1520)$ resonance. This is consistent with the results obtained in Ref. [34].

In Fig. 7.6 we present separately the photon energy distributions of each resonance, for neutrinos with 3 GeV energy and both MAID and PDG sets of parameters. These results plots clearly show the dominant role of the $\Delta(1232)$, with some strength coming from the $N(1520)$ for $E_\gamma < 1$ GeV. For $E_\gamma > 1$ GeV, several resonances overlap but the only non negligible strength is provided by $\Delta(1700)$ and $\Delta(1950)$.

In the case of the $\Delta(1232)$ the two curves overlap. For some resonances, instead, big differences are apparent. We have identified the different values in masses, total widths and electromagnetic couplings as the main origin of the discrepancies rather than the different treatment of the invariant mass dependence of the width. An example of this effect is represented in Fig. 7.7, for the $N(1650)$ resonance. There we show curves for the MAID set using different combinations of the parameters with the PDG result as a reference. When all the values are adopted while keeping the $\Gamma_R(W)$ parametrization

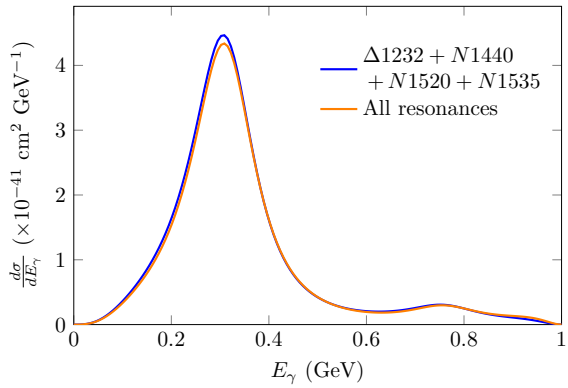

Figure 7.5: Differential cross section for coherent NCγ on ^{12}C as a function of the outgoing photon energy, with 1 GeV incoming neutrinos. Results taking the Ref. [153] model.

of Eq. (7.38) (green dashed line), the result is very close to the PDG one. In the case of $N(1720)$, where there is a huge difference in the parameter values, the discrepancy in the cross section is around an order of magnitude. In almost all cases, the peak position is the same for both sets with the clear exception of $\Delta(1620)$ where the maximum is shifted due to the disparity in the resonance mass.

In Fig 7.8 the E_γ distributions are shown at 1, 3 and 6 GeV of incoming neutrino energy.[9] The tendency of the cross section towards saturation is apparent with small differences between the results at 3 and 6 GeV. In Fig. 7.9 the comparison between MAID and PDG sets are shown for 3 and 6 GeV energy incoming neutrinos. As there is no significant difference in the $\Delta(1232)$ region, we show the results above 0.5 GeV, where the discrepancies are present. The differences between sets exposed in Fig. 7.6 do not lead to significant variations in the total cross sections due to the smallness of many of the individual contributions. Looking back to Fig. 7.6, it is clear that the differences in the $N(1520)$, $\Delta(1700)$ and $\Delta(1950)$states are the cause of the observed distinctions.

We now discuss distributions over the photon angle. In this regard, we warn the reader that only photon energies up to 2.5 GeV have been considered as explained at the beginning of the section. We reflect this by writing $\tilde{\sigma}$ instead of σ for observables integrated over the photon energy.

[9]The peaks of MINERνA's low and medium energy fluxes are close to 3 and 6 GeV respectively.

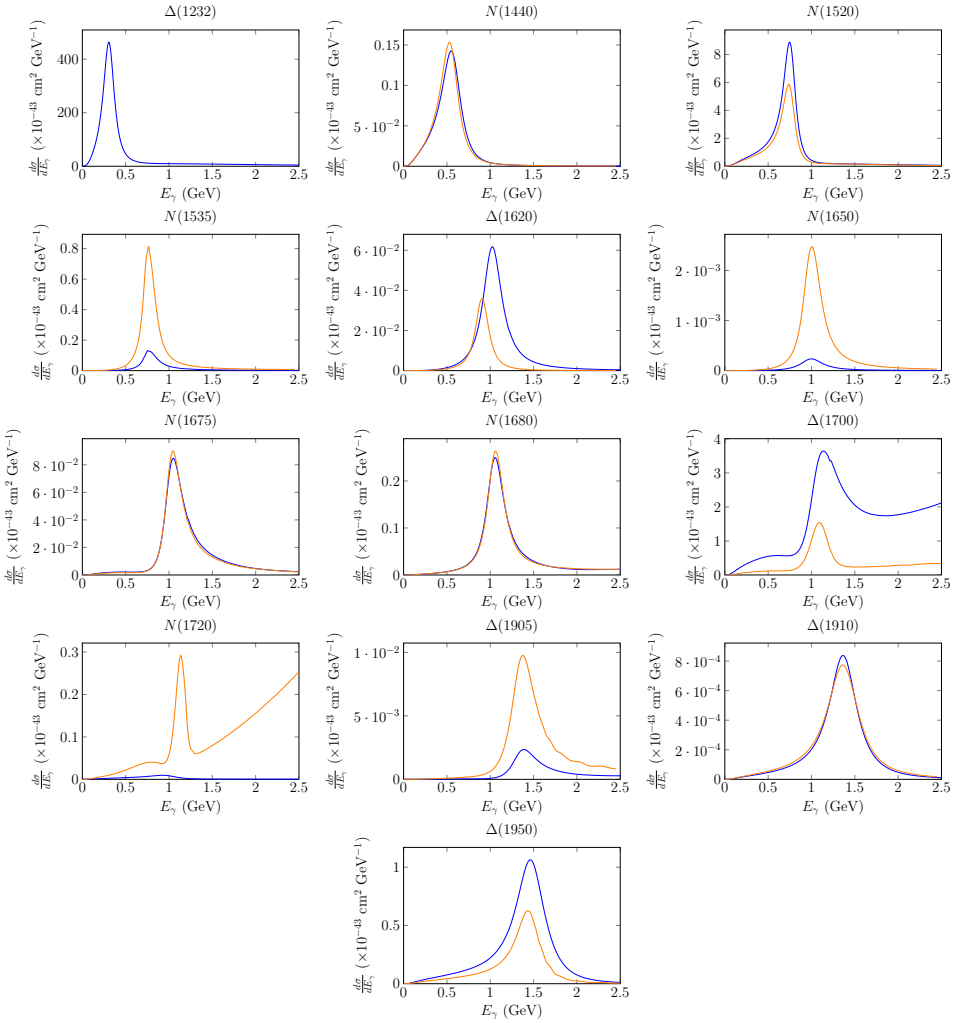

Figure 7.6: Differential cross section for coherent NCγ on ^{12}C as a function of the emitted photon energy, with 3 GeV incoming neutrinos. Individual contributions of each baryon resonance obtained with the MAID (blue) and PDG (orange) parameter sets are displayed.

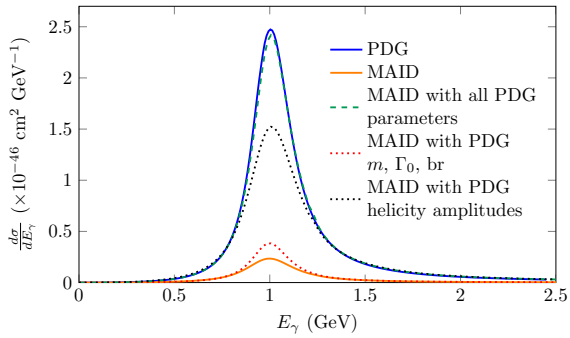

Figure 7.7: Contribution of the $N(1650)$ state to the photon energy distribution in coherent NCγ on ^{12}C with 3 GeV incoming neutrinos. The curves show the difference in the results using the MAID and PDG parameter sets.

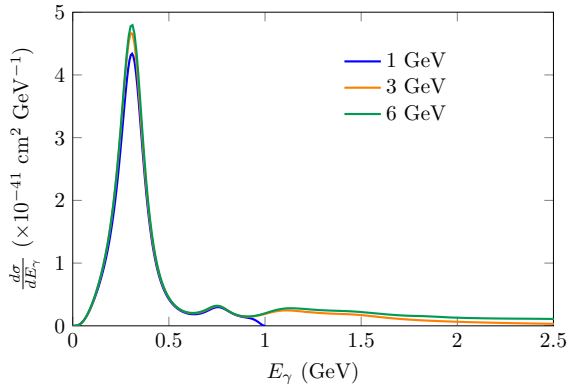

Figure 7.8: Photon energy distribution for coherent NCγ on ^{12}C for 1 GeV, 3 GeV and 6 GeV incoming neutrinos obtained with the MAID set.

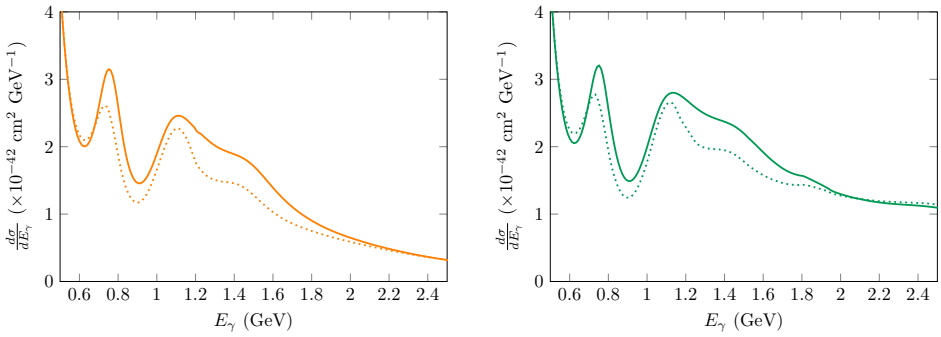

Figure 7.9: Photon energy distribution for coherent NCγ on ^{12}C for 3 GeV (left) and 6 GeV (right) incoming neutrinos obtained with the MAID (solid) and PDG (dashed) sets.

Angular distributions, Fig 7.10, are forward peaked as expected for coherent scattering. As the neutrino energy increases, more strength is accumulated at small photon angles. To minimize the momentum transfer to the nucleus, most of the momentum transferred by the neutrino is taken away by the emitted photon. In other words, for large values of $\left|\vec{q}-\vec{k}_\gamma\right|$ in Eq. (7.7), the integral is dumped due to the rapid oscillations of $\sin\left|\vec{q}-\vec{k}_\gamma\right| r$. That is, higher values of the nuclear FF correspond to small $\left|\vec{q}-\vec{k}_\gamma\right|$. Furthermore, because $q^0 \approx |\vec{k}_\gamma|$ and $q^0 < |\vec{q}|$ the cancellation of $\left|\vec{q}-\vec{k}_\gamma\right|$ also favors small q^2 for which $\vec{q}$ and, therefore, $\vec{k}_\gamma$ are aligned with the incoming neutrino. Note that, for high energy photons, a small change in the angle will be highly disfavored by the nuclear FF. The consequence is that the forward peak is a reflection of the contribution of the high energy tail in the energy distribution.

To explore the dependence on the target mass, we have calculated the integrated cross section as a function of the neutrino energy, Fig. 7.11. As noticed in Ref. [34], we observe that cross-section dependence on the number of nucleons in the nucleus does not scale with A^2 as one would naively expect: while the amplitude in coherent scattering scales with the number of nucleons, the presence of the nuclear FF alters the distribution. As we mentioned before, the FF has a strong dependence on the momentum transferred to the nucleus, vanishing at high values. A consequence of this strong dependence is that a change in the nuclear FF can significantly alter the results, changing the relative position of the different curves in the plot.

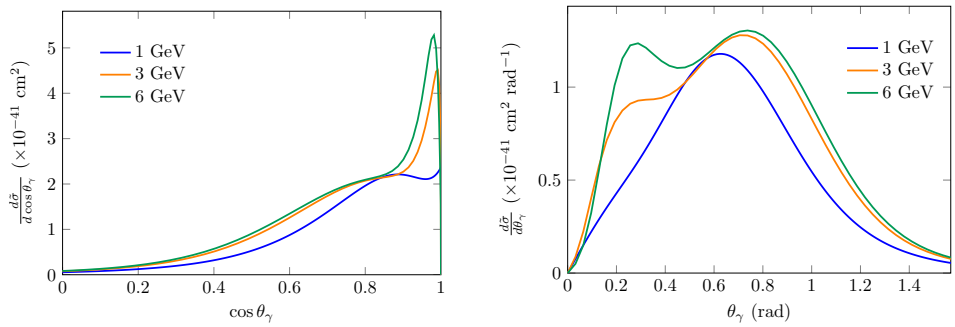

Figure 7.10: Photon angular distribution of the neutrino cross section on ^{12}C, as a function of the cosine of the photon angle (left) and the angle (right). Results for 1 GeV, 3 GeV and 6 GeV incoming neutrinos are shown.

This sensibility to the details of nuclear FF is reflected in the fact that the curve for ^{56}Fe is above the rest, with the exception of ^{12}C, in contrast to the results of Ref. [34], where it is below the lighter nuclei. In any case, the relative size of the cross section for different nuclei shows a soft energy dependence .

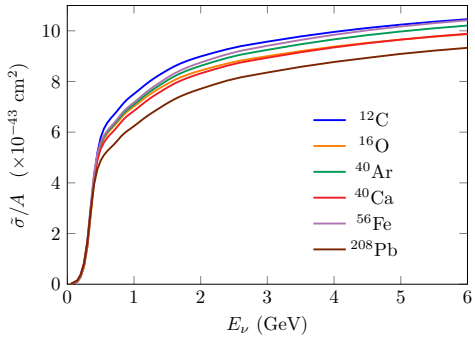

Figure 7.11: Integrated cross section as a function of the incoming neutrino energy, normalized to the number of nucleons. Results are shown for different nuclei.

Finally, we present observables in antineutrino mode. The distributions exhibit the same general features as neutrino mode. The differences between the curves of Fig.7.12 imply a stiffer energy dependence compared to the neutrino case. On the other hand, the peak from the $N(1520)$ is relatively smaller and the tail of the distribution, corresponding to high energy photons, does not decrease as in neutrino mode. We have checked that the

main contributions to the cross section come from the same resonant processes as in the case of neutrino interactions. Analogously to the neutrino

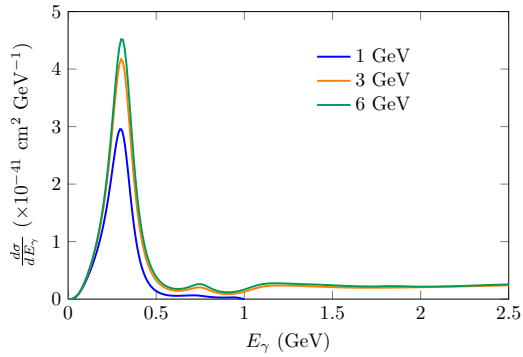

Figure 7.12: Same as Fig. 7.8 but for incoming antineutrinos.

case, we find a forward peaked angular distribution, Fig. 7.13. While the difference in the interference pattern between neutrinos and antineutrinos is barely visible in the energy distribution, it is more apparent in the angular distribution.

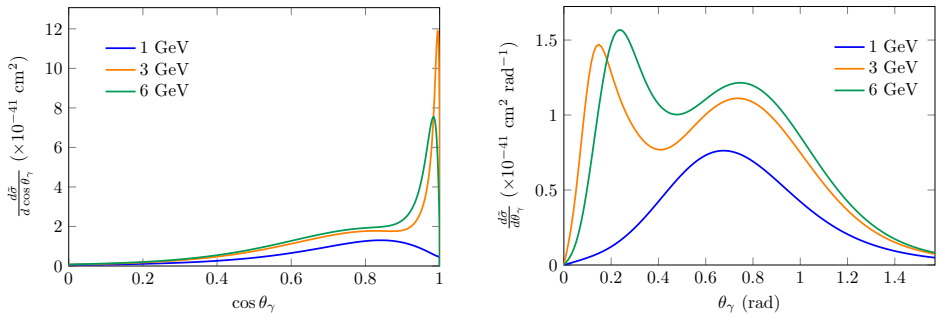

Figure 7.13: Same as Fig. 7.10 but for incoming antineutrinos.

7.5 Summary

The main objective of this study is to extend the validity range of the microscopic model for NC coherent photon emission in neutrino-nucleus scattering introduced in Ref. [34], motivated by the possibility to measure this rare but important process at MINERνA. To accomplish this, we have added heavier resonances to the model, extending the range to an estimated maximum outgoing photon energy of 2.5 GeV. We have verified that, for neutrino energies below 1 GeV, the effect of this addition does not have an appreciable impact on the results. The process mediated by the $\Delta(1232)$ resonance is reported as the main contribution at all incoming neutrino energies. Energy and angular distributions of the emitted photons in the neutrino-nucleus coherent scattering were calculated for both neutrino and antineutrino interactions. The target mass dependence of the integrated cross section was also explored.

The results we obtain predict a strong signal for emitted photons of around 0.3 GeV due to the $\Delta(1232)$ followed by a tail where the $N(1520)$, $\Delta(1700)$ and $\Delta(1950)$ also contribute. The strength of this tail is found predominantly at forward photon angles. To gauge the uncertainties in the present knowledge of baryon resonance properties, including their electromagnetic excitation, we have performed the calculations with two different sets of parameters with different parametrizations of the invariant mass dependence of the resonance width. As expected, the contribution from well known $\Delta(1232)$ is largely independent of these changes, while several other states show a high sensitivity to modifications in the mass, width, πN branching ratio (from which the leading axial couplings are obtained) and, particularly, helicity couplings.

In passing, we performed and validated several approximations in the treatment of nuclear corrections and the $N-\Delta(1232)$ transition form factors aimed at increasing the speed of the computations, making the ongoing implementation of the present model in GENIE. As no model for coherent NCγ emission is currently available in event generators, this effort shall facilitate the experimental study of this reaction at MINERνA but also at MicroBooNE and SBND experiments.

Part III

Conclusions

Neutrino physics have proven to be one of the most challenging fields of modern physics, both theoretically and experimentally. Despite the great progress achieved, there are still many unanswered questions starting from the fact that the SM is not able to fully accommodate these particles. An important branch of neutrino physics is concerned with the modeling of neutrino interactions with matter, where the processes involving strongly interacting hadrons are specially hard to manage. Along this thesis we have tried to bring some light into some open problems in this field.

Several years have been passed since the MiniBooNE anomaly was reported, yet there is still not a definitive explanation to this problem. In Chapter 4 we critically investigated the proposal of the Refs. [4, 5] to explain the excess of events with the production and radiative decay of heavy neutrinos. We have significantly improved previous calculations for both coherent and incoherent processes relying on our present understanding of electroweak interactions with nucleons and nuclei. We have presented results taking into account the electromagnetic, as well as the weak production of heavy neutrinos. We have also investigated the propagation of the heavy neutrino inside the detector, before its decay into a photon and a light neutrino. We initially obtained a bad agreement between our results and the MiniBooNE data for the electron-like excess using the parameters proposed in Ref. [4]. Adding the detector efficiency to the calculation made the results closer to the data but showing a poor agreement. The main discrepancy between this theory and the data are the photon angular distributions. With the original model parameters, the incoherent contribution is very suppressed, resulting in a very forward peaked angular distribution, far away form observations. We therefore fitted the model parameters, within allowed values, to the data. With the new set of values, the influence of the incoherent channel is stronger than the coherent one, resulting in wider angular distributions. In the energy distributions, the new calculations were also closer but still below the data. Indeed, in spite of the improved agreement, the results are not able to provide a full description of the excess: the constraints in the parameter space prevents a better description of the data. Nonetheless, we can not discard this model as a source of part of the signal in the detector. In order to shed further light into this open problem we have predicted the signal that would originate from the production and radiative decay of heavy neutrinos at the three detectors of the SBN program exposed to the Booster neutrino beam at FNAL, which are able to distinguish photons from electrons.

In Chapter 5 we report an analysis of the nucleon axial FF, which is an important source of uncertainty for neutrino cross section modeling. Using the semi-parametric model provided by feedforward neural networks, and the data from the ANL experiment, we were able to obtain a parametrization of this FF. To select the best model, we adopted a Bayesian framework which allows to avoid overfitting problems. After looking at the results, we observed an unexpected behavior at low Q^2, when comparing with previous determinations of the axial FF. The introduction of deuteron corrections in the calculation softened the differences, but there was still no good agreement. When the very low-Q^2 data is not taking into account, our parametrization is fully compatible with other models but with smaller uncertainties. We also performed fits with the dipole parametrization, for the same cases we considered with the neural network. We displayed our results for both parameterizations, showing that the agreement of the neural network with the experimental data is better than for the dipole ansatz. New experiments would be necessary to determine this important quantity with a satisfactory precision and with small systematic errors. The tool we have developed shall be valuable to analyze such data.

In Chapter 6 we describe our improvements to the calculation of single kaon production in neutrino-nucleon scattering reported in Ref. [30]. We partially restored the unitarity of the S-matrix, by imposing Watson's theorem. For this purpose we identified the dominant contribution in each reaction channel and uses them to calculate the Olsson's phases for the vector and axial parts of the elementary amplitudes. This method leads to different solutions for the phases. From these solutions, there is one that has a small impact on the cross section, and another one that changes significantly the observables. The weakness of the kaon-nucleon interaction leads us to think that the set of phases which give a larger correction may not be justified from the physical point of view. Nonetheless we report both extreme result: future experiments should be able to discriminate between them. We also have also calculated the structure functions that characterize the cross section dependence on the azimuthal angle. Remarkably, the terms responsible of parity violation, which vanish at tree level become finite, although small, in presence of the unitarity corrections.

Cherenkov detectors have been very useful in neutrino physics. For this kind of detectors, having good models of their background signals is crucial. As we mentioned before, this type of detector can interpret signal from photons as electron-like events. In Chapter 7 we presented an extension of the Ref. [34] microscopic model for coherent photon emission in neutrino-nucleus

neutral current scattering to higher energies to make it more appropriate for the MINERνA experiment. We also performed and validated several approximations that significantly speed up the computing time, which can be useful when implementing this model in Monte Carlo event generators. The improvement of the model relies on the introduction of heavier baryon resonances that mediate the elementary photon emission process. We explored the impact of uncertainties in our current knowledge of resonance properties on the NCγ cross section. We observed a particular sensitivity to the uncertainties in the electromagnetic helicity amplitudes which influence both the weak resonance production via isospin rotations and its radiative decay. In spite of the large differences found for some states, the overall impact in the cross section is small because of the dominant role of the well understood $\Delta(1232)$ resonance. The angular distributions of photons resulted to be very forward peaked, as expected for coherent scattering. In the case of antineutrinos we observed similar effects than in neutrino mode. We have also obtained the A dependence of the integrated cross section, comparing the results for different nuclei. We observe a strong influence of the nuclear FF, resulting in a behavior which is closer to an A scaling than an A^2 that would be naively expected for coherent scattering. This scaling was found to be rather insensitive of the incoming neutrino energy.

Part IV

Appendix

Appendix A

Conventions

All the calculations contained in this thesis were done in natural units with,

$$\hbar = c = 1 \,, \tag{A.1}$$

where $\hbar$ is the reduced Plank constant and c is the speed of light in the vacuum.

For the metric tensor we follow the convention where

$$g_{\mu\nu} = g^{\mu\nu} = \begin{pmatrix} 1 & 0 & 0 & 0 \\ 0 & -1 & 0 & 0 \\ 0 & 0 & -1 & 0 \\ 0 & 0 & 0 & -1 \end{pmatrix} . \tag{A.2}$$

Pauli matrices read

$$\tau_1 = \begin{pmatrix} 0 & 1 \\ 1 & 0 \end{pmatrix} , \qquad \tau_2 = \begin{pmatrix} 0 & -\mathbb{i} \\ \mathbb{i} & 0 \end{pmatrix} , \qquad \tau_3 = \begin{pmatrix} 1 & 0 \\ 0 & -1 \end{pmatrix} , \tag{A.3}$$

and satisfy the commutation rules given by

$$[\tau_i, \tau_j] = \mathbb{i} 2\epsilon_{ijk}\tau_k \,, \qquad \{\tau_i, \tau_j\} = \delta_{ij} \,, \tag{A.4}$$

where $i, j, k = 1, 2, 3$, δ_{ij} is the Kronecker delta and the tensor ϵ_{ijk} is totally antisymmetric, with $\epsilon_{123} = 1$.

A.1 Dirac algebra

The Dirac matrices are defined in such a way that they satisfy

$$\{\gamma^\mu, \gamma^\nu\} \equiv \gamma^\mu\gamma^\nu + \gamma^\nu\gamma^\mu = 2g^{\mu\nu} \,. \tag{A.5}$$

and

$$\gamma^{\mu\dagger} = \gamma^0 \gamma^\mu \gamma^0 \,. \tag{A.6}$$

We also define

$$\gamma_5 = \gamma_5^\dagger = \mathbb{i}\gamma^0\gamma^1\gamma^2\gamma^3 = -\frac{\mathbb{i}}{4!}\epsilon_{\mu\nu\sigma\rho}\gamma^\mu\gamma^\nu\gamma^\sigma\gamma^\rho \,, \tag{A.7}$$

where for the totally antisymmetric tensor we have

$$\epsilon^{0123} = +1 \,. \tag{A.8}$$

From the Dirac matrices we determine

$$\sigma^{\mu\nu} = \frac{\mathbb{i}}{2}\left[\gamma^\mu, \gamma^\nu\right] \,. \tag{A.9}$$

The quirality projectors are given by

$$P_L = \frac{1}{2}\left(1 - \gamma_5\right) \,, \qquad P_R = \frac{1}{2}\left(1 + \gamma_5\right) \,. \tag{A.10}$$

For the Dirac spinor normalization we use the convention

$$\begin{gathered} \overline{u}_r\left(\vec{p}\right) u_s\left(\vec{p}\right) = 2m\delta_{rs} \,, \qquad \overline{v}_r\left(\vec{p}\right) v_s\left(\vec{p}\right) = -2m\delta_{rs} \,, \\ \overline{u}_r\left(\vec{p}\right) v_s\left(\vec{p}\right) = \overline{v}_r\left(\vec{p}\right) u_s\left(\vec{p}\right) = 0 \,. \end{gathered} \tag{A.11}$$

A.2 Isospin operators on nucleons

The action of the isospin operators over the nucleon isospin states, $|p\rangle$ and $|n\rangle$, is

$$\begin{gathered} \tau_3 |p\rangle = |p\rangle \,, \quad \tau_3 |n\rangle = -|n\rangle \,, \\ \tau_- |p\rangle = |n\rangle \,, \quad \tau_+ |n\rangle = |p\rangle \,, \\ \tau_+ |p\rangle = \tau_- |n\rangle = |0\rangle \,, \\ \tau_\pm = \frac{\tau_1 \pm \mathbb{i}\tau_2}{2} \,, \end{gathered} \tag{A.12}$$

with $\tau_{1,2,3}$ the Pauli matrices:

A.3 Cabibbo-Kobayashi-Masakawa matrix

For three generations of fermions the mixing between quark states are given by the CKM matrix

$$U = \begin{pmatrix} V_{ud} & V_{us} & V_{ub} \\ V_{cd} & V_{cs} & V_{cb} \\ V_{td} & V_{ts} & V_{tb} \end{pmatrix} , \tag{A.13}$$

with [40]

$$\begin{pmatrix} |V_{ud}| & |V_{us}| & |V_{ub}| \\ |V_{cd}| & |V_{cs}| & |V_{cb}| \\ |V_{td}| & |V_{ts}| & |V_{tb}| \end{pmatrix} = \begin{pmatrix} 0.97370 \pm 0.00014 & 0.2245 \pm 0.0008 & (3.82 \pm 0.24) \times 10^{-3} \\ 0.221 \pm 0.004 & 0.987 \pm 0.011 & (41.0 \pm 1.4) \times 10^{-3} \\ (8.0 \pm 0.3) \times 10^{-3} & (38.8 \pm 1.1) \times 10^{-3} & 1.013 \pm 0.030 \end{pmatrix} . \tag{A.14}$$

A.4 Gell-Mann matrices

This representation of the infinitesimal SU(3) group is given by

$$\lambda_1 = \begin{pmatrix} 0 & 1 & 0 \\ 1 & 0 & 0 \\ 0 & 0 & 0 \end{pmatrix} , \quad \lambda_2 = \begin{pmatrix} 0 & -\mathbb{i} & 0 \\ \mathbb{i} & 0 & 0 \\ 0 & 0 & 0 \end{pmatrix} , \quad \lambda_3 = \begin{pmatrix} 1 & 0 & 0 \\ 0 & -1 & 0 \\ 0 & 0 & 0 \end{pmatrix} ,$$
$$\lambda_4 = \begin{pmatrix} 0 & 0 & 1 \\ 0 & 0 & 0 \\ 1 & 0 & 0 \end{pmatrix} , \quad \lambda_5 = \begin{pmatrix} 0 & 0 & -\mathbb{i} \\ 0 & 0 & 0 \\ \mathbb{i} & 0 & 0 \end{pmatrix} , \quad \lambda_6 = \begin{pmatrix} 0 & 0 & 0 \\ 0 & 0 & 1 \\ 0 & 1 & 0 \end{pmatrix} ,$$
$$\lambda_7 = \begin{pmatrix} 0 & 0 & 0 \\ 0 & 0 & -\mathbb{i} \\ 0 & \mathbb{i} & 0 \end{pmatrix} , \quad \lambda_8 = \frac{1}{\sqrt{3}} \begin{pmatrix} 1 & 0 & 0 \\ 0 & 1 & 0 \\ 0 & 0 & -2 \end{pmatrix} . \tag{A.15}$$

Appendix B

Useful integrals

Given a function

$$F_R = \frac{\Theta(q^0)\delta\left(p^0+q^0-E\left(\vec{p}+\vec{q}\right)\right)}{p^0\left(p^0+q^0-E\left(\vec{p}+\vec{q}\right)\right)} n(\vec{p})\left(1-n\left(\vec{p}+\vec{q}\right)\right) \,, \tag{B.1}$$

where p, q are four-vectors, $E(\vec{p}) = \sqrt{\vec{p}^2+m^2}$, m is a constant, Θ is the Heaviside or step function and

$$n(\vec{k}) = \begin{cases} 0; & |\vec{k}| \geq k_F \\ 1; & |\vec{k}| < k_F \end{cases} \,, \tag{B.2}$$

with k_F constant. For the imaginary part of a function defined as

$$\mathrm{Im}\, U_R = \int \frac{d^3p}{4\pi^2} F_R = \frac{\Theta(q^0)\Theta(-q^2)}{4\pi|\vec{q}|}\Theta\left(E_F-\mathcal{E}_R\right)\left(E_F-\mathcal{E}_R\right) \,, \tag{B.3}$$

where

$$\begin{aligned} E_F =& \sqrt{M_{\mathrm{N}}^2+k_F^2} \,, \\ \mathcal{E}_R =& \mathrm{Max}\left\{ M_{\mathrm{N}}, E_F-q^0, \frac{-q^0+|\vec{q}|\sqrt{1-4M_{\mathrm{N}}^2/q^2}}{2} \right\} \,, \end{aligned} \tag{B.4}$$

we have that

$$\int \frac{d^3p}{4\pi^2} F_R E(\vec{p}) = \frac{1}{2}\left(E_F-\mathcal{E}_R\right)\mathrm{Im}\, U_R \,, \tag{B.5}$$

and

$$\int \frac{d^3p}{4\pi^2} F_R E^2(\vec{p}) = \frac{1}{3}\left[E_F^2+\mathcal{E}_R^2+E_F\mathcal{E}_R\right]\mathrm{Im}\, U_R \,. \tag{B.6}$$

B.1 Gaussian integrals

The Gaussian function can be cast as

$$f(x) = e^{-x^2} \,. \tag{B.7}$$

The result of integrating a function of this type over $\mathbb{R}$ reads

$$\int_{-\infty}^{\infty} e^{-a(x+b)^2} dx = \sqrt{\frac{\pi}{a}} \,. \tag{B.8}$$

The n-dimensional generalization of this result, where $\vec{x} = (x_1, \ldots, x_n)$, is

$$\int_{-\infty}^{\infty} e^{-\frac{1}{2}\vec{x}^{\,T}\mathbf{A}\vec{x}} d^n x = \sqrt{\frac{(2\pi)^n}{\det\mathbf{A}}} \,, \tag{B.9}$$

where $\mathbf{A}$ is a symmetric positive-definite $n \times n$ matrix. In the case of having a linear term, then

$$\int_{-\infty}^{\infty} e^{-\frac{1}{2}\vec{x}^{\,T}\mathbf{A}\vec{x} + \vec{B}^{\,T}\vec{x}} d^n x = \sqrt{\frac{(2\pi)^n}{\det\mathbf{A}}} e^{\frac{1}{2}\vec{B}^{\,T}\mathbf{A}^{-1}\vec{B}} \,. \tag{B.10}$$

B.2 Fourier transform properties

The Fourier transform of a function in three dimensions is defined as

$$\tilde{f}(\vec{x}) = \int_{-\infty}^{\infty} f(\vec{\omega}) e^{-\mathrm{i}\vec{\omega}\cdot\vec{x}} d^3\omega \,. \tag{B.11}$$

The inverse Fourier transform, defined as

$$f(\vec{\omega}) = \int_{-\infty}^{\infty} \tilde{f}(\vec{x}) e^{\mathrm{i}\vec{\omega}\cdot\vec{x}} d^3 x \,, \tag{B.12}$$

in the case of a function which only depends on the radial component when transformed in spherical coordinates, can be written as

$$\begin{aligned} f(\vec{\omega}) &= \int_0^{\infty} dr \int_0^{\pi} d\theta \int_0^{2\pi} d\phi f(r) e^{\mathrm{i}\omega r\cos\theta} r^2 \sin\theta \\ &= 2\pi \int_0^{\infty} dr \int_0^{\pi} d\cos\theta \, f(r) e^{\mathrm{i}\omega r\cos\theta} r^2 \\ &= \frac{4\pi}{\omega} \int_0^{\infty} dr \, f(r) \sin(\omega r) r \,. \end{aligned} \tag{B.13}$$

Appendix C

Decay width and cross section

In a given particle interaction, if we label the four-momenta of the initial particles as $p_i = (E_i, \vec{p}_i)\,, i = a, b, \ldots$, and their masses as m_i; and the final as $p_f = (E_f, \vec{p}_f)\,, f = 1, 2, \cdots N$, with masses m_f, the phase space is defined as

$$d\Phi_N \equiv \prod_{f=1}^{N} \left(\frac{d^3 p_f}{(2\pi)^3 2E_f} \right) (2\pi)^4 \delta^{(4)} \left(\sum_f p_f - \sum_i p_i \right) \tag{C.1}$$

C.1 General expression for the decay width

For an unstable particle, a which decay on any number N of other particles, the general expression of the differential decay width reads

$$d\Gamma \left(a \to 1 + 2 + \cdots + N \right) = \frac{1}{2m_a} d\Phi_N |\overline{\mathcal{M}}|^2 \,, \tag{C.2}$$

where $\mathcal{M}$ is the Lorentz-invariant matrix element of the S-matrix which describes the interaction, and

$$|\overline{\mathcal{M}}|^2 \equiv \overline{\sum_{\text{spin}}} |\mathcal{M}|^2 \,, \tag{C.3}$$

is the sum of its modulus squared, over the final particles polarizations and, in the case of non-polarized initial particles, the average over the initial ones.

C.2 General expression for the cross section

In a given reaction where two particles collide producing N outgoing particles, the differential cross section is given by

$$d\sigma\left(a+b\to 1+2+\cdots+N\right)=\frac{1}{2\lambda^{1/2}\left(s,m_a^2,m_b^2\right)}d\Phi_N\left|\overline{\mathcal{M}}\right|^2\ , \qquad \text{(C.4)}$$

where $\lambda\left(x,y,z\right)=x^2+y^2+z^2-2xy-2xz-2yz$ is the Källén function, and $s=\left(p_a+p_b\right)^2$ is the invariant mass of the initial system.

Appendix D

Probability

Given an experiment, the probability to obtain an specific result when a measure is performed is the ratio, Ref. [166],

$$\mathcal{P} = \frac{\text{number of occasion on which that result occurs}}{\text{total number of measurements}} \,. \tag{D.1}$$

If we define $P(A)$ and $P(B)$ as the probabilities to occur of the events labelled as A and B respectively, we have that

$$\mathcal{P}(A+B) \leq \mathcal{P}(A) + \mathcal{P}(B) \,, \tag{D.2}$$

where equality applies for exclusive A and B events.

We define the probability of obtaining both events, A and B, as $\mathcal{P}(A \cap B)$. It can be calculated in terms of the probability of obtaining A, given that B has occurred, $P(A|B)$,

$$\mathcal{P}(A \cap B) = \mathcal{P}(A|B)\mathcal{P}(B) = \mathcal{P}(B|A)\mathcal{P}(A) \,. \tag{D.3}$$

From this result we can obtain

$$\mathcal{P}(A|B) = \frac{\mathcal{P}(A \cap B)}{\mathcal{P}(B)} \,. \tag{D.4}$$

For the case when A is not affected by the occurrence of B, we say that these events are independent, and we have

$$\mathcal{P}(A|B) = \mathcal{P}(A) \,. \tag{D.5}$$

Hence, in this case we obtain

$$\mathcal{P}(A \cap B) = \mathcal{P}(A)\mathcal{P}(B) \,. \tag{D.6}$$

Appendix E

Best-fit results

It is worth noting that each of the sigmoids that constitute the neural networks typically describes a particular feature of the function. If a soft dependence is preferred by the data, some units might be redundant and take very similar values for the weights.

E.1 BIN0 with deuteron corrections

The best-fit parametrization for the BIN0 data set with the deuteron correction included is

$$\begin{aligned}\mathcal{N}(Q^2,\{w_j\}) =& \frac{w_9}{e^{-\frac{Q^2}{Q_0^2}w_1-w_2}+1} + \frac{w_{10}}{e^{-\frac{Q^2}{Q_0^2}w_3-w_4}+1} + \frac{w_{11}}{e^{-\frac{Q^2}{Q_0^2}w_5-w_6}+1} \\ &+ \frac{w_{12}}{e^{-\frac{Q^2}{Q_0^2}w_7-w_8}+1} + w_{13}\,.\end{aligned} \tag{E.1}$$

The weights w_{1-13} take the following values:

$$\begin{aligned}\{w_j\} =\{&-2.174061, 0.1991515, 2.140942, -0.1947798, -2.174070,\\ &0.1991740, -5.481409, 2.501837, -2.502352, 2.308397,\\ &-2.502347, 3.120895, -0.1638095\}\end{aligned} \tag{E.2}$$

with a covariance matrix

$$A^{-1} = \begin{pmatrix}
3.037317 & -0.1350095 & 0.7164281 & 0.6028375 & -0.9106402 & -0.7254212 & -0.1375870 & 0.1193517 & 1.744848 & 0.7934970 & -1.638952 & -0.6857111 & -0.6863036 \\
-0.1350095 & 6.839114 & 0.5963543 & 2.241853 & -0.7253642 & -2.521010 & 0.08826055 & 0.08952850 & 0.5380971 & -0.4953074 & 0.7737700 & 0.5333276 & 0.3832513 \\
0.7164281 & 0.5963543 & 3.129677 & -0.3601146 & 0.7164453 & 0.5964068 & 0.08461544 & -0.05068235 & 1.066743 & 1.171111 & 1.066819 & 0.6044601 & -1.304295 \\
0.6028375 & 2.241853 & -0.3601146 & 7.284083 & 0.6028388 & 2.242126 & -0.1002227 & -0.05207626 & -0.8354786 & 0.1749902 & -0.8355188 & -0.4839537 & -0.08842895 \\
-0.9106402 & -0.7253642 & 0.7164453 & 0.6028388 & 3.037309 & -0.1350448 & -0.1375865 & 0.1193541 & -1.638966 & 0.7934769 & 1.744873 & -0.6857391 & -0.6862827 \\
-0.7254212 & -2.521010 & 0.5964068 & 2.242126 & -0.1350448 & 6.839396 & 0.08828352 & 0.08953791 & 0.7736800 & -0.4953435 & 0.5381072 & 0.5333633 & 0.3832724 \\
-0.1375870 & 0.08826055 & 0.08461544 & -0.1002227 & -0.1375865 & 0.08828352 & 1.348550 & -0.7524626 & -0.8319859 & 0.4259322 & -0.8320014 & 1.535086 & -0.3655335 \\
0.1193517 & 0.08952850 & -0.05068235 & -0.05207627 & 0.1193541 & 0.08953791 & -0.7524626 & 0.5275705 & 0.6937163 & -0.3336553 & 0.6937285 & -0.9665196 & 0.3068238 \\
1.744848 & 0.5380971 & 1.066743 & -0.8354786 & -1.638966 & 0.7736800 & -0.8319859 & 0.6937163 & 13.95026 & 2.966996 & -6.650710 & -1.081263 & -3.213450 \\
0.7934970 & -0.4953074 & 1.171111 & 0.1749902 & 0.7934769 & -0.4953435 & 0.4259322 & -0.3336553 & 2.966996 & 8.333349 & 2.967110 & 0.5435698 & -8.166890 \\
-1.638952 & 0.7737700 & 1.066819 & -0.8355188 & 1.744873 & 0.5381072 & -0.8320014 & 0.6937285 & -6.650710 & 2.967110 & 13.95042 & -1.081328 & -3.213562 \\
-0.6857111 & 0.5333276 & 0.6044601 & -0.4839537 & -0.6857391 & 0.5333633 & 1.535086 & -0.9665196 & -1.081263 & 0.5435698 & -1.081328 & 2.761672 & -0.4607885 \\
-0.6863036 & 0.3832513 & -1.304295 & -0.08842895 & -0.6862827 & 0.3832724 & -0.3655335 & 0.3068238 & -3.213450 & -8.166890 & -3.213562 & -0.4607885 & 8.103694
\end{pmatrix}. \tag{E.3}$$

As explained in Sec. 5.2.2, Eq. 5.7, to obtain $F_A(Q^2)$, function $\mathcal{N}(Q^2, \{w_j\})$ given above should be multiplied by the dipole Eq. (3.54) with $M_A = 1$ GeV.

E.2 BIN1 with deuteron corrections

In this case,

$$\mathcal{N}(Q^2, \{w_j\}) = \frac{w_7}{e^{-\frac{Q^2}{Q_0^2}w_1 - w_2} + 1} + \frac{w_8}{e^{-\frac{Q^2}{Q_0^2}w_3 - w_4} + 1} + \frac{w_9}{e^{-\frac{Q^2}{Q_0^2}w_5 - w_6} + 1} + w_{10}\,, \quad \text{(E.4)}$$

with

$$\begin{aligned}\{w_j\}_{MP} =\{&-0.0703401, 0.0404197, -0.0703404, 0.0404186, -0.0703372,\\ &0.0404192, 0.299085, 0.299087, 0.299086, 0.554479\}\end{aligned}\,, \quad \text{(E.5)}$$

and a covariance matrix

$$A^{-1} = \begin{pmatrix}
0.501347 & 0.000475574 & -0.133756 & 0.00312538 & -0.133756 & 0.00312517 & -0.0951767 & 0.0545460 & 0.0545442 & -0.00759898 \\
0.000475574 & 0.563049 & 0.00312506 & -0.00641521 & 0.00312465 & -0.00641482 & 0.0538884 & -0.0236924 & -0.0236923 & -0.0444412 \\
-0.133756 & 0.00312506 & 0.501346 & 0.000475531 & -0.133757 & 0.00312475 & 0.0545453 & -0.0951765 & 0.0545448 & -0.00759898 \\
0.00312538 & -0.00641521 & 0.000475531 & 0.563050 & 0.00312457 & -0.00641496 & -0.0236928 & 0.0538882 & -0.0236918 & -0.0444415 \\
-0.133756 & 0.00312465 & -0.133757 & 0.00312457 & 0.501347 & 0.000474719 & 0.0545458 & 0.0545457 & -0.0951783 & -0.00759868 \\
0.00312517 & -0.00641482 & 0.00312475 & -0.00641496 & 0.000474719 & 0.563050 & -0.0236928 & -0.0236921 & 0.0538888 & -0.0444415 \\
-0.0951767 & 0.0538884 & 0.0545453 & -0.0236928 & 0.0545458 & -0.0236928 & 0.505143 & -0.101488 & -0.101488 & -0.154622 \\
0.0545460 & -0.0236924 & -0.0951765 & 0.0538882 & 0.0545457 & -0.0236921 & -0.101488 & 0.505144 & -0.101488 & -0.154623 \\
0.0545442 & -0.0236923 & 0.0545448 & -0.0236918 & -0.0951783 & 0.0538888 & -0.101488 & -0.101488 & 0.505144 & -0.154623 \\
-0.00759898 & -0.0444412 & -0.00759898 & -0.0444415 & -0.00759868 & -0.0444415 & -0.154622 & -0.154623 & -0.154623 & 0.246587
\end{pmatrix}. \quad \text{(E.6)}$$

Bibliography

[1] J. A. Formaggio, G. P. Zeller, *Rev. Mod. Phys.* **84**, 1307 (2012).

[2] T. Katori, J. Conrad, *Adv.High Energy Phys.* **2015**, 362971 (2015).

[3] E. Wang, L. Alvarez-Ruso, J. Nieves, *Phys.Lett.* **B740**, 16 (2015).

[4] M. Masip, P. Masjuan, D. Meloni, *JHEP* **1301**, 106 (2013).

[5] S. N. Gninenko, *Phys. Rev.* **D83**, 015015 (2011).

[6] D. McKeen, M. Pospelov, *Phys. Rev. D* **82**, 113018 (2010).

[7] J. Arrington, C. D. Roberts, J. M. Zanotti, *J. Phys.* **G34**, S23 (2007).

[8] T. Katori, M. Martini, *J. Phys.* **G45**, 013001 (2018).

[9] W. A. Mann, *et al.*, *Phys. Rev. Lett.* **31**, 844 (1973).

[10] S. J. Barish, *et al.*, *Phys. Rev.* **D16**, 3103 (1977).

[11] K. L. Miller, *et al.*, *Phys. Rev.* **D26**, 537 (1982).

[12] N. J. Baker, *et al.*, *Phys. Rev.* **D23**, 2499 (1981).

[13] T. Kitagaki, *et al.*, *Phys. Rev.* **D42**, 1331 (1990).

[14] T. Kitagaki, *et al.*, *Phys. Rev.* **D28**, 436 (1983).

[15] D. Allasia, *et al.*, *Nucl. Phys.* **B343**, 285 (1990).

[16] A. Bodek, S. Avvakumov, R. Bradford, H. S. Budd, *Eur. Phys. J.* **C53**, 349 (2008).

[17] A. S. Meyer, M. Betancourt, R. Gran, R. J. Hill, *Phys. Rev.* **D93**, 113015 (2016).

[18] R. J. Hill, P. Kammel, W. J. Marciano, A. Sirlin, *Rept. Prog. Phys.* **81**, 096301 (2018).

[19] C. Alexandrou, *et al.*, *Phys. Rev.* **D96**, 054507 (2017).

[20] S. Capitani, *et al.*, *Int. J. Mod. Phys. A* **34**, 1950009 (2019).

[21] R. Gupta, Y.-C. Jang, H.-W. Lin, B. Yoon, T. Bhattacharya, *Phys. Rev.* **D96**, 114503 (2017).

[22] D.-L. Yao, L. Alvarez-Ruso, M. J. Vicente-Vacas, *Phys. Rev.* **D96**, 116022 (2017).

[23] K. M. Graczyk, C. Juszczak, *Phys. Rev.* **C90**, 054334 (2014).

[24] R. D. Ball, *et al.*, *Nucl. Phys.* **B874**, 36 (2013).

[25] K. Hornik, M. Sinchcombe, W. Halbert, *Neural Networks* **2**, 359 (1989).

[26] G. D'Agostini, *Bayesian Reasoning in Data Analysis* (World Scientific, 2003).

[27] D. MacKay, Bayesian methods for adaptive models, Ph.D. thesis, California Institute of Technology (1991).

[28] K. M. Graczyk, P. Plonski, R. Sulej, *JHEP* **09**, 053 (2010).

[29] C. M. Marshall, *et al.*, *Phys. Rev.* **D94**, 012002 (2016).

[30] M. Rafi Alam, I. Ruiz Simo, M. Sajjad Athar, M. J. Vicente Vacas, *Phys. Rev.* **D82**, 033001 (2010).

[31] L. Alvarez-Ruso, E. Hernández, J. Nieves, M. J. Vicente Vacas, *Phys. Rev.* **D93**, 014016 (2016).

[32] R. J. Hill, *Phys. Rev. D* **81**, 013008 (2010).

[33] X. Zhang, B. D. Serot, *Phys. Rev. C* **86**, 035504 (2012).

[34] E. Wang, L. Alvarez-Ruso, J. Nieves, *Phys. Rev. C* **89**, 015503 (2014).

[35] J. Conrad, C. Ignarra, G. Karagiorgi, M. Shaevitz, J. Spitz, *Adv. High Energy Phys.* **2013**, 163897 (2013).

[36] D. Rein, L. Sehgal, *Phys. Lett. B* **104**, 394 (1981). [Erratum: Phys.Lett.B 106, 513 (1981)].

[37] M. E. Peskin, D. V. Schroeder, *An Introduction to quantum field theory* (Addison-Wesley, Reading, USA, 1995).

[38] F. Mandl, G. Shaw, *QUANTUM FIELD THEORY* (1985).

[39] C. Giunti, C. W. Kim, *Fundamentals of Neutrino Physics and Astrophysics* (2007).

[40] P. Zyla, *et al.*, *PTEP* **2020**, 083C01 (2020).

[41] S. Scherer, M. R. Schindler, *Lect. Notes Phys.* **830**, pp.1 (2012).

[42] A. W. Thomas, W. Weise, *The Structure of the Nucleon* (Wiley-VCH, 2001).

[43] A. Pich, *Reports on Progress in Physics* **58**, 563–609 (1995).

[44] M. Gell-Mann, M. Levy, *Nuovo Cim.* **16**, 705 (1960).

[45] N. Cabibbo, E. C. Swallow, R. Winston, *Ann. Rev. Nucl. Part. Sci.* **53**, 39 (2003).

[46] M. Rafi Alam, I. Ruiz Simo, M. Sajjad Athar, M. J. Vicente Vacas, *Phys. Rev. D* **82**, 033001 (2010).

[47] E. Hernández, J. Nieves, M. Valverde, *Phys. Rev. D* **76**, 033005 (2007).

[48] J. D. Walecka, *Electron scattering for nuclear and nucleon structure*, vol. 16 (Cambridge University Press, 2005).

[49] S. Galster, *et al.*, *Nucl. Phys.* **B32**, 221 (1971).

[50] V. Bernard, L. Elouadrhiri, U.-G. Meissner, *J. Phys.* **G28**, R1 (2002).

[51] M. González-Alonso, O. Naviliat-Cuncic, N. Severijns (2018).

[52] F. Halzen, A. D. Martin, *Quarks and Leptons: An Introductory Course in Modern Particle Physics* (1984).

[53] S. Boffi, C. Giusti, F. d. Pacati, M. Radici, *Electromagnetic Response of Atomic Nuclei*, vol. 20. 20 of *Oxford Studies in Nuclear Physics* (Clarendon Press, Oxford UK, 1996).

[54] Y.-S. Tsai, *Rev. Mod. Phys.* **46**, 815 (1974). [Erratum: Rev. Mod. Phys.49,521(1977)].

[55] H. De Vries, C. De Jager, C. De Vries, *Atom.Data Nucl.Data Tabl.* **36**, 495 (1987).

[56] A. A. Aguilar-Arevalo, *et al.*, *Phys. Rev. Lett.* **102**, 101802 (2009).

[57] A. Aguilar-Arevalo, *et al.*, *Phys.Rev.Lett.* **110**, 161801 (2013).

[58] A. Aguilar-Arevalo, *et al.* (2020).

[59] C. Giunti, M. Laveder, Y. F. Li, H. W. Long, *Phys. Rev.* **D88**, 073008 (2013).

[60] M. Ericson, M. V. Garzelli, C. Giunti, M. Martini, *Phys. Rev.* **D93**, 073008 (2016).

[61] R. J. Hill, *Phys. Rev.* **D84**, 017501 (2011).

[62] X. Zhang, B. D. Serot, *Phys. Lett.* **B719**, 409 (2013).

[63] E. Bertuzzo, S. Jana, P. A. Machado, R. Zukanovich Funchal, *Phys. Rev. Lett.* **121**, 241801 (2018).

[64] C. A. Argüelles, M. Hostert, Y.-D. Tsai, *Phys. Rev. Lett.* **123**, 261801 (2019).

[65] S. N. Gninenko, *Phys. Rev. Lett.* **103**, 241802 (2009).

[66] MiniBooNE collaboration, https://www-boone.fnal.gov/for_physicists/data_release/. [Online; accessed 28-October-2020].

[67] C. Broggini, C. Giunti, A. Studenikin, *Adv. High Energy Phys.* **2012**, 459526 (2012).

[68] A. Gil, J. Nieves, E. Oset, *Nucl. Phys.* **A627**, 543 (1997).

[69] J. Nieves, J. E. Amaro, M. Valverde, *Phys. Rev.* **C70**, 055503 (2004). [Erratum: Phys. Rev.C72,019902(2005)].

[70] D. Akimov, *et al.*, *Science* **357**, 1123 (2017).

[71] A. Aguilar-Arevalo, *et al.*, *Phys.Rev.* **D81**, 092005 (2010).

[72] A. Aguilar-Arevalo, *et al.*, *Phys. Rev.* **D64**, 112007 (2001).

[73] A. Aguilar-Arevalo, *et al.*, *Phys.Rev.* **D79**, 072002 (2009).

[74] A. Radionov, *Phys. Rev.* **D88**, 015016 (2013).

[75] R. Acciarri, *et al.*, A proposal for a three detector short-baseline neutrino oscillation program in the fermilab booster neutrino beam (2015).

[76] G. Karagiorgi, *Phys. Procedia* **37**, 1319 (2012).

[77] Z. Pavlovic, O. Palamara, private communication.

[78] L. Alvarez-Ruso, K. M. Graczyk, E. Saul-Sala, *Phys. Rev.* **C99**, 025204 (2019).

[79] B. Bhattacharya, R. J. Hill, G. Paz, *Phys. Rev.* **D84**, 073006 (2011).

[80] B. Bhattacharya, G. Paz, A. J. Tropiano, *Phys. Rev.* **D92**, 113011 (2015).

[81] C. Chang, *et al.*, *Nature* **558**, 91 (2018).

[82] E. Shintani, K.-I. Ishikawa, Y. Kuramashi, S. Sasaki, T. Yamazaki, *Phys. Rev. D* **99**, 014510 (2019).

[83] C. M., Bishop, *Neural Networks for Pattern Recognition* (Oxford University Press, 1995).

[84] L. De Cruz, T. Vrancx, P. Vancraeyveld, J. Ryckebusch, *Phys. Rev. Lett.* **108**, 182002 (2012).

[85] J. D. McDonnell, *et al.*, *Phys. Rev. Lett.* **114**, 122501 (2015).

[86] K. M. Graczyk, *Phys. Rev.* **C84**, 034314 (2011).

[87] K. M. Graczyk, *Phys. Rev.* **C88**, 065205 (2013).

[88] K. M. Graczyk, C. Juszczak, *J. Phys.* **G42**, 034019 (2015).

[89] K. M. Graczyk, C. Juszczak, *Phys. Rev.* **C91**, 045205 (2015).

[90] F. Rosenblatt, *Principles of Neurodynamics* (New York: Spartan, 1962).

[91] G. Cybenko, *Math Control, Signal* **2**, 303 (1989).

[92] K.-I. Funahashi, *Neural Networks* **2**, 183 (1989).

[93] R. Hecht-Nielsen, *International 1989 Joint Conference on Neural Networks* (1989), pp. 593–605 vol.1.

[94] N. E. Cotter, *IEEE Transactions on Neural Networks* **1**, 290 (1990).

[95] Y. Ito, *Neural Networks* **4**, 385 (1991).

[96] V. Y. Kreinovich, *Neural Networks* **4**, 381 (1991).

[97] S. Geman, E. Bienenstock, R. Doursat, *Neural Computation* **4**, 1 (1992).

[98] J. O. Berger, W. H. Jefferys, *Journal of the Italian Statistical Society* **1**, 17 (1992).

[99] W. H. Jefferys, J. O. Berger, *American Scientist* **80**, 64 (1992).

[100] R. Pohl, *et al.*, *Nature* **466**, 213 (2010).

[101] I. Sick, *Atoms* **6**, 2 (2018).

[102] D. J. C. MacKay, *Neural Computation* **4**, 415 (1992).

[103] D. J. C. MacKay, *Neural Computation* **4**, 448 (1992).

[104] G. P. Lepage, *et al.*, *Nucl. Phys. Proc. Suppl.* **106**, 12 (2002).

[105] G. E. Hinton, *PARLE Parallel Architectures and Languages Europe*, J. W. de Bakker, A. J. Nijman, P. C. Treleaven, eds. (Springer Berlin Heidelberg, Berlin, Heidelberg, 1987), pp. 1–13.

[106] A. M. Chen, H.-m. Lu, R. Hecht-Nielsen, *Neural Computation* **5**, 910 (1993).

[107] V. Kurková, P. Kainen, *Neural Computation* **6**, 543 (1994).

[108] C. H. Llewellyn Smith, *Phys. Rept.* **3**, 261 (1972).

[109] S. K. Singh, H. Arenhövel, *Z. Phys.* **A324**, 347 (1986).

[110] S. J. Barish, *et al.*, *Phys. Rev.* **D19**, 2521 (1979).

[111] G. D'Agostini, *Nucl. Instrum. Meth.* **A346**, 306 (1994).

[112] K. M. Graczyk, D. Kielczewska, P. Przewlocki, J. T. Sobczyk, *Phys. Rev.* **D80**, 093001 (2009).

[113] K. Levenberg, *Quart. Appl. Math.* **2**, 164 (1944).

[114] D. W. Marquardt, *J. Soc. Indust. Appl. Math.* **11**, 431–441 (1963).

[115] G. Shen, L. E. Marcucci, J. Carlson, S. Gandolfi, R. Schiavilla, *Phys. Rev.* **C86**, 035503 (2012).

[116] O. Moreno, T. W. Donnelly, J. W. Van Orden, W. P. Ford, *Phys. Rev.* **D92**, 053006 (2015).

[117] O. Lalakulich, K. Gallmeister, U. Mosel, *Phys. Rev.* **C86**, 014607 (2012).

[118] R. E. Shrock, *Phys. Rev.* **D12**, 2049 (1975).

[119] W. Mecklenburg, *Acta Phys. Austriaca* **48**, 293 (1978).

[120] A. A. Amer, *Phys. Rev.* **D18**, 2290 (1978).

[121] H. K. Dewan, *Phys. Rev.* **D24**, 2369 (1981).

[122] G. B. Adera, B. I. S. Van Der Ventel, D. D. van Niekerk, T. Mart, *Phys. Rev.* **C82**, 025501 (2010).

[123] S. X. Nakamura, H. Kamano, T. Sato, *Phys. Rev.* **D92**, 074024 (2015).

[124] M. R. Alam, I. R. Simo, M. S. Athar, M. J. Vicente Vacas, *Phys. Rev.* **D85**, 013014 (2012).

[125] X.-L. Ren, E. Oset, L. Alvarez-Ruso, M. J. Vicente Vacas, *Phys. Rev.* **C91**, 045201 (2015).

[126] K. M. Watson, *Phys. Rev.* **88**, 1163 (1952). [Riv. Nuovo Cim.31,1(2008)].

[127] M. G. Olsson, *Nucl. Phys.* **B78**, 55 (1974).

[128] E. Hernández, J. Nieves, *Phys. Rev. D* **95**, 053007 (2017).

[129] E. Hernandez, J. Nieves, M. Valverde, *Phys. Rev.* **D76**, 033005 (2007).

[130] A. D. Martin, T. D. Spearman, *Elementary-particle theory* (North-Holland, Amsterdam, 1970).

[131] Institute for Nuclear Studies. The George Washington University Virginia Science and Technology Campus, http://http://gwdac.phys.gwu.edu/. [Online; accessed 22-February-2019].

[132] M. Antonello, *et al.*, A Proposal for a Three Detector Short-Baseline Neutrino Oscillation Program in the Fermilab Booster Neutrino Beam (2015).

[133] J. Sobczyk, E. Hernández, S. Nakamura, J. Nieves, T. Sato, *Phys. Rev.* **D98**, 073001 (2018).

[134] E. Hernandez, J. Nieves, M. Valverde, *Phys. Lett.* **B647**, 452 (2007).

[135] L. Alvarez-Ruso, *et al.*, *Prog. Part. Nucl. Phys.* **100**, 1 (2018).

[136] C. Berger, L. Sehgal, *Phys. Rev. D* **79**, 053003 (2009).

[137] E. Paschos, D. Schalla, *Phys. Rev. D* **80**, 033005 (2009).

[138] J. Amaro, E. Hernandez, J. Nieves, M. Valverde, *Phys. Rev. D* **79**, 013002 (2009).

[139] S. Nakamura, T. Sato, T.-S. Lee, B. Szczerbinska, K. Kubodera, *Phys. Rev. C* **81**, 035502 (2010).

[140] A. Aguilar-Arevalo, *et al.*, *Phys. Rev. Lett.* **121**, 221801 (2018).

[141] E. Valencia, *et al.*, *Phys. Rev. D* **100**, 092001 (2019).

[142] J. Morfin, private communication.

[143] L. Alvarez-Ruso, L. Geng, S. Hirenzaki, M. Vicente Vacas, *Phys. Rev. C* **75**, 055501 (2007). [Erratum: Phys.Rev.C 80, 019906 (2009)].

[144] B. D. Serot, X. Zhang, *Phys. Rev. C* **86**, 015501 (2012).

[145] D. Drechsel, S. Kamalov, L. Tiator, *Eur. Phys. J. A* **34**, 69 (2007).

[146] L. Tiator, D. Drechsel, S. Kamalov, M. Vanderhaeghen, *Eur. Phys. J. ST* **198**, 141 (2011).

[147] D. Manley, E. Saleski, *Phys. Rev. D* **45**, 4002 (1992).

[148] T. Leitner, O. Buss, L. Alvarez-Ruso, U. Mosel, *Phys. Rev. C* **79**, 034601 (2009).

[149] E. Hernandez, J. Nieves, M. Valverde, M. Vicente Vacas, *Phys. Rev. D* **81**, 085046 (2010).

[150] S. L. Adler, *Annals Phys.* **50**, 189 (1968).

[151] J. Bijtebier, *Nucl. Phys. B* **21**, 158 (1970).

[152] D. Drechsel, O. Hanstein, S. Kamalov, L. Tiator, *Nucl. Phys. A* **645**, 145 (1999).

[153] K. Nakayama, H. Haberzettl, *Phys. Rev. C* **73**, 045211 (2006).

[154] O. Buss, Photon- and Pion-induced Reactions in a Transport Approach, Other thesis (2008).

[155] T. E. O. Ericson, W. Weise, *Pions and Nuclei*, vol. 74 (Clarendon Press, Oxford, UK, 1988).

[156] V. Kashevarov, *et al.*, *Phys. Rev. Lett.* **118**, 212001 (2017).

[157] E. Oset, H. Toki, W. Weise, *Phys. Rept.* **83**, 281 (1982).

[158] M. Hirata, J. Koch, E. Moniz, F. Lenz, *Annals Phys.* **120**, 205 (1979).

[159] R. Freedman, G. Miller, E. Henley, *Nucl. Phys. A* **389**, 457 (1982).

[160] E. Oset, L. Salcedo, *Nucl. Phys. A* **468**, 631 (1987).

[161] J. Nieves, E. Oset, C. Garcia-Recio, *Nucl. Phys. A* **554**, 509 (1993).

[162] S. Singh, M. Vicente-Vacas, E. Oset, *Phys. Lett. B* **416**, 23 (1998). [Erratum: Phys.Lett.B 423, 428 (1998)].

[163] J. Lehr, M. Effenberger, U. Mosel, *Nucl. Phys. A* **671**, 503 (2000).

[164] J. Nieves, E. Oset, C. Garcia-Recio, *Nucl. Phys. A* **554**, 554 (1993).

[165] X. Zhang, B. D. Serot, *Phys. Rev. C* **86**, 035502 (2012).

[166] L. Lyons, *Statistics for Nuclear and Particle Physicists* (Cambridge University Press, 1986).

Glossary

$\mathcal{T}$ time reversal. 30, 31, 40, 150

C charge conjugation. 31

G G-parity. 31, 32

P parity. 31

T weak isospin. 9, 14

1p1h one particle one hole. 60, 66

ANL Argonne National Laboratory. 109, 116, 117, 120, 128, 129, 130, 132, 133, 134, 135, 136, 139, 174, 195

BNL Brookhaven National Laboratory. 109, 174

BSM Beyond Standard Model. 108

CC charged-current. 2, 9, 11, 14, 18, 25, 31, 34, 35, 36, 135, 143, 161, 171

CCQE charged-current quasi-elastic. 37, 49, 109, 117, 127, 129, 139

CERN European Organization for Nuclear Research. 109

ChPT chiral perturbation theory. 18, 141

CKM Cabibbo-Kobayashi-Masakawa. 14, 15, 19, 143, 202

CM center of mass. 33, 146, 147, 175, 176

CP combination of charge conjugation and parity symmetries. 52

CVC conservation of the vector current. 43

DIS Deep Inelastic Scattering. 2

EM electromagnetic. 9, 10, 11, 12, 25, 28, 29, 32, 33, 34, 35, 38, 40, 42, 43, 50, 51, 52, 54, 55, 57, 60, 61, 62, 63, 65, 67, 68, 69, 70, 72, 80, 81, 84, 85, 94, 108, 109, 166, 170, 171, 173

FF form factor. 4, 30, 32, 33, 34, 35, 36, 37, 39, 40, 41, 42, 43, 44, 45, 52, 55, 64, 65, 68, 69, 109, 110, 112, 116, 117, 128, 130, 133, 134, 136, 139, 141, 144, 165, 170, 171, 173, 174, 182, 183, 184, 185, 188, 195, 196

FNAL Fermi National Accelerator Laboratory. 78, 93, 109, 195

GT Goldberger-Treiman. 37, 171, 174, 176, 178, 179

HCM hadronic center-of-mass. 142, 151, 156

ICARUS Imaging Cosmic And Rare Underground Signals. 51, 91, 102

KARMEN KArlsruhe Rutherford Medium Energy Neutrino experiment. 83

LArTPC liquid argon time projection chamber. 91

LDA Local Density Approximation. 57, 66

LSND Liquid Scintillator Neutrino Detector. 51, 83, 84, 91

MAID Mainz Unitary Isobar model. 166, 168, 170, 174, 175, 179, 183, 184, 185, 184, 185

MBF many body framework. 57

MicroBooNE Micro Booster Neutrino Experiment. 51, 55, 91, 92, 93, 94, 99, 161, 191

MiniBooNE Mini Booster Neutrino Experiment. 3, 4, 49, 50, 51, 50, 51, 55, 57, 77, 78, 79, 81, 83, 84, 85, 84, 85, 91, 92, 93, 94, 108, 161, 195

MLP multilayer perceptron. 113, 114, 115, 116, 118, 119, 130, 131, 132, 137

NC neutral-current. 2, 4, 9, 11, 13, 14, 19, 25, 35, 36, 37, 43, 49, 61, 62, 63, 64, 65, 67, 68, 69, 70, 72, 80, 81, 84, 108, 161, 162, 170, 171, 173, 179, 183, 184, 185, 191, 196

NNPDF neural network parton distribution function. 110

PCAC partial conservation of the axial current. 4, 16, 161, 162

PDG Particle Data Group. 116, 130, 131, 136, 166, 168, 175, 179, 184, 185, 184, 185

PMT photomultiplier tube. 77

POT protons on target. 72, 78

QCD Quantum Chromodynamics. 15, 16, 17, 18, 110, 133, 134

QE quasi-elastic. 2, 3, 4, 25, 30, 40, 55, 60, 61, 67, 135

QFT Quantum Field Theory. 9

SAID Scattering Analyses Interactive Dialin. 155, 166

SBN Short-Baseline Neutino Program. 4, 51, 91, 92, 93, 94, 102, 108, 195

SBND Short-Baseline Near Detector. 51, 85, 91, 94, 99, 155, 161, 191

SM Standard Model. 1, 9, 10, 53, 61, 62, 94, 195

SSB spontaneous symmetry breaking. 17

TPC time projection chamber. 92, 94, 102